

Magnetohydrodynamic Simulation of Reconnection in Turbulent Astrophysical Plasmas

Dissertation

zur Erlangung des mathematisch-naturwissenschaftlichen Doktorgrades

“Doctor rerum naturalium”

der Georg-August-Universität Göttingen

im Promotionsprogramm PROPHYS

der Georg-August University School of Science (GAUSS)

vorgelegt von

Fabien Widmer

aus Genf, Schweiz

Göttingen, 2016

Betreuungsausschuss

Prof. Dr. Jörg Büchner

Max-Planck-Institut für Sonnensystemforschung, Göttingen, Germany

Dr. Wolfram Schmidt

Hamburger Sternwarte, Fachbereich Physik, Universität Hamburg, Germany

Prof. Dr. Laurent Gizon

Institut für Astrophysik, Georg-August-Universität Göttingen, Göttingen, Germany

Max-Planck-Institut für Sonnensystemforschung, Göttingen, Germany

Mitglieder der Prüfungskommission

Referent: Prof. Dr. Jörg Büchner

Max-Planck-Institut für Sonnensystemforschung, Göttingen, Germany

Korreferent: Prof. Dr. Stefan Dreizler

Institut für Astrophysik, Georg-August-Universität Göttingen, Göttingen, Germany

Weitere Mitglieder der Prüfungskommission:

Prof. Dr. Laurent Gizon

Institut für Astrophysik, Georg-August-Universität Göttingen, Göttingen, Germany

Max-Planck-Institut für Sonnensystemforschung, Göttingen, Germany

Prof. Dr. Hardi Peter

Max-Planck-Institut für Sonnensystemforschung, Göttingen, Germany

Dr. Wolfram Schmidt

Hamburger Sternwarte, Fachbereich Physik, Universität Hamburg, Germany

Prof. Dr. Andreas Tilgner

Institut für Geophysik, Georg-August-Universität Göttingen, Göttingen, Germany

Tag der mündlichen Prüfung: 19.07.2016

Bibliografische Information der Deutschen Nationalbibliothek

Die Deutsche Nationalbibliothek verzeichnet diese Publikation in der Deutschen Nationalbibliografie; detaillierte bibliografische Daten sind im Internet über <http://dnb.d-nb.de> abrufbar.

ISBN 978-3-944072-52-4

uni-edition GmbH 2016

<http://www.uni-edition.de>

© Fabien Widmer



This work is distributed under a
Creative Commons Attribution 3.0 License

Printed in Germany

Contents

1	Summary	13
2	Introduction	15
2.1	The Sun	15
2.2	The Importance of Magnetic Reconnection	18
2.3	Turbulence	21
2.4	Addressing the Open Questions	22
3	Magnetohydrodynamics (MHD)	25
3.1	Single fluid and Non-Relativistic Maxwell's Equations	26
3.1.1	Ideal MHD	28
3.1.2	Ideal Invariants	29
3.1.3	Resistive MHD	31
3.2	Resistive MHD equations	32
4	Mean-Field MHD Turbulence Theory	33
4.1	Reynolds-Averaged Navier-Stokes Equations	33
4.1.1	Turbulence Nomenclature, Symmetry Laws and Averaging Rules	33
4.1.2	Mean and Fluctuating Fields Equations	35
4.2	Reynolds-Averaged Turbulence Model	40
4.2.1	Bulk Turbulence Model	41
4.3	Turbulent Electromotive Force and Turbulence Productions	43
4.3.1	Production of Turbulent Energy and Turbulent Cross-Helicity . .	43
5	Subgrid-Scale Phenomena	47
5.1	Filtered Equations	47
5.2	Non-Linear Turbulence Model	49
6	Kolmogorov Theory	51
6.1	Dimensional Consideration and Energy Cascade	51
7	Magnetic Reconnection	55
7.1	Sweet-Parker Reconnection	55
7.2	Petschek Reconnection	57
7.2.1	Angle of Reconnection	57
7.3	Mean-Field Turbulent Reconnection	58

7.3.1	Turbulent Sweet-Parker Reconnection	58
7.3.2	Petschek Turbulent Reconnection	61
7.4	Guide Field Reconnection	61
7.4.1	Turbulent Guide Field Reconnection	63
7.5	Reconnection from MHD Instabilities	63
7.5.1	Tearing mode instability	64
7.5.2	The Plasmoid Instability	67
8	Single ‘X’-Point Turbulent Reconnection - Mean-Field Theory and Simulation	69
8.1	Simplified Bulk Turbulence Model	70
8.1.1	Initial Configurations	71
8.1.2	Regimes of Reconnection and Energy Transfer	73
8.1.3	Limits of Large Magnetic Reynolds Numbers	77
8.1.4	Energy Transfer	79
8.1.5	Guide Magnetic Field Effects on Turbulence	84
8.1.6	Mean-Field Inhomogeneities, Turbulence and Reconnection Rate	86
8.2	Importance of the Cross-Helicity Due to Turbulence for Fast Magnetic Reconnection	88
9	Self Consistent Turbulence Timescale	91
9.1	Energy Dissipation Rate Equation	91
10	Influence of Turbulence on the Plasmoid Instability	97
10.1	Introduction	97
10.2	High Resolution Simulations of Plasmoid-Unstable Current Sheets	98
10.2.1	Plasmoid Instability Reconnection Rate	100
10.3	Turbulent Electromotive Force and Stress-Tensor in the Reconnection Regimes	103
10.4	Applicability of Turbulence Models to Magnetic Reconnection	106
10.4.1	Applicability of the Non-linear SGS Model	106
10.4.2	Applicability of the Mean-Field Turbulence Model	107
10.5	Influence of Turbulence on the Plasmoid Instability	113
10.5.1	Turbulent Energy Transfer	116
10.5.2	Reconnection Rate in Presence of Turbulence	118
11	Conclusions	121
11.1	Outlook	126
	Appendices	127
A	Normalisation and Numerical Scheme	129
A.1	Normalisations	129
A.2	MacCormack Scheme	132
B	Mean Mass Density Fluctuations	135

C Two-Scales Direct-Interaction Approximation: TSDIA	137
D Filtering Minimisation	139
Bibliography	141

List of Figures

2.1	The Sun. Credits: SOHO (ESA & NASA)	15
2.2	Electron temperature and density above the photosphere.	16
2.3	Plasma- β_p in the Sun's atmosphere.	17
2.4	Schematic of a flare model. Credits: NASA	17
2.5	Schematic of magnetic reconnection	19
2.6	Structure of the Earth's magnetosphere. Credit: NASA/Goddard/Aaron Kaase.	20
2.7	Range of applicability of turbulence models.	23
4.1	Schematic of the turbulence production terms at and around a current sheet diffusion region.	44
6.1	Schematic of a log-log plot of the energy spectrum or cascade.	53
7.1	Schematic of the internal and external region for an SP current sheet.	56
7.2	Schematic of the angle of reconnection θ	58
7.3	Sketch of the internal and external region of a current sheet reconnection in the presence of a guide magnetic field.	62
8.1	Force-free initial in-plane current density.	73
8.2	Spatial distribution of the turbulent energy, the turbulent cross-helicity, the mean current density and the mean vorticity.	74
8.3	Reconnection rate in time and regimes of reconnection for various turbu- lence timescale parameter. Harris-type CS.	75
8.4	Reconnection rate in time and regimes of reconnection for various turbu- lence timescale parameter. Force-free CS.	76
8.5	Reconnection rate in time as the resistivity is varied.	78
8.6	Maximum reconnection rate as a function of β_0 and η for the Harris-type current sheet equilibrium ($b_g = 0$).	78
8.7	Reconnection rate in time for various β_0 and dependance of the resistivity η	79
8.8	Kinetic and magnetic energy spectra for various τ	80
8.9	Energy spectra averaged in time for the timescales representing the regimes of energy conversion.	81
8.10	Total energy spectrum for various resistivity η taken at different times.	82
8.11	Plasma kinetic and magnetic energy spectrum averaged in time for various resistivity η	83
8.12	Estimated α terms proportional to the residual helicity H	85

8.13	Time evolution of the reconnection rate of an Harris-type current sheet equilibrium with constant guide magnetic fields B_g	85
8.14	Time history of the mean current density, the mean vorticity, turbulent energy and turbulent cross-helicity W amplitudes.	87
8.15	Reconnection rate as a function of time and turbulent timescale for a fixed η . Case of $W \equiv 0$	88
8.16	Reconnection rate as a function of time and resistivity for a fixed τ . Case of $W \equiv 0$	89
9.1	Spatial distribution of the mean current density, the mean vorticity, the turbulent energy, its dissipation rate, the turbulent cross-helicity and the turbulent timescale.	93
9.2	Time history of the reconnection rate for different initial values of the turbulent energy.	94
9.3	Schematics of the mean forces balance for a current sheet equilibrium.	95
10.1	Reconnection rate with respect to the time for plasmoid-unstable current sheets.	100
10.2	Spatial distribution of the magnetic field and velocity flow of plasmoid-unstable current sheets.	102
10.3	Spatial distribution of the current density and the vorticity of plasmoid-unstable current sheets.	103
10.4	Spatial distribution of the turbulent stress-tensor components of a Harris-type plasmoid-unstable current sheet.	104
10.5	Spatial distribution of the turbulent stress-tensor components of a force-free plasmoid-unstable current sheet.	105
10.6	Spatial distribution of the turbulent electromotive force components of a force-free- and Harris-type plasmoid-unstable current sheet.	106
10.7	Spatial distribution of the non-linear SGS turbulent stress-tensor components of a force-free- and Harris-type plasmoid-unstable current sheet.	107
10.8	Correlations of the non-linear SGS stress-tensor for a force-free- and Harris-type plasmoid-unstable current sheet.	108
10.9	Spatial distribution of the SGS electromotive force model of a force-free and a Harris-type plasmoid-unstable current sheet.	109
10.10	Correlations of the non-linear SGS electromotive force for a force-free and a Harris-type plasmoid-unstable current sheet.	110
10.11	Spatial distribution of the SGS stress-tensor model components of a force-free and a Harris-type plasmoid-unstable current sheet.	111
10.12	Correlations of the turbulent stress-tensor for a force-free- and Harris-type plasmoid-unstable current sheet.	111
10.13	Spatial distribution of the SGS energy K_{SGS} and cross-helicity W_{SGS} for a force-free- and Harris-type plasmoid-unstable current sheet.	112
10.14	Spatial distribution of the SGS residual helicities for a force-free and a Harris-type plasmoid-unstable current sheet.	113
10.15	Spatial distribution of the SGS electromotive force model for a force-free and Harris-type plasmoid-unstable current sheet.	114

10.16	Correlations of the turbulent electromotive force for a force-free and Harris-type plasmoid-unstable current sheet.	115
10.17	Time history of the evolution of the magnetic and kinetic energy for a force-free and a Harris-type plasmoid-unstable current sheet	115
10.18	Components of $(\nabla \times \mathcal{E})_{SGS}$ along the center of a Harris-type plasmoid-unstable current sheet.	117
10.19	Schematic of the turbulence dynamics in the vicinity of an ‘X’-point. . . .	118
10.20	Time evolution of the reconnection rate obtained as the out-of plane electric field and the turbulent estimation for a Harris-type and a force-free plasmoid-unstable current sheet.	119
10.21	Time evolution of the amount of turbulence for a Harris-type and a force-free plasmoid-unstable current sheet.	120
10.22	Deviation of the reconnection rate from the Sweet-Parker scaling for a Harris-type plasmoid-unstable current sheet.	120
11.1	Schematics of the evolution of a current sheet depending on the turbulence timescale.	122
D.1	Amplitude of the box average of the ratio $\overline{f'}/\overline{f}$ and $\overline{f}/\overline{f}$ with respect to the filter width.	139

1 Summary

Words can be meaningless. If they are used in such a way that no sharp conclusions can be drawn.

Richard Feynmann.

The problem of magnetic reconnection is usually described by two theories: i) the Sweet-Parker (SP) model of reconnection through long current sheet and ii) the Petschek model of reconnection. The SP model does not provide the rate of energy conversion required to bridge the time and scale gap for the eruption of a solar flare or a coronal mass ejection (CMEs). Moreover, the SP model predicts a reconnection rate inversely proportional to the magnetic-Reynolds-number R_e , making that model unusable for astrophysical plasmas whose magnetic-Reynolds-numbers are large: $R_e \in \mathcal{O}(10^{10} - 10^{17})$. The Petschek model, in the other hand, is able to produce a reconnection rate fast enough to be comparable with the observed one during the impulsive phase of solar flares or coronal mass ejections. The Petschek model was, however, found to be viable only for a localized anomalous molecular resistivity and for specific boundary conditions. In other circumstances, the Petschek model is unstable and the current sheet turns into a Sweet-Parker-type with a small reconnection rate.

Since high-magnetic-Reynolds-numbers astrophysical plasmas are known to be turbulent, the time and scale gap problem between the usual theoretical models and observations are, in this work, addressed through magnetohydrodynamics (MHD) turbulence. Instead of imposing turbulence externally through a constant forcing, it is through a Reynolds-averaged turbulence model that the effects of turbulence are investigated. The reason is that the small scales fluctuations and large scales inhomogeneities are in fact two faces of the same coin. Through that model, turbulence is self-sustained and -generated by the mean (large scale) fields and their gradients. At the same time, the feedback of the turbulence to the mean-fields in the induction equation through the turbulent electromotive force allows to consider the influence of the small scales fluctuating fields on the large scale mean-fields. The closure problem of turbulence is solved, in this formalism, by means of governing equations for the mean field turbulence variables.

Such turbulence model is constructed on a few statistical quantities representing turbulence. They are chosen based on MHD ideal invariants such as the energy or cross-helicity. Practically, it is the energy (K), its dissipation rate (ε), the cross-helicity (W) and the residual helicity (H) of the turbulence that are used to parametrize the turbulence model. The turbulence transport coefficients enter the expression for the turbulent electromotive force by means of an apparent turbulent resistivity β for the energy of the

turbulence and two dynamo-like terms, γ and α , for the cross- and residual helicity of the turbulence. The turbulence transport coefficients α , β and γ are related to the residual helicity H , energy K and cross-helicity W of the turbulence by a turbulence correlation time τ which is algebraically expressed as $\tau = K/\varepsilon$.

As a first approach, the evolution equations for the turbulent energy and turbulent cross-helicity are numerically solved together with the mean field MHD equations. The consequences of turbulence on the reconnection rate are tested by varying the turbulence timescale τ which is considered as constant, i.e., the turbulence energy dissipation rate governing equation is not numerically solved. In order to extend the experiments to conditions closer to the solar corona, a force-free current sheet equilibrium is considered for a plasma-beta smaller than unity. The consequences of a guide magnetic field parallel to the current flow are explored and important relations between the turbulence level and the reconnection rate are inferred. A governing equation for the turbulence energy dissipation rate is then used to consistently solve for the turbulence correlation time. The outcomes of such a self-determined timescale on the reconnection rate are investigated.

The last part of this work is dedicated to high resolution direct numerical simulations (DNSs) of the turbulence. The repercussions of turbulence on the reconnection rate are inspected by considering an extension of the Reynolds-averaged turbulence model to a subgrid-scale one. Turbulence is then statistically computed from the MHD variables filtered off the DNSs by a Gaussian filter. The applicability of the Reynolds-averaged turbulence model, as well as of a non-linear subgrid-scale model, to the problem of magnetic reconnection is investigated and the relation between turbulence and the reconnection rate of both turbulence models is obtained. The energy, its dissipation rate, the cross-helicity and the helicity of the turbulence are later called "turbulent energy", "turbulent energy dissipation rate", "turbulent cross-helicity" and "turbulent residual helicity".

2 Introduction

Nobody ever figures out what life is all about, and it doesn't matter. Explore the world. Nearly everything is really interesting if you go into it deeply enough.

Richard Feynman

2.1 The Sun

The Sun is the star closest to the Earth. It is, therefore, a very special and important laboratory for physics and astrophysics. For instance, the first observation (by the Sudbury Neutrino Observatory) of neutrinos produced in the Sun's core constituted a major breakthrough for particle physics.¹ Even though the Sun is globally well understood, several processes remain a mystery. An important unsolved question is the coronal heating problem. In the core of the Sun, exothermic nuclear reactions convert protons into helium through the proton-proton chain. This nuclear fusion generates a temperature of

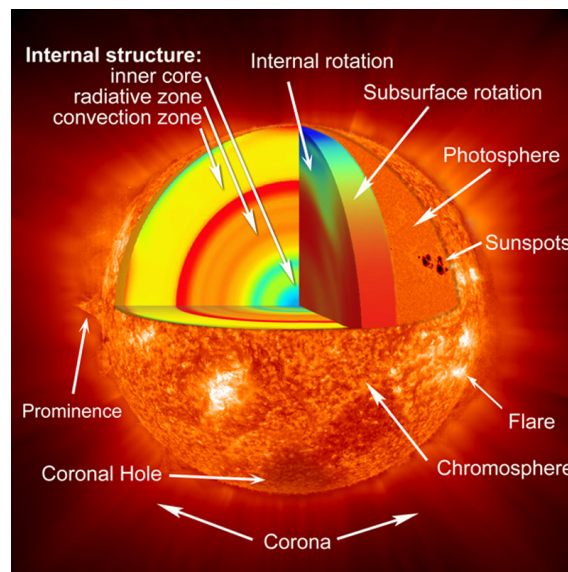


Figure 2.1: Image of the Sun illustrating its interior, surface and activity. Credits: SOHO (ESA & NASA)

the order of $15 \cdot 10^6 \text{K}$ which decreases to about 6000K in the photosphere and down to approximately 4500K above it. The temperature of the solar corona is, however, close to one million degrees (figure 2.2).² The second law of thermodynamics states that heat flows from a hot to a cold body. This means that the temperature should rather decrease away from the Sun's surface as it is expected for thermal conducting environments. The temperature of the solar corona seems, therefore, to contradict thermodynamic principles. Several processes were proposed to additionally heat the corona such as different waves models (AC models), current cascading or magnetic reconnection (DC models).³⁻⁶ Unlike the temperature, the particle density drops dramatically from the photosphere to the solar corona (figure 2.2). There, the electron density is below 10^8 cm^{-3} for a temperature above 10^6 K . These parameters make the solar corona atmosphere filled with a fully

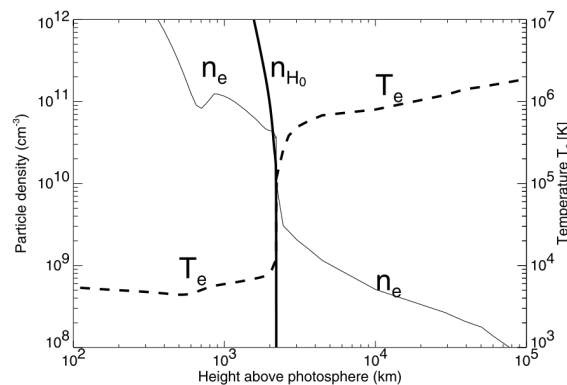


Figure 2.2: Profile of the electron temperature T_e and number density n_e as a function of the height above the photosphere. From Aschwanden.⁷

ionised plasma with a large particles mean free path of the order of kilometers. Particles encounters and scatterings are, therefore, rare events. In the solar corona, the motion of the particles is determined by the strong magnetic field. Their initial velocity parallel to the magnetic field and the Lorentz force make the particles propagating with a cyclotron motion along the magnetic field lines. The relative strength of the thermal energy of a plasma compared with the magnetic energy is provided by the plasma- β_p parameter

$$\beta_p = \frac{p_{th}}{p_{mag}} = \frac{2\rho k_B T_e}{\mu_0 B^2}, \quad (2.1)$$

where p_{th} and p_{mag} are the thermal and magnetic pressure (energy), T_e the electron temperature, ρ the plasma density, μ_0 is the magnetic permeability of the vacuum, k_B the Boltzmann constant and B the magnetic field strength. The magnetic field determines the particles behavior for $\beta_p < 1$ while they can slip from its grasp for $\beta_p > 1$. In most of the solar corona, the plasma- β_p is much lower than unity, i.e., the magnetic pressure dominates the thermal pressure (figure 2.3).

The magnetic field properties of the solar corona distinguish two regions on the surface of the Sun. In the polar regions, the magnetic field lines are opened to the interplanetary space.¹ It is also the locations of the fast solar winds ($\approx 800 \text{ km s}^{-1}$) carrying

I. Maxwell's law $\nabla \cdot \mathbf{B}$ requires theoretically that these field lines connect somewhere in the interplanetary space.

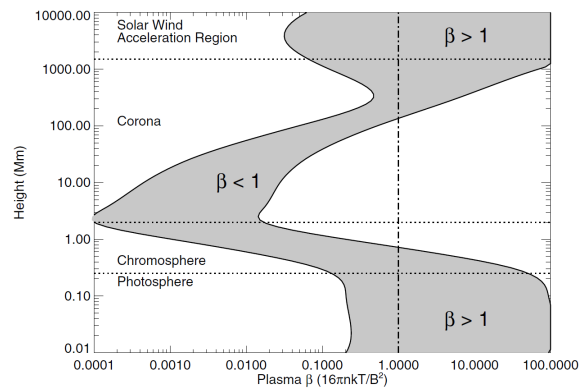


Figure 2.3: Plasma- β_p in the Sun's atmosphere. From Aschwanden.⁷

the plasma towards the heliosphere. The rest of the solar surface is connected by closed magnetic field lines. These regions hold coronal loops which are filled with the cold or heated plasma from the chromosphere. Their topology is determined by the magnetic field. The loops can also open into the interplanetary space producing a slow solar wind with a speed of the order of 400 km s^{-1} .

The Sun exhibits flares (figure 2.4) above active regions (sunspots) where the magnetic field is strong. The occurrences of such phenomena are related to the solar activity and the magnetic cycle. For instance, the solar flares number can be up to three per day

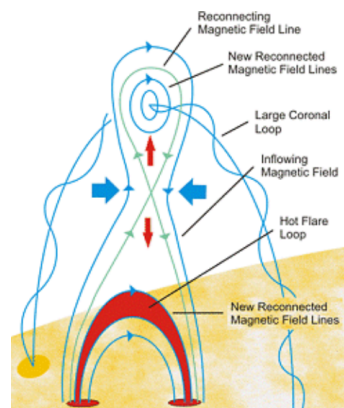


Figure 2.4: Schematic of a flare model. Credits: NASA

during a solar maxima with a large number of sunspots (regions of strong magnetic field). During solar minima, the fewer sunspots reduce the eruption of flares to about one every five days. The heated plasma trapped in strong magnetic fields can be ejected into the interplanetary space following a large solar flare. Such an event is called a coronal mass ejection (CME). The ejected magnetic flux and plasma (mostly electrons and protons) is called a plasmoid. Solar flares are characterized by the rapid release (a few minutes) of the stored coronal magnetic field energy which is converted to particle acceleration and heat.^{II} The magnetic instability responsible for the topological reconfiguration of the magnetic field in solar flares and CMEs, as well as the rapid release of a large amount of energy, could be related to magnetic reconnection.

II. Red dwarfs, stars similar to the sun and *UV Ceti* type variable stars also exhibit flares.^{8,9}

2.2 The Importance of Magnetic Reconnection

The idea that the magnetic field may change its topology, and by so be able to release its energy rapidly, anchored in the 40s.¹⁰ This process is called *magnetic reconnection*. The key point of magnetic reconnection is its ability to rapidly convert the stored magnetic energy into other forms of energy. In the Sun, magnetic reconnection could reshape dynamical structures such as coronal loops and trigger events above active regions from critically stressed magnetized structures. Flares or coronal mass ejections (CMEs) could be triggered, in the solar corona, by magnetic reconnection. The exact thresholds and reasons for reconnection to happen are, however, still not understood.

The Sun is not the only astrophysical object where reconnection takes place. Other stars, mainly fast rotator red dwarfs, also exhibit large stars flares. The phenomenon is similar to solar flares except that the amount of energy released by stellar flares is much larger.^{III} Additionally to stars, planets endowed with a magnetosphere and hit by solar or stellar winds show evidence of reconnection events. For instance, the day- and nightside Earth's magnetopause can exhibit reconnection. At the dayside, the solar wind magnetic field interacts with the Earth's magnetic field. Part the solar wind energy is converted by reconnecting the wind magnetic field with the Earth's field into kinetic energy and heat. Following the dayside reconnection, the interconnection of the solar wind and Earth magnetic field allows the solar wind to stretch and carry the Earth's combined magnetic flux toward the magnetotail. More energy is then released at the tail when reconnection occurs. Reconnection of the Earth's magnetic field at the nightside is, therefore, a consequence of the reconnection of the solar wind magnetic field at the dayside. Other astrophysical objects like accretion disks also manifest reconnection events. The disks exhibit jets of gas along their polar axis. Such jets release the angular momentum of the disks, losing only a few percentage of mass in the process. The reduction of the angular momentum by magnetic reconnection allows the gas to collapse on the massive object in the center of the disk.¹³ Magnetic reconnection is not only an important phenomenon for astrophysics but also for fusion plasmas. Fusion plasma experiments try to confine hot plasma at a timescale sufficient to sustain nuclear reactions. Tokamak experiments show, however, several instabilities due to magnetic reconnection that render the plasma confinement difficult. The sawtooth oscillation is an example of magnetic reconnection producing a relaxation of the plasma which may considerably degrade the confinement.¹⁴

Magnetic reconnection can be globally defined as a rapid change of magnetic field topology which results in an efficient release of the stored magnetic component of the field energy. The key ingredients for reconnection to happens are oppositely directed magnetic field and a finite magnetic diffusivity (non-ideality of the plasma). Figure 2.5 represents magnetic field lines before and after being reconnected. The field line originally connecting A to B is, after reconnection, connecting A to C. The plasma trapped by the reconnecting field lines is rapidly ejected by the released magnetic tension. The speed at which plasma is ejected is a measure of the efficiency of reconnection. This is our current understanding of reconnection in two dimensions. The same concept can be exported to three dimensions. The important common point between two- and three-dimensional

III. There is an important link between the rotation of a star, its activity and its magnetic field. The magnetic field increases with rotation.^{11,12} The strength of the stored magnetic energy is therefore greater for fast rotator stars resulting in a larger amount of energy released.

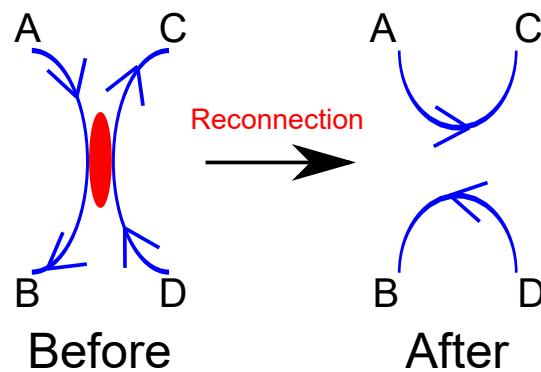


Figure 2.5: Schematic representation of magnetic reconnection. A magnetic field line connecting A to B is, after reconnection, connecting A to C. The red area represents the location of the current sheet.

reconnection is the rapid change of magnetic field topology and energy release. The efficiency of the magnetic energy conversion into other forms is characterized by the reconnection rate.

A plasma is a conducting ionised gas. On Earth, plasma is hardly found in the nature, except for lightnings. On the contrary, plasmas are widely spread in the Universe and compose approximatively 99% of the known visible matter. Even though a plasma is a conducting gas made of particles, its magnetohydrodynamics (MHD) description (chapter (3)) is used to tackle the reconnection problem. MHD is a theoretical framework which allows to study electrically neutral fluids by a few variables without taking into account the particles dynamics. The ideal MHD is a theory able to describe the behavior of large magnetized structures filled with plasmas such as coronal loops. Since MHD describes a magnetized fluid, the Navier-Stokes and Maxwell's equations are solved together to determine the fluid behavior. The power of the MHD theory resides in its ability to describe a phenomenon by considering the forces balance and instabilities acting on a magnetized fluid. The MHD approach is further able to consider a problem from the viewpoint of ideal invariants such as the magnetic helicity or the total (magnetic plus fluid kinetic) energy of the plasma. This makes MHD an efficient tool to describe the global behavior of a plasma. For the MHD approximation to be valid, fundamental assumptions on the length and time scales under considerations must be made. It is required, in principle, that the minimum non-ideal MHD length scale is larger than the mean free path between particle collision (ion inertial length) and the cyclotron (Larmor) radius. It is further assumed that the time needed for a light wave to cross the medium is much shorter than the MHD timescale. Finally, the fluid can be assumed to be in thermodynamical equilibrium such that the exchange of heat flux is adiabatic.

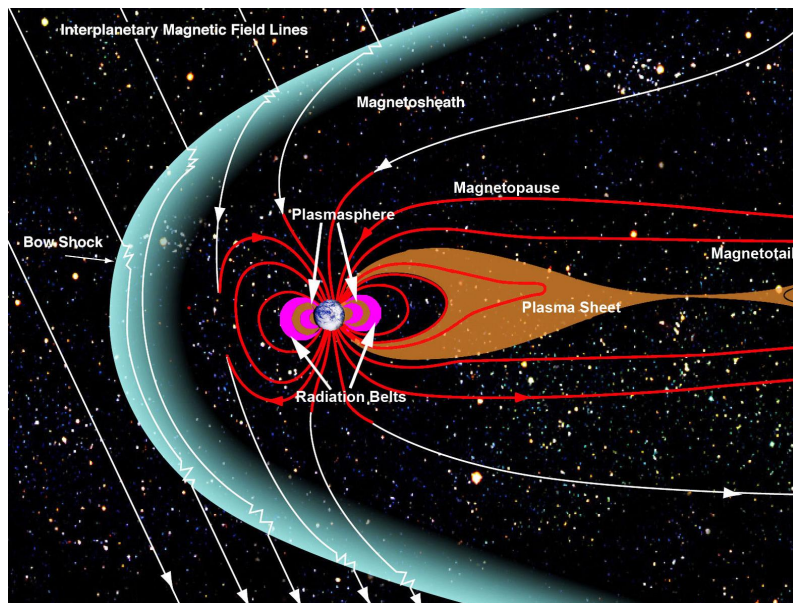


Figure 2.6: Structure of the Earth's magnetosphere. Credit: NASA/Goddard/Aaron Kaase.

MHD is said to be "ideal" when the plasma resistivity is negligible and "resistive" when finite plasma resistivity is considered. In ideal MHD, the plasma resistivity is neglected and magnetic field moves together with the surrounding fluid and vice versa (section (3.1)). The fluid can move along the direction of the magnetic field but not across it. For instance, a "tube" of fluid wrapped around a magnetic field line will stay connected to it whatever the deformation the "tube" feels under the external (fluid) forces acting on it. This interaction of the fluid with the electromagnetic field is called the *frozen-in* condition of the plasma. Ideal MHD condition can be broken if the plasma resistivity is non-negligible. This extension is called resistive MHD. When magnetic flux with field components in opposite directions are pushed towards each others, e.g. in narrow regions filled with an electric current (current sheet), reconnection can take place. In collisional plasmas, the enhanced friction between electrons and ions gives rise to an electric resistivity which allows for reconnection. In collisionless plasmas such as the solar corona, such encounters are rare but the frictions of the ions and electrons might be a source of ambipolar diffusion able to reconnect magnetic field lines.¹⁵ While a plasma resistivity might break the frozen-in condition, its role is not clear in collisionless plasmas.

A current sheet is a region between two oppositely directed magnetic field where an electric current density appears. The motion of the fluid may produce tangential discontinuities of the field. The intensity of the current density can rise in time due to the continuous pressure of the inflow but its growth is slowed down as soon as the magnetic field is dissipated. The increased current density in this thin region together with a finite value of the molecular resistivity cause a non-negligible diffusion of the magnetic field. The frozen-in condition is broken and magnetic reconnection can take place. A current sheet is, therefore, an appropriate environment for magnetic reconnection to happen. Current sheets can be found in the magnetopause at the Earth's day- and nightside.¹⁶ The solar system largest known current sheet is found in the heliosphere at the Earth's

nightside (figure 2.6). Aurorae might be a result of the particles acceleration in the Earthward direction due to magnetic reconnection in the tail current sheet. On the Sun, current sheets appearing above active regions possibly allow a quick release of the stored magnetic energy.¹⁷ Once reconnection takes place, the magnetic flux inflow is balanced by the magnetic flux outflow. Such a steady state reconnection has a "Y"-point geometry for a finite uniform resistivity (Sweet-Parker (SP) model^{18,19}) and an "X"-point geometry when the finite resistivity is localized (Petschek-like reconnection model²⁰).²¹ These two different models and their associated rate of magnetic energy conversion are discussed further in sections (7.1)-(7.2). The open question is: how can fast reconnection be obtained in the collisionless plasma of the solar corona? A possible answer can be given considering turbulence a trigger for fast reconnection.

2.3 Turbulence

As soon as a fluid is set into motion, turbulence may develop. Turbulence encompasses all chaotic changes and unpredictable behavior of a fluid. One striking point of a turbulent flow is its irregularity. Rather than considering turbulence from a deterministic point of view, its complex influence on the fluid's behavior should be considered statistically. Since non-magnetized fluids are largely spread on Earth, hydrodynamic turbulence is well studied. This is not the case for magnetohydrodynamics turbulence even though it is ubiquitous in astrophysical plasmas. Magnetic turbulence is important for MHD since magnetic field fluctuations are more important at macro than micro scales.²²

Even though it is possible to obtain similar properties for different realisations of the same turbulent plasma, the genuine unpredictable nature of turbulence renders difficult its reproducibility. Furthermore, measurements of turbulence in space environments such as the solar wind are not easily comparable with theory. These difficulties are partially addressed by means of numerical simulations whose results can be compared with theoretical models. Numerical simulations face, however, difficulties to fully resolve all scales of turbulence due to the extreme astrophysical parameters. For instance, the magnetic Reynolds number R_e which provides an estimation of the relative effects of the magnetic field advection to its dissipation, i.e. $R_e = VL/\eta$ where V is the fluid velocity scale, L the typical length scale of the flow and η is the molecular resistivity, can be in the range $10^{10} - 10^{17}$. In terms of the magnetic Reynolds number R_e , the ratio of the largest turbulent eddy size l to the smallest one η is given as $l/\eta = R_e^{3/4}$. For a three-dimensional simulation to solve all the scales from the large containing scales to the smallest dissipative one, the number of grid points required is $\approx R_e^{9/4}$.²³ Three-dimensional numerical simulations of the solar convection zone ($Re \approx 10^{15}$) requires at least 10^{34} grid points or floating-point operations per seconds (FLOPS) to resolve all fluid processes. The supercomputer presently available are able to reach up 10^{22} FLOPS. The necessary computational power is unfortunately not reachable in the foreseeable future due the slow down of the computational power increase of the fastest HPCs. The scale gap between the resolvable grid scales (GS) of numerical simulation and the small-scale influence on turbulence on the large ones can be grasped by statistical turbulence modelling.

A model is a simplification of a given situation. Turbulence models usually simplify the complexity of the fluctuations by decomposing any field into its mean (steady) and

fluctuating component. Such a decomposition of the MHD variables results in the turbulence closure problem: there are more unknowns than available equations. This kind of turbulence models try, therefore, to close the system of equations by expressing the unknowns quantities in terms of the available (resolved) fields. Turbulence models distinguish the mean- and fluctuating fields. The former being the part of the plasma holding most of the energy while the latter is the length scale at which energy can be dissipated. Mean variables are defined for the slowly varying fields and flows. In this work, two kinds of turbulence simulations are used: (i) large eddy simulations (LES) and (ii) Reynolds-averaged turbulence approach.^{24–26} The LES resolves the large scale motions containing most of the energy and models the unavailable subgrid-scale (SGS) where the turbulence resides. On the contrary, all plasma scales are modeled in the Reynolds-averaged turbulence models and solely the mean field variables are computed. Reynolds-averaged turbulence models need, therefore, to model turbulent motion with transport equations of statistical quantities. They are often chosen as statistical properties of ideal MHD invariants such as the energy, its dissipation or the cross-helicity.

The Richardson’s picture of turbulence describes a dissipation of large scale fluid energy towards the small scales: *Big whirls have little whirls that feed on their velocity, and little whirls have lesser whirls, and so on to viscosity.* -Richardson, (1922). The large scale energy supplies and sustains turbulence which in turns dissipates the energy at small scale by the viscosity ν . The process is similar to magnetic reconnection which converts the large scale magnetic energy into other forms in a small region of space through the magnetic diffusivity η . Since turbulence interacts nonlinearly over a wide range of scales, it may play an important role in magnetic reconnection.²⁷ For instance, Turbulence is capable of breaking the ‘frozen-in’ condition allowing for reconnection.^{28–30} From that point of view, the energy dissipation by turbulence at small scales can be a part of the reconnection process. It has to be noted that turbulence does not only breaks large scale structures into smaller one. For instance, large scale magnetic field can be enhanced by a dynamo effect due to small scales fluctuations.^{31,32} In particular, the turbulent dynamo is an active field of research in the generation of strong magnetic field from turbulence at the surface of the Sun and Sun-like stars.^{33–36}

The MHD approach is adequate for describing fluid turbulence as long as it concerns only fluid and magnetic field fluctuations. Most of the interesting information that can be retrieved from turbulence are obtained in the frequency domain (Fourier analysis). In terms of the wave number k , the global properties of the inertial range of self-similar processes of a transfer of energy from large to small scales is characterized by power laws. A well known power law providing spectral information on energy transfer is the Kolmogorov (K41) power law which predicts an energy spectrum $E_{K41} \sim k^{-5/3}$.³⁷ The Kolmogorov picture of turbulence is presented in chapter (6). Solar wind turbulence are found to follow K41 spectrum at MHD scales but changes to exponential power laws at kinetic scales where dissipations take place.^{38,39}

2.4 Addressing the Open Questions

Magnetic reconnection is a key process for understanding the dynamics of the solar corona. The rate of magnetic energy conversion can be theoretically estimated. The

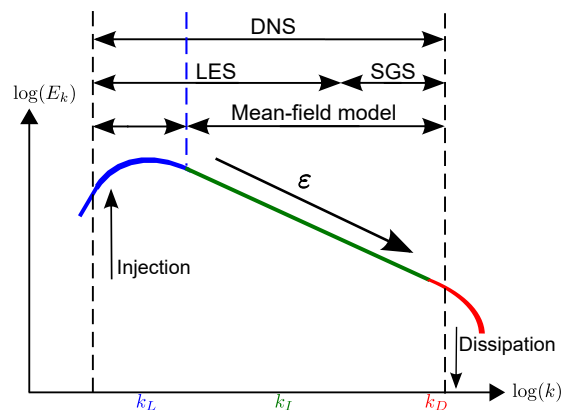


Figure 2.7: Range of applicability of turbulence models.

Sweet-Parker model of reconnection for incompressible plasmas is such a model. It provides a reconnection rate $V_{in} = V_A S^{-1/2}$ for the Alfvén velocity V_A and the Lundquist number $S = LV_A/\eta$ (Reynolds number for $V = V_A$).¹⁸ Most of astrophysical process involving reconnection have large Lundquist numbers and the reconnection rate based on the Sweet-Parker model is tiny. For instance, $S \sim 10^{12}$ in solar corona which provides a solar flare diffusion time $t \approx \sqrt{S}L/v_A \approx 0.3$ years. This is way too long compared with the duration of the impulsive phase of a flare which lasts a few minutes only.⁴⁰ To enhance the reconnection rate, Petschek considered slow shocks in compressible plasmas increasing the reconnection rate to $V_{in} = V_A/\ln(S)$ able to match observations.²⁰ A Petschek-like current sheet is, however, only formed for a localized anomalous resistivity.⁴¹ In order to enhance the reconnection rate, several processes for collisionless plasmas were proposed spanning from kinetic models,^{42,43} to anomalous resistivity^{44,45} and Hall physics.^{46,47} In MHD, the plasmoid instability has been proposed to produce fast reconnection for a given threshold of the Lundquist number.⁴⁸ In two-dimensional numerical simulations, the instability was found to reach a faster reconnection rate than the Sweet-Parker model (see section (10.1)).^{49,50} In three dimensions, the plasmoid instability is found to reach lower reconnection rates than in two-dimensional simulations.⁵¹ The most interesting fact about plasmoid instability is its deviation from the Sweet-Parker scaling for high-Reynolds-number-plasmas.⁵² Such a behavior indicates that other mechanisms than the molecular resistivity η are at the origin of fast magnetic reconnection.

Magnetic reconnection is a multi-scale process capable to liberate a large amount of energy at large scales by diffusive processes at small ones. How this large scale difference can be bridged is an important open question. The fact that turbulence also spans a large range of scales might provide some answers to this question. Since astrophysical plasmas are ubiquitously turbulent,⁵³ turbulence is an appropriate approach to this question. Furthermore, solar winds *in-situ* observations revealed that turbulence and reconnection are closely related to each other.^{54,55} This relationship was also observed in numerical simulations.^{56,57} Three-dimensional simulations of the plasmoid instability also revealed that the non-linear phase of magnetic reconnection is related to turbulence.⁵¹ For strong imposed Alfvénic turbulence, it was proposed that turbulence can lead to significantly faster reconnection rate than the Sweet-Parker reconnection at large-Reynolds-numbers.^{28,29,58}

The relation between turbulence and reconnection is related to the size of the current

sheet diffusive layer. The Sweet-Parker reconnection is enhanced by any processes able to enlarge the thickness of the diffusion layer to a size comparable to its length. For instance, the fluctuations of the magnetic field in the diffusion region could enhance the diffusion region thickness.²⁸ The argument provides an upper limit of the turbulent reconnection rate proportional to the Reynolds number $V_{in} = V_A M_A^2$ for the Alfvén Mach number $M_A = V_{rms}/V_A$.²⁸ This specific argument was shown, however, to not hold for three-dimensional reconnection with stratified turbulence which deviates from the Sweet-Parker scaling.⁵⁷ The weak dependence of the reconnection rate on the resistivity agrees, however, with Lazarian and Vishniac.²⁸ Note that the intrinsic spatio-temporal randomness of turbulence does not require any external forcing,⁵⁹ especially for large-Reynolds-number-plasmas.⁵⁸ The enhanced transport due to turbulence may directly affect the mean-fields. At the same time, the properties of turbulence are determined by the large scale (mean) fields. The turbulence should, therefore, be treated simultaneously with the large scale mean-field evolution instead of being externally imposed. Reynolds-averaged turbulence models for which turbulence is self-generated and -sustained by the mean-field inhomogeneities provide such a simultaneous treatment of turbulence and mean-field evolution.^{34,60} Such models provide a rate of energy conversion faster than the Sweet-Parker scaling and hold a very weak dependence on the Ohmic resistivity at large-Reynolds-numbers. Reynolds-averaged turbulence models are, therefore, good candidates to study magnetic reconnection in a turbulent plasma.

3 Magnetohydrodynamics (MHD)

You must understand that there is more than one path to the top of the mountain.

Miyamoto Musashi.

Magnetohydrodynamics treats about magnetized fluids. By fluid, it is understood a ionised gas which is electrically neutral over macroscopic scales. The fluid is considered as macroscopic for global length scales much larger than the Debye length and the Larmor radii of the charged particles. Another important assumption is that the MHD frequency ω is much smaller than the cyclotron frequency of the ions ω_{ci} . Under these approximations, the plasma can be described by fluid motions. Hence, the Navier-Stokes equations can be used. Since the fluid is magnetized, the Maxwell's equations are needed. This chapter describes, therefore, the non-relativistic MHD equations (section (3.1))

Formally, the equations describing magnetohydrodynamics are obtained from microscopic physics equations (kinetic theory). By the appropriate statistical quantities, MHD equations are obtained taking the different moments of the Boltzmann's equations. It is, however, not the purpose of this dissertation to deal with this derivation and only an heuristic approach is used to obtain the MHD equations. A full derivation can be found in Aschwanden.⁷

The foundation of the magnetic reconnection theory of MHD lies in the magnetic field properties inside a fluid which conduct electricity. Any electrically conducting material is characterized by a resistance to the movement of the charge carriers. It is represented by the magnetic diffusivity $\eta = 1/(\mu_0\sigma)$ where sigma is the electric conductivity. The magnetic diffusivity is called resistivity for the rest of this dissertation. Two MHD limits which depend on the resistivity are presented. The limit of vanishing resistivity^I leads to the notion of magnetic flux conservation and the description of the magnetic field topology. This limit is called ideal MHD (section (3.1.1)) which bears several invariants (section (3.1.2)). On the other hand, the MHD equations for a finite resistivity η is the resistive MHD limit (section (3.1.3)) for which the diffusion of magnetic field occurs. These two limits distinguish whether the magnetic field can be reconnected or not.

I. Similar to a perfect conductor

3.1 Single fluid and Non-Relativistic Maxwell's Equations

The single fluid MHD equations are described in terms the mass density ρ , the fluid velocity \mathbf{V} , the scalar pressure p and the magnetic field \mathbf{B} . Considering a small volume element dV inside the fluid, the total mass is $\mathbf{M} = \int \rho dV$ where ρ is the mass density. Assuming that the total mass \mathbf{M} is conserved, any flux of mass through a volume's surface given by $\rho\mathbf{V}$ is equal to the rate of mass density change $\partial_t\rho$. This yields the following MHD continuity equation

$$\partial_t\rho + \nabla \cdot (\rho\mathbf{V}) = 0, \quad (3.1)$$

where \mathbf{V} is the bulk velocity of the plasma

Since the magnetic field \mathbf{B} is part of the MHD description, its behaviour is determined by Faraday's law

$$\partial_t\mathbf{B} = -\nabla \times \mathbf{E}, \quad (3.2)$$

for the electric field \mathbf{E} . The current density \mathbf{J} is provided by Ampère's law which, under the MHD assumption $\mathbf{V} \ll c$, is^{II}

$$\nabla \times \mathbf{B} = \mu_0\mathbf{J}. \quad (3.3)$$

Finally, the non-existence on magnetic monopoles yields

$$\nabla \cdot \mathbf{B} = 0. \quad (3.4)$$

The momentum equation for the fluid motion is obtained by considering and adding the forces acting on it. A charged particle is moving under the effect of the Lorentz force (\mathbf{F}_L), which is the sum of the interaction over all charged particles inside a volume \mathcal{V} . Moreover, a fluid being electrically quasi-neutral, the Lorentz force reads

$$\mathbf{F}_L = \mathbf{J} \times \mathbf{B}. \quad (3.5)$$

The pressure is considered as isotropic and gravitational forces are, in magnetized plasmas, negligible compared to Lorentz force. The viscous forces are considered through the (constant) kinematic viscosity μ . Hence, the fluid momentum equation is

$$\rho\partial_t\mathbf{V} = -\rho\mathbf{V} \cdot \nabla\mathbf{V} - \nabla p + \mathbf{J} \times \mathbf{B} + \mu\nabla^2\rho\mathbf{V}, \quad (3.6)$$

where ρ is the mass density from equation (3.1). Note that the quasi-neutrality of the plasma enforces no force from the electric field \mathbf{E} .

The energy equation exists under different forms but in the present dissertation, it is the internal energy form which is used. To a good approximation, heat conduction effects can be neglected on MHD scale and adiabatic changes are assumed for the heat transfer. Moreover, the plasmas can be considered to follow the ideal gas law with the equation of state $p = 2nk_B T$ linking the pressure p to the total number of particles per unit volume n , the Boltzmann constant k_B and the temperature T . Under these assumptions, the energy equation may take the form⁶¹

$$\frac{\rho^{\gamma_0}}{\gamma_0 - 1} \frac{D}{Dt} \left(\frac{p}{\rho^{\gamma_0}} \right) = -\mathcal{Q}, \quad (3.7)$$

II. The displacement current $\partial_t\mathbf{E}/c^2$ is negligible. This can be understood by dimensional analysis of equation (3.2), see the discussion in Priest.⁶¹

where p is the thermal pressure, γ_0 is the specific heat ratio C_v/C_p equal to 5/3 and \mathcal{Q} is an energy function accounting for all possible losses and gains of energy. The symbol D/Dt is the convective derivative defined as

$$\frac{D}{Dt} = \frac{\partial}{\partial t} + \mathbf{v} \cdot \nabla. \quad (3.8)$$

Applying the convective derivative of equation (3.7) on p and ρ^{γ_0} yields

$$\frac{\partial p}{\partial t} + \mathbf{V} \cdot \nabla p + \gamma_0 p \cdot \nabla \mathbf{V} = -(\gamma_0 - 1)\mathcal{Q}. \quad (3.9)$$

Finally, using the change of variable $p = 2h^{\gamma_0}$ gives

$$\frac{\partial h}{\partial t} + \nabla \cdot (h\mathbf{V}) = -\left(\frac{\gamma_0 - 1}{2\gamma_0 h^{\gamma_0 - 1}}\right)\mathcal{Q}. \quad (3.10)$$

The energy function \mathcal{Q} can be determined by considering the Poynting flux S . In electromagnetism, the equivalent of the work-energy theorem is the Poynting theorem. This work done on the charge carriers increases their mechanical energy U_{mec} which is composed of the plasma kinetic and internal energy in MHD. The differential form of the Poynting theorem can be written as

$$\frac{\partial}{\partial t} \left(U_{mec} + \frac{\mathbf{B}^2}{2\mu_0} \right) = -\nabla \cdot \mathbf{S} \equiv -\nabla \cdot \left(\frac{1}{\mu_0} \mathbf{E} \times \mathbf{B} \right), \quad (3.11)$$

where U_{mec} is the mechanical energy density of the plasma. The energy function \mathcal{Q} can be obtained by computing the total energy density of the plasma by multiplying equation (3.6) by \mathbf{V} , equation (3.2) by \mathbf{B} and adding the internal energy e

$$\frac{\partial}{\partial t} \frac{\mathbf{B}^2}{2\mu_0} + \rho \frac{D}{Dt} \left(\frac{\mathbf{V}^2}{2} + e \right) = -(\nabla \times \mathbf{E}) \cdot \mathbf{B} + \mathbf{V} \cdot (\mathbf{J} \times \mathbf{B}) - \mathbf{V} \cdot \nabla p + \rho \frac{D}{Dt} e,$$

where the internal energy e is given by

$$e = \frac{1}{\gamma_0 - 1} \frac{p}{\rho}. \quad (3.12)$$

Applying the convective derivative to the internal energy, the equation for the thermal pressure becomes

$$\frac{\partial p}{\partial t} + \mathbf{V} \cdot \nabla p + \gamma_0 p \cdot \nabla \mathbf{V} = -(\gamma_0 - 1)[\nabla \cdot \mathbf{S} - (\nabla \times \mathbf{E}) \cdot \mathbf{B} + \mathbf{V} \cdot (\mathbf{J} \times \mathbf{B})], \quad (3.13)$$

where the divergence of the Poynting flux is

$$\nabla \cdot \mathbf{S} = (\nabla \times \mathbf{E}) \cdot \mathbf{B} - \mathbf{E} \cdot (\nabla \times \mathbf{B}), \quad (3.14)$$

since the heat flux is neglected. In this context, the energy source/sink function can be identified as

$$\mathcal{Q} = \mathbf{V} \cdot (\mathbf{J} \times \mathbf{B}) - \mathbf{E} \cdot (\nabla \times \mathbf{B}), \quad (3.15)$$

for a given electric field \mathbf{E} .

In electrodynamics, a flow of current is generated as soon as a force (per unit charge) \mathbf{f} of any kind is applied on the charge carriers in a material. Their velocity is proportional to the force \mathbf{f} modulo some resistance of the material in which they move

$$\mathbf{J} = \zeta \mathbf{f}, \quad (3.16)$$

where ζ represents all the non-ideal effects of the plasma. The plasma is considered as a perfect conductor in the limit $\zeta \rightarrow \infty$. The force \mathbf{f} (per unit charge) in the present context is the electromotive force $\mathbf{E} + \mathbf{V} \times \mathbf{B}$ and the non-ideal effects ζ are considered through the plasma resistivity η . The electric field \mathbf{E} in the fluid moving frame (laboratory reference frame) is then

$$\mathbf{E} = \eta \mathbf{J} - \mathbf{V} \times \mathbf{B}. \quad (3.17)$$

The magnetic field dynamic is obtained by inserting equation (3.17) into equation (3.2)

$$\partial_t \mathbf{B} = \nabla \times (\mathbf{V} \times \mathbf{B} + \eta \mathbf{J}), \quad (3.18)$$

which is called the MHD induction equation. There exist two important limits for equation (3.18): i) ideal MHD for $\eta \rightarrow 0$, and ii) resistive MHD when the Ohmic dissipation $\eta \mathbf{J}$ cannot be neglected in front of the advection term $\mathbf{V} \times \mathbf{B}$. In ideal MHD (limit i)), the magnetic field is said to be "frozen-in" to the plasma and magnetic reconnection is impeded while reconnection is possible in limit ii). The limit of ideal MHD provides invariant quantities of interest which characterise the constraints on the fluid dynamics due to the frozen-in conditions. Ideal MHD is discussed in section (3.1.1), ideal invariants in section (3.1.2) and resistive MHD in section (3.1.3).

3.1.1 Ideal MHD

In ideal MHD, the resistivity η is neglected and the plasma is free to move along the direction of the magnetic field. The Ohm's law (equation (3.17)) reduces to

$$\mathbf{E} = -\mathbf{V} \times \mathbf{B}, \quad (3.19)$$

resulting in the ideal induction equation

$$\partial_t \mathbf{B} = \nabla \times (\mathbf{V} \times \mathbf{B}). \quad (3.20)$$

The evolution of the magnetic field is only provided by the plasma velocity, it cannot be diffused as in equation (3.18). The integral form of equation (3.20) expresses the conservation of the magnetic flux through a surface S bounded by a closed curve C moving with the fluid

$$\phi = \int_S \mathbf{B} \cdot d\mathbf{S}. \quad (3.21)$$

The time derivative of the magnetic flux ϕ is given by: i) the variation of the magnetic field in time, and ii) how much magnetic flux flew through the surface S between the time

t and $t + dt$. Taking the time derivative of equation (3.21) yields

$$\begin{aligned}
 \frac{d\phi}{dt} &= \int_S \partial_t \mathbf{B} \cdot d\mathbf{S} + \oint_C \mathbf{B} \cdot \mathbf{V} \times d\mathbf{l} \\
 &= - \int_S \nabla \times \mathbf{E} \cdot d\mathbf{S} + \oint_C \mathbf{B} \cdot \mathbf{V} \times d\mathbf{l} \\
 &= - \oint_C \mathbf{E} \cdot d\mathbf{l} - \oint_C \mathbf{V} \times \mathbf{B} \cdot d\mathbf{l} \\
 &= 0,
 \end{aligned} \tag{3.22}$$

where $d\mathbf{l}$ is a line element at every point tangent to the curve C . A flux tube is defined by the gliding in time of the curve C around the magnetic field which provides a physical interpretation of magnetic field lines frozen-in to the plasma. Equation (3.22) states that the magnetic field cannot change its topology, i.e., the magnetic field lines only swirl around in the plasma without being able to reconnect.

3.1.2 Ideal Invariants

The fact that the magnetic field cannot be diffused away in ideal MHD provide invariant quantities of interest such as the energy, the magnetic- or cross-helicity. These invariants are later used in the mean field turbulence modeling (section (4.1.2)) to derive statistical turbulent quantities describing the effect of small scale turbulence on large scales (mean) fields.

The first invariant to be considered is the total energy density. Since the resistivity η is neglected, the Poynting flux for the electric field equation (3.19) is

$$\nabla \cdot \mathbf{S} = (\nabla \times \mathbf{E}) \cdot \mathbf{B} - \mathbf{V} \cdot (\mathbf{J} \times \mathbf{B}). \tag{3.23}$$

Inserting equation (3.23) into equation (3.13) gives

$$\partial_t p + \mathbf{V} \cdot \nabla p + \gamma_0 \mathbf{V} \cdot \nabla p = 0, \tag{3.24}$$

which means that the energy density $U_{mec} + U_{mag}$ is a conserved quantity. There is no conversion of magnetic or kinetic energy into heat.

Since the magnetic flux is frozen in to the plasma, it may be bent, distorted or have any other complicated shape. Determining the magnetic field is considered from the vector potential \mathbf{A} as $\mathbf{B} = \nabla \times \mathbf{A}$. Such complexity of the magnetic field is characterized by the magnetic helicity H_{mag}

$$H_{mag} = \int_{\mathcal{V}} \mathbf{A} \cdot \mathbf{B} d\mathcal{V}, \tag{3.25}$$

which depends on the choice of a gauge. The gauge can be chosen as the Coulomb gauge because of the conservation of the total mass \mathbf{M} . With this choice, the electric field becomes $\mathbf{E} = -\partial_t \mathbf{A}$ and the convective derivative of the magnetic helicity is

$$\frac{DH_{mag}}{Dt} = \int_{\mathcal{V}} (\mathbf{B} \cdot \partial_t \mathbf{A} + \mathbf{A} \cdot \partial_t \mathbf{B}) d\mathcal{V} + \int_{\mathcal{V}} (\mathbf{A} \cdot \mathbf{B}) \frac{d}{dt} d\mathcal{V} \tag{3.26}$$

$$= 0, \tag{3.27}$$

where equation (3.19) is used from equation (3.26) to (3.27). The frozen-in conditions enforces the magnetic field to retain its topology.

The last invariant to be considered is the cross-helicity \mathcal{W} which gives information on the alignment of the magnetic and velocity field:

$$\mathcal{W} = \int_{\mathcal{V}} \mathbf{V} \cdot \mathbf{B} d\mathcal{V}. \quad (3.28)$$

Its conservation is obtained by multiplying \mathbf{B} to equation (3.6), \mathbf{V} to equation (3.20) and integrating over the volume \mathcal{V} .^{III}

III. The full derivation of the magnetic- and cross-helicity can be found in Biskamp.²²

3.1.3 Resistive MHD

The frozen-in condition is broken as soon as any non-ideal processes are not negligible in front of the convective term in equation (3.18). For a finite resistivity η , this situation is realised within a current sheet where the intense current density compensates for the small amplitude of the resistivity, making the Ohmic dissipation $\eta\mathbf{J}$ comparable to the convective term $\mathbf{V} \times \mathbf{B}$. In such a situation, the electric field is given as $\mathbf{E} = \mathbf{V} \times \mathbf{B} - \eta\mathbf{J}$. A finite resistivity is required to break the frozen-in condition, allowing magnetic reconnection to happen.

The consideration of a finite resistivity modifies the energy source/sink function \mathcal{Q} in equation (3.15). For a finite resistivity η , the divergence of the Poynting flux for the electric field equation (3.17) yields

$$\nabla \cdot \mathbf{S} = (\nabla \times \mathbf{E}) \cdot \mathbf{B} - \mathbf{V} \cdot (\mathbf{J} \times \mathbf{B}) + \eta\mathbf{J}^2. \quad (3.29)$$

As done for equation (3.24), inserting equation (3.29) in equation (3.13) gives the resistive MHD internal energy equation

$$\partial_t p + \mathbf{V} \cdot \nabla p + \gamma_0 \mathbf{V} \cdot \nabla p = (\gamma_0 - 1)\eta\mathbf{J}^2. \quad (3.30)$$

Equation (3.30) states that the magnetic and kinetic energy are converted to heat through the Ohmic dissipation when thermal conduction, particle radiation or turbulence are neglected. The energy function \mathcal{Q} is a source of heat identified as the Joule heating. The identification $\eta\mathbf{J}^2 = -\mathcal{Q}$ in equation (3.10) results in the internal energy equation for the variable h

$$\frac{\partial h}{\partial t} + \nabla \cdot (h\mathbf{V}) = \frac{\gamma_0 - 1}{2\gamma_0 h^{\gamma_0 - 1}} (\eta\mathbf{J}^2). \quad (3.31)$$

The total energy density is no longer conserved due to a production of heat from the Ohmic dissipation.

An important number related to the resistivity η is found by comparing the order magnitude of the first and second term of the right-hand side of equation (3.18). For a typical length scale L_0 and velocity V_0 , the magnetic-Reynolds-number R_m is defined as

$$R_m = \frac{V_0 L_0}{\eta}. \quad (3.32)$$

In most astrophysical plasmas, R_m is very large due to a small resistivity and the extremely large length scales; the plasma is frozen-in. Reducing the typical length scale increases the magnetic-Reynolds-number. A situation where $R_m \lesssim 1$, realised for instance within a current sheet, reduces the induction equation to a diffusion equation

$$\partial_t \mathbf{B} = \eta \nabla^2 \mathbf{B}, \quad (3.33)$$

for a uniform resistivity. Equation (3.33) provides a time scale over which the magnetic field \mathbf{B} is diffused away: $\tau_D = L_0^2/\eta$. For instance, an active region in the solar corona has a length scale $L_0 \approx 10^5 m$ and resistivity $\eta \approx 1 m^2 s^{-1}$. A sunspot has, therefore, a decay time of 30.000 years.¹³ This decay time is, as the one obtained for a solar flare for the Spitzer resistivity in the solar corona,⁶² much longer than observations.

It is finally important to note that, in resistive MHD, the magnetic helicity (equation (3.28)) and cross-helicity (equation (3.26)) are not conserved anymore and dissipate as

$$\frac{DH_{mag}}{Dt} = -2\eta \int_{\mathcal{V}} \mathbf{J} \cdot \mathbf{B} d\mathcal{V} \quad (3.34)$$

$$\frac{DH^c}{Dt} = -(\mu + \eta) \int_{\mathcal{V}} \boldsymbol{\Omega} \cdot \mathbf{J} d\mathcal{V} \quad (3.35)$$

where $\boldsymbol{\Omega} = \nabla \times \mathbf{V}$ is the vorticity and μ the constant kinematic viscosity. The resistivity η in equation (3.34) is the parameter which allow the magnetic field to change its topology. Magnetic reconnection can, therefore, be seen as a change of magnetic topology or connectivity.

3.2 Resistive MHD equations

Together with the conservation of mass, the set of resistive MHD equations to be used for the rest of the dissertation is

$$\frac{\partial \rho}{\partial t} = -\nabla \cdot (\rho \mathbf{V}), \quad (3.36)$$

$$\frac{\partial \rho \mathbf{V}}{\partial t} = -\nabla \cdot \left[\rho \mathbf{V} \otimes \mathbf{V} + \frac{1}{2}(p + B^2)\mathbf{I} - \mathbf{B} \otimes \mathbf{B} \right] + \mu \nabla^2 \rho \mathbf{V}, \quad (3.37)$$

$$\frac{\partial \mathbf{B}}{\partial t} = \nabla \times (\mathbf{V} \times \mathbf{B}) + \eta \nabla^2 \mathbf{B}, \quad (3.38)$$

$$\frac{\partial h}{\partial t} = -\nabla \cdot (h \mathbf{V}) + \frac{\gamma_0 - 1}{\gamma_0 h^{\gamma_0 - 1}} (\eta \mathbf{J}^2), \quad (3.39)$$

where \otimes denotes the tensorial product. The set of equations (3.36)-(3.39) use dimensionless variables for a typical length scale L_0 , a normalizing mass density ρ_0 and a magnetic field strength B_0 . The full normalisation can be found in appendix (A.1).

4 Mean-Field MHD Turbulence Theory

If his forces are united, separate them.

Sun Tzu, *The Art of War*

Once turbulence takes place in a fluid, the variations of the fields become irregular in space and time. Small structures can develop and instabilities can take place in the original smooth fields. The turbulent small scale fluctuations influence large scale structures. The small scale turbulence is reciprocally modified by the large scale dynamics. By means of statistical averaging, the complex interactions between small and large scales can be studied. For that purpose, a separation of time and length scale can be used. In particular, it is through the decomposition of a physical quantity into its mean and fluctuating parts that turbulence is investigated. Especially, the Reynolds decomposition of the variables is considered to describe the physical situations in the following chapters.

In this chapter, MHD turbulence is considered through a mean-field approach. In the mean-field MHD equations, the turbulence effect appears in the equations as averaged second order fluctuating variables as the turbulent stress-tensor and the turbulent electromotive force.

4.1 Reynolds-Averaged Navier-Stokes Equations

4.1.1 Turbulence Nomenclature, Symmetry Laws and Averaging Rules

Turbulence is defined by the statistical average properties of the fluctuating fields. The averaged fluctuations correlate the turbulent fields to each other in a statistical sense. Important notions in turbulence are:

1. Homogeneity: Statistical property does not change with position (translation invariance). A steady turbulent field is homogeneous with respect to time.
2. Isotropy: Invariance under a rotation about any axis, no directions are preferred.
3. Mirror-symmetry: Invariance under reflection with an arbitrary plane.

A mean quantity obtained from a turbulent field can have the properties 1-3 or be inhomogeneous, anisotropic or non-mirror-symmetric. Certain physical quantities possess right-handedness. It is the case for variables defined by means of the curl operator such as the current density or vorticity. Such quantities have different transformation properties than other variables which are not defined by this operator. They are called pseudo and axial vectors. Such vectors do not follow the usual rules of vector calculations. For instance, for two vectors \mathbf{b} and \mathbf{c} , the vector $\mathbf{a} = \mathbf{b} \times \mathbf{c}$ transforms under a reflection of the axis as

$$\mathbf{a} = \mathbf{b} \times \mathbf{c} \xrightarrow{\text{reflexion}} (-\mathbf{b}) \times (-\mathbf{c}) = \mathbf{a}. \quad (4.1)$$

The curl operator produces a pseudo vector as

$$\mathbf{a} = \nabla \times \mathbf{b} \xrightarrow{\text{reflexion}} \nabla \times (-\mathbf{b}) = \mathbf{a}. \quad (4.2)$$

For a fluctuating field, a variable f is divided into its expected mean value \bar{f} and its fluctuation f' as

$$f = \bar{f} + f', \quad (4.3)$$

and the fluctuating fields are defined as the difference $f' = f - \bar{f}$. A Reynolds decomposition is defined for two fluctuating fields f and g through the following relations³²

$$f = \bar{f} + f', \quad \bar{f} = \bar{\bar{f}}, \quad \bar{f}' = 0, \quad (4.4)$$

$$\overline{f + g} = \bar{f} + \bar{g}, \quad \overline{fg} = \bar{f}\bar{g}, \quad \overline{f'g'} = 0, \quad (4.5)$$

$$\overline{f'g'} \neq 0 \quad \partial_n \bar{f} = \overline{\partial_n f}, \quad \int \bar{f} dn = \overline{\int f dn}. \quad (4.6)$$

where the derivative and integration can be carried over space or time. The average procedure can be of three kind:

$$\text{I) Time average: } \bar{f}_T(\mathbf{x}, t) = \frac{1}{T} \int_{-T/2}^{T/2} f(\mathbf{x}, t + t') dt', \quad (4.7)$$

$$\text{II) Space average: } \bar{f}_{\mathcal{V}}(\mathbf{x}, t) = \frac{1}{\mathcal{V}} \int_{\mathcal{V}} f(\mathbf{x}, t) d\mathcal{V}, \quad (4.8)$$

$$\text{III) Ensemble average: } \bar{f}(\mathbf{x}, t) = \lim_{N \rightarrow \infty} \sum_i^N f_i(\mathbf{x}, t), \quad (4.9)$$

where the index i in equation (4.9) refers the i -th realisation of the variable f and N is the total number of realisations. The relations (4.4)-(4.6) are strictly fulfilled for the ensemble average [equation (4.9)]. Spatial or time average are often technically favored over an ensemble average since the latter can be numerically very expensive. A caveat of the average procedure I [equation (4.7)] or II [equation (4.8)] is that the relations (4.4)-(4.6) are only approximated. This shortcoming is reduced by minimizing the variation of the mean variables over the average procedure under consideration.

4.1.2 Mean and Fluctuating Fields Equations

The mean and fluctuating governing equations for a turbulent field are obtained by applying the decomposition (4.3). The momentum and induction equations [equations (3.6)-(3.18)] become

$$\begin{aligned} \partial_t [(\bar{\rho} + \rho')(\bar{V}_i + V'_i)] &= -\partial_j [(\bar{\rho} + \rho')(\bar{V}_i + V'_i)(\bar{V}_j + V'_j) \\ &\quad + \frac{1}{2}((p + p') + (B + B')^2)\delta_{ij} \\ &\quad - (\bar{B}_i + B'_i)(\bar{B}_j + B'_j)] + \mu\partial_j\partial_j(V_i + V'_i), \end{aligned} \quad (4.10)$$

$$\partial_t(\bar{B}_i + B'_i) = \epsilon_{ijk}\partial_j[\epsilon_{klm}(\bar{V}_l + V'_l)(\bar{B}_m + B'_m) - \eta(\bar{J}_k + J'_k)], \quad (4.11)$$

where $\partial_i \equiv \partial/\partial x_i$ and the indices run over spatial dimensions. Einstein's summation is further assumed. For simplicity, it is assumed that $\rho' = 0$. This assumption does not deny the importance of the mass density fluctuations, especially for compressible fluids (see appendix (B)). Such an approximation is a first step towards a full turbulence model applicable to magnetic reconnection. From now on, Alfvén normalized quantities, obtained by dividing by the mean mass density $\bar{\rho}$, are assumed. The magnetic field, current density and pressure become

$$\frac{B_i}{(\mu_0\bar{\rho})^{1/2}} = B_i, \quad J_i\left(\frac{\mu_0}{\bar{\rho}}\right)^{1/2} = J_i, \quad \frac{p}{\bar{\rho}} = p \quad \text{and} \quad \frac{\mu}{\bar{\rho}} = \nu. \quad (4.12)$$

These units are applied to the mean and fluctuating variables. Taking the ensemble average of equations (4.10)-(4.11) and following the rules (4.3) yields

$$\partial_t\bar{V}_i = -\partial_j\left[\bar{V}_i\bar{V}_j + \frac{1}{2}(p + B^2)\delta_{ij} - \bar{B}_i\bar{B}_j + R_{ij}\right] + \nu\partial_j\partial_j\bar{V}_i, \quad (4.13)$$

$$\partial_t\bar{B}_i = \epsilon_{ijk}\partial_j[\epsilon_{klm}\bar{V}_l\bar{B}_m - \eta\bar{J}_k + \mathcal{E}_k], \quad (4.14)$$

where the information about turbulence is contained in the turbulent stress-tensor R_{ij} and the electromotive force \mathcal{E}_k . The turbulent stress-tensor contains the information of the velocity and magnetic field fluctuations autocorrelation. It is composed of two parts, the Reynolds tensor $R_{ij}^V = \langle V'_i V'_j \rangle$ (autocorrelation of the velocity field fluctuations) and the Maxwell's tensor $R_{ij}^M = \langle B'_i B'_j \rangle$ (autocorrelation of the magnetic field fluctuations) as

$$R_{ij} = \langle V'_i V'_j - B'_i B'_j \rangle. \quad (4.15)$$

On the other hand, the electromotive force holds the information about the correlation of the velocity and the magnetic field fluctuations as

$$\mathcal{E}_k = \langle \epsilon_{knm} V'_n B'_m \rangle. \quad (4.16)$$

As discussed in section (3.1.2), the total energy and cross-helicity are conserved quantities in ideal MHD. Their turbulent counterparts are of particular importance in turbulence. They are defined as

$$K = \frac{1}{2} \langle V'_i V'_i + B'_i B'_i \rangle, \quad (4.17)$$

$$W = \langle V'_i B'_i \rangle, \quad (4.18)$$

where the symbol K is the turbulent energy and W the turbulent cross-helicity. The information about turbulence is obtained by relating the turbulent stress-tensor R_{ij} , the electromotive force \mathcal{E}_k , the turbulent energy K and the turbulent cross-helicity W to the mean velocity and magnetic field. How to determine these relations is called the closure problem. It can be addressed in two ways: i) relating algebraically the mean-fields to \mathcal{E} , R_{ij} , K and W or ii) to use equations for them in addition to the mean-field MHD equations. It is the latter approach that is used to address the closure problem.¹ For that purpose, the equations for the velocity and magnetic field fluctuations V'_i and B'_i are needed.

Neglecting mass density fluctuations as previously, the equations for the velocity and magnetic field fluctuations are obtained by subtracting equations (4.10)-(4.11) to equations (4.13)-(4.14). This provides the following equations

$$\begin{aligned} \partial_t V'_i + \bar{V}_j \partial_j V'_i + \partial_j (V'_i V'_j - B'_i B'_j + R_{ij}) + \partial_i p'_M - \nu \partial_j \partial_j V'_i \\ = \bar{B}_j \partial_j B'_i - V'_j \partial_j \bar{V}_i + B'_j \partial_j \bar{B}_i, \end{aligned} \quad (4.19)$$

$$\begin{aligned} \partial_t B'_i + \bar{V}_j \partial_j B'_i + \partial_j (V'_j B'_i - V'_i B'_j + \epsilon_{ijl} \mathcal{E}_l) - \eta \partial_j \partial_j B'_i \\ = \bar{B}_j \partial_j V'_i - V'_j \partial_j \bar{B}_i + B'_j \partial_j \bar{V}_i. \end{aligned} \quad (4.20)$$

The fluctuation of the MHD pressure $p_M = p + \mathbf{B}^2/2$ in equation (4.19) is given by

$$p'_M = p + \frac{\mathbf{B}^2}{2} - \overline{p + \frac{\mathbf{B}^2}{2}}. \quad (4.21)$$

The evolution equation for the turbulent stress-tensor R_{ij} is obtained by subtracting the Maxwell stress-tensor R_{ij}^M to the Reynolds stress-tensor R_{ij}^V . It is achieved by multiplying (4.20) with B'_j for the former and (4.19) with V'_j for the latter. The governing equation for the turbulent energy is obtained similarly but adding R_{ij}^M to R_{ij}^V . It is useful to define a turbulent tensor R_{ij}^\pm as

$$\langle R_{ij}^\pm \rangle = R_{ij}^V \pm R_{ij}^M = \begin{cases} R_{ij} & \text{for } R_{ij}^- \\ K & \text{for } R_{ij}^+. \end{cases} \quad (4.22)$$

I. Note that due to the complexity of the turbulent equations, algebraic relations are often used in combinations with the governing equations of the mean variables derived from the turbulent fields.

for which the governing equation is

$$\frac{D}{Dt} R_{ij}^{\pm} \equiv \frac{D}{Dt} (V_i' V_j' \pm B_i' B_j') = (-V_j' V_k' \pm B_j' B_k') \partial_k V_i + (-V_i' V_k' \pm B_i' B_k') \partial_k V_j \quad (4.23a)$$

$$+ (B_k' V_j' \mp B_j' V_k') \partial_k B_i + (V_i' B_k' \mp B_i' V_k') \partial_k B_j \quad (4.23b)$$

$$- 2\nu \partial_k V_i' \partial_k V_j' \mp 2\eta \partial_k B_j' \partial_k B_i' \quad (4.23c)$$

$$+ \partial_k \nu \partial_k (V_i' V_j') \pm \partial_k \eta \partial_k (B_i' B_j') \quad (4.23d)$$

$$+ V_j' B_k \partial_k B_i' \pm B_i' B_k \partial_k V_j' + V_i' B_k \partial_k B_j' \pm B_j' B_k \partial_k V_i' \quad (4.23e)$$

$$+ V_j' B_k' \partial_k B_i' \pm B_i' B_k' \partial_k V_j' + V_i' B_k' \partial_k B_j' \pm B_j' B_k' \partial_k V_i' \quad (4.23f)$$

$$\mp B_j' V_k' \partial_k B_i' \mp B_i' V_k' \partial_k B_j' + V_k' \partial_k (V_i' V_j') - \partial_k (V_i' V_j' V_k') \quad (4.23g)$$

$$- V_j' \partial_k R_{ik} - V_i' \partial_k R_{kj} \mp B_j' \epsilon_{ikn} \partial_k E_n \mp B_i' \epsilon_{jkn} \partial_k E_n \quad (4.23h)$$

$$- \partial_k (V_i' p_M' \delta_{kj} + V_j' p_M' \delta_{ki}) + p_M' (\partial_j V_i' + \partial_i V_j'). \quad (4.23i)$$

From equation (4.17), the evolution equation for the turbulent energy K is obtained by taking the plus sign of equation (4.22), taking its trace, dividing by two and finally taking the ensemble average as

$$\frac{DK}{Dt} \equiv \frac{D}{Dt} \left\langle \frac{V_i' V_i' + B_i' B_i'}{2} \right\rangle = - R_{ik} \partial_k \bar{V}_i - \mathcal{E}_M \cdot \bar{\mathbf{J}} \quad (4.24a)$$

$$- \nu \langle \partial_k V_i' \partial_k V_i' \rangle - \eta \langle \partial_k B_i' \partial_k B_i' \rangle \quad (4.24b)$$

$$+ \partial_k \left(\langle V_i' B_i' \rangle \bar{B}_k + \left\langle - \left(\frac{V_i' V_i' + B_i' B_i'}{2} + p_M' \right) V_k' \right\rangle \right. \\ \left. + V_i' B_i' B_k' + \nu \partial_k \left\langle \frac{V_i' V_i'}{2} \right\rangle + \eta \partial_k \left\langle \frac{B_i' B_i'}{2} \right\rangle \right). \quad (4.24c)$$

The terms (4.24a), (4.24b) and (4.24c) are the production term P_K , the dissipation term \mathcal{E}_K and the transport term T_K of the turbulent energy. The latter only transports the turbulent energy from one place to another. Except for inflow or outflow from the boundaries, T_K does not contribute to the production or dissipation of the turbulent energy.

The evolution equation for the turbulent cross-helicity is obtained by multiplying (4.20) with V_j' and (4.19) with B_j' . The resulting evolution equation is

$$\frac{D}{Dt} (V_i' B_j') = V_i' \bar{B}_k \partial_k V_j' + \bar{V}_i \epsilon_{jkm} \partial_n \mathcal{E}_m + V_i' \eta \partial_{kk} B_j' \quad (4.25a)$$

$$- B_j' \partial_j p_M' + B_j' \bar{B}_k \partial_k B_i' - \bar{B}_j \partial_k R_{kj} + B_j' \nu \partial_{kk} V_i', \quad (4.25b)$$

where $\partial_{kk} = \partial^2 / (\partial_k \partial_k)$. The ensemble average of equation (4.25) gives the governing

equation for the turbulent cross-helicity

$$\frac{DW}{Dt} \equiv \frac{D}{Dt} \langle V'_i B'_i \rangle = -R_{ik} \partial_k \bar{B}_i - \mathcal{E}_M \cdot \bar{\Omega} \quad (4.26a)$$

$$- (\nu + \eta) \langle \partial_k V'_i \partial_k B'_i \rangle \quad (4.26b)$$

$$+ \partial_k \left[\left\langle \frac{V'_i V'_i + B'_i B'_i}{2} \right\rangle \bar{B}_k + \left\langle \left(\frac{V'_i V'_i + B'_i B'_i}{2} - p'_M \right) B'_k \right\rangle \right. \\ \left. - V'_i B'_i V'_k + \nu \langle B'_i \partial_k V'_i \rangle + \eta \langle V'_i \partial_k B'_i \rangle \right] \quad (4.26c)$$

$$- \bar{B}_j R_{ki} + \epsilon_{jnm} \bar{V}_i \mathcal{E}_n \Big]. \quad (4.26d)$$

As for the turbulent energy K [equation (4.24)], the production term P_W for the turbulent cross-helicity W is given by equation (4.26a), its dissipation ε_W by equation (4.26b) and the transport term T_W as equation (4.26d). Both equations (4.24) and (4.26) can be cast in the form

$$\frac{DA}{Dt} = P_A - \varepsilon_A + \nabla \cdot A \quad \text{where } A = (K, W). \quad (4.27)$$

Integrating equation (4.27) for the turbulent energy K over a volume element $d\mathcal{V}$ and using the Gauss integral theorem yields

$$\int_{\mathcal{V}} \partial_t K = \int_{\mathcal{V}} P_K d\mathcal{V} - \int_{\mathcal{V}} \varepsilon_K d\mathcal{V} + \int_S (-K\bar{V} + T_K) \cdot \mathbf{e}_n dS, \quad (4.28)$$

where \mathbf{e}_n is the unit vector pointing outwards the surface S which encloses the volume \mathcal{V} . Equation (4.28) shows that without energy inflow from the boundary by the transport term T_K , the production term P_K sustains the turbulence while the dissipation term ε_K contributes to the conversion of the energy into heat. The same reasoning holds for the turbulent cross-helicity because it has the units of an energy density when the magnetic field is written in Alfvén units [equation (4.12)]. The mean-field energy equation counterpart of equation (4.24) is obtained by multiplying both equations (4.13)-(4.14) by \bar{V}_j and \bar{B}_j , taking the trace and finally dividing by two. The resulting mean-field energy equation is

$$\frac{D\bar{E}}{Dt} \equiv \frac{D}{Dt} \left(\frac{\bar{V}_i \bar{V}_i + \bar{B}_i \bar{B}_i}{2} \right) = +R_{ik} \partial_k \bar{V}_i + \mathcal{E}_M \cdot \bar{\mathbf{J}} \quad (4.29a)$$

$$- \nu (\partial_k \bar{V}_i \partial_k \bar{V}_i) - \eta (\partial_k \bar{B}_i \partial_k \bar{B}_i) \quad (4.29b)$$

$$+ \partial_k \left[-(\bar{B}_i \bar{V}_i) \bar{B}_k + P \bar{V}_k + \epsilon_{kmi} \mathcal{E}_m \bar{B}_i \right. \\ \left. - \bar{V}_i R_{ki} - \nu \partial_k (\bar{V}_i \bar{V}_i) - \eta \partial_k (\bar{B}_i \bar{B}_i) \right]. \quad (4.29c)$$

Equation (4.29a) is the production term $P_{\bar{E}}$ of the mean MHD energy due to fluctuations, equation (4.29b) its dissipation $\varepsilon_{\bar{E}}$ and equation (4.29c) its transport term $T_{\bar{E}}$. Integrating equation (4.29) over a volume element $d\mathcal{V}$ gives

$$\int_{\mathcal{V}} \partial_t \bar{E} = \int_{\mathcal{V}} -P_{\bar{E}} d\mathcal{V} - \int_{\mathcal{V}} \varepsilon_{\bar{E}} d\mathcal{V} + \int_S (-\bar{E} \bar{V} + T_{\bar{E}}) \cdot \mathbf{e}_n dS, \quad (4.30)$$

where $P_{\bar{E}}$ has been identified to $-P_K$. Hence, the sustainment of turbulent energy K by P_K is obtained by draining energy from the mean-fields. This transfer of energy from the mean to the fluctuating field is represented by the energy spectrum or cascade.^{II} Similarly, the governing equation for the mean cross-helicity is obtained as

$$\frac{D\mathcal{W}}{Dt} \equiv \frac{D}{Dt} (V_i B_i) = + R_{ik} \partial_k \bar{B}_i + \mathcal{E}_M \cdot \bar{\Omega} \quad (4.31a)$$

$$- (\nu + \eta) \partial_k \bar{V}_i \partial_k \bar{B}_i \quad (4.31b)$$

$$+ \partial_k \left[\left(\frac{\bar{V}_i \bar{V}_i + \bar{B}_i \bar{B}_i}{2} \right) \bar{B}_k + P \bar{B}_k + (\nu + \eta) \partial_k \bar{B}_i \bar{V}_i \right], \quad (4.31c)$$

and the production of turbulent cross-helicity is also due to a pumping of the large scale fields from the turbulence. In fact, the conservation of the total MHD energy and cross-helicity in ideal MHD (vanishing ν and η), without source or sink from the boundaries, allows us to write equations (4.24) and (4.26) in the exact form of equation (4.27) for which production, dissipation and transport terms can be identified. For instance, the residual helicity H defined as

$$H = \langle B'_i J'_i - V'_i \Omega'_i \rangle, \quad (4.32)$$

is not conserved in ideal MHD and its governing equation in mean-field theory is much more complicated, its production or dissipation cannot be clearly identified.^{III} The residual helicity vanishes in isotropic plasmas because the statistical properties of V'_i and B'_i remain the same under a reflection while H must change its sign since it is a pseudo scalar.

The main point of the turbulent model used later in the present work is the consideration of the mean velocity field inhomogeneities in the turbulent electromotive force \mathcal{E} . Traditionally, the mean electromotive force is assumed to be a linear functional of the mean magnetic field and its derivatives as

$$(\mathcal{E}_M)_i = \alpha_{ij} \bar{B}_j - \beta_{ijk} \partial_j \bar{B}_k + \dots, \quad (4.33)$$

under the assumption that the mean magnetic field \bar{B}_i depends only weakly on time and position.³² It is further assumed that the mean flow \bar{V}_i vanishes and that V'_i is homogeneous, isotropic and steady in the statistical sense. The α and β tensors represent the dynamo and dissipation of the magnetic field due to turbulence. In most astrophysical flows, the approximation $\bar{V}_i = 0$ as well as the steadiness of V'_i is not valid anymore. Relaxing these approximations, the electromotive force becomes

$$(\mathcal{E}_M)_i = \alpha_{ij} \bar{B}_j + \gamma_{ijk} \partial_j \bar{V}_k - \beta_{ijk} \partial_j \bar{B}_k + \dots, \quad (4.34)$$

where the transport coefficients α , β and γ contain the contributions of the fluctuating fields to the mean-fields. Deriving the governing equation for \mathcal{E} is helpful to understand the reasons for retaining a term proportional to the mean-field velocity in equation (4.34) as well as to relate the transport coefficients to the fluctuating fields. Following Yokoi,⁶³ it is shown that the basic dependence of the transport coefficients on the turbulent quantities can be obtained even with the simplest assumptions on the fluctuations: isotropic

II. See chapter (6).

III. The reader is referred to Yoshizawa^{34,60} for more details about the governing equation of the residual helicity.

and homogeneous fields. The evolution equation for the turbulent electromotive force is obtained multiplying equation (4.25) by the Levi-Civita symbol ϵ_{nij} and then taking the ensemble average. This gives

$$\begin{aligned} \frac{D\mathcal{E}_n}{Dt} &= \frac{1}{3} \langle B'_j \epsilon_{jki} \partial_k B'_i - V'_j \epsilon_{jki} \partial_k V'_i \rangle \bar{B}_n - \frac{1}{3} \langle V'_j V'_j + B'_m B'_m \rangle \epsilon_{nki} \partial_k \bar{B}_i \\ &\quad + \frac{2}{3} \langle V'_j B'_j \rangle \epsilon_{nki} \partial_k \bar{V}_i - \epsilon_{nij} \langle B'_j \partial_i p'_M \rangle + \text{H.O.T.}, \end{aligned} \quad (4.35)$$

where H.O.T. stands for higher order terms which are neglected. Assuming that the transport coefficients α_{ij} , β_{ijk} and γ_{ijk} can be written as

$$\alpha_{ij} = \alpha \delta_{ij}, \quad (4.36a)$$

$$\beta_{ijk} = \beta \epsilon_{ijk}, \quad (4.36b)$$

$$\gamma_{ijk} = \gamma \epsilon_{ijk}, \quad (4.36c)$$

where δ_{ij} is the Kronecker symbol, the electromotive force of equation (4.34) takes the form

$$(\mathcal{E}_M)_i = \alpha \delta_{ij} \bar{B}_j + \gamma \epsilon_{ijk} \partial_j \bar{V}_k - \beta \epsilon_{ijk} \partial_j \bar{B}_k + \dots \quad (4.37)$$

The transport coefficients can be identified as

$$\alpha = \tau \frac{1}{3} \langle B'_j \epsilon_{jki} \partial_k B'_i - V'_j \epsilon_{jki} \partial_k V'_i \rangle, \quad (4.38a)$$

$$\beta = \tau \frac{1}{3} \langle V'_n V'_n + B'_n B'_n \rangle, \quad (4.38b)$$

$$\gamma = \tau \frac{2}{3} \langle V'_n B'_n \rangle, \quad (4.38c)$$

when equation (4.37) is compared with equation (4.35). The symbol τ is the timescale over which the electromotive force evolves. Equation (4.38) provides a strong relation between the turbulent energy K [equation (4.17)], turbulent cross-helicity W [equation (4.18)] and residual helicity H [equation (4.32)] to the coefficients β , γ and α respectively. The point of turbulence modelling is to obtain the transport terms α , β and γ in terms of the mean-fields V_i , B_i , K , W and H .

4.2 Reynolds-Averaged Turbulence Model

As already mentioned before, the most important quantities for MHD turbulence are the turbulent stress-tensor R_{ij} [equation (4.15)] and the turbulent electromotive force \mathcal{E}_M [equation (4.16)]. They characterize the transport due to turbulence of the mean magnetic field and velocity flow. In order to express the symmetry between R_{ij} and E_M , the latter is written in terms of the turbulent magnetic Reynolds stress M_{ij}

$$M_{ij} = - \langle V'_i B'_j - V'_j B'_i \rangle, \quad (4.39)$$

$$\mathcal{E}_k = - \frac{1}{2} \epsilon_{kij} M_{ij}. \quad (4.40)$$

Assuming isotropy and homogeneity of the fluctuating electromagnetic fields, flows and plasma density, the equations for the turbulent Reynolds stress-tensor (obtained from equation (4.23)) and the turbulent magnetic Reynolds stress (obtained from equation (4.16)) read

$$R_{ij} = -\frac{1}{3} \langle B'_n B'_n - V'_n V'_n \rangle \delta_{ij} - \nu_R (\partial_i \bar{V}_j + \partial_j \bar{V}_i) + \nu_M (\partial_i \bar{B}_j + \partial_j \bar{B}_i), \quad (4.41)$$

$$M_{ij} = -\alpha \epsilon_{ijk} \bar{B}_k - \beta_R (\partial_i \bar{V}_j - \partial_j \bar{V}_i) + \beta_M (\partial_i \bar{B}_j - \partial_j \bar{B}_i). \quad (4.42)$$

The coefficient ν_R is the traditional eddy-viscosity coefficient which is the viscosity due to velocity fluctuations while ν_M arises from the magnetic field fluctuations. The α coefficient is the usual dynamo term which is genuine to magnetic field. Its effect is the generation of magnetic field due to small scale fluctuations.^{35,64,65} The coefficient β_M is an apparent turbulent resistivity, sometimes called anomalous resistivity, which causes a diffusion of magnetic flux. Finally, the coefficient β_R is a term corresponding to the correlation of the magnetic field and velocity fluctuations. Comparing equation (4.42) with equation (4.37), the term β_R is related to the cross-helicity W through the γ term [equation (4.38c)] and β_M to the turbulent energy K [equation (4.38b)]. The coefficients ν_R and β_M [equations (4.41)-(4.42)], which represent an enhancement of the mean-field dissipations due to small scales fluctuations, are related in two-scales direct-Interaction approximation (TSDIA)^{IV} as

$$\beta_M = \frac{5}{7} \nu_R. \quad (4.43)$$

From equation (4.37), the term β_M is related to the turbulent energy K through the β -term in equation (4.38b). A similar relation is obtained from TSDIA for the coefficients β_R and ν_M as

$$\beta_R = \frac{5}{7} \nu_M, \quad (4.44)$$

which is mostly written in terms of the cross-helicity due to relation of β_R with the γ -term when equations (4.37) and (4.38c) are compared. In fact, the deformations of the magnetic field lines from the fluid motion generates the coefficients in equation (4.44) which means that the cross-helicity is converting the kinetic/magnetic energy into magnetic/kinetic energy.^{34,67} The concept of cross-helicity is, therefore, of certain importance for magnetic reconnection which is an energy conversion phenomenon.

4.2.1 Bulk Turbulence Model

A simple approach to turbulence is reached by considering statistical turbulent quantities relevant for the problem under consideration. Since magnetic reconnection relies on the possibility to convert the magnetic energy into other forms, the turbulence energy K [equation (4.17)] is necessary to account for the annihilation of the magnetic field due to the field fluctuations. The turbulent cross-helicity W [equation (4.18)] is further required since it is related to the energy conversion. In addition, the turbulent energy decay rate ε_K is also a necessary variable to describe the transfer of the turbulent energy from large/small scales to small/large scales.^V The last turbulence quantity to be considered is the residual

IV. Appendix (C) summarizes the key steps of the TSDIA formalism. The detailed description can be found in Yoshizawa.⁶⁶

V. See chapter (6).

helicity H [equation (4.32)] which is related to the dynamo effect through the α term in equations (4.37)-(4.38a). The residual helicity has to be considered in two-dimensional guide field reconnection (see section (7.4)) as well as three-dimensional reconnection.⁶⁸

The set of model equations for mean-field MHD turbulence results from the TS-DIA.^{34,66} The Alfvén units [equation (4.12)] prevail for the rest of the section. In this formalism, the mean momentum equation reads

$$\partial_t \bar{\mathbf{V}} + \nabla \cdot (\bar{\mathbf{V}} \otimes \bar{\mathbf{V}} - \bar{\mathbf{B}} \otimes \bar{\mathbf{B}}) = -\nabla \bar{P}_M + \nabla \cdot \mathbf{R} + \nu \nabla^2 \bar{\mathbf{V}}, \quad (4.45)$$

where \mathbf{R} is the turbulent stress-tensor. The mean-field induction equation yields

$$\partial_t \bar{\mathbf{B}} = \nabla \times (\bar{\mathbf{V}} \times \bar{\mathbf{B}} + \mathcal{E}_M - \eta \bar{\mathbf{J}}), \quad (4.46)$$

where $\bar{\mathbf{J}} = \nabla \times \bar{\mathbf{B}}$ and \mathcal{E}_M is the turbulent electromotive force. The solenoidal conditions $\nabla \cdot \bar{\mathbf{V}} = 0$ and $\nabla \cdot \bar{\mathbf{B}} = 0$ hold for both equations (4.45) and (4.46). In the bulk turbulence formalism,^{34,66,69} the turbulent stress-tensor and turbulent electromotive force are written in terms of the turbulent energy K , turbulent cross-helicity W , the residual helicity H and the turbulent energy dissipation rate as

$$R_{ij} = C_{\nu R} \frac{K^2}{\varepsilon_K} (\partial_i \bar{V}_j + \partial_j \bar{V}_i) - C_{\nu M} \frac{KW}{\varepsilon_K} (\partial_i \bar{B}_j + \partial_j \bar{B}_i), \quad (4.47)$$

$$\mathcal{E}_M = C_\alpha \frac{KH}{\varepsilon_K} \bar{\mathbf{B}} - C_{\beta M} \frac{K^2}{\varepsilon_K} \bar{\mathbf{J}} + C_{\beta R} \frac{KW}{\varepsilon_K} \bar{\mathbf{\Omega}}, \quad (4.48)$$

where $\nabla \times \bar{\mathbf{V}} = \bar{\mathbf{\Omega}}$. The constants C_\square are model constants related to the constants in equations (4.41)-(4.42). In order to close the system of equations, the following governing equations for the turbulent energy K and turbulent cross-helicity W are needed

$$\frac{DK}{Dt} = -R_{ij} \partial_i \bar{V}_j - \bar{\mathbf{J}} \cdot \mathcal{E}_M - \varepsilon_K + \nabla \cdot \left(W \bar{\mathbf{B}} + C_K \frac{K^2}{\varepsilon_K} \nabla K \right), \quad (4.49)$$

$$\frac{DW}{Dt} = -R_{ij} \partial_i \bar{B}_j - \bar{\mathbf{\Omega}} \cdot \mathcal{E}_M - C_W \frac{\varepsilon_K W}{K} + \nabla \cdot \left(K \bar{\mathbf{B}} + C_{W2} \frac{K^2}{\varepsilon_K} \nabla W \right). \quad (4.50)$$

The last two equations to be considered are the governing equation for the residual helicity H and the dissipation rate of the turbulent energy ε_K . The TSDIA leads to

$$\begin{aligned} \frac{DH}{Dt} = & C_{H1} \frac{\varepsilon_K}{K} \bar{\mathbf{B}} \cdot \bar{\mathbf{J}} - \frac{\varepsilon_K H}{K^2} \left[C_{H2} \bar{\mathbf{B}}^2 + C_{H3} \bar{\mathbf{\Omega}} \cdot \bar{\mathbf{B}} \right] \\ & - C_{H4} \frac{\varepsilon_K H}{K} + \nabla \cdot \left(C_{H5} \frac{K^2}{\varepsilon_K} \nabla H \right), \end{aligned} \quad (4.51)$$

$$\begin{aligned} \frac{D\varepsilon_K}{Dt} = & C_{\varepsilon_1} \frac{\varepsilon_K}{K} (R_{ij} \partial_i \bar{V}_j - \bar{\mathbf{J}} \cdot \mathcal{E}_M) - C_{\varepsilon_2} \frac{\varepsilon_K^2}{K} \\ & + C_{\varepsilon_3} \frac{\varepsilon_K}{K} \nabla \cdot (W \bar{\mathbf{B}}) + \nabla \cdot \left(C_{\varepsilon_4} \frac{K^2}{\varepsilon_K} \nabla \varepsilon_K \right). \end{aligned} \quad (4.52)$$

The multiple constants C_* in equations (4.49)-(4.52) have to be determined and optimized depending on the physical situation under considerations.³⁴ In order to treat the problem

of magnetic reconnection from the viewpoint of mean-field theory, the production mechanism of the chosen statistical quantities is important. From equation (4.27), the production mechanism for the turbulent energy and turbulent cross-helicity are written as

$$P_K = R_{ij}\partial_i\bar{V}_j - \bar{\mathbf{J}} \cdot \mathcal{E}_M, \quad (4.53)$$

$$P_W = R_{ij}\partial_i\bar{B}_j - \bar{\mathbf{\Omega}} \cdot \mathcal{E}_M. \quad (4.54)$$

Equations (4.53)-(4.54) show that the production of turbulent energy K and cross-helicity W is of two kinds: i) the production due to the turbulent stress-tensor R_{ij} , and ii) the production due to the electromotive force \mathcal{E}_M . The residual helicity H has similar terms as equation (4.27) but they cannot be identified to production, dissipation or transport because the residual helicity is not a conserved quantity in MHD.⁶⁰ Keeping this point in mind, the principle term responsible for the generation of residual helicity can be identified as

$$G_H = C_{H1} \frac{\varepsilon_K}{K} \bar{\mathbf{B}} \cdot \bar{\mathbf{J}} - \frac{\varepsilon_K H}{K^2} (C_{H3} \bar{\mathbf{\Omega}} \cdot \bar{\mathbf{B}}). \quad (4.55)$$

Finally, equations (4.38a)-(4.38c) are written in terms of the turbulent energy K , turbulent cross-helicity W and residual helicity H as

$$\alpha = \tau C_\alpha H, \quad (4.56)$$

$$\beta = \tau C_\beta K, \quad (4.57)$$

$$\gamma = \tau C_\gamma W, \quad (4.58)$$

where $\tau = K/\varepsilon_K$ is the turbulence timescale and C_* model constants of the order of $O(10^{-1})$.

4.3 Turbulent Electromotive Force and Turbulence Productions

As described in section (4.2.1), the production of the bulk turbulence is important to grasp the influence of turbulence on reconnection. As far as the turbulent energy K and turbulent cross-helicity W are concerned, the turbulent stress-tensor R_{ij} [equation (4.47)] as well as the turbulent electromotive force \mathcal{E}_M [equation (4.48)] contribute to the production of turbulence. This is related to the fact that R_{ij} and \mathcal{E}_M represent the mean-field correlations of the magnetic and velocity fluctuations. The physical arguments on the production of turbulence can be found in Yokoi and Hoshino.⁷⁰ In the present work, only the production of turbulence due to the turbulent electromotive force is considered because the influence of the residual helicity H on the reconnection problem is investigated.

4.3.1 Production of Turbulent Energy and Turbulent Cross-Helicity

The production mechanism P_K due to the electromotive force is obtained by inserting equation (4.48) into equation (4.53)

$$P_K = \beta \bar{\mathbf{J}}^2 - \gamma \bar{\mathbf{\Omega}} \cdot \bar{\mathbf{J}} - \alpha \bar{\mathbf{J}} \cdot \bar{\mathbf{B}}, \quad (4.59)$$

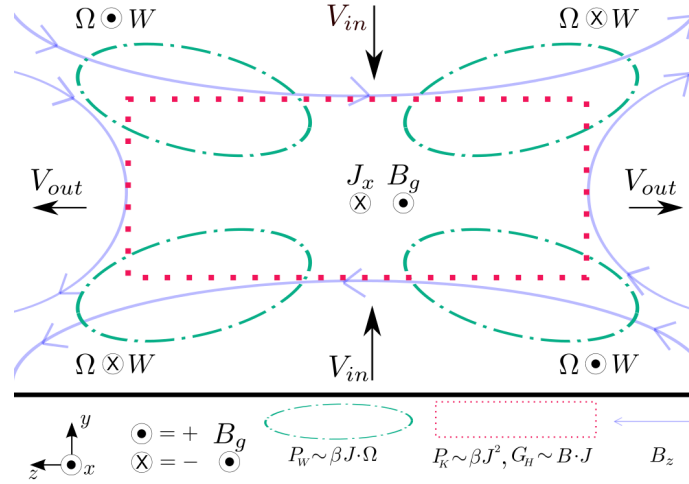


Figure 4.1: Schematic depicting the position of the production term of i) the turbulent energy P_K , ii) the turbulent cross-helicity P_W and the generation term of the residual helicity G_H . The term P_W always contributes to localise the turbulent resistivity $\beta = C_\beta \tau K$ inside the diffusion region while G_H can suppress K for a sufficiently large guide magnetic field \mathbf{B}_g .

where α , β and γ are defined by equations (4.56)-(4.58). The first case to be considered is a vanishing mean flow gradients and a non-alignment of the mean current density to the mean magnetic field. In such a situation, only the first term on the right hand side of equation (4.59) remains, the turbulent energy is then located where the current density is defined. There is also no contribution of the cross-helicity to electromotive force and the mean-field induction equation reads

$$\partial_t \bar{\mathbf{B}} = \nabla \times (\bar{\mathbf{V}} \times \bar{\mathbf{B}} - \eta_T \bar{\mathbf{J}}), \quad (4.60)$$

where $\eta_T \equiv \eta + \beta$. In such situations, the magnetic field cannot be frozen in to the plasma even in the limit of vanishing resistivity η . It is therefore required that another phenomena balance the diffusion of magnetic field by the turbulent resistivity β . This might be achieved in presence of a strong guide magnetic field parallel to the mean current density. For vanishing mean flow gradients, the generation of residual helicity H ($\propto \alpha$) is given only by a term proportional to $\bar{\mathbf{B}} \cdot \bar{\mathbf{J}}$. This means that: i) the sign of α is that of $\bar{\mathbf{B}} \cdot \bar{\mathbf{J}}$ and ii) the residual helicity H is also located where the current density accumulates. The production mechanism for the turbulent energy becomes

$$P_K = (\beta \bar{\mathbf{J}} - \alpha \bar{\mathbf{B}}) \cdot \bar{\mathbf{J}}, \quad (4.61)$$

For a moderate guide magnetic field strength, the residual helicity contributes to reduce the production of turbulent energy. For a sufficiently large guide magnetic field parallel to the mean current density, the turbulent energy K can be suppressed by the residual helicity H . If such a balance of turbulence happens, the mean-field induction equation in the limit of vanishing mean flow gradients reads

$$\partial_t \bar{\mathbf{B}} = \nabla \times (\bar{\mathbf{V}} \times \bar{\mathbf{B}} - \eta \bar{\mathbf{J}}). \quad (4.62)$$

For sufficiently large-Reynolds-number-plasmas, the magnetic field can be frozen in to the plasma. It is, however, due to the balance of turbulence. In this specific situation, the frozen-in condition may break and magnetic field can be diffused or generated by the β or α term.

A similar balance of the turbulence happens for non-vanishing mean flow gradients.⁷⁰ An important point is the reduction of turbulent energy by the production of turbulent cross-helicity. Inserting equation (4.48) into equation (4.54), the production of cross-helicity due to the electromotive force is

$$P_w = \beta \bar{\mathbf{J}} \cdot \bar{\boldsymbol{\Omega}} - \gamma \bar{\boldsymbol{\Omega}}^2 - \alpha \bar{\boldsymbol{\Omega}} \cdot \bar{\mathbf{B}}. \quad (4.63)$$

The turbulent cross-helicity is mostly localised where the mean vorticity $\bar{\boldsymbol{\Omega}}$ is defined. From equation (4.58), the γ term has the same sign as the turbulent cross-helicity W and the second term always acts to the suppression of the turbulent cross-helicity. The cross-helicity further bears similar sign as the mean vorticity. Therefore, the production of cross-helicity is mainly due to the alignment of the mean current density and mean vorticity. It also has to be noted that without the production of turbulent energy K ($\propto \beta$), the turbulent cross-helicity cannot be generated. According to equation (4.59), the cross-helicity W ($\propto \gamma$) always contributes to the suppression of the turbulent energy at the locations where the mean vorticity $\bar{\boldsymbol{\Omega}}$ is defined. A schematic representation is depicted in figure 4.1 for a simple ‘X’-point reconnecting current sheet. In such situations, the turbulent cross-helicity vanishes at the center of the current sheet since it is a pseudo-scalar. It is only defined around the reconnection region where it can suppress the turbulent resistivity β . The turbulent resistivity is constrained by the action of the cross-helicity to the center of the diffusion region.

5 Subgrid-Scale Phenomena

Ne nous laissons pas étourdir par un repos qui mènerait la paresse.

Charlemagne.

The recent capabilities of super computers allow to describe the turbulence of a magnetized plasma over a wide range of scales. This is technically realised e.g. by means of large eddy simulations (LES), implicit large-eddy simulations (ILES) or direct numerical simulations (DNS). Each of these Eulerian methods determine the variables on a numerical grid. The MHD variables on the grid are called grid-scale (GS) quantities while the quantities which are not resolved by the grid are called "subgrid-scale" (SGS) quantities. The principle of LES is to use DNS results to model the SGS quantities. It is achieved by suppressing the SGS quantities of the DNS by means of a filter. Once modeled, the subgrid-scale variables are then introduced on the grid-scale. This is the core of LES methods. The ILES solve the unfiltered MHD equations without any SGS model. The numerical procedures of ILES are such that the non-linear terms in the MHD equations are solved with an highly-dissipative discretization. Such a discretization replaces the dissipation effects that a turbulence model would provide.

5.1 Filtered Equations

Large eddy simulations resort on a filtering procedure to filter-out contributions from the DNSs small scales. The filter depends on a filter width Δ_F related to grid resolution of the LES. Applying a filter L_F on a DNS grid resolved variable $f(x)$ yields

$$\bar{f}^F(x) = \int_{-\infty}^{\infty} L_F(\varphi - x, \Delta_F) f(\varphi) d\varphi. \quad (5.1)$$

where the filter kernel

$$\int_{-\infty}^{\infty} L_F(\varphi - x, \Delta_F) d\varphi = 1. \quad (5.2)$$

is a normalised function. The filter L_F must further commutes with the differentiation operator. The filters that are commonly used in LES formulations are: i) the sharp filter which is a step function in the Fourier space cutting high frequencies, ii) the top-hat filters which correspond to a sinc(k) function in the Fourier space, and iii) Gaussian filters. The

last two kinds of models reduce the amplitude of the small scales without sharply cutting at a certain frequency. The filters ii) and iii) are both defined for a chosen filter width as

$$L_T(x) = \frac{1}{\Delta_T} \text{ if } x < \frac{\Delta_T}{2} \text{ and } 0 \text{ otherwise,} \quad (5.3)$$

$$L_G(x) = \frac{1}{\Delta_G} \sqrt{\frac{a}{\pi}} \exp\left(-a\left(\frac{x}{\Delta_G}\right)^2\right), \quad (5.4)$$

where the constant a of the Gaussian filter L_G is related to the grid resolution of the DNS. A variable f is divided into a grid- and subgrid-scale component \bar{f}^F and f'' . The SGS component represents the deviation from the mean and is defined as

$$f'' = f - \bar{f}^F. \quad (5.5)$$

Contrary to the ensemble average [equation (4.9)] with rules (4.4)-(4.6), a filter follows

$$\overline{\bar{f}^F}^F \neq \bar{f}^F, \quad \overline{f''}^F \neq 0, \quad \overline{\bar{f}^F f''}^F \neq 0, \quad (5.6)$$

where the GS correlation for a variable f with g is denoted

$$C_{GS} = \overline{\bar{f}^F \bar{g}^F}, \quad (5.7)$$

while the SGS counterpart is defined by

$$C_{SGS} = \overline{f g}^F - \overline{\bar{f}^F \bar{g}^F}. \quad (5.8)$$

The influence of the filtered small scales on the LES turbulence representation may not be negligible. Their importance depends on the filter width chosen. If the filtering procedure has the property

$$\overline{\bar{f}^F}^F = \bar{f}^F \quad (\text{when } \overline{f''}^F = 0), \quad (5.9)$$

the C_{SGS} recovers the usual Reynolds-averaging [equations (4.4)-(4.6)]:

$$\begin{aligned} C_{SGS} &= \overline{f g}^F - \overline{\bar{f}^F \bar{g}^F} = \overline{(\bar{f}^F + f'')(\bar{g}^F + g'')}^F - \overline{\bar{f}^F \bar{g}^F} \\ &= \overline{\bar{f}^F \bar{g}^F}^F + \overline{\bar{f}^F g''}^F + \overline{f'' \bar{g}^F}^F + \overline{f'' g''}^F - \overline{\bar{f}^F \bar{g}^F} \\ &= \overline{f'' g''}^F. \end{aligned} \quad (5.10)$$

Convolving the MHD equations with a Gaussian kernel, the MHD equations for a mass-weighted filter read

$$\partial_t \bar{\rho}^F = -\partial_k \left(\bar{\rho}^F \bar{V}_k^F \right), \quad (5.11)$$

$$\partial_t \bar{\rho}^F \bar{V}_i^F = -\partial_k \left(\bar{\rho}^F \bar{V}_i^F \bar{V}_k^F + \bar{B}_i^F \bar{B}_k^F \right) - \partial_i \bar{p}^F - \partial_k \tau_{ik} - \mu \partial_{kk} \bar{V}_i^F, \quad (5.12)$$

$$\partial_t \bar{B}_i^F = \epsilon_{ijk} \partial_j \left(\epsilon_{klm} \bar{V}_l^F \bar{B}_m^F \right) + \epsilon_{ijk} \partial_j (\mathcal{E}_M)_k + \eta \partial_{kk} \bar{B}_i^F. \quad (5.13)$$

As for the mean-field MHD equations [equations (4.13)-(4.14)], the influence of the small scales is contained in a SGS stress-tensor τ_{ij} for the momentum equation and in the SGS electromotive force \mathcal{E}_M for the induction equation. The SGS stress-tensor τ_{ij} is analytically defined as

$$\tau_{ij} = \bar{\rho}^F \left(\overline{V_i V_j^F} - \overline{V_i^F V_j^F} \right) - \left(\overline{B_i B_j^F} - \overline{B_i^F B_j^F} \right) + \left(\overline{B_k B_k^F} - \overline{B_k^F B_k^F} \right) \frac{\delta_{ij}}{2}, \quad (5.14)$$

where the first term is the Reynolds stress SGS formulation and the second is the Maxwell's stress SGS formulation. On the other hand, the SGS formulation of the electromotive force \mathcal{E}_M reads

$$(\mathcal{E}_M)_i = \epsilon_{ijk} \left(\overline{V_j B_k^F} - \overline{V_j^F B_k^F} \right). \quad (5.15)$$

As for the mean-field approach of turbulence, both τ_{ij} and $(\mathcal{E}_M)_i$ contain the information about turbulence. The SGS energy K_{SGS} , SGS cross-helicity W_{SGS} and SGS residual helicity H_{SGS} densities counterparts of the mean-field approach [equations (4.17), (4.18) and (4.32)] are determined as⁷¹

$$K_{SGS} = \frac{1}{2} \left[\bar{\rho}^F \left(\overline{V_i V_i^F} - \overline{V_i^F V_i^F} \right) + \frac{\left(\overline{B_i B_i^F} - \overline{B_i^F B_i^F} \right)}{\mu_0 \bar{\rho}^F} \right], \quad (5.16)$$

$$W_{SGS} = \left(\frac{\overline{V_i B_i^F} - \overline{V_i^F B_i^F}}{\sqrt{\mu_0 \bar{\rho}^F}} \right), \quad (5.17)$$

$$H_{SGS} = - \left(\overline{V_i \Omega_i^F} - \overline{V_i^F \Omega_i^F} \right) + \left(\frac{\overline{B_i J_i^F} - \overline{B_i^F J_i^F}}{\bar{\rho}^F} \right). \quad (5.18)$$

The resolved grid-scale counterparts of equation (5.16) and equation (5.17) are

$$\overline{E}^F = \frac{1}{2} \left[\bar{\rho}^F \overline{V_i V_i^F} + \overline{B_i B_i^F} \right], \quad (5.19)$$

$$\overline{\mathcal{W}}^F = \left(\overline{V_i B_i^F} \right). \quad (5.20)$$

Traditionally, it is by means of algebraic relations that the closure for τ_{ij} and \mathcal{E}_M are obtained. For instance, Smagorinsky gave a closure in hydrodynamics for the SGS energy flux.⁷² Concerning the SGS stress-tensor, it is often closed by the eddy-viscosity representation.^{24,26} It is also possible to use governing equations to close the system as it is done for the mean-field approach. They are usually not favored in SGS models since they require additional closures.

5.2 Non-Linear Turbulence Model

A possible set of instantaneous closure for the SGS stress-tensor τ_{ij} and SGS electromotive force \mathcal{E}_M is the non-linear closure of Grete *et al.*⁷³ In contrast to the electromotive force closure

$$\mathcal{E}_M = \alpha \overline{\mathbf{B}}^F + \gamma \overline{\mathbf{\Omega}}^F - \beta \overline{\mathbf{J}}^F, \quad (5.21)$$

a non-linear closure extension from Balarac *et al.*⁷⁴ to the MHD compressible regime is proposed as

$$(\mathcal{E}_M)_i = \epsilon_{ijk} \Delta^2 C_{nl}^E \partial_n \widetilde{V}_j^F \partial_n \overline{B}_k^F. \quad (5.22)$$

where $\widetilde{\cdot}$ is a mass-weighted filtering: $\widetilde{V}^F = \overline{V}^F / \overline{\rho}^F$. The electromotive force closure depends on the filter width Δ and a model constant C_{nl}^E that has to be determined.¹ The closure for the stress-tensor τ_{ij} is proposed to be an extension of the hydrodynamic non-linear closure to MHD

$$\tau_{ij}^V = 2C_{nl}^V E_{SGS}^V \left(\frac{\partial_k \widetilde{V}_i^F \partial_k \widetilde{V}_j^F}{\partial_n \widetilde{V}_m^F \partial_n \widetilde{V}_m^F} - \frac{1}{3} \delta_{ij} \right), \quad (5.23)$$

$$\tau_{ij}^B = 2C_{nl}^B E_{SGS}^B \left(\frac{\partial_k \overline{B}_i^F \partial_k \overline{B}_j^F}{\partial_n \overline{B}_m^F \partial_n \overline{B}_m^F} - \frac{1}{3} \delta_{ij} \right), \quad (5.24)$$

where the stress-tensor is written as

$$\tau_{ij} = \tau_{ij}^V - \tau_{ij}^B + \frac{2}{3} (E_{SGS}^V - E_{SGS}^B) \delta_{ij}. \quad (5.25)$$

For the model to be complete, a closure for the SGS energies is given in terms of Smagorinsky closures as

$$E_{SGS}^V = C_E^V \Delta^2 \overline{\rho}^F \left[(\partial_j \widetilde{V}_i^F + \partial_i \widetilde{V}_j^F) (\partial_j \widetilde{V}_i^F + \partial_i \widetilde{V}_j^F) \right], \quad (5.26)$$

$$E_{SGS}^B = C_E^B \Delta^2 \left[(\partial_j \overline{B}_i^F + \partial_i \overline{B}_j^F) (\partial_j \overline{B}_i^F + \partial_i \overline{B}_j^F) \right], \quad (5.27)$$

where C_{nl}^V , C_{nl}^B , C_E^V and C_E^B are model constants to be evaluated.

Using the same dimensional argument as the mean-field approach, a filter formulation of turbulent resistivity β [equation (4.57)] in equation (5.21) can be written in terms of the SGS energies

$$\beta = \tau C_K \Delta \sqrt{E_{SGS}^V + E_{SGS}^B} \equiv \tau C_K K_{SGS}^{nl}. \quad (5.28)$$

Similarly, the SGS cross-helicity related term γ [equation (4.58)] becomes

$$\gamma = \tau C_W \Delta^2 \frac{\overline{\rho}^F}{2} \sqrt{(\partial_j \widetilde{V}_i^F + \partial_i \widetilde{V}_j^F) (\partial_j \overline{B}_i^F + \partial_i \overline{B}_j^F)} \equiv \tau C_W W_{SGS}^{nl}, \quad (5.29)$$

where C_K and C_W are model constants and τ is a time scale for the turbulence evolution. This latter can be construct dimensionally as $\tau = K/\epsilon_K$ for the turbulent energy dissipation rate ϵ_K . This form requires, however, knowledge about ϵ_K . It has to be noted that equations (5.28)-(5.29) are very similar to equations (4.57)-(4.58). For a well chosen filter width Δ , the SGS correlation equation (5.8) has a property which leads to equation (5.10). In such a situation, the governing equations [equations (4.47)-(4.52)] for the mean-field turbulent energy K and turbulent cross-helicity W , residual helicity H and turbulent energy dissipation rate ϵ_K can be extended to LES formalism. Such an extended approach is utilized in chapter (10).

¹ I. Grete *et al.*⁷³ used a three-dimensional ILES of isotropic homogeneous turbulence to determine the different model constants for the non-linear model.

6 Kolmogorov Theory

Perceive that which cannot be seen
with the eye.

Miyamoto Musashi

An important aspect of turbulence is grasped not from its analysis in the real space but in the wave number or Fourier space. The key point of the Fourier space is its capability to infer information on turbulence by power laws.

Assuming self-similar turbulent process, Kolmogorov (1941) derived a relation for the energy transfer from the large (or injection) scale down to the small or dissipation scale in hydrodynamics.³⁷ For magnetohydrodynamics, the Kolmogorov spectrum can still apply even if the influence of the magnetic field must be taken into account (turbulence of Alfvén waves). The power law then changes, due to electromagnetic forces, into an Iroshnikov-Kraichnan spectrum (IK).^{75,76} Nevertheless, many solar wind data still reveal Kolmogorov-like power law.⁷⁷ In this chapter, the Kolmogorov theory (*K41*) is presented since it bears the main idea to describe turbulence by power laws in the wave number space. Such aspect is utilized in chapter (8).

6.1 Dimensional Consideration and Energy Cascade

Solely three quantities are necessary to build the foundation of the *K41* theory of turbulence: a length scale in terms of the wave number k , the kinetic energy in the wave number space $E(k)$ and its dissipation rate ε_k . The energy spectrum E_s is given in terms of $E(k)$ as

$$E_s = \int_0^{\infty} E(k)dk. \quad (6.1)$$

The idea is that the energy is stored at a scale k_L from which it is transferred over a scale k_I towards a scale k_D where the energy is eventually dissipated by viscosity (or resistivity) effects. This picture of cascading energy is realized only for a sufficiently large separation of the energy containing and dissipation scale $k_L \ll k_I \ll k_D$. Under that assumption, the scale over which energy is transferred is called the inertial range. The full wave number range is then composed of three regions as depicted in figure 6.1. Over the inertial range, turbulence develops under non-linear dynamics independently of the injection or diffusion

of energy. The energy decrease from the k_L to k_D is provided by the dissipation rate as

$$\varepsilon = -\frac{d}{dt} \int_{k_L \leq k}^{k \leq k_D} E(k) dk, \quad (6.2)$$

which can be written in terms of the wave number k and the energy $E(k)$ from equation (4.29b) as^I

$$\varepsilon = 2\nu \int_{k_L \leq k}^{k \leq k_D} k^2 E(k) dk. \quad (6.3)$$

The energy transferred in the inertial range can be estimated in terms of the wave number k and the energy dissipation ε . Denoting the length and time dimension as $[L]$ and $[T]$, the energy is written as

$$E(k) \sim \varepsilon^a k^b, \quad (6.4)$$

$$\frac{[L]^3}{[T]^2} = \left(\frac{[L]^2}{[T]^3} \right)^a [L]^b. \quad (6.5)$$

Matching the exponents a and b leads to the Kolmogorov phenomenological spectrum

$$E(k) = C_{K41} \varepsilon^{2/3} k^{-5/3}. \quad (6.6)$$

The constant C_{K41} cannot be inferred from the Kolmogorov phenomenology but is determined empirically from experiment. From several experiments data, Sreenivisan (1995) found that C_{K41} is a universal constant in the range 1.6-1.7.⁷⁸

The length of the inertial range is determined by the Reynolds number $R_e = LV/\nu$. For the energy equation (6.6), integrating equation (6.1) from k_L to ∞ and equation (6.3) from 0 to k_D over the wave number k gives

$$k_L = \frac{\varepsilon}{E_s^{3/2}}, \quad (6.7)$$

$$k_D = \left(\frac{\varepsilon}{\nu^3} \right)^{1/4}, \quad (6.8)$$

$$\frac{k_L}{k_D} = \frac{\nu \varepsilon}{E_s^2} \equiv R_e^{-3/4} \ll 1. \quad (6.9)$$

Equation (6.9) shows that the length of the inertial range is longer for a large Reynolds number. It is therefore the value of the diffusivity ν , for a fixed length scale, that determines the length of the inertial range.^{II}

I. Considering that only dissipation occurs in the inertial range, only $\varepsilon_{\bar{E}}$ is considered in the hydrodynamics limit ($\bar{\mathbf{B}} = 0$).

II. Similar results holds for magnetohydrodynamics with vanishing mean flows but for the resistivity η instead of the viscosity ν .

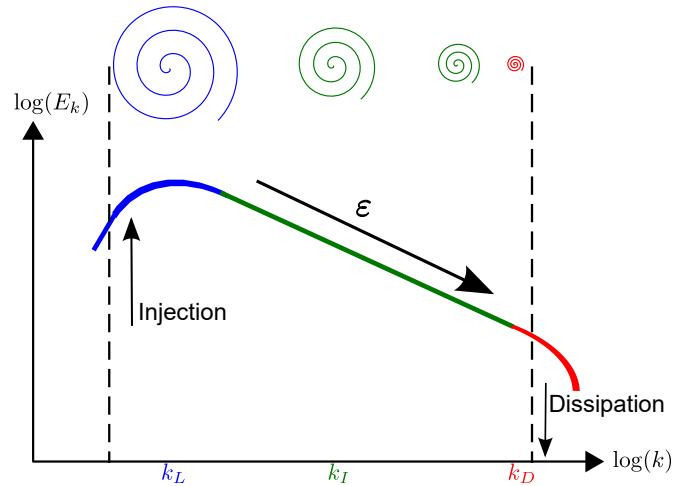


Figure 6.1: Schematic of a log-log plot of the energy spectrum or cascade. Energy is injected at large scales, cascades down towards the dissipation scales through the energy dissipation rate ε . The spirals schematically represent the eddies as they are being broken and reduced in size from the large to the small scales where dissipation occurs.

The Richardson's picture of turbulence describes large eddies being broken onto smaller one up to the scales where they are dissipated by viscosity. A lifetime for these eddies can be defined in terms of their size. For instance, an eddy of scale $2\pi/k$ in the wave number space has a lifetime (dimensional analysis)

$$\tau(k) = C_\tau \varepsilon^{-1/3} k^{-2/3}, \quad (6.10)$$

where C_τ is an empirical constant. Equation (6.10) shows that a small eddy (large k) is living a shorter life than a large eddy (small k). Inserting equation (6.7) into equation (6.10) gives

$$\tau(k) = \frac{E_s}{\varepsilon} \equiv \tau_L, \quad (6.11)$$

which is similar to the dimensional construction of the turbulent timescale $\tau = K/\varepsilon$ used in section (4.1.2).

7 Magnetic Reconnection

Rien ne se perd, rien ne crée, tout se transforme.

Antoine Lavoisier

The first part of this chapter describes the magnetic reconnection phenomenon in the limit of resistive MHD. The Sweet-Parker model of reconnection through long current sheet as well as the Petschek model of shock waves are discussed in sections (7.1)-(7.2). The chapter further describes the influence of turbulence on reconnection through the turbulent electromotive force. The reconnection rate for both Sweet-Parker and Petschek model are then obtained when turbulence is taken into account through a mean-field turbulence model (section (7.3)).

The last section of the chapter addresses the question of the onset of magnetic reconnection. For that purpose, linear theories of magnetic instabilities of i) the tearing mode, and ii) plasmoids are derived in a mean-field turbulence theory. Since turbulence may trigger reconnection in large-Reynolds-number-plasmas, an heuristic derivation of the tearing mode (section (7.5.1)) and the plasmoid instability are given as turbulence is considered through a mean-field turbulence model (section (7.5.2)). The onset of the instabilities is then related to the level of the turbulence.

7.1 Sweet-Parker Reconnection

In order to discriminate the possible role played by turbulence in reconnection, the Alfvén Mach number M_A of the plasma inflow and the width Δ_d of the diffusion region are first discussed for a Sweet-Parker (SP) current sheet model. It appears that the Alfvén Mach number M_A provides a measure of the reconnection rate. The SP model is based on the conservation of the mass between the inflow and outflow regions of reconnection for a plasma in a steady state flow. The derivation is further based on the non-existence of magnetic monopoles ($\nabla \cdot \mathbf{B} = 0$). Furthermore, it is assumed that two regions can be identified in the vicinity of the current sheet: i) an ideal region where the magnetic field is frozen into the plasma, and ii) a region where dissipative effects are considered (figure 7.1). The first region is assumed to be outside the current sheet while the second is inside it. The internal layer is the location where the magnetic fluxes reconnect. It is finally assumed that the resistive term balances the convective term of the constant electric field at the boundary between both regions.¹ From a dimensional analysis, the conserva-

I. Similar to the tearing mode regions section (7.5.1).

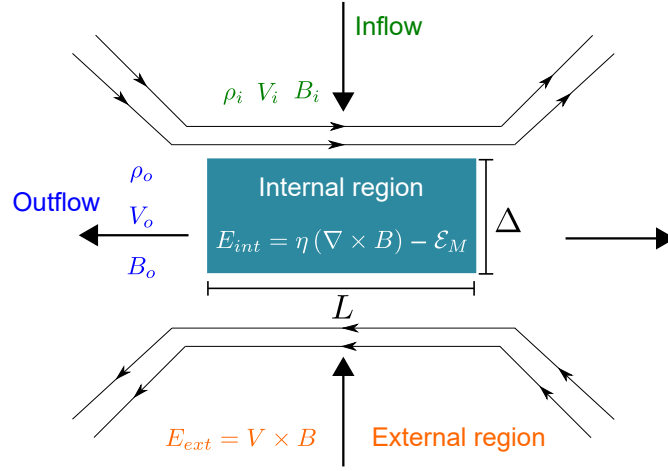


Figure 7.1: Schematic of the internal and external region for an SP current sheet.

tion of the mass density [equation (7.1)], the magnetized plasma flow [equation (7.2)] and divergence of magnetic field [equation (7.3)] are respectively written as

$$V_o \Delta = V_i L, \quad (7.1)$$

$$V_i B_i = V_o B_o, \quad (7.2)$$

$$B_o L = B_i \Delta, \quad (7.3)$$

where the index o stands for outflow and i for inflow. Following Priest and Forbes,¹³ the (Alfvén) Mach number as well as the width of the diffusion region for a SP current sheet have the form

$$M_{A,SP}^2 = \left(\frac{\rho_o}{\rho_i} \right)^{1/2} \frac{\eta}{V_A L}, \quad (7.4)$$

$$\Delta_{d,SP}^2 = L^2 \left(\frac{\rho_i}{\rho_o} \right)^{3/2} \frac{\eta}{V_A L}, \quad (7.5)$$

without considering any pressure variation along the current sheet and

$$M_{Ap,SP}^2 = \left(\frac{\rho_o}{\rho_i} \right)^{1/2} \sqrt{\left[2 + \beta_p \left(1 + \left(\frac{h_o}{h_i} \right)^{\gamma_0} \right) \right]} \left(\frac{\eta}{V_A L} \right), \quad (7.6)$$

$$\Delta_{d,SP}^2 = \left(\frac{\rho_i}{\rho_o} \right)^2 L^2 M_{Ap,SP}^2, \quad (7.7)$$

when pressure effects are taken into account. The thermal pressure is represented by the variable h [equation (3.10)]. For a long current sheet, the outflow is assumed to be the Alfvén speed V_A . This results from the conversion of magnetic energy into kinetic energy of the plasma through the Joule heating. In fact, the SP model states that half of the magnetic energy is converted into plasma kinetic energy and the other half is transformed into heat.¹³ Since the Alfvén Mach number M_A is an estimation of the reconnection rate amplitude, it is clear from equation (7.4) and equation (7.6) that the reconnection rate

increases or decreases together with the resistivity.^{II}

The magnetic Reynolds number represents the relative amplitude of the advective terms to the dissipative terms of the induction equation. The magnetic Reynolds number is given as $R_m = VL/\eta$ for the resistivity η and typical length and plasma velocity scale L and V . Astrophysical plasmas have a large-magnetic-Reynolds-numbers and the associated SP reconnection rate is tiny. The SP model of reconnection cannot, for instance, explain the rapid conversion of the magnetic energy into kinetic energy and heat in the Solar atmosphere. One problem of the SP model is the small aspect ratio of the diffusion region. Sweet-Parker current sheets are thin and long in order to have a large current density compensating for the small value of the resistivity. Strong currents render possible the annihilation in the diffusion region of the incoming magnetic flux from the sides. At the same time, the small width of the resistive layer limits the outflow of the mass flux. A possible option to enhance the rate of energy conversion in the SP model is to enlarge the resistive layer such that its width is comparable to its length without reducing the current density intensity. Such considerations lead to the Petschek case.

7.2 Petschek Reconnection

In 1964, Petschek proposed a model to enhance the rate of energy conversion by reconnection through standing shock waves.²⁰ Instead of requiring that most of the incoming plasma passes through a long resistive layer, the flow is redirected through standing shock waves. The Petschek model assumes a smaller diffusion region than the Sweet-Parker (SP) model by considering a length l of the diffusion region shorter than the length L of the SP model. The reconnection rate is enhanced from the SP to the Petschek case by a factor L/l . The maximum value that the reconnection rate can attain is

$$M_{Pet} \approx \frac{\pi}{8 \log(R_m)}. \quad (7.8)$$

The logarithmic denominator does not vary much with the Reynolds number. The Petschek model provides, therefore, a faster reconnection rate than the SP model. It is able to attain rate as large as a tenth of the one for the maximum possible electric field. The Petschek model is, however, stable only for a localised inhomogeneous resistivity whose intensity decreases away from the ‘X’-point.^{21,41} The Petschek model can also happen when a Hall term is taken into account.^{79,80}

7.2.1 Angle of Reconnection

The Sweet-Parker (SP) and the Petschek (\mathcal{P}) model of reconnection and their reconnection rates can be discussed in terms of the reconnection angle θ . The angle formed between the incoming (B_i) and reconnected (B_o) magnetic field lines is related to the reconnection rate through equations (7.2)-(7.3) as

$$\tan(\theta) \equiv \frac{B_o}{B_i} = \frac{\Delta}{\mathcal{L}}, \quad (7.9)$$

II. Similar to the tearing mode growth rate, i.e., γ_r increases with η . Dimensionally $\gamma_r = \eta/L^2$.

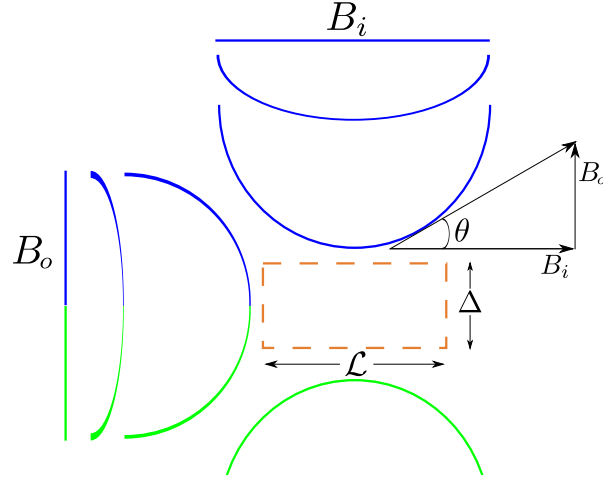


Figure 7.2: Schematic of the angle of reconnection θ . The incoming component of the magnetic flux is denoted by B_i while B_o denotes the component of the reconnected magnetic field. The dashed box represent the diffusion region of length \mathcal{L} and width Δ .

where Δ is the width and \mathcal{L} the length of the diffusion region for any reconnection model under consideration. Figure 7.2 is a schematic of the two-dimensional situation. The angle of reconnection is then proportional to L for the SP model and to l for the \mathcal{P} model. The small diffusion region of the \mathcal{P} model speeds up the reconnection process by producing a large angle of reconnection. For homogeneous finite resistivity, numerical simulations and theoretical studies found that a SP reconnection-like current sheet is formed out of a Petschek-type situation which slows down the reconnection process and reduces the reconnection rate.^{21,81,82} So the question is, whether the turbulence, which is ubiquitous in high Reynolds number astrophysical plasmas, can speed up reconnection.

7.3 Mean-Field Turbulent Reconnection

7.3.1 Turbulent Sweet-Parker Reconnection

Considering the mean-field turbulence approach described in section (4.2), the mean-field electric field $\overline{\mathbf{E}}$ takes the form

$$\overline{\mathbf{E}} = -\overline{\mathbf{V}} \times \overline{\mathbf{B}} + \eta(\nabla \times \overline{\mathbf{B}}) - \mathcal{E}_M. \quad (7.10)$$

The turbulent electromotive \mathcal{E}_M and the dissipative terms $\eta(\nabla \times \overline{\mathbf{B}})$ can be neglected in the outer ideal plasma region while $\overline{\mathbf{V}} \times \overline{\mathbf{B}}$ is neglected in the inner (dissipative) region (figure 7.1). Requiring that the solution is smooth at the boundary between the two regions yields

$$\overline{\mathbf{V}} \times \overline{\mathbf{B}} = \eta(\nabla \times \overline{\mathbf{B}}) - \mathcal{E}_M. \quad (7.11)$$

Considering only the dimensions of the variables, equation (7.11) can be estimated as

$$V_i B_i = \eta \frac{B_i}{\Delta} - \mathcal{E}_M, \quad (7.12)$$

where Δ is the width of the diffusion region. The dimensions of \mathcal{E}_M are those of $\bar{\mathbf{V}} \times \bar{\mathbf{B}}$. Utilizing equations (7.1)-(7.3), equation (7.12) becomes

$$V_i^2 = \eta \frac{V_o}{L} - \frac{V_o}{B_o} \left(\frac{\Delta}{L} \right)^2 \mathcal{E}_M. \quad (7.13)$$

In a general approach, the mean-field electromotive force is assumed to take the form (Taylor like expansion, instantaneous values)

$$\mathcal{E}_M = \alpha \bar{\mathbf{B}} + \beta (\nabla \times \bar{\mathbf{B}}) + \delta [\nabla \times (\nabla \times \bar{\mathbf{B}})] + \psi \bar{\mathbf{V}} + \gamma (\nabla \times \bar{\mathbf{V}}) + \zeta [\nabla \times (\nabla \times \bar{\mathbf{V}})], \quad (7.14)$$

which bears the same units as $\bar{\mathbf{V}} \times \bar{\mathbf{B}}$, i.e., $\mathcal{E}_M \cong V_i B_i$. This means that the units of the coefficients of the electromotive force [equation (7.14)] are

$$[\alpha] = V_A \quad [\beta] = V_A L_0 \quad [\delta] = V_A L_0^2, \quad (7.15)$$

$$[\psi] = B_i \quad [\gamma] = B_i L_0 \quad [\zeta] = B_i L_0^2. \quad (7.16)$$

Multiplying the coefficients in the velocity expansion by $\sqrt{\mu_0 \bar{\rho}} / \sqrt{\mu_0 \bar{\rho}}$, the electromotive force becomes

$$\begin{aligned} \mathcal{E}_M = & \alpha \bar{\mathbf{B}} + \beta (\nabla \times \bar{\mathbf{B}}) + \delta [\nabla \times (\nabla \times \bar{\mathbf{B}})] \\ & + \sqrt{\mu_0 \bar{\rho}} [\psi^* \bar{\mathbf{V}} + \gamma^* (\nabla \times \bar{\mathbf{V}}) + \zeta^* [\nabla \times (\nabla \times \bar{\mathbf{V}})]], \end{aligned} \quad (7.17)$$

where

$$\begin{aligned} [\psi^*] &= \frac{B_i}{\sqrt{\mu_0 \bar{\rho}}} = V_A, & [\gamma^*] &= \frac{B_i}{\sqrt{\mu_0 \bar{\rho}}} L_0 = V_A L_0, \\ [\zeta^*] &= \frac{B_i}{\sqrt{\mu_0 \bar{\rho}}} L_0^2 = V_A L_0^2. \end{aligned} \quad (7.18)$$

The renormalization implies that the coefficients of the velocity and magnetic expansion have the same units at each order of the expansion, i.e.,

$$[\psi^*] = [\alpha], \quad [\gamma^*] = [\beta], \quad [\zeta^*] = [\delta]. \quad (7.19)$$

Utilizing the electromotive force of the Reynolds-averaged turbulent model (section (4.2)),^{III} the electromotive force reads

$$\mathcal{E}_M = -\beta (\nabla \times \bar{\mathbf{B}}) + \sqrt{\mu_0 \bar{\rho}} \gamma^* (\nabla \times \bar{\mathbf{V}}), \quad (7.20)$$

for which equation (7.13) becomes

$$V_i^2 = \eta \frac{V_o}{L} + \frac{V_o}{B_o} \left(\frac{\Delta}{L} \right)^2 \left(\beta \frac{B_i}{\Delta} - \sqrt{\mu_0 \bar{\rho}} \gamma^* \frac{V_i}{\Delta} \right). \quad (7.21)$$

III. The derivation is carried for an Harris-type current sheet equilibrium without guide magnetic field. The mirror-symmetry in the direction perpendicular to the reconnection plane enforces $\alpha = 0$.

The influence of the mean-fields on the reconnection rate can be estimated from the Alfvén Mach number as

$$M_{A,T}^2 = \left(\frac{\rho_o}{\rho_i}\right)^{1/2} \eta \left(1 + \frac{\beta}{\eta} \left(1 - \frac{|\gamma|}{\beta} \eta\right)\right), \quad (7.22)$$

$$\Delta_{T,p}^2 = \left(\frac{\rho_i}{\rho_o}\right)^2 L^2 M_{A,T}^2, \quad (7.23)$$

when the variation of pressure along the current sheet is not taken into account and

$$M_{A,p}^2 = \left(\frac{\rho_o}{\rho_i}\right)^{1/2} \sqrt{\left[2 + \beta_p \left(1 + \left(\frac{h_o}{h_i}\right)^{\gamma_0}\right)\right]} \eta \left(1 + \frac{\beta}{\eta} \left(1 - \frac{|\gamma|}{\beta} \eta\right)\right), \quad (7.24)$$

$$\Delta_{d,p}^2 = \left(\frac{\rho_i}{\rho_o}\right)^2 L^2 M_{A,p}^2, \quad (7.25)$$

when the pressure variation along the current sheet center is not neglected. The normalisation for η , β and γ is given by the Alfvén speed V_A and the length L_0 [equation (7.18)]. The Sweet-Parker reconnection rate is recovered for:

$$\frac{\beta}{\eta} \ll 1, \quad (7.26)$$

or

$$|\gamma|/\beta \ll 1. \quad (7.27)$$

A laminar non-turbulent regime of energy conversion is recovered (SP Mach number) when equation (7.26) is fulfilled. In the limit of equation (7.27), the laminar flow is recovered for a low level of turbulence. This matches the model prediction that the maximum value of the reconnection is reached when $|\gamma|/\beta \geq 1$.³⁰

In the framework of mean-field turbulence theory, the condition (7.26) can be used to distinguish between turbulent and laminar regime of energy conversion. The reconnection rate M_A can be rewritten (neglecting compressibility) as

$$M_{A,T}^2 \propto \eta \left(1 + \frac{\beta}{\eta} \left(1 - \frac{|\gamma|}{\beta} \eta\right)\right), \quad (7.28)$$

which for $\beta \ll \eta$ reduces to

$$M_{A,SP}^2 \propto \eta. \quad (7.29)$$

This reveals the well know proportionality for a SP current sheet without turbulence.^{IV} The important implication from the Alfvén Mac number [equation (7.28)] in regimes of small η [(7.22) or (7.24)] is that the ratio β/η together with $|\gamma|/\beta$ are strongly affecting the reconnection rate (see section (8.2)).

The dynamical balance between the turbulent energy K ($\propto \beta$) and the turbulent cross-helicity W ($\propto \gamma$) is important for the reconnection rate. In fact, the Sweet-Parker reconnection rate increases if the width of the diffusion region is comparable to its length. The action of the turbulent cross-helicity W localises the turbulent energy K around the diffusion region. The turbulent cross-helicity increases, therefore, the angle of reconnection.

IV. Since $|\gamma|/\beta \leq 1$, if $\beta \ll \eta$ then $|\gamma| \ll \eta$. As a reminder, the production mechanism of the turbulent cross-helicity is [equation (4.54)] $P_W \sim \beta \bar{\mathbf{J}} \cdot \bar{\boldsymbol{\Omega}} - \gamma \bar{\boldsymbol{\Omega}}^2$. In the limit of vanishing turbulent resistivity β , W is only dissipated by the term $\gamma \bar{\boldsymbol{\Omega}}^2$.

7.3.2 Petschek Turbulent Reconnection

The Petschek reconnection rate reaches, without the aid of turbulence, the regime of fast reconnection. Including turbulence, the reconnection rate for the Petschek model becomes

$$M_{Pet,T} \approx \frac{\pi \log(\eta + \beta - |\gamma|\eta)}{8}, \quad (7.30)$$

which weakly varies with a decreasing resistivity η . The influence of turbulence on the rate of Petschek reconnection is tiny. The importance of turbulence comes into play, however, due to the spatial localisation of the apparent turbulent resistivity β inside the diffusion layer where it is maximum at ‘X’-points. Turbulence can also initiate the Petschek reconnection spontaneously, becoming then a steady state. In terms of the reconnection angle θ [equation (7.9)], the localized inhomogeneous turbulent resistivity reduces \mathcal{Q} . The angle of reconnection θ is then increased. In a similar manner as the Petschek model, the turbulence could provide a much faster reconnection rate than the Sweet-Parker model.

7.4 Guide Field Reconnection

In this section, the influences of a guide magnetic fields \mathbf{B}_g parallel to the current flow on reconnection is investigated. In particular, guide fields are important for the solar atmosphere since the low plasma- β in the solar corona due to large guide field may produce interlinked flux tubes in three-dimensions.⁸³ Also, diverse numerical simulations as well as laboratory experiments found an influence of a guide field \mathbf{B}_g on the rate of reconnection. For instance, kinetic simulations of force-free current sheets found that the non-linear phase of reconnection is affected by a strong guide field while the maximum value of the reconnection rate is reduced proportionally to the guide field.^{84,85} Such reductions of the reconnection rate in presence of a guide field were also observed in two- and three-dimensional PIC-code simulations of Harris-type current sheet.^{86–88} Laboratory experiments and MHD simulations with a strong guide field also showed an influence on the reconnection rate during the non-linear phase.^{40,50} It was found that the reconnection rate was slowed down in three-dimensional MHD simulations with finite guide magnetic field.^{89–91} It is then important to investigate the influence of a strong guide field on the reconnection problem for both theory and simulations. The reduction of the reconnection rate due to a guide magnetic field can be determined in an heuristic way by considering the action of the Lorentz force around the reconnection region. For definitiveness, the situation shown in figure 7.3 is considered. Let’s follow the blue dashed magnetic flux as it is brought towards the diffusion region (orange dashed box) by the inflow velocity V_{in} . As the magnetic flux approaches the diffusion region, the action of the Lorentz forces increases. As soon as the magnetic flux becomes reconnected, the component of the Lorentz force across the current sheet vanishes identically. As a result, the plasma is ejected by the component of the Lorentz force directed along the current sheet. The reconnection rate maybe inferred from this process. At the boundary between regions 1 and 2, $\eta \mathbf{J} \approx \mathbf{V} \times \mathbf{B}$ and the Lorentz force can be written at the boundary as

$$\mathbf{J} \times \mathbf{B}|_{B_g \neq 0} \approx \frac{1}{\eta} \begin{pmatrix} V_z B_x B_z + V_y B_y B_x \\ -V_y B_z^2 + V_z B_y B_z - V_y B_x^2 \\ V_y B_y B_z - V_z B_y^2 - B_z B_x^2 \end{pmatrix} (\mathbf{e}_x, \mathbf{e}_y, \mathbf{e}_z), \quad (7.31)$$

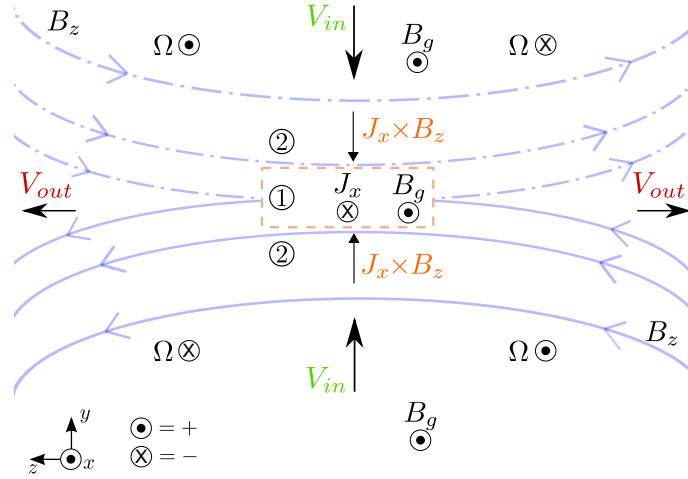


Figure 7.3: Sketch of the internal and external region of a current sheet reconnection in the presence of a guide magnetic field \mathbf{B}_g parallel to the current direction \mathbf{J} . $\boldsymbol{\Omega} = \nabla \times \mathbf{V}$ corresponds to the vorticity.

where \mathbf{e}_i is the unity vector in direction i and $B_x = B_g$ is the guide magnetic field. Equation (7.31) reduces to

$$\mathbf{J} \times \mathbf{B}|_{B_g=0} \approx \frac{1}{\eta} \begin{pmatrix} 0 \\ -V_y B_z^2 + V_z B_y B_z \\ V_y B_y B_z - V_z B_y^2 \end{pmatrix} (\mathbf{e}_x, \mathbf{e}_y, \mathbf{e}_z), \quad (7.32)$$

when the guide magnetic field is null. Setting the y (or z) component of equation (7.32) to zero yields

$$\frac{V_y}{V_z} = \frac{B_z}{B_y} = \frac{\Delta}{L} \quad (7.33)$$

which is the reconnection rate for a long Sweet-Parker current sheet. The same procedure for the y component of equation (7.31) gives

$$\frac{V_y}{V_z} = \frac{B_z B_y}{B_z^2 + B_x^2}. \quad (7.34)$$

Recalling that the ratio of the inflow over the outflow velocity is a measure of the reconnection rate in terms of the Alfvén Mach number M_A , the ratio of equations (7.34) and (7.33) reveals

$$M_{A,B_g} = \frac{B_z^2}{B_z^2 + B_x^2} M_A, \quad (7.35)$$

where M_{A,B_g} is the Alfvén Mach number of a SP current sheet with a guide magnetic field and M_A that of a non-guide field SP current sheet. Equation (7.35) shows that irrespective of its alignment, a guide magnetic field directed parallel to the current flow always reduces the amplitude of the reconnection rate. In the limit of vanishing guide field ($B_x \ll B_z$), the reconnection rate is that of a SP current sheet [equation (7.4)].

7.4.1 Turbulent Guide Field Reconnection

The influence of turbulence on the guide magnetic field during the non-linear phase of reconnection can be addressed as follow. In the framework of the mean-field turbulence model (section (4.2)), the guide magnetic field fluctuations takes the form $\mathbf{B}_g = \mathbf{B}'_g + \overline{\mathbf{B}}_g$ and the turbulent electromotive force reads

$$\mathcal{E}_M = \beta (\nabla \times \overline{\mathbf{B}}) - \sqrt{\mu_0 \rho \gamma} (\nabla \times \overline{\mathbf{V}}) + \alpha \overline{\mathbf{B}}_g. \quad (7.36)$$

The Alfvén Mach number obtained from equation (7.13) becomes

$$M_{A,T}^2 = \eta + \beta - \eta \left(|\gamma| + \alpha \frac{B_g}{B_0} \right), \quad (7.37)$$

where B_0 is the amplitude of the reconnecting magnetic field and B_g that of the guide magnetic field. In the nomenclature of figure 7.3, the ratio B_g/B_0 is the same as B_g/B_z . In the presence of a large guide magnetic field, the generation of the α term is proportional to the production of residual helicity H

$$G_\alpha \cong \tau G_H \cong \tau \overline{\mathbf{B}} \cdot \overline{\mathbf{J}}, \quad (7.38)$$

where equations (4.55)-(4.56) have been used. Without changing the geometry of a two-dimensional reconnection model, the direction of the guide field can be either co- or anti-aligned with the current density. By reversing the guide magnetic field direction, $G_\alpha \rightarrow -G_\alpha$ also $\overline{\mathbf{B}} \cdot \overline{\mathbf{J}} \rightarrow -\overline{\mathbf{B}} \cdot \overline{\mathbf{J}}$. Because the residual helicity related term α is a function of the guide magnetic field alignment to the current density (whose sign is that of the product $\overline{\mathbf{B}} \cdot \overline{\mathbf{J}}$), the product αB_g in equation (7.37) is always positive. It reduces, therefore, always the reconnection rate. The reduction is largest for a guide magnetic field larger than the amplitude of the reconnecting magnetic field B_0 . In fact, it is the balance of the turbulent terms in equation (7.37) which determines the rate of energy conversion in the non-linear phase of turbulent guide-field reconnection in large-Reynolds-number-plasmas. As discussed in section (4.3.1), a large guide magnetic field generates a large residual helicity whose intensity may suppress the turbulent resistivity β . Turbulence cannot sustain the enhancement of diffusion region width anymore. Such a suppression results in a Sweet-Parker-like size of the diffusion region and a small value of the reconnection rate. In terms of the reconnection angle θ [equation (7.9)], a suppression of the turbulent resistivity reduces θ such than it might become comparable to that of the Sweet-Parker model.

7.5 Reconnection from MHD Instabilities

The models of reconnection discussed in sections (7.1)-(7.3.2) describe the reconnection problem once a steady state is reached. The question of the onset of reconnection is discussed in the following. This section presents two theories dedicated to the onset of reconnection: i) the tearing mode instability (Furth, Killeen & Rosenbluth (1963)),⁹² and ii) the plasmoid instability (Loureiro (2007)).⁴⁸ The tearing mode instability addresses the onset of reconnection due to a spontaneous instability of a resistive current sheet. The plasmoid instability is a typical instability for long current sheets in high Reynolds number plasmas.

7.5.1 Tearing mode instability

In the following, the tearing mode instability is written in the framework of a mean-field theory and for an electromotive force \mathcal{E}_M due to turbulence. Its influence on the tearing mode onset is considered through the amplitude of \mathcal{E}_M . This can be of particular importance for large Reynolds number plasmas which are usually turbulent.

Assuming that the mean magnetic field and velocity can be written in the form $\bar{\mathbf{C}} = \bar{\mathbf{C}}_0 + \delta\bar{\mathbf{C}}$ where δ is the parameter quantifying the deviation, equation (4.14) becomes

$$\partial_t (\bar{\mathbf{B}}_0 + \delta\bar{\mathbf{B}}) = \nabla \times \left((\bar{\mathbf{V}}_0 + \delta\bar{\mathbf{V}}) \times (\bar{\mathbf{B}}_0 + \delta\bar{\mathbf{B}}) + \mathcal{E}_M + \delta\mathcal{E}_M \right) + \eta \nabla^2 (\bar{\mathbf{B}}_0 + \delta\bar{\mathbf{B}}). \quad (7.39)$$

Assuming that the mean velocity is initially zero and that the non-perturbed quantities are in a steady state ($\partial_t \bar{\mathbf{B}}_0 = 0$), the mean induction equation yields $\nabla \times \mathcal{E}_M = \eta \nabla^2 \bar{\mathbf{B}}_0$. Equation (7.39) becomes

$$\partial_t \delta\bar{\mathbf{B}} = \nabla \times \left(\delta\bar{\mathbf{V}} \times \bar{\mathbf{B}} + \delta\mathcal{E}_M \right) + \eta \nabla^2 \delta\bar{\mathbf{B}}. \quad (7.40)$$

Following Treumann and Baumjohann⁹³ for the rest of the derivation, the mean magnetic field and the mean velocity are written in terms of stream functions

$$\bar{\mathbf{B}}_0 = (-\partial_z \psi, \bar{\mathbf{B}}_y, \partial_x \psi), \quad \delta\bar{\mathbf{B}} = (-\partial_z \delta\psi, 0, \partial_x \delta\psi), \quad (7.41)$$

$$\bar{\mathbf{V}}_0 = (-\partial_z \phi, \bar{\mathbf{V}}_y, \partial_x \phi), \quad \delta\bar{\mathbf{V}} = (-\partial_z \delta\phi, 0, \partial_x \delta\phi), \quad (7.42)$$

which leads to the following form of the induction equation for the mean-fields

$$\partial_t \delta\psi = \bar{\mathbf{B}}_x \partial_x \delta\phi + \eta \nabla^2 \delta\psi + \delta\mathcal{E}_M, \quad (7.43)$$

where $\bar{\mathbf{B}}_x$ is written as $\bar{\mathbf{B}}_x = \delta\bar{\mathbf{B}}G(z)$ with $\delta\bar{\mathbf{B}}$ a constant. The function $G(z)$ is taken to be the hyperbolic tangent since the magnetic field needs to be described by a function which reverses its sign across the region where the current density gradient is defined. Linearizing the momentum equation and using the Ansatz

$$\delta\psi = \delta\psi_0(z) e^{ik_x x + \gamma_r t}, \quad \delta\phi = -\delta g(z) \frac{\gamma_r}{k_x \delta B} e^{ik_x x + \gamma_r t}, \quad (7.44)$$

$$\delta\mathcal{E}_M = \delta\mathcal{E}_M e^{ik_x x + \gamma_r t}, \quad (7.45)$$

leads to the following system of equations

$$\delta\psi_0 - G(z) \delta g(z) = \frac{1}{\gamma_r \tau_d} \left(\frac{d^2}{dz^2} \delta\psi_0 - \mathcal{K}^2 \delta\psi_0 \right) + \frac{\delta\mathcal{E}_M}{\gamma_r}, \quad (7.46)$$

$$-\frac{\gamma_r^2 \tau_A^2}{\mathcal{K}^2} \left(\frac{d^2}{dz^2} \delta g(z) - \mathcal{K}^2 \delta g(z) \right) = G(z) \left(\frac{d^2}{dz^2} \delta\psi_0 - \mathcal{K}^2 \delta\psi_0 \right) - \delta\psi_0 \frac{d^2}{dz^2} G(z), \quad (7.47)$$

with $\mathcal{K} = k_x d$ (d the halfwidth of the current sheet), $\tau_A = d/V_A$ and $\tau_d = d^2/\eta$. Two regions exist around the current sheet, an external one where the frozen-in condition rules and an internal one dominated by diffusive process. In order to obtain the solution, these regions are matched using jump conditions. For the external region, the jump condition is⁹³

$$\mathcal{D} = 2 \left(\frac{1 - \mathcal{K}^2}{\mathcal{K}} \right). \quad (7.48)$$

Since the tearing mode develops only when its wavelength is much larger than the width of the diffusive layer, the following ordering is obtained

$$\mathcal{K}^2 |\delta\psi_0| \ll \left| \frac{d^2}{dz^2} \delta\psi_0 \right|, \quad (7.49)$$

$$\mathcal{K}^2 |\delta g(z)| \ll \left| \frac{d^2}{dz^2} \delta g(z) \right|. \quad (7.50)$$

Assuming the constant-psi approximation^V and that in the narrow diffusion region $G(z) = \tanh z \cong z$, the electromotive force enters the equation as

$$\gamma_r \tau_d (\delta\psi_0 - z \delta g(z)) = \frac{d^2}{dz^2} \delta\psi_0 + \tau_d \mathcal{E}_M, \quad (7.51)$$

$$\frac{d^2}{dz^2} \delta\psi_0 = -\frac{\gamma_r^2 \tau_A^2}{\mathcal{K}^2} \frac{1}{z} \frac{d^2}{dz^2} \delta g(z). \quad (7.52)$$

Integrating equation (7.52) over z and using that for the external region $\mathcal{D} = (\delta\psi'_{0,+} - \delta\psi'_{0,-})|_{z=0} / \delta\psi_0(0)$, yields

$$\mathcal{D} = \frac{-\gamma_r^2 \tau_A^2}{\mathcal{K}^2 \delta\psi_0(0)} \int_{\mathbb{R}} \frac{dz}{z} \frac{d^2}{dz^2} \delta g(z). \quad (7.53)$$

The matching condition depends therefore on $\delta g(z)$. Its form can be found by solving equations (7.51)-(7.52) as done in the case without \mathcal{E}_M .⁹³ This leads to the following maximum wave number and growth rate for the tearing mode

$$\mathcal{K}_{max} = \left(4 \frac{\tau_A}{\tau_d} \right)^{1/4}, \quad (7.54)$$

$$\gamma_{r,max} \cong (2\tau_A \tau_d)^{-1/2}. \quad (7.55)$$

However, the electromotive force perturbation in its general form considerably complicates the resolution of the equations. As a first approach, it is assumed that the turbulent electromotive force perturbation takes the form

$$\delta \mathcal{E}_M = -\beta \delta \bar{\mathbf{J}} + \gamma \delta \bar{\boldsymbol{\Omega}}, \quad (7.56)$$

as described in section (4.2.1). The residual helicity related term α is dropped since the derivation is considered for an Harris-type equilibrium without guide magnetic field in the out-of-reconnecting-plane direction. Since the initial mean velocity is assumed to be zero, the term related to the mean vorticity is zero as well. The diffusion time in equations (7.46)-(7.47) is now related to turbulence as

$$\tilde{\tau}_d = \frac{d^2}{\eta + \beta}. \quad (7.57)$$

V. The magnetic field perturbation is constant across the diffusion region.

The maximum wavelength and growth rate according to this new diffusion time become

$$\mathcal{K}_{max,T} = (4\tau_A)^{1/4} \left(\frac{\beta \left(\frac{\eta}{\beta} + 1 \right)}{d^2} \right)^{1/4}, \quad (7.58)$$

$$\gamma_{r,max,T} \cong \frac{1}{(2\tau_A)^{1/2}} \left(\frac{\beta \left(\frac{\eta}{\beta} + 1 \right)}{d^2} \right)^{1/2}. \quad (7.59)$$

Depending on η/β , three different cases can be distinguished:

$$\beta \ll \eta \Rightarrow \mathcal{K}_{max,T} = \mathcal{K}_{max}, \quad \gamma_{r,max,T} = \gamma_{r,max}, \quad (7.60)$$

$$\beta \cong \eta \Rightarrow \mathcal{K}_{max,T} \cong 2^{1/4} \mathcal{K}_{max}, \quad \gamma_{r,max,T} \cong 2^{1/2} \gamma_{r,max}, \quad (7.61)$$

$$\beta \gg \eta \Rightarrow \mathcal{K}_{max,T} \cong (4\tau_A)^{1/4} \left(\frac{\beta}{d^2} \right)^{1/4}, \quad \gamma_{r,max,T} = \frac{1}{(2\tau_A)^{1/2}} \left(\frac{\beta}{d^2} \right)^{1/2}. \quad (7.62)$$

In the form (7.56), the \mathcal{E}_M increases the value of the growth rates as well as its wavelength in case of $\beta \cong \eta$. That limit favors the tearing mode to develop and attain a larger growth rate. In situation of large-magnetic-Reynolds-numbers, in the limit of equation (7.62), turbulence triggers the tearing mode. It is nevertheless only valid for an initial level of turbulence comparable to the mean magnetic field perturbation. In fact, considering that $|\delta\mathcal{E}_M| \gg |d^2\delta\psi_0/dz^2|$ changes the ordering in equation (7.46) which leads to

$$\delta g(z) = \frac{1}{z} (\tau_d \delta\mathcal{E}_M + \gamma_r \tau_d \delta\psi_0(0)). \quad (7.63)$$

The jump condition for the internal region becomes

$$\mathcal{D} = \frac{\gamma_r^2 \tau_A^2}{\mathcal{K}^2 \delta\psi_0(0)} (\tau_d \delta\mathcal{E}_M + \gamma_r \tau_d \delta\psi_0(0)) \int_{\mathbb{R}} \frac{dz}{z} \frac{d^2}{dz^2} \frac{1}{z} \rightarrow 0. \quad (7.64)$$

The matching condition for the external region with the internal one implies

$$0 = \frac{2}{\mathcal{K}} (1 - \mathcal{K}^2) \Rightarrow \mathcal{K}^2 = 1 \Rightarrow k_x^2 = \frac{1}{d^2}. \quad (7.65)$$

As a result, the tearing mode is not unstable since its wavelength is comparable to the width of the diffusion region. These statements confirmed the findings in Widmer *et al.*⁹⁴ of the reconnection rate maximum value in function of the initial level of turbulence. It is important to be noted that the derivation has been carried out assuming implicitly that the electromotive force is anti-aligned with the mean current density. Considering that the \mathcal{E}_M is co-aligned with the mean current density, i.e. $\mathcal{E}_M \cdot \bar{\mathbf{J}} > 0$, the maximum wavelength and growth rate associated to \mathcal{E}_M are

$$\mathcal{K}_{max,T} = (4\tau_A)^{1/4} \left(\frac{\beta \left(\frac{\eta}{\beta} - 1 \right)}{d^2} \right)^{1/4}, \quad (7.66)$$

$$\gamma_{r,max,T} \cong \frac{1}{(2\tau_A)^{1/2}} \left(\frac{\beta \left(\frac{\eta}{\beta} - 1 \right)}{d^2} \right)^{1/2}. \quad (7.67)$$

Assuming that the amplitude of turbulence is of the same order as the magnetic field perturbation, three limits are obtained. The resistive MHD limit is recovered when $\beta \ll \eta$ while for $\beta \gg \eta$, $\gamma_r \in \mathbb{C}$. In such situations, the disturbance are oscillating waves for which no growth are expected. In the limit $\beta \cong \eta$, different cases are found

$$\eta < \beta \Rightarrow \gamma_{r,max,T}, \mathcal{K}_{max,T} \in \mathbb{C}, \quad (7.68)$$

$$\eta = \beta \Rightarrow \gamma_{r,max,T} = \mathcal{K}_{max,T} = 0, \quad (7.69)$$

$$\eta > \beta \Rightarrow \gamma_{r,max,T}, \mathcal{K}_{max,T} \in \mathbb{R}. \quad (7.70)$$

Solely equation (7.70) gives a growth rate but smaller than the one obtained in resistive MHD. Assuming a larger amplitude of the turbulent electromotive force compared with the magnetic field perturbation, the tearing mode is not unstable (wavelength equal to the halfwidth). Consequently, the electromotive force has to be anti-aligned with the mean current density to produce larger growth than the usual resistive MHD limit.

The amplitude of turbulent electromotive force dramatically affects the onset of the instability. If the initial intensity of \mathcal{E}_M is too large, the system is so turbulent that no reconnection can take place. In this limit, magnetic diffusion leads to a broadening of the current sheet which suppresses the instability. On the other hand, if the amplitude of \mathcal{E}_M is too small, the behaviour of the instability is similar to the resistive MHD limit. It is for the right amplitude of the turbulent electromotive force that the instability can be enhanced by turbulence.

7.5.2 The Plasmoid Instability

Since the mathematics of the plasmoid instability is similar to the tearing mode (section (7.5.1)), the full derivation including the turbulent electromotive force is not repeated here and only an heuristic derivation is given.⁴⁸ The maximum wavenumber, the growth rate and the inner-layer width are written in terms of the Lundquist number $S = L_{cs} V_A / \eta$ (magnetic Reynolds number for $V = V_A$) for a Sweet-Parker current sheet. The equilibrium length d (current sheet halfwidth) from the previous derivations is expressed through the length of the current sheet as

$$d \equiv \delta_{cs} \cong L_{cs} S^{-1/2}. \quad (7.71)$$

Equations (7.54)-(7.55) as well as the ratio of the inner-layer width to the current sheet thickness are written in terms of the Lundquist number as

$$k_{max} L_{cs} \cong S^{3/8}, \quad (7.72)$$

$$\gamma_{p,max} \tau_A \cong S^{1/4}, \quad (7.73)$$

$$\frac{\delta_{inner}}{\delta_{cs}} \cong S^{-1/8}. \quad (7.74)$$

The plasmoid instability is triggered for $\gamma_{p,max} \tau_A \gg 1$, $k_{max} L_{cs} \gg 1$ and $\delta_{inner} / \delta_{cs} \ll 1$. Requiring that the ratio of equation (7.74) is a most 1/3, the current sheet is Sweet-Parker stable under a critical Lundquist number $S_{crit} \cong 10^4$.⁹⁵ In the framework of mean-field turbulence modelling, a first approximation is to consider $\eta \rightarrow \eta + \beta$. In this limit, the

Lundquist number is promoted to $S_T = L_{cs} V_A / (\beta + \eta)$. Proceeding to a similar analysis as the tearing instability, the following limits are obtained

$$\eta \gg \beta \Rightarrow \text{Resistive MHD} \quad (7.75)$$

$$\eta \cong \beta \Rightarrow k_{max,T} \cong \frac{1}{2^{3/8}} k_{max}, \quad \gamma_{max,T} \cong \frac{1}{2^{1/4}} \gamma_{p,max} \quad (7.76)$$

$$\beta \gg \eta \Rightarrow \eta \rightarrow \beta \quad (7.77)$$

Equation (7.77) shows that for large Reynolds numbers, the turbulent resistivity β can be behind a plasmoid instability. It is important to note that in the limit of equation (7.76), the maximum growth rate $\gamma_{max,T}$ and wave number $k_{max,T}$ are lower than their non-turbulent counterparts. This can be understood from the viewpoint that turbulence enhances the width Δ of the diffusion region. Assuming that the latter is of the order of the current sheet halfwidth δ_{CS} ,^{VI} the width of diffusion region in presence of turbulence, denoted Δ_T , is

$$\Delta_T = \begin{cases} L \left(\frac{\eta}{V_A L} \right)^{1/2} = \delta_{CS} & \eta \gg \beta, \\ L \left(\frac{\eta + \beta}{V_A L} \right)^{1/2} = 2^{1/2} \delta_{CS} & \eta \cong \beta, \\ L \left(\frac{\beta}{V_A L} \right)^{1/2} = \delta_{CS,\beta} & \eta \ll \beta, \end{cases} \quad (7.78)$$

where equation (7.71) has been used. In terms of the width Δ_T , equation (7.74) becomes

$$\frac{\delta_{inner}}{\Delta_T} = \begin{cases} \frac{\delta_{inner}}{\Delta_T} = S^{-1/8} & \eta \gg \beta, \\ \frac{\delta_{inner}}{\Delta_T} = 2^{1/2} S^{-1/8} & \eta \cong \beta, \\ \frac{\delta_{inner}}{\Delta_T} = S^{-1/8} & \eta \ll \beta, \end{cases} \quad (7.79)$$

where $S_\beta = L V_A / \beta$. The increased width of the diffusion layer in the limit $\beta \cong \eta$ gives a critical Lundquist number of the order of 10^6 under which a current sheet is stable against the plasmoid instability. As for the tearing instability, a large amplitude of turbulence compared with the amplitude of the magnetic field perturbation avoids the instability to set on. These limits are again for an electromotive force anti-aligned with the mean current density. In the case of $\mathcal{E}_M \cdot \mathbf{J} > 0$, only the limit $\eta \gg \beta$ causes an instability comparable to the resistive MHD limit. This means that the electromotive force \mathcal{E}_M obtained in the framework of a Reynolds-averaged turbulence model is anti-aligned to the mean current direction.

VI. It is, in fact, two times the current sheet halfwidth but this can be neglected for the heuristic discussion.

8 Single ‘X’-Point Turbulent Reconnection - Mean-Field Theory and Simulation

If you are going through hell, keep going.

Winston S. Churchill

The mean-field approach for turbulence was discussed in section (4). It was shown to reproduce the solar wind Alfvénicity and some turbulent electromotive force expressions were further validated by direct numerical simulations of a Kolmogorov flow.^{96,97} In the context of magnetic reconnection, the self-generated and -sustained turbulence model described in section (4.1) was shown to enhance the reconnection process for an Harris-type current sheet.³⁰ The increased energy conversion was argued to be related to localisation of the turbulent energy around the ‘X’-point due to the influence of the turbulent cross-helicity effects. The turbulent energy is proportional to a turbulent resistivity [equation (4.57)] which decreases away from the ‘X’-point. The angle of reconnection [equation (7.9)] is then strongly enlarged and the reconnection rate is enhanced above a Sweet-Parker rate towards the Petschek rate of reconnection (see section (7.2)). Turbulence might be able to support the fast reconnection with the genuine capability of bridging the time- and length scale gap between classical resistive MHD theories and observations.

This chapter is separated into two main sections. In section (8.1) the simulation of Higashimori *et al.*⁹⁸ is re-conducted for an Harris-type current sheet but also with a guide magnetic field parallel to the mean current direction. Also, turbulent reconnection through a force-free current sheet with a finite guide magnetic field is investigated. To extend the results and confirm the importance of the turbulence cross-helicity effects, numerical simulations of an Harris-type current sheet are carried out where the turbulence cross-helicity is set to zero (section (8.2)).

The text of section (8.1) is based on an paper published in *Physics of Plasmas*. The material is reproduced with permission from F. Widmer, J.Büchner and N.Yokoi, *Physics of Plasmas* **23**, 042311, (2016). Copyright 2016, AIP Publishing LLC. When a figure is reused, it is cited as: "Taken from Widmer *et al.*⁹⁴"

8.1 Simplified Bulk Turbulence Model

The turbulence model described in section (4.2.1) is simplified by neglecting second order derivative terms such as $R_{ij}\partial_i\bar{V}_i$. The resulting MHD and turbulence equations, which are numerically solved, are

$$\frac{\partial\rho}{\partial t} = -\nabla \cdot (\rho\bar{\mathbf{V}}), \quad (8.1)$$

$$\frac{\partial\rho\bar{\mathbf{V}}}{\partial t} = -\nabla \cdot \left[\rho\bar{\mathbf{V}} \otimes \bar{\mathbf{V}} + \frac{1}{2}(\bar{p} + \bar{B}^2)\mathbf{I} - \bar{\mathbf{B}} \otimes \bar{\mathbf{B}} \right] + \chi\nabla^2\rho\bar{\mathbf{V}}, \quad (8.2)$$

$$\frac{\partial\bar{\mathbf{B}}}{\partial t} = \nabla \times (\bar{\mathbf{V}} \times \bar{\mathbf{B}} + \mathcal{E}_M) + \eta\nabla^2\bar{\mathbf{B}}, \quad (8.3)$$

$$\frac{\partial\bar{h}}{\partial t} = -\nabla \cdot (\bar{h}\bar{\mathbf{V}}) + \frac{\gamma_0 - 1}{\gamma_0\bar{h}^{\gamma_0-1}} \left(\eta\bar{\mathbf{J}}^2 + \rho\varepsilon \right) + \chi\nabla^2\bar{h}, \quad (8.4)$$

$$\frac{\partial K}{\partial t} = -\bar{\mathbf{V}} \cdot \nabla K - \mathcal{E}_M \cdot \bar{\mathbf{J}} + \frac{\bar{\mathbf{B}}}{\sqrt{\rho}} \cdot \nabla W - \varepsilon, \quad (8.5)$$

$$\frac{\partial W}{\partial t} = -\bar{\mathbf{V}} \cdot \nabla W - \mathcal{E}_M \cdot \bar{\boldsymbol{\Omega}} + \frac{\bar{\mathbf{B}}}{\sqrt{\rho}} \cdot \nabla K - C_W \frac{W}{\tau_t}, \quad (8.6)$$

The normalisation can be found in appendix (A.1). The symbol ρ denotes the mean mass density (mass density fluctuations are neglected), $\bar{\mathbf{V}}$ the mean velocity and $\bar{\mathbf{B}}$ the mean magnetic field. The latter is used to compute the mean current density from Ampère's law $\mu_0\bar{\mathbf{J}} = \nabla \times \bar{\mathbf{B}}$. The mean vorticity is obtained from the mean velocity as $\nabla \times \bar{\mathbf{V}} = \bar{\boldsymbol{\Omega}}$. The background resistivity η is taken as constant and homogeneous. As presented in section (3), the variable \bar{h} is used instead of the thermal pressure \bar{p} such that the internal energy equation is in conservative form if no dissipation takes place. The thermal pressure \bar{p} and the variable \bar{h} are related by the equation of state $p = 2h^{\gamma_0}$ where the ratio of specific heats γ_0 is taken for adiabatic conditions ($\gamma_0 = 5/3$). It has to be noted that in addition to the Joule heating, a turbulent energy dissipation rate ε enters the equation of the internal energy. It represents the increase of internal energy due to the amount of the energy transferred from large to small scales. The numerical parameter χ is used to locally smooth strong gradients which locally can cause numerical instability.^I The turbulent electromotive force \mathcal{E}_M is given in terms of the mean magnetic field $\bar{\mathbf{B}}$, mean current density $\bar{\mathbf{J}}$, mean vorticity $\bar{\boldsymbol{\Omega}}$

$$\mathcal{E}_M = \alpha\bar{\mathbf{B}} - \beta\bar{\mathbf{J}} + \gamma\bar{\boldsymbol{\Omega}}. \quad (8.7)$$

The transport coefficients α , β and γ are determined by a closure theory for inhomogeneous turbulence described in appendix (C).^{34,67} The relation of the transport coefficients and the mean turbulence quantities can be modelled following TSDIA as

$$\alpha = \tau_t C_\alpha H, \quad (8.8)$$

$$\beta = \tau_t C_\beta K, \quad (8.9)$$

$$\gamma = \tau_t C_\gamma W, \quad (8.10)$$

I. See appendix (A.2) for more details.

for the model constants estimated as $C_\beta = 0.3$, $C_\gamma = 0.3$, $C_\alpha = 0.01$ and $C_W = 1.3$ [equation (8.6)].^{70,99} The symbol K , W and H denote the turbulent energy, turbulent cross-helicity and residual helicity as described in section (4.2.1). In terms of the mean current density and mean vorticity, the production mechanism P_K for the turbulent energy and P_W for the turbulent cross-helicity are given as

$$P_K = \tau_t \left(C_\beta K \frac{\overline{\mathbf{J}}^2}{\rho} - C_\gamma W \frac{\overline{\boldsymbol{\Omega}} \cdot \overline{\mathbf{J}}}{\sqrt{\rho}} \right), \quad (8.11)$$

$$P_W = \tau_t \left(C_\beta K \frac{\overline{\boldsymbol{\Omega}} \cdot \overline{\mathbf{J}}}{\sqrt{\rho}} - C_\gamma W \overline{\boldsymbol{\Omega}}^2 \right). \quad (8.12)$$

A large turbulent timescale τ_t produces a large amplitude of turbulence while a small amplitude is produced for small τ . The timescale of turbulence τ_t is prescribed as an external parameter. From the discussion in section 4.1.2 and 6.1, the timescale of turbulence can be expressed as

$$\tau_t = \frac{K}{\varepsilon}, \quad (8.13)$$

where ε is the turbulent energy dissipation rate. As a first step, the governing equation for the turbulent energy dissipation rate [equation (4.52)] is not used and the timescale of turbulence is parametrized by a constant τ_t [equation (8.13)]. Previous investigations of an anti-parallel magnetic field reconnection showed that a constant timescale of turbulence distinguishes three regimes of energy conversion: i) a *laminar* regime for which the energy conversion rate is similar than that of the resistive MHD limit, ii) a *turbulent reconnection* regime which enhances the reconnection rate strongly, and iii) a *turbulent diffusion* regime where the saturation of turbulence suppresses reconnection.⁹⁸ The timescale of the turbulence determines the initial amplitude of turbulence. The first two regimes of energy conversion are similar to equations (7.60)-(7.62) obtained for the tearing mode instability (section (7.5.1)) while the third limit is due to the large initial amplitude of turbulence compared with the magnetic field perturbation [equations (7.63)-(7.65)]. The regimes of energy conversion are related to the rate of energy transfer from large to small scales as discussed in section (8.1.2).

8.1.1 Initial Configurations

The MHD equations are solved using the GOEMHD3 code.¹⁰⁰ A MacCormack scheme has been additionally implemented to deal with the non-linearity of the turbulence evolution equations (8.5)-(8.6) (see appendix (A.2)). The coordinate system is defined by the orthogonal unity vectors \mathbf{e}_x , \mathbf{e}_y and \mathbf{e}_z . The reconnection plane is spanned by \mathbf{e}_y and \mathbf{e}_z which are directed across and along the initial current sheet. The direction perpendicular to the current sheets is along \mathbf{e}_x . The simulation box size is $L_x \times L_y \times L_z = 0.4 \times 64 \times 64 L_0^3$ resolved by $4 \times 1026 \times 1026$ grid points. The length scale used for normalisation is the current sheet half width L_0 which is resolved by 16 grid points.

The initial values of the reconnecting magnetic field B_0 , the turbulent energy K_0 and turbulent energy W_0 are chosen the same for all numerical simulations. An exception is made for the investigation of the influence of the initial turbulent energy K_0 (sec-

tion (8.1.3)). The initial values are taken as

$$B_0 = 1.0, \quad (8.14)$$

$$K_0 = 0.001, \quad (8.15)$$

$$W_0 = 0. \quad (8.16)$$

In order to trigger a certain configuration of reconnection, the initial equilibria are perturbed by a (divergence free) magnetic field perturbation $\bar{\mathbf{B}}_p$

$$\bar{\mathbf{B}}_p = B_{0,p} \left[\sin(\psi) \sin(\phi)^2 \mathbf{e}_y + \frac{L_z}{L_y} \cos(\psi) \sin(2\phi) \mathbf{e}_z \right], \quad (8.17)$$

where $\psi = 2\pi z/L_z$, $\phi = 2\pi y/L_y$, $L_i = (L/L_0)\mathbf{e}_i$ for $i = y, z$ are the box sizes and $B_{0,p}$ is the initial amplitude of the magnetic field perturbation. Finally, a set of two current sheets is initialised so that periodic boundary conditions can be used. The pair of current sheets are separated by a distance $d = 32L_0$ sufficient to avoid an initial interaction between them.¹⁰¹ Each current sheet is located at $\pm d = \pm 16L_0$ in the simulation box.

The Harris-type current sheets are initialised as

$$\bar{\rho}_0 = 1, \quad (8.18)$$

$$\bar{\mathbf{V}}_0 = 0, \quad (8.19)$$

$$\bar{\mathbf{B}}_0 = B_g \mathbf{e}_x + B_0 (\tanh(y+d) - \tanh(y-d) - 1) \mathbf{e}_z, \quad (8.20)$$

$$\bar{h}_0 = \frac{1}{2} \left(1 + \beta_p - \bar{B}_0 \mathbf{e}_z \right)^{1/\gamma_0}, \quad (8.21)$$

where β_p is the plasma beta and B_g a constant guide magnetic field. Both β_p and B_g are normalised to the amplitude of the reconnecting magnetic field B_0 . The second current sheet equilibrium used to test the averaged turbulence model is a initial force-free, i.e. $\bar{\mathbf{J}} \times \bar{\mathbf{B}} = 0$, current sheet model.⁸⁴ The initial conditions for this equilibrium are

$$\bar{\rho}_0 = 1, \quad (8.22)$$

$$\bar{\mathbf{V}}_0 = 0, \quad (8.23)$$

$$\bar{\mathbf{B}}_0 = B_0 \left[\sqrt{(B_g^2 + \cosh^{-2}(y+d) + \cosh^{-2}(y-d))} \mathbf{e}_x + (\tanh(y+d) - \tanh(y-d) - 1) \mathbf{e}_z \right], \quad (8.24)$$

$$\bar{h}_0 = \frac{1}{2} (\beta_p)^{1/\gamma_0}, \quad (8.25)$$

Equation (8.24) is appropriate for the solar corona since it is valid for low plasma beta and bears an out-of-plane guide magnetic field dependence. It is further deprived of currents perpendicular to the reconnecting magnetic field direction (\mathbf{e}_y). The initial mean current density $\bar{\mathbf{J}}_0$ is given for equations (8.22)-(8.25) as

$$\bar{\mathbf{J}}_0 = (\cosh^{-2}(a) + \cosh^{-2}(b)) \mathbf{e}_x \quad (8.26)$$

$$+ \frac{\tanh(a) \cosh^{-2}(a) + \tanh(b) \cosh^{-2}(b)}{\sqrt{b_g^2 + \cosh^{-2}(a) + \cosh^{-2}(b)}} \mathbf{e}_z, \quad (8.27)$$

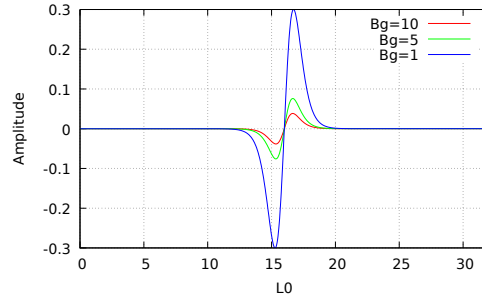


Figure 8.1: Case of finite out-of-plane guide magnetic field B_g : initial amplitude of the in-plane mean current density in normalised simulation units in force-free equilibrium current sheet. Taken from Widmer *et al.*⁹⁴

where $a = y + d$ and $b = y - d$. The in-plane current \bar{J}_z is smaller for larger initial constant guide magnetic fields B_g (see figure 8.1). As discussed in sections (7.4)-(7.4.1), a guide magnetic field can efficiently reduce the reconnection rate. The efficiency of the apparent turbulent resistivity is also dramatically affected by a guide magnetic field parallel to the mean current flow. The corresponding generation of the residual helicity H suppresses the generation of turbulent energy K in the diffusion region (section (4.3.1)). Without solving the governing equation for the residual helicity H [equation (4.51)], it is expected that the breakage of mirror-symmetry due to the out-of plane guide field influences the reconnection rate through the residual helicity.

8.1.2 Regimes of Reconnection and Energy Transfer

The spatial distribution of the mean current density \bar{J} (figure 8.2a), the mean vorticity $\bar{\Omega}$ (figure 8.2b), the turbulent energy K (figure 8.2c) and the turbulent cross-helicity W (figure 8.2d) is depicted in figure 8.2. The snapshot is taken at the time the reconnection rate is maximum. The turbulent energy K is localised where the mean current density accumulates and is surrounded by the turbulent cross-helicity W . The latter is found to be distributed in a quadrupolar shape around the diffusion region as the mean vorticity. This situation is found for all investigated current sheets at each time the turbulent reconnection regime is obtained. Figure 8.2 confirms the localisation of the turbulent energy and turbulent cross-helicity at and around the reconnection region as discussed in sections (4.2.1)-(4.3) and by Yokoi and Hoshino.⁷⁰

The influence of turbulence is studied by varying the timescale of turbulence for the current sheet equilibria defined in the previous section. From the initial conditions for the mean velocity and the turbulent cross-helicity, the initial balance of turbulence is

$$P_K - \frac{K}{\tau} = 0, \quad (8.28)$$

where P_K is the production term of the turbulent energy $\beta \bar{J}^2$ [equation (4.59)]. Equation (8.28) gives the initial timescale of turbulence

$$\tau_0 = \sqrt{\frac{\rho}{\mu_0}} \frac{1}{C_\beta^{1/2}} \frac{1}{|\bar{J}|}. \quad (8.29)$$

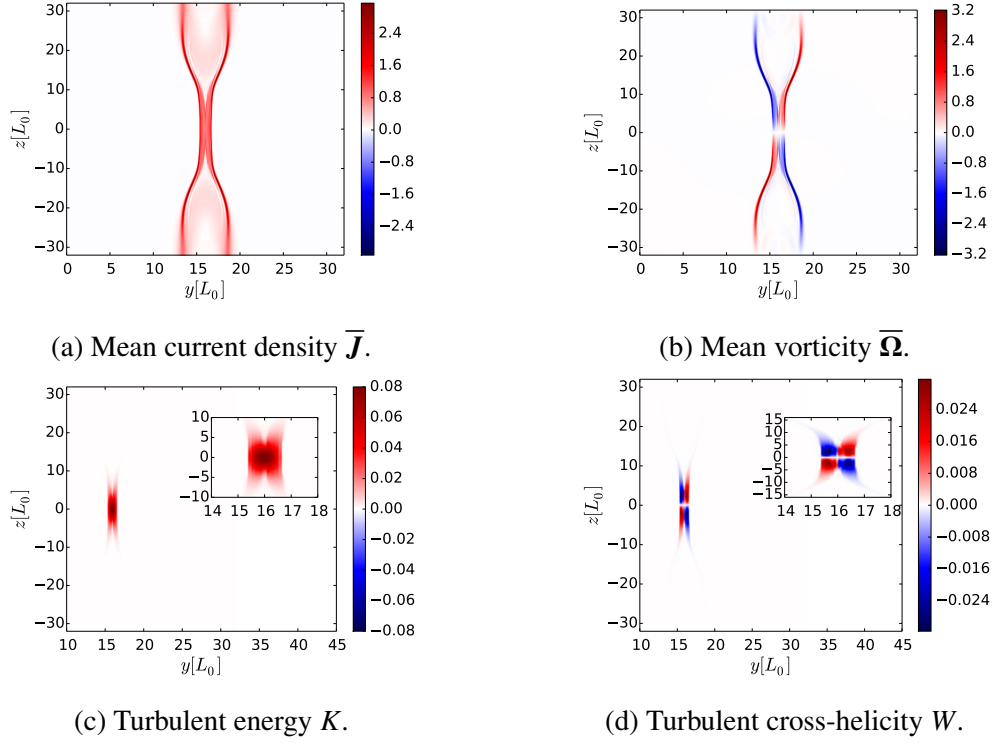


Figure 8.2: Spatial distribution at the time the reconnection rate reaches its maximum value of the turbulent energy K , the turbulent cross-helicity W , the mean current density \bar{J} and the mean vorticity $\bar{\Omega}$. Taken from Widmer *et al.*⁹⁴

The influence of the timescale of turbulence is tested through a variation of the variable $\tau \equiv \tau_t/\tau_0$.

The reconnection rate is obtained by calculating the amount of magnetic flux ϕ reconnected in time. It is calculated as the integral along the current sheet, from the ‘O’-point to the ‘X’-point, of the magnetic field component B_y (across the current sheet) as

$$\frac{\phi}{B_0 L_0} = \int_{z_0}^{z_X} \frac{B_y}{B_0 L_0} dz. \quad (8.30)$$

Here the center of a magnetic island is denoted by z_0 and the ‘X’-point location by z_X . They are both located along the current sheets center $y = \pm d$ and the integration is carried out over dz . The reconnection rate is taken as the time derivative of the reconnected flux [equation (8.30)]

$$M_A = \frac{\partial_t \phi}{B_0 V_A}. \quad (8.31)$$

Figure 8.3 shows the reconnection rate using equations (8.30) and (8.31). As previously obtained for an Harris-type current sheet without guide magnetic field,⁹⁸ the timescale parameter τ controls the regimes of energy conversion. They are also found in the presence of a finite out-of-plane guide magnetic field B_g . The guide field is, however, reducing the maximum possible reconnection rate. This matter is discussed in section (8.1.5). The regimes of energy conversion are also obtained for the force-free equilibrium as it can

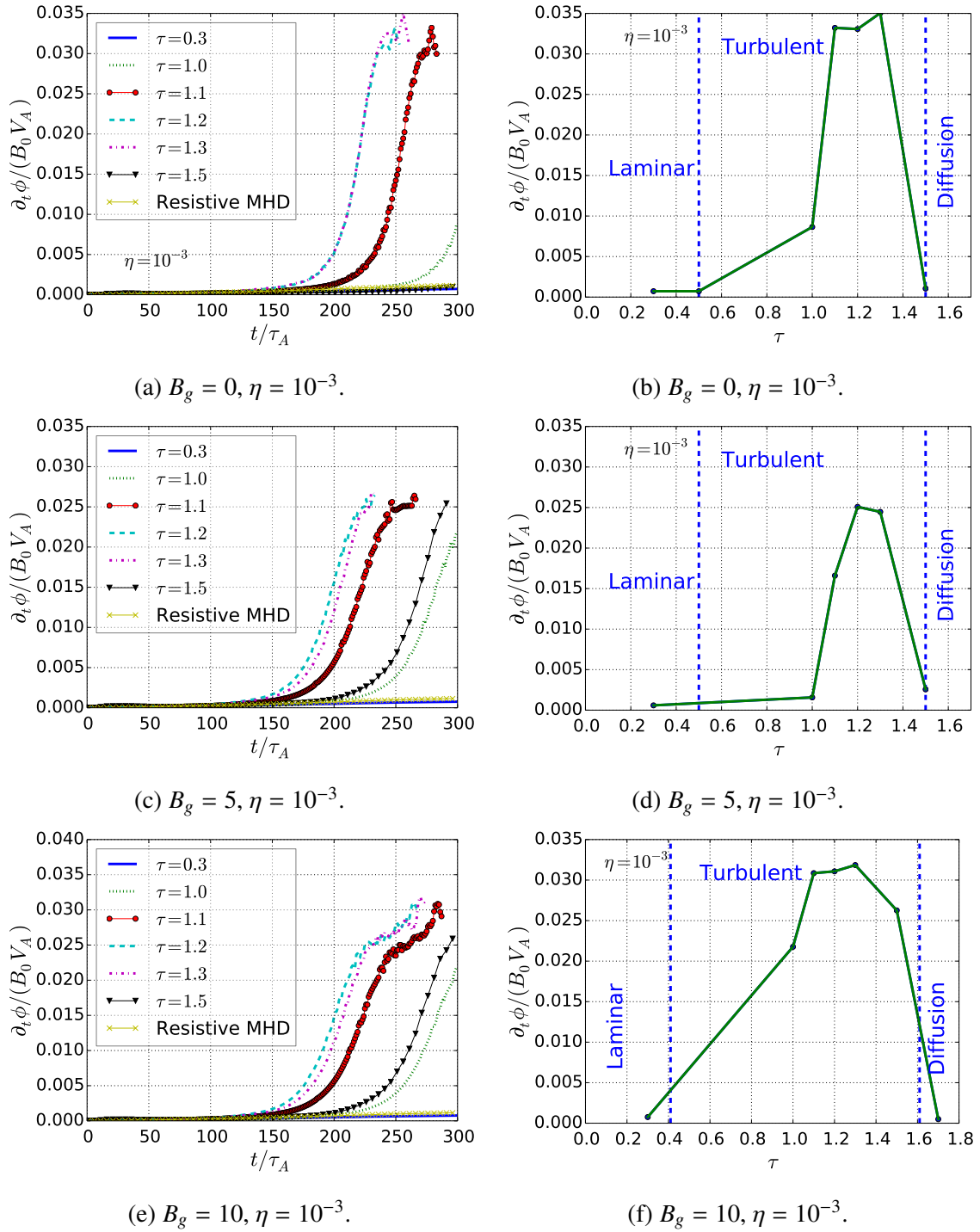


Figure 8.3: The upper row depicts the evolution of the reconnection rate $\partial_t \phi$ for Harris-type current sheets. The second line represents the regimes of reconnection obtained for the reconnection rate at the time the first peak is reached, i.e., $t = 250\tau_A$ for figure 8.3a, $t = 225\tau_A$ for figure 8.3c and $t = 260\tau_A$ for figure 8.3e. Figures 8.3a and 8.3b taken from Widmer *et al.*⁹⁴

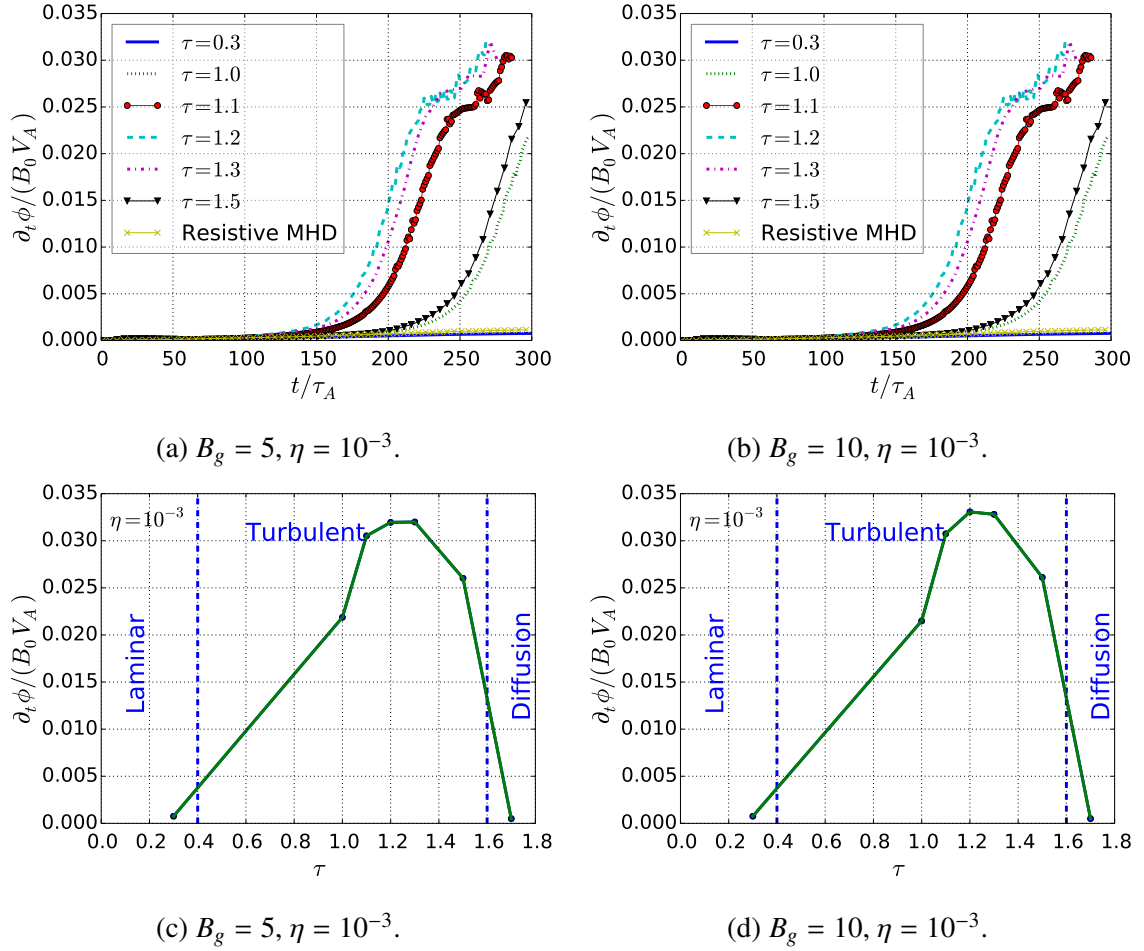


Figure 8.4: Figure 8.4a and 8.4b represent the evolution of the reconnection rate $\partial_t \phi$ for the force-free current sheets equilibrium. Figure 8.4c and 8.4d present the regimes of reconnection obtained by taking the value of the reconnection rate at the time when the first peak is reached, i.e., $t = 225\tau_A$ for figure 8.4a and $t = 260\tau_A$ for figure 8.4b. Figure 8.4c is adapted from Widmer *et al.*⁹⁴

be seen in figure 8.4. As for the Harris equilibrium, the guide magnetic field reduces the maximum reconnection rate. In addition to that reduction, the time required to reach saturation is longer for a force-free-type equilibrium. These results are summarized in table (8.1). The maximum value that each current sheets type can reached is highlighted in blue. The reconnection rate reaches its maximum value later for current sheet equilibria in the presence of a finite guide magnetic field. The value is also lower than the Harris-type equilibrium without guide magnetic field. The regime of fast turbulent energy conversion is broader for a larger guide magnetic field. They are in a turbulent timescale range of $[0.6; 1.6]$ instead of $[1.0; 1.4]$ for cases without guide magnetic field. Since the results for a guide magnetic field amplitude of 5 are similar to the results for an amplitude of 10 (for both equilibrium), only the force-free results for a constant guide magnetic field amplitude of 5 are discussed in the following.

Table 8.1: Maximum reconnection rates in time ($\eta = 10^{-3}$) for different types of current sheet (CS) models: Harris (I) and force-free (II) ($\eta = 10^{-3}$). Adapted from Widmer *et al.*⁹⁴

CS	τ	b_g	t/τ_A	$\partial_t\phi$	CS	τ	b_g	t/τ_A	$\partial_t\phi$	CS	τ	b_g	t/τ_A	$\partial_t\phi$
I	0.3	0	298	0.001	I	0.3	5	298	0.001	II	0.3	5	298	0.001
I	1.0	0	299	0.008	I	1.0	5	298	0.022	II	1.0	5	299	0.022
I	1.1	0	278	0.034	I	1.1	5	265	0.026	II	1.1	5	281	0.031
I	1.2	0	248	0.034	I	1.2	5	232	0.026	II	1.2	5	267	0.032
I	1.3	0	255	0.035	I	1.3	5	231	0.027	II	1.3	5	270	0.032
I	1.5	0	299	0.002	I	1.5	5	292	0.026	II	1.5	5	298	0.026
I	0.3	10	298	0.001	II	0.3	10	298	0.001					
I	1.0	10	298	0.022	II	1.0	10	299	0.022					
I	1.1	10	284	0.031	II	1.1	10	281	0.031					
I	1.2	10	264	0.031	II	1.2	10	268	0.034					
I	1.3	10	269	0.032	II	1.3	10	276	0.034					
I	1.5	10	298	0.026	II	1.5	10	298	0.026					

8.1.3 Limits of Large Magnetic Reynolds Numbers

The enhancement of reconnection by turbulence was derived for a Sweet-Parker model of reconnection in presence of guide magnetic field parallel to the current flow (section (7.4)). The equation for the Alfvén Mach number M_A , representing an estimation of the reconnection rate, is given as

$$M_A^2 = \beta + \eta \left(1 - |\gamma| + \alpha \frac{B_G}{B_0} \right). \quad (8.32)$$

Expression (8.32) states that for a small resistivity η , the turbulence determines the value of the reconnection rate. The discussion is focused on the influence of the Reynolds number on the reconnection rate, the action of the α term is discussed in section (8.1.5). As presented in table (8.1), the results for a constant guide magnetic field amplitude of 5 are similar to those obtained for a amplitude of 10. Only the results for a constant guide magnetic field amplitude of 5 are considered for the two initial equilibria. Figure 8.5 confirms that the maximum value of the reconnection rate increases as the resistivity η is decreased. In such a case, the turbulent energy acts as turbulent resistivity localised at the diffusion region and Petschek reconnection can be achieved (see discussion in section (7.3.2)). There is a clear deviation from the Sweet-Parker model of reconnection which scales as $\eta^{1/2}$. It has to be noted that the reconnection rate saturates for a value of the resistivity smaller than $\eta = 10^{-5}$. This is the order of magnitude of the numerical resistivity due to the finite grid resolution. At large Reynolds numbers, the energy conversion due to turbulence is large. It exceeds the effects of the molecular resistive dissipation. In such situations, the turbulent Reynolds number R_T exceeds the magnetic Reynolds number R such that $\eta/\beta_0 \equiv R_T/R \ll 1$. The ratio of the initial turbulent resistivity β_0 to the resistivity η has, therefore, to be investigated. Figure 8.6 shows the dependence of the reconnection rate as a function of the initial amplitude of the turbulent and resistivity β_0 and η . A large amplitude of β_0 results in small value of the reconnection rate. The initial

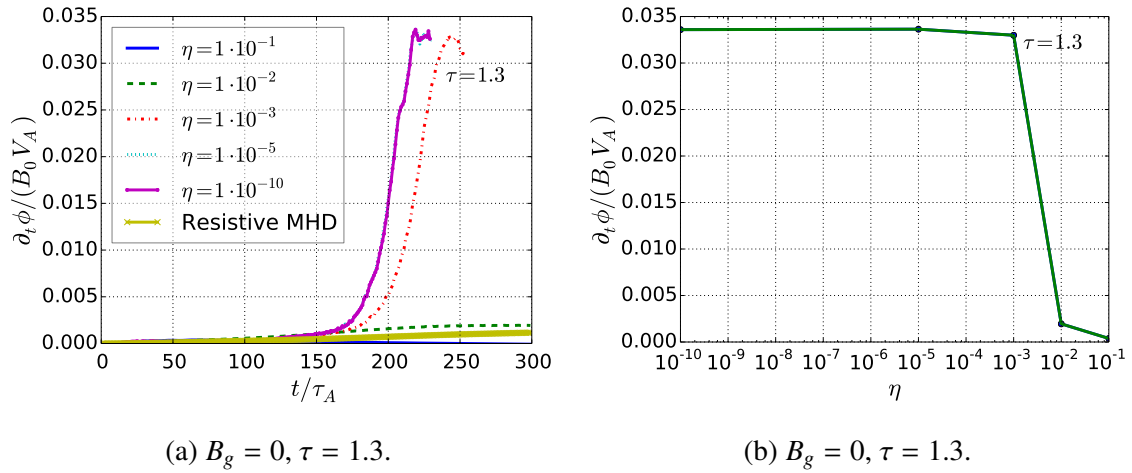


Figure 8.5: Reconnection rates obtained for Harris-type current sheets. As the resistivity η is decreased, the reconnection rate $\partial_t \phi$ is increased in presence of turbulence. Adapted from Widmer *et al.*⁹⁴

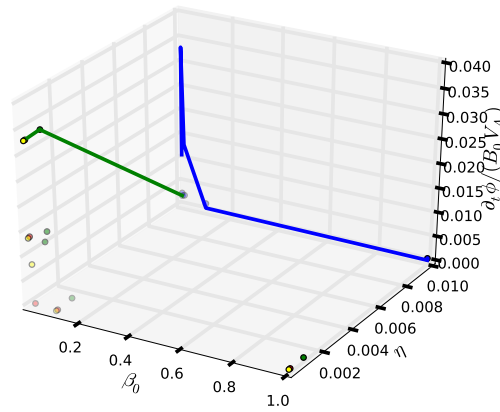


Figure 8.6: Maximum reconnection rate as a function of the initial amplitude of turbulent and magnetic resistivity β_0 and η for the Harris-type current sheet equilibrium ($b_g = 0$)

amplitude of turbulence β_0 depends on both the timescale of turbulence τ and the initial amplitude of turbulent energy K_0 as

$$\beta_0 = C_\beta \tau K_0. \quad (8.33)$$

The influence of β_0 is then of two kinds: i) the influence of the timescale of turbulence τ , and ii) the initial amplitude of turbulent energy K_0 . The investigation on the influence of τ was already implicitly carried out by keeping fixed the initial amplitude of turbulent energy K_0 and the resistivity η , i.e., varying the timescale of turbulence. A large amplitude of the timescale of turbulence only produces a broadening of the current sheet.

The second point ii) is now considered. As presented in section (7.5.1), as soon as the amplitude of the turbulence exceeds that of the magnetic field perturbation, the tearing mode is stable. If this statement is true, a large initial amplitude of turbulent energy K_0 compared with the amplitude of the magnetic field perturbation $B_{0,p}$ must also stabilise the tearing mode. Figure 8.7 presents the results of the reconnection rate obtained

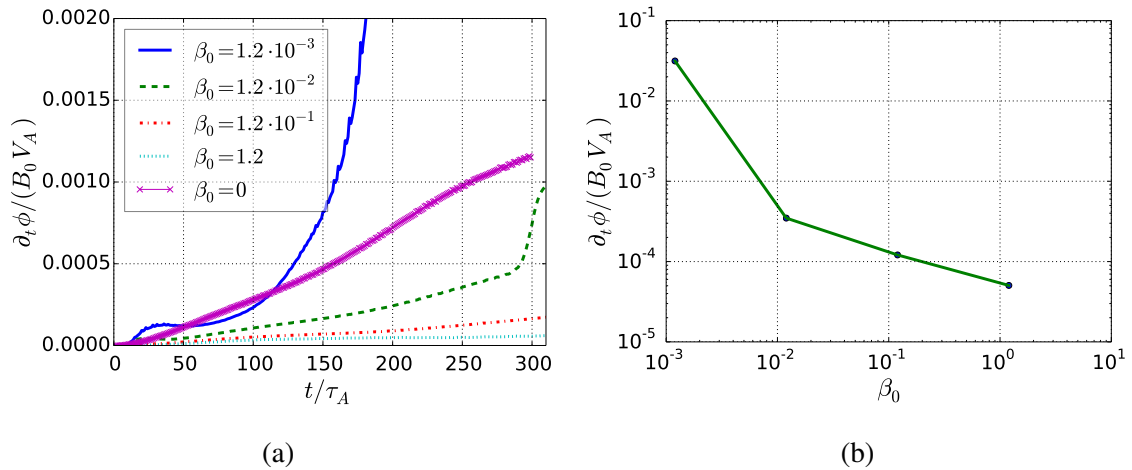


Figure 8.7: Value of the reconnection rate $\partial_t \phi$ as a function of: (a) the time, and (b) the initial amplitude of the turbulent resistivity $\beta_0 = C_\beta \tau K_0$ for an Harris-type current sheet ($B_g = 0$). The initial amplitude of turbulence K_0 is varied and $\tau = 1.3$ is kept constant. Taken from Widmer *et al.*⁹⁴

by keeping the timescale of turbulence constant but varying the initial amplitude of K_0 . The reconnection rate is largely suppressed in case of a large turbulence energy K_0 as for large τ . Both K_0 and τ control the regimes of energy conversion. This is, however, an artefact of the turbulence timescale model which assumes τ as a constant independent of the initial turbulence energy K_0 . To avoid such artefacts, the turbulence timescale has to be determined by turbulence itself rather than being imposed as an external parameter. Such a situation is considered in chapter (9) where the governing equation for the turbulent energy dissipation rate is solved together with the other evolution equations of the turbulence.

8.1.4 Energy Transfer

In the turbulence cascade representation discussed in section (6.1), the turbulence timescale τ_t is written in terms of the energy dissipation rate ε . The latter transports the energy from large scales down to the small scales (figure 6.1) where it can be dissipated due to a finite molecular viscosity (μ) or resistivity (η). Equation (8.13) shows that a large timescale of turbulence implies, for a fixed K_0 , a small ε . In such a situation, only a small portion of the energy is transported to smaller scales. This tiny amount of transported energy results in a small reconnection rate.

For Reynolds-averaged turbulence model used here, the plasma kinetic and magnetic energy transfers are analysed at two different times: i) at the time t_s when the reconnection rate starts to growth, and ii) at the time t_e when the reconnection rate reaches its maximum. Figure 8.8 presents the energy spectra for different parameters τ . Only the results for an Harris-type current sheet with $B_g = 0$ are presented since similar regimes of energy conversion are obtained for the force-free and Harris-type current sheets with guide magnetic field. A larger amount of energy is transferred for $\tau = 1.0$ and 1.3 compared with $\tau = 0.3$ or 1.5 . Three intervals are defined to analyse the plasma kinetic and magnetic

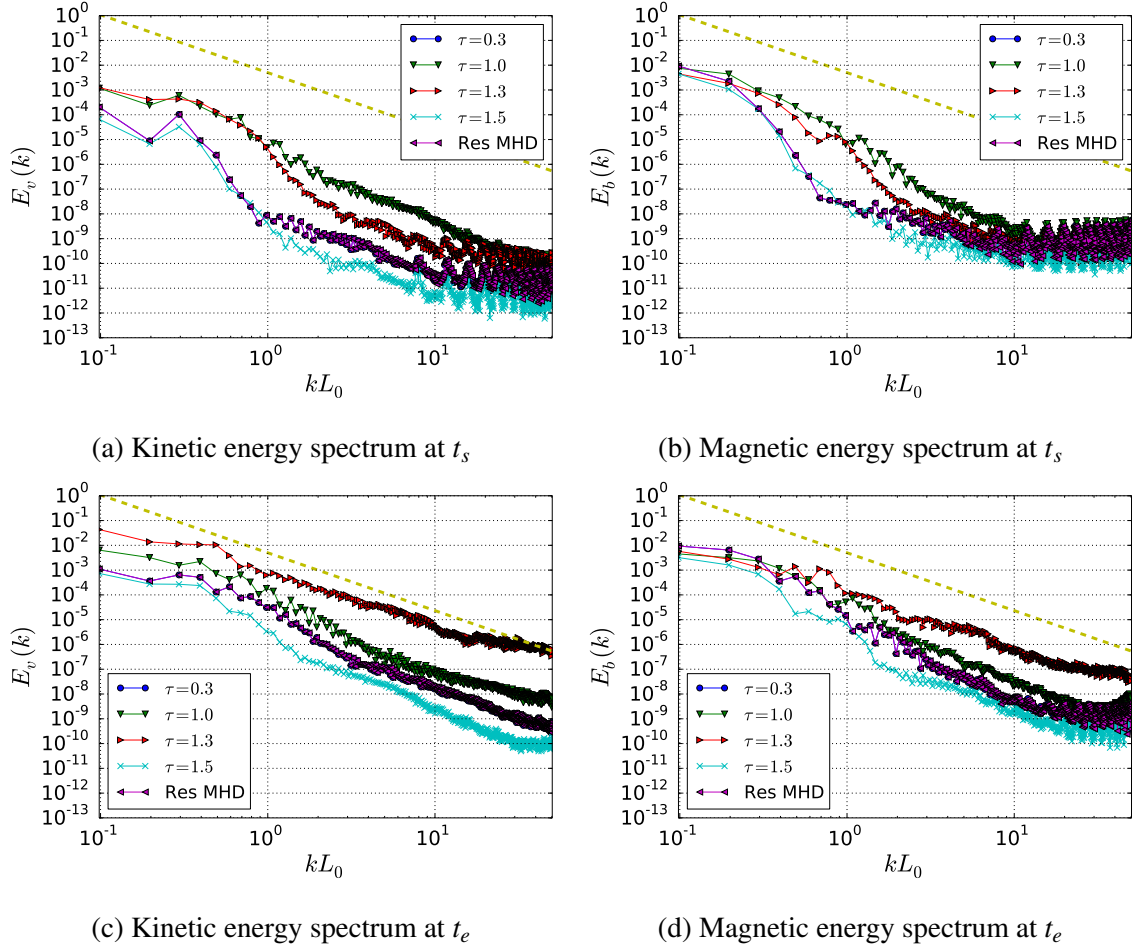


Figure 8.8: The left column represents the kinetic energy spectrum taken at the time the reconnection starts (t_s) and at the time the reconnection rate reaches its maximum value (t_e). The right column corresponds to the magnetic energy spectrum at t_s and t_e . Harris-type current sheets, $B_g = 0$. The dashed line corresponds to a $7/3$ Kolmogorov spectrum. Adapted from Widmer *et al.*⁹⁴

energy transfer: i) $\tau \in [1.0; 1.3]$ which corresponds to the turbulent reconnection regime, ii) $\tau \in]0; 0.5]$ which is the resistive MHD limit with a Sweet-Parker-like rate of energy conversion, and iii) $\tau \in [1.5; \infty[$ which is the turbulent regime limiting the energy transfer.

The interval i) about the turbulent reconnection is now considered. The amount of plasma kinetic energy for $\tau = 1.0$ and 1.3 are of the same order when reconnection starts while the kinetic energy amplitude for $\tau = 1.3$ is approximately two orders of magnitude larger than for $\tau = 1.0$ when the reconnection rate reaches its maximum value. The situation is similar for the magnetic energy. The length of the inertial range is also larger for $\tau = 1.3$ than $\tau = 1.0$.

The intervals ii) and iii) are now discussed. Figure 8.3 shows that a turbulent timescale parameter in the range $]0; 0.5]$ provides a similar value of the reconnection rate as the resistive MHD limit. In terms of energy spectra, exactly the same amount of plasma kinetic (and magnetic) energy is transferred from the injection scale to the dissipation scale for

$\tau = 0.3$ and the resistive MHD limit. This corresponds to the almost identical reconnection rate obtained for $\tau = 0.3$ and the resistive MHD limit. Concerning the last interval, figure 8.8 shows that the amount of energy transferred for $\tau = 1.5$ is even smaller than the resistive MHD limit and that the inertial range length is tiny. In terms of energy dissipation rates ε , a large τ for a fixed K_0 corresponds to a small amplitude of ε . As a result, no energy is dissipated at the small scales, i.e., reconnection does not happen.

A larger inertial range corresponds to an increased resistivity. The inertial range length is larger for the interval corresponding to the turbulent reconnection regime than the laminar or turbulent diffusion limit of energy conversion. Hence, a larger inertial range implies a larger turbulent resistivity β which according to equation (8.32) enhances the reconnection rate. The limit of $\tau = 1.3$ generates, therefore, a larger turbulent resistivity than $\tau = 1.0$. That is the reason why $\tau = 1.3$ corresponds to the largest reconnection rate. The time average of the energy spectra presented in figure 8.9 shows the averaged length of the inertial range in time for $\tau = 0.3, 1.3$ and 1.5 which emphasises that fast reconnection rate obtained by $\tau = 1.3$ is a consequence of a large turbulent resistivity β .

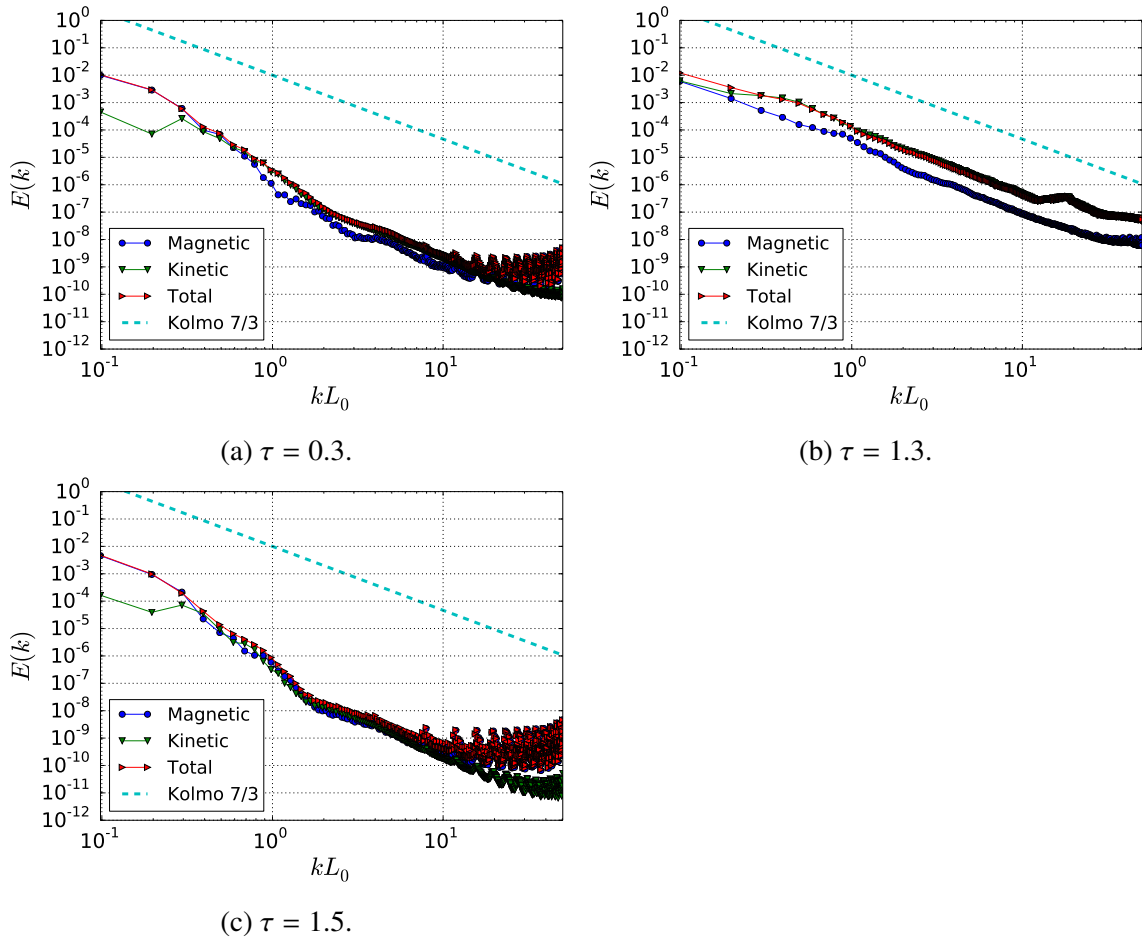


Figure 8.9: Energy spectra averaged in time for the timescales representing the regimes of energy conversion. Harris-type current sheets, $B_g = 0$. The dashed line corresponds to a 7/3 Kolmogorov spectrum. Adapted from Widmer *et al.*⁹⁴

The lifetime of a turbulent eddy was presented to be proportional to its size $\tau \propto \varepsilon^{-1/3} L_e^{2/3}$ [equation (6.10)], i.e., large eddy live longer. From that point of view, $\tau_t \gg \tau_A$ implies that $L_e \gg L_0$ and $\tau_t \ll \tau_A$ gives $L_e \ll L_0$ where L_0 is the current sheet halfwidth. From equation (8.29), $\tau = 1.3$ gives

$$\tau_t \equiv \tau \cdot \tau_0 = 2.4\tau_A, \quad (8.34)$$

which is the timescale required to cross the full current sheet width.^{II} The associated

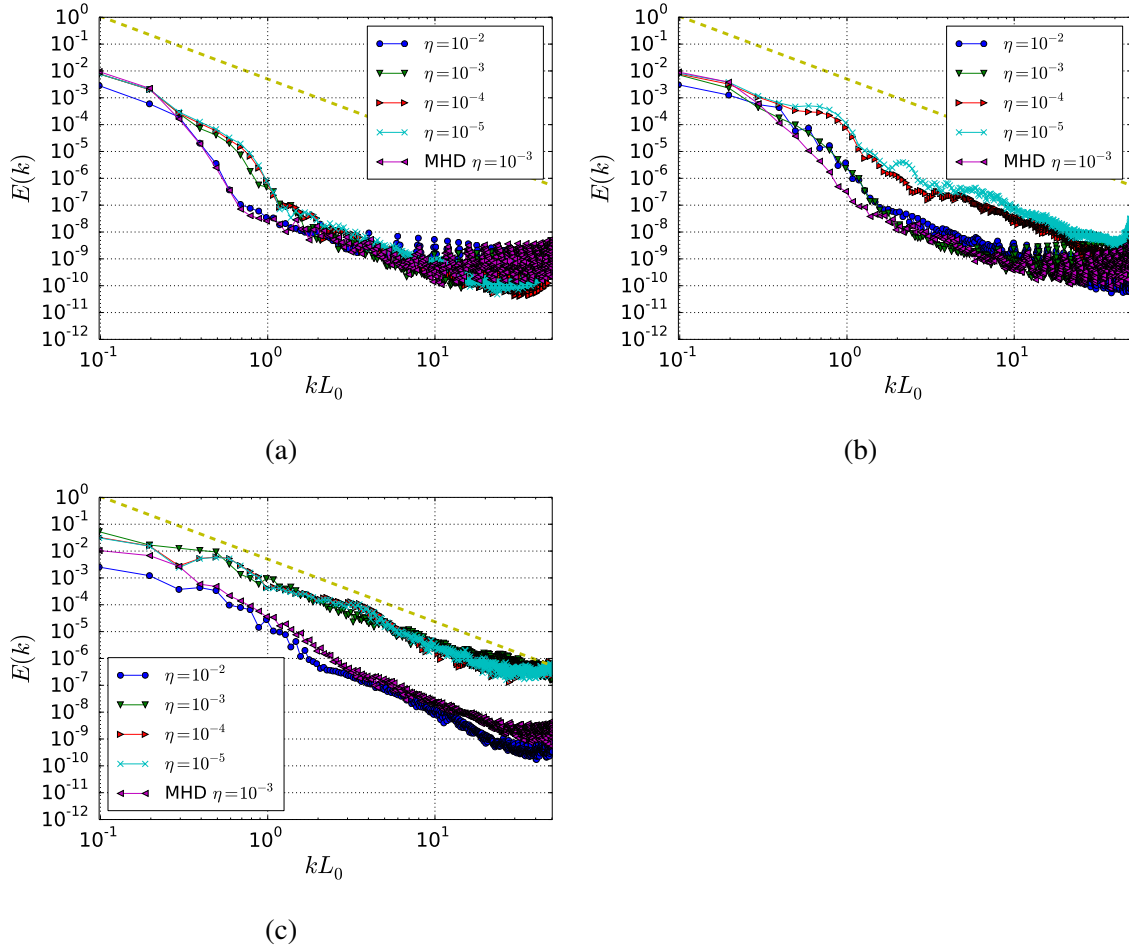


Figure 8.10: Total energy spectrum for various resistivity η taken at: (a) the time t_s that reconnection starts, (b) the time t_m in the middle of the reconnection process and (c) at the time t_e that energy conversion saturation is reached. Harris-type current sheets, $B_g = 0$. The dashed line corresponds to a $7/3$ Kolmogorov spectrum. Adapted from Widmer *et al.*⁹⁴

eddy size is $L_e \cong 2.4L_0 \equiv L_{CS}$ where L_{CS} is the size of the total width of the current sheet. In such a situation, the width of the diffusion region is enhanced by the turbulent eddy and turbulent reconnection can take place. Turbulence is not affecting the diffusion of magnetic energy as long as $L_e \ll L_0$. The reason is that turbulence develops at a scale much smaller than the scale at which the incoming magnetic flux is converted into

II. The normalisation of the Alfvén time is in term of the current sheet halfwidth L_0 : $\tau_A = L_0/V_A$

outflowing flux in the diffusion region. For $L_e \gg L_0$, the incoming magnetic flux cannot reach the current sheet since it encounters turbulence before it. As a result, the internal thermal pressure broadens the current sheet until it reaches the size of the turbulent eddy L_e . In such situations, the amount of energy converted is almost negligible.

A similar investigation is carried out for the variation of the resistivity η . Figure 8.10 presents the amplitude of the plasma kinetic and magnetic energy at three different times defined as: i) the start of reconnection t_s , ii) at time t_m when the reconnection rate has reached the middle point in time between its start and its maximum value, and iii) when reconnection saturates t_e . A resistivity smaller than 10^{-3} has a larger inertial range at the time t_m than for larger values. The effective resistivity due to turbulence (β) has, therefore, a larger amplitude at that time for $\eta < 10^{-3}$. It corresponds to the earlier start of the reconnection process as depicted by figure 8.5a. The saturation of the maximum value reached by the reconnection rate results in an almost similar amount of energy transferred from the large to the small scales for $\eta \leq 10^{-3}$. For a resistivity $\eta = 10^{-2}$, the amount of energy transferred by turbulence is smaller than the resistive MHD limit for $\eta = 10^{-3}$. According to equation (8.32), the reconnection rate is that of the Sweet-Parker model for $\eta \gg \beta$. In such situation, the reconnection rate decreases with the resistivity. The resistive MHD limit with $\eta = 10^{-3}$ attains, therefore, a larger rate of energy conversion than that of the turbulent laminar limit obtained for $\eta \geq 10^{-2}$.

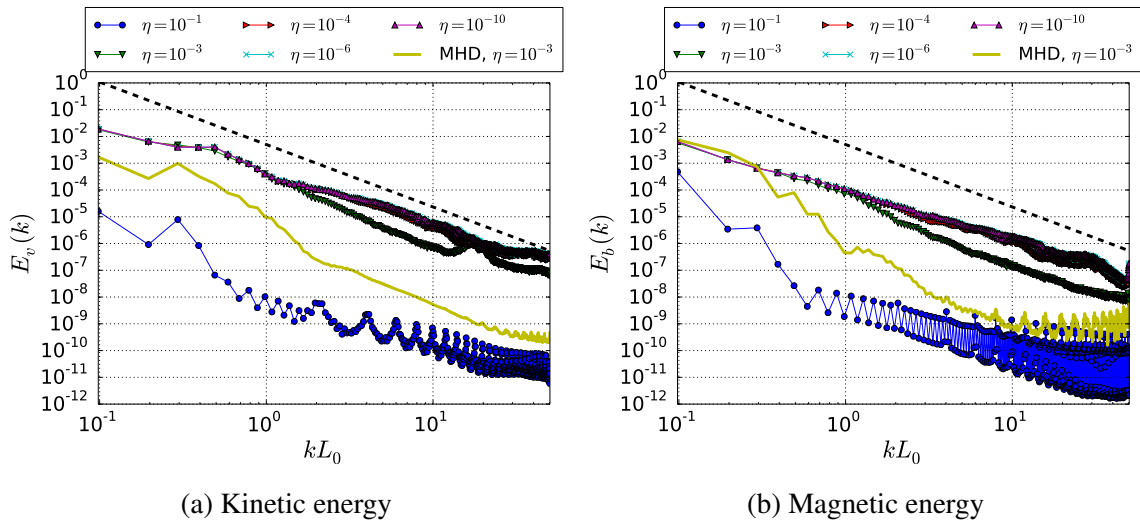


Figure 8.11: Plasma kinetic and magnetic energy spectrum averaged in time for various resistivity η . Harris-type current sheets, $B_g = 0$. The dashed line corresponds to a $7/3$ Kolmogorov spectrum. Taken from Widmer *et al.*⁹⁴

Finally, the saturation of the maximum value that the reconnection can attain as the resistivity decreases (figure 8.5b) is discussed. The time averaged energy spectra are presented in figure 8.11 for various value of the resistivity η . Due to turbulence, the plasma kinetic and magnetic energy transfer is larger for $\eta \leq 10^{-3}$ compared with the resistive MHD limit for $\eta = 10^{-3}$. The inertial range is also broader which is due to an enhanced turbulent resistivity β as already discussed. For a resistivity $\eta = 10^{-1}$, the reconnection process becomes slow Sweet-Parker-like [equation (8.32)] instead of being fast due to turbulence. In such a situation, the resistive MHD limit for $\eta = 10^{-3}$ has

a larger amount of energy transferred to the small scales than for $\eta = 10^{-1}$. The latter reaches a smaller amplitude of the reconnection rate than the former. As a final remark, the comparable amount of energy (plasma kinetic and magnetic) transferred from large to small scales for $\eta \leq 10^{-4}$ corresponds to the saturation of the maximum value reached by the reconnection rate in figure 8.5b. A further decrease of the resistivity does not enhance further the reconnection rate since no more energy can be brought to small scales to be dissipated.

8.1.5 Guide Magnetic Field Effects on Turbulence

The effect a guide magnetic field parallel to the current flow was shown to reduce the maximum reconnection (section (7.4)). From the point of view of mean-field turbulence theory, the alignment of the guide magnetic field with the mean current flow causes a residual helicity H which reduces the efficiency of the turbulent resistivity β (section (4.3.1)). The result of such reduction is a diminished reconnection rate [equation (8.32)]. The influence of the turbulent residual helicity is proportional to the α term [equation (4.56)] whose governing equation is approximated using equation (4.55) as

$$\frac{D\alpha}{Dt} \simeq -\frac{1}{\beta} \mathcal{E}_M \cdot \bar{\mathbf{B}} \simeq \bar{\mathbf{J}} \cdot \bar{\mathbf{B}}. \quad (8.35)$$

For a finite guide field, whether co- or anti-aligned with the mean current density $\bar{\mathbf{J}}$, a residual helicity is produced where

$$\text{sign}(\alpha) = \text{sign}(\bar{\mathbf{J}} \cdot \bar{\mathbf{B}}), \quad (8.36)$$

and the influence of the α term is proportional to that of the guide magnetic field. Figure 8.12 depicts the estimation of the α term by equation (8.35) for the Harris-type with guide magnetic field and the force-free current sheets. The α term increases for a larger guide magnetic field. An interesting point of an Harris equilibrium current sheet is the possibility to reverse the direction of the constant guide magnetic field B_g [equation (8.20)]. That means that the sign of $\bar{\mathbf{J}} \cdot \bar{\mathbf{B}}$ can be positive or negative. Figures 8.12a-8.12b show that the sign of the α term is that of the product $\bar{\mathbf{J}} \cdot \bar{\mathbf{B}}$. In presence of large guide magnetic field, the production of the turbulent resistivity β is given as

$$\frac{1}{\tau_t} \frac{D\beta}{Dt} \simeq -\mathcal{E}_M \cdot \bar{\mathbf{J}} = \beta \bar{\mathbf{J}}^2 - \alpha \bar{\mathbf{J}} \cdot \bar{\mathbf{B}} - \gamma \bar{\boldsymbol{\Omega}} \cdot \bar{\mathbf{J}}. \quad (8.37)$$

Because of equation (8.36), the α term always reduces the amplitude of the turbulent resistivity β . The mean magnetic field can be written in terms of the guide magnetic field as

$$\bar{\mathbf{B}} = \bar{\mathbf{B}}_r \left(1 + \frac{\bar{\mathbf{B}}_g}{|\bar{\mathbf{B}}_r|} \right), \quad (8.38)$$

where $\bar{\mathbf{B}}_r$ refers to the reconnecting magnetic field. A guide magnetic field larger than the reconnecting magnetic field efficiently suppresses the production of turbulence-related resistivity β , reducing in turn its influence on the reconnection process.

The reduction of the reconnection rate in presence of a guide magnetic field can also

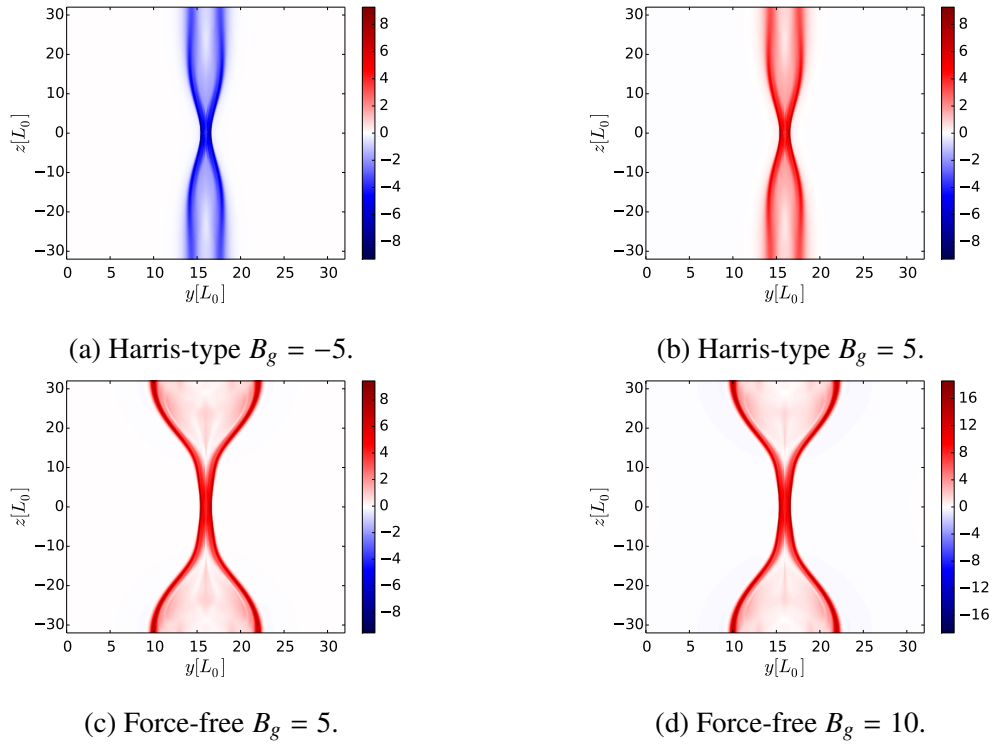


Figure 8.12: Estimated α terms proportional to the residual helicity H for: (a) Harris-type equilibrium with $\overline{\mathbf{J}} \cdot \overline{\mathbf{B}} < 0$, (b) Harris-type equilibrium with $\overline{\mathbf{J}} \cdot \overline{\mathbf{B}} > 0$, (c) force-free equilibrium with $\overline{\mathbf{J}} \cdot \overline{\mathbf{B}} > 0$ and $B_g = 5$ and (d) force-free equilibrium with $\overline{\mathbf{J}} \cdot \overline{\mathbf{B}} > 0$ and $B_g = 10$. Taken from Widmer *et al.*⁹⁴

be seen in equation (8.32). Independent on the direction of the constant magnetic field, the reconnection is reduced by the α term. Figure 8.13 confirms that a guide magnetic field, whether co- or anti-aligned to the mean current flow, produces the same reconnection rate.

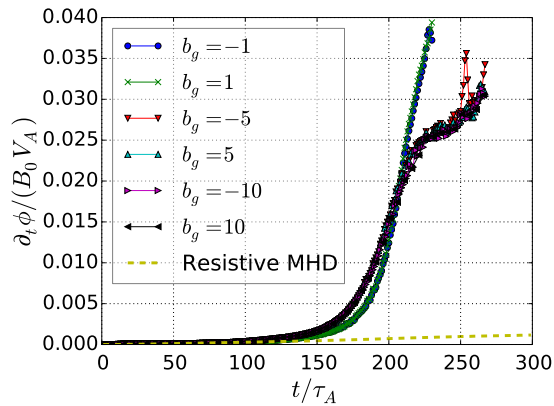


Figure 8.13: Time evolution of the reconnection rate of an Harris-type current sheet equilibrium with constant guide magnetic fields $B_g \equiv b_g$ (as shown in the legend). There is no difference whether the constant finite guide magnetic field is directed parallel (+) or anti-parallel (-) to the mean current. Taken from Widmer *et al.*⁹⁴

8.1.6 Mean-Field Inhomogeneities, Turbulence and Reconnection Rate

The reconnection rate is largely enhanced in the presence of turbulence. According to equations (8.11)-(8.12) the production of turbulence is mainly due to the mean current density $\nabla \times \bar{\mathbf{B}} = \bar{\mathbf{J}}$, the mean vorticity $\nabla \times \bar{\mathbf{V}} = \bar{\boldsymbol{\Omega}}$ and their product. It was shown in the previous section that a decrease of the resistivity η results in an enhancement of the reconnection process. It was argued that this phenomenon is caused by an enhanced turbulence-related resistivity β . According to equation (8.11), an enhancement of β is, for fixed τ , a result of an increased mean current density and vorticity. Figure 8.14 presents the mean current density maximum amplitude $|\bar{\mathbf{J}}|$ and mean vorticity maximum amplitude $|\bar{\boldsymbol{\Omega}}|$ evolution for a resistivity $\eta = 10^{-3}$ and 10^{-6} . The ratio $|\bar{\boldsymbol{\Omega}}|/|\bar{\mathbf{J}}|$ saturates in each equilibrium at a time which corresponds to the maximum possible reconnection rate (figures 8.14a, 8.14c and 8.14e for $\eta = 10^{-3}$). The gradients grow earlier for a smaller resistivity. Since the mean current density and mean vorticity are principal production terms for the turbulence, an earlier growth of these mean-fields also results in an earlier growth of the turbulence energy K and cross-helicity W . Their time evolution is shown at the bottom of figure 8.14. The turbulent energy and the turbulent cross-helicity grow in time as the mean current density and mean vorticity do.

The mean current density and the mean vorticity are due to the gradients of the mean magnetic field $\bar{\mathbf{B}}$ and mean velocity $\bar{\mathbf{V}}$. In section (7.3.1), turbulence was related to the Sweet-Parker reconnection of a long current sheet using the mean-field induction equation for a steady state. This assumption yielded equation (8.32). The mean induction equation is again considered in order to obtain the relation of the mean-fields inhomogeneities and turbulence. Following the argument of Yokoi and Hoshino,⁷⁰ the mean magnetic field $\bar{\mathbf{B}}$ and mean current density $\bar{\mathbf{J}}$ are split into

$$\bar{\mathbf{B}} = \bar{\mathbf{B}}_o + \delta\bar{\mathbf{B}}, \quad \bar{\mathbf{J}} = \bar{\mathbf{J}}_o + \delta\bar{\mathbf{J}}, \quad (8.39)$$

where $\delta\bar{\mathbf{B}}$ is the mean magnetic field induced by the effect of the turbulent cross-helicity W and $\delta\bar{\mathbf{J}} = \nabla \times \delta\bar{\mathbf{B}}$. According to (8.39), the mean-field induction equation [equation (8.3)] is split into a part freed of the cross-helicity effects as

$$\partial_t \bar{\mathbf{B}}_o = \nabla \times (\bar{\mathbf{V}} \times \bar{\mathbf{B}}_o) - \nabla \times (\eta_T (\nabla \times \bar{\mathbf{B}}_o)), \quad (8.40)$$

and a part for the magnetic induction $\delta\bar{\mathbf{B}}$

$$\partial_t \delta\bar{\mathbf{B}} = \nabla \times (\bar{\mathbf{V}} \times \delta\bar{\mathbf{B}}) - \nabla \times [\eta_T (\nabla \times \delta\bar{\mathbf{B}}) - \gamma (\nabla \times \delta\bar{\mathbf{V}})], \quad (8.41)$$

where $\eta_T = \eta + \beta$. In the limit of large Reynolds numbers, a particular solution of equation (8.41) is⁷⁰

$$\delta\bar{\mathbf{B}} = \frac{\gamma}{\beta} \bar{\mathbf{V}} \Rightarrow \frac{\bar{\mathbf{V}}}{\delta\bar{\mathbf{B}}} = \frac{1}{C_w} \frac{K}{W}. \quad (8.42)$$

where $C_w = C_\gamma/C_\beta$ is a constant of order $O(10^{-1})$. Figure 8.14 shows a close relation between the ratio $|\bar{\boldsymbol{\Omega}}|/|\bar{\mathbf{J}}|$ and $|W|/K$.

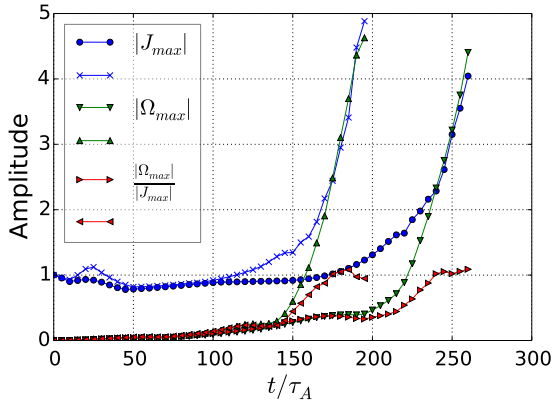
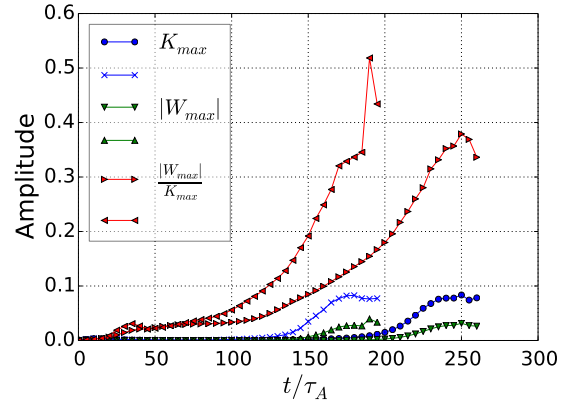
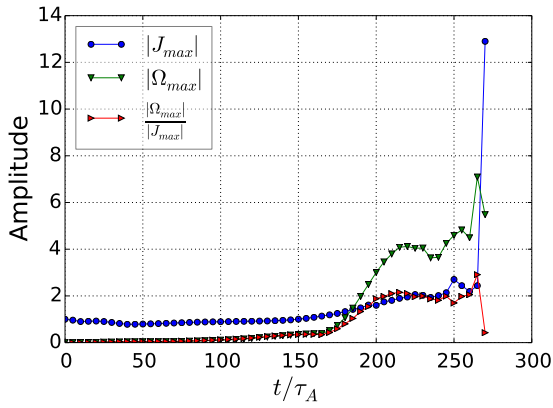
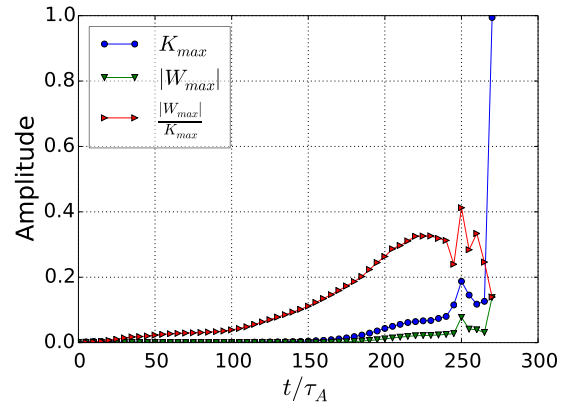
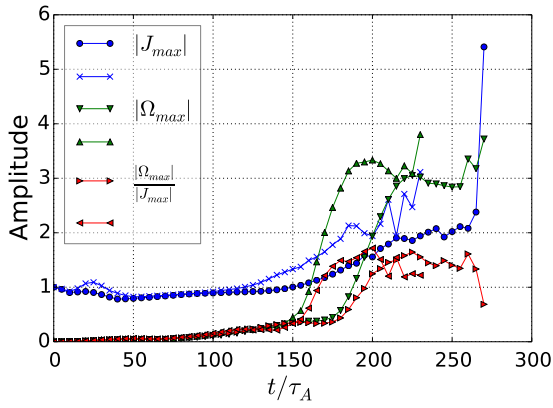
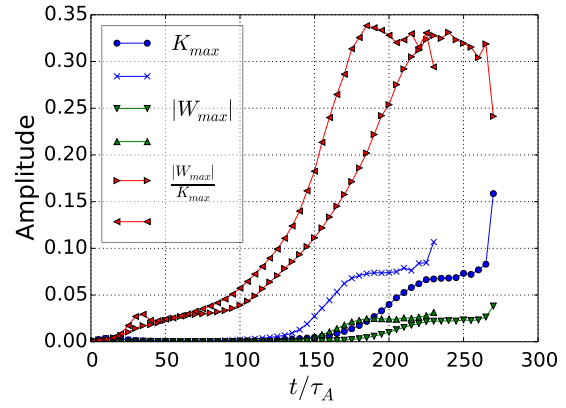

 (a) Harris-type $B_g = 0$.

 (b) Harris-type $B_g = 0$.

 (c) Harris-type $B_g = 5$.

 (d) Harris-type $B_g = 5$.

 (e) Force-free-type $B_g = 5$.

 (f) Force-free-type $B_g = 5$.

Figure 8.14: Figures 8.14a, 8.14c and 8.14e show the time history of the maximum amplitude of the mean current density $|\mathbf{J}|$, mean vorticity $|\boldsymbol{\Omega}|$ and their ratio $|\mathbf{J}|/|\boldsymbol{\Omega}|$ (over-lines are omitted). Figures 8.14b, 8.14d and 8.14f present the maximal amplitude in time of the turbulent energy K and turbulent cross-helicity $|W|$ as well as their ratio $|W|/K$. The results are for the Harris-type current sheet with $B_G = 0$ and 5 and the force-free type current sheet $B_g = 5$. Symbols \bullet , ∇ and \triangleright correspond to $\eta = 10^{-3}$ while \times , \triangle and \triangleleft to $\eta = 10^{-6}$. Figure 8.14a taken from Widmer *et al.*⁹⁴

Since the variation of the magnetic induction $\delta\bar{\mathbf{B}}$ across the current sheet produces $\delta\bar{\mathbf{J}}$ and that the mean velocity variation along the diffusion region causes $\bar{\mathbf{\Omega}}$, the ratio yields

$$\frac{|\bar{\mathbf{\Omega}}|}{|\bar{\mathbf{J}}|} \cong \frac{|\bar{\mathbf{V}}|}{|\delta\bar{\mathbf{B}}|} \frac{\Delta}{L}, \quad (8.43)$$

where Δ and L are the width and the length of the current sheet diffusion region. The relation for the ratios of figure 8.14 is found by inserting equation (8.41) into equation (8.43) as

$$\frac{|\bar{\mathbf{\Omega}}|}{|\bar{\mathbf{J}}|} \cong \left(C_w \frac{|W|}{K} \right)^{-1} \frac{\Delta}{L}. \quad (8.44)$$

Equation (8.44) relates the ratio $|\bar{\mathbf{\Omega}}|/|\bar{\mathbf{J}}|$ to the current sheet aspect ratio diffusion region aspect ratio Δ/L which is a proxy of the Sweet-Parker reconnection rate.

8.2 Importance of the Cross-Helicity Due to Turbulence for Fast Magnetic Reconnection

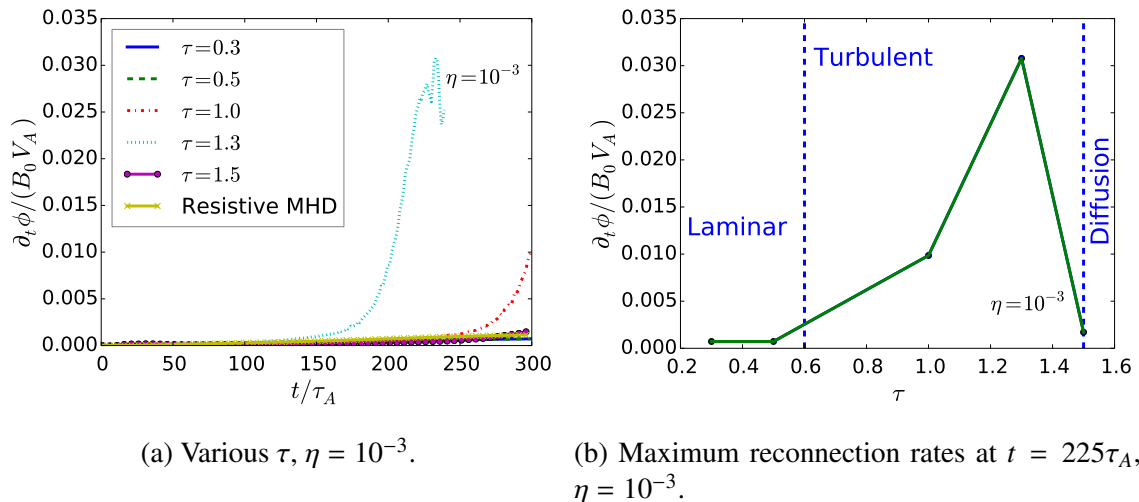


Figure 8.15: Reconnection rate depending on: (a) the time, and (b) the timescale of turbulence τ taken at the time of the first reconnection rate maximal value in figure 8.16a. Case $W \equiv 0$. Harris-type current sheet equilibrium, no constant guide magnetic field ($B_g = 0$).

In the investigation presented in this section, the cross-helicity due to turbulence is set to zero at all time. The reconnection rate is computed as previously for various resistivity and turbulence timescale τ . As shown in figure 8.15, the regimes of energy conversion are still controlled by τ . The maximum reconnection rate is smaller than the value obtained in the presence of turbulence-related cross-helicity. Figure 8.16 presents the value of the reconnection rate as the resistivity is decreased. Similar to the case of non-vanishing turbulent cross-helicity, a smaller amplitude of the resistivity produces an earlier start of reconnection. The maximum reconnection is, however, not larger for a smaller resistivity.

In absence of turbulent cross-helicity, the maximum value that the reconnection rate can reach is smaller than when it is taken into account. This experiment confirms that the action of the turbulent cross-helicity enhances the rate of energy conversion. The reason is that the resistivity is extending around the diffusion region instead of being constrained at its center. As a result, a smaller reconnection angle is formed and the rate of energy conversion is reduced.

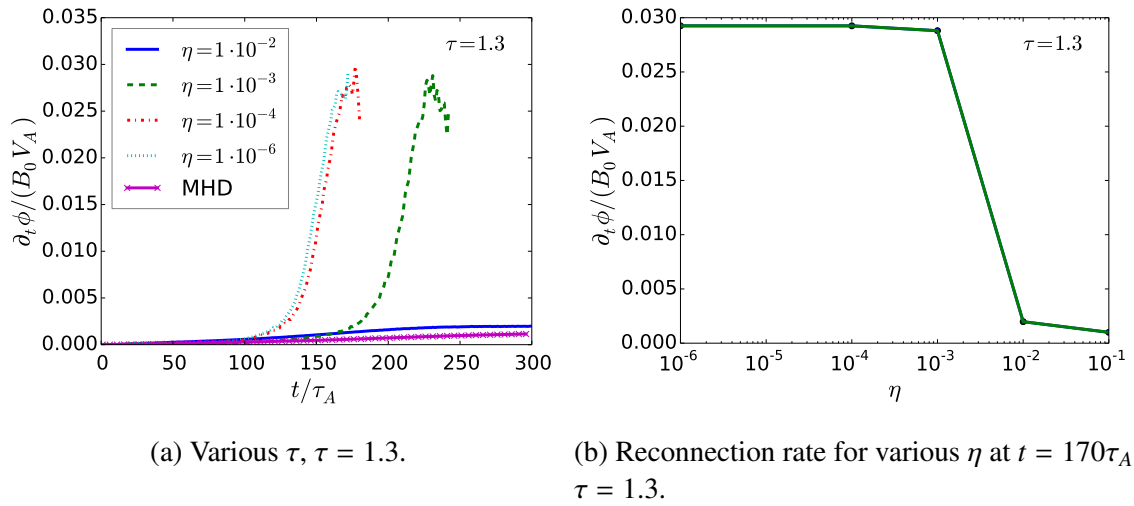


Figure 8.16: Reconnection rate with respect to: (a) the time, and (b) the resistivity taken at the time of the first reconnection rate maximal value in figure 8.16a. Case $W \equiv 0$. Harris-type current sheet $B_g = 0$.

9 Self Consistent Turbulence Timescale

Pleasure in the job puts perfection in the work.

Aristotle.

The simplified approach of a constant turbulent timescale τ_t results in different regimes of energy conversion depending on the initial value of τ_t . Depending on the value of τ_t , magnetic reconnection can be either faster or slower than the case of a resistive MHD flow. The constant- τ_t approach is, however, similar as forcing turbulence externally without letting it to self-adjust. In fact, the timescale of turbulence should be obtained by the dynamic evolution of the turbulence. Its spatio-temporal evolution should either be determined by the transport equation of the timescale or by some quantities representing it. Since the ratio of the turbulence energy to its dissipation rate corresponds to a timescale [equation (8.13)], solving the transport equation of the energy dissipation rate as well as the turbulent energy equation gives the spatio-temporal distribution of the turbulence timescale.

9.1 Energy Dissipation Rate Equation

In addition to the system of mean field MHD equations (8.1)-(8.4), the governing equation for the turbulent energy K , its dissipation rate ε and the turbulent cross-helicity W are solved as

$$\frac{\partial K}{\partial t} = -\bar{\mathbf{V}} \cdot \nabla K - \mathcal{E}_M \cdot \bar{\mathbf{J}} + \frac{\bar{\mathbf{B}}}{\sqrt{\rho}} \cdot \nabla W - \varepsilon, \quad (9.1)$$

$$\frac{\partial W}{\partial t} = -\bar{\mathbf{V}} \cdot \nabla W - \mathcal{E}_M \cdot \bar{\boldsymbol{\Omega}} + \frac{\bar{\mathbf{B}}}{\sqrt{\rho}} \cdot \nabla K - C_W \frac{\varepsilon W}{K}, \quad (9.2)$$

$$\frac{\partial \varepsilon}{\partial t} = -\bar{\mathbf{V}} \cdot \nabla \varepsilon + \frac{\varepsilon}{K} (C_{\varepsilon_1} P_K - C_{\varepsilon_2} \varepsilon + C_{\varepsilon_3} \bar{\mathbf{B}} \cdot \nabla W), \quad (9.3)$$

where \mathcal{E}_M is the turbulent electromotive force [equation (8.7)] and C_{ε_*} model constants of order $\mathcal{O}(1)$.³⁴ They are chosen as $C_{\varepsilon_1} = 1.4$, $C_{\varepsilon_2} = 1.9$ and $C_{\varepsilon_3} = 1.0$ according to TSDIA. The symbol P_K is the turbulent energy production mechanism given as

$$P_K = \frac{K}{\varepsilon} \left(C_{\beta K} \frac{\bar{\mathbf{J}}^2}{\rho} - C_{\gamma W} \frac{\bar{\boldsymbol{\Omega}} \cdot \bar{\mathbf{J}}}{\sqrt{\rho}} \right). \quad (9.4)$$

The purpose of solving equation (9.3) in addition to equations (9.1)-(9.2) and the mean field MHD equations (8.1)-(8.4) is to test the validity of the regimes of reconnection found in the previous chapter in the constant- τ approximation. Since they were obtained whatever the initial current sheet configuration used, the results for the case of an Harris-type current sheet are shown here. The initial conditions for the mean velocity field $\bar{\mathbf{V}}$, the mean magnetic field $\bar{\mathbf{B}}$ and the mean internal energy \bar{h} are given by equations (8.18)-(8.21). The constant guide magnetic field is set to zero. The initial perturbation $B_{0,p}$ is the same as equation (8.17) but its amplitude is, however, larger in order to initiate the reconnection process earlier. The initial amplitude of the turbulent energy K_0 , its dissipation rate ε_0 and the turbulent cross-helicity W_0 are given as

$$K_0 = K_{init}, \quad (9.5)$$

$$W_0 = 0, \quad (9.6)$$

$$\varepsilon_0 = \sqrt{C_\beta} K_0 |\bar{\mathbf{J}}_0|, \quad (9.7)$$

where $\bar{\mathbf{J}}_0 = \nabla \times \bar{\mathbf{B}}_0$ and ε_0 is obtained from the initial balance of turbulence $P_{K_0} - \varepsilon_0 = 0$. Here P_{K_0} is the initial turbulent energy production given by

$$P_{K_0} = \frac{C_\beta K^2 \bar{\mathbf{J}}^2}{\varepsilon_0 \rho}. \quad (9.8)$$

Figure 9.1 depicts the spatial distribution of the mean current density $\bar{\mathbf{J}}$, the mean vorticity $\bar{\boldsymbol{\Omega}}$, the turbulent cross-helicity W , the turbulent energy K , its dissipation rate ε and the turbulence timescale τ estimated from the evolution of K and ε . The turbulent energy dissipation rate ε is finite at and around the diffusion region where the turbulent energy K is maximum. The location where ε is finite also represents the region in which the large scale magnetic field energy is transported to smaller scales where it can be dissipated. The timescale of turbulence τ is also maximum near the diffusion region and it is in the range [1.2;1.4]. This range corresponds to the regime of fast turbulent reconnection obtained for a constant turbulence timescale in section (8.1.2).^{94,98}

The regimes of energy conversion were obtained by varying the turbulence timescale parameter $\tau_t \equiv K/\varepsilon$ or the initial turbulent energy amplitude K_0 . In this context, solely the initial amplitude of the turbulent energy K_{init} can be varied since the constant C_β is determined by the TSDIA formalism. Also, the current density amplitude is determined by the Harris-type current sheet initialisation. Figure 9.2 presents the time evolution of the reconnection rate as K_{init} is varied for a resistivity $\eta = 10^{-2}$. Turbulence produces fast reconnection in comparison to the resistive MHD regime. Contrary to the results obtained for a constant timescale parameter τ_t , only *fast turbulent reconnection* is obtained. In fact, the other regimes of energy conversion defined as *laminar* and *turbulent diffusion*,^{94,98} are artefacts of the simplified constant- τ algebraic turbulence timescale approach. The turbulent energy governing equation can be written as [equation (4.27)]

$$\frac{DK}{Dt} = \underbrace{\tau_t \left(C_\beta K \frac{\bar{\mathbf{J}}^2}{\rho} - C_\gamma W \frac{\bar{\mathbf{J}} \cdot \bar{\boldsymbol{\Omega}}}{\sqrt{\rho}} \right)}_{P_K} - \underbrace{\frac{K}{\tau_t}}_{\varepsilon_K} + \underbrace{\frac{\bar{\mathbf{B}}}{\sqrt{\rho}} \cdot \nabla W}_{T_K} \quad (9.9)$$

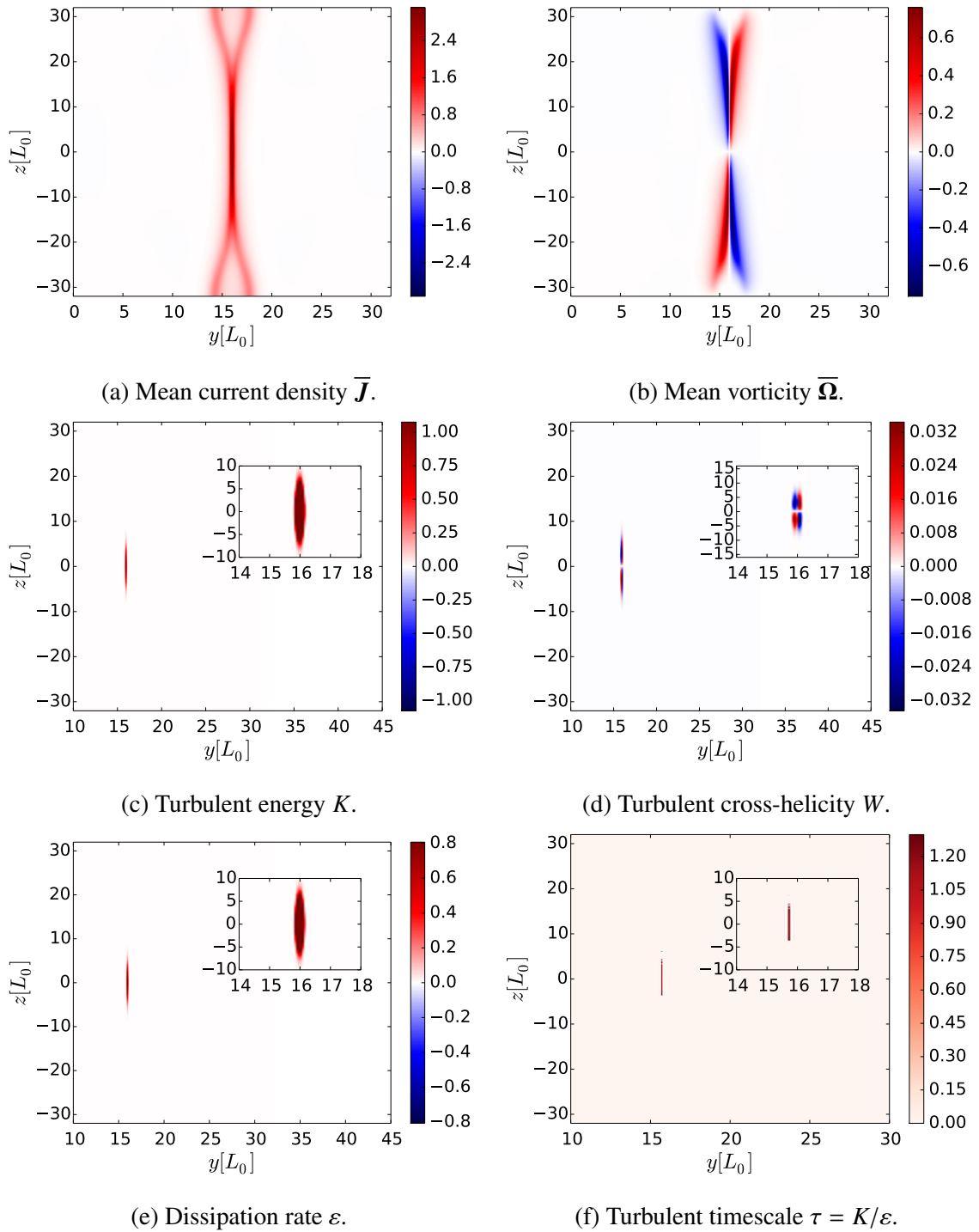


Figure 9.1: Spatial distribution of the mean current density $\bar{\mathbf{J}}$, the mean vorticity $\bar{\boldsymbol{\Omega}}$, the turbulent energy K , its dissipation rate ε , the turbulent cross-helicity W and the turbulent timescale $\tau = K/\varepsilon$ at the time the reconnection rate reaches its maximum ($t = 50\tau_A$). The resistivity is $\eta = 10^{-3}$.

where $\tau_t \equiv K/\varepsilon$, P_K is the production rate of the turbulent energy, ε_K its dissipation rate and T_K its transport term. The latter does not contribute to the turbulent energy dissipation or production unless energy is gained or lost from the boundaries. Using τ_t as an input parameter, its value is fixed during the whole current sheet evolution. The limit $\tau_t \gg 1$ produces a large amount of turbulence constantly. In such a situation, $\varepsilon_K \ll P_K$ and no process is able to transport the energy due to turbulence down to smaller scales where it can be dissipated. In the limit $\tau_t \ll 1$, $P_K \ll \varepsilon_K$ and the turbulent energy dissipation rate inhibits turbulence to grow. As a result, the system behaves like in the resistive MHD limit. In fact, turbulence increases the initial mean thermal pressure \bar{p}_{th} which in a current sheet equilibrium is given by

$$\bar{p}_{th} = 1 + \beta_p + \overline{\mathbf{B}}^2 + K_{mag}, \quad (9.10)$$

where β_p is the plasma beta and K_{mag} is the turbulent energy due to the magnetic field fluctuations only since $\overline{\mathbf{V}} = 0$ initially. As plasma is flowing at both sides current sheet which has reached a steady state, the mean thermal force $\nabla \bar{p}_{th}$ compensates the mean Lorentz force due to turbulence, i.e., $-\nabla \bar{p}_{th} \approx \overline{\mathbf{J}} \times \overline{\mathbf{B}}$. The Lorentz force derived from the mean fields is

$$\overline{\mathbf{J}} \times \overline{\mathbf{B}} = \frac{1}{\eta + \beta} \left(-(\overline{\mathbf{V}} \times \overline{\mathbf{B}}) \times \overline{\mathbf{B}} + \overline{\mathbf{E}} \times \overline{\mathbf{B}} + \gamma \overline{\boldsymbol{\Omega}} \times \overline{\mathbf{B}} \right). \quad (9.11)$$

Figure 9.3 is a schematic representation of the mean-field forces in a current sheet equilibrium. A moderate amplitude of turbulence results in an broadening of the current sheet around the ‘X’-point. As turbulence is increased by a large τ or K_0 , the thermal pressure increases while the Lorentz force is reduced and the current sheet broadens further. In the limit $\tau \ll \tau_A$ (or small K_0), the thermal- and Lorentz forces are the same as in the resistive MHD limit. These limits are, however, not obtained when the turbulence timescale is determined by the turbulence dynamics.

Hence, from the mean-field-turbulence-model viewpoint, only the limit of fast recon-

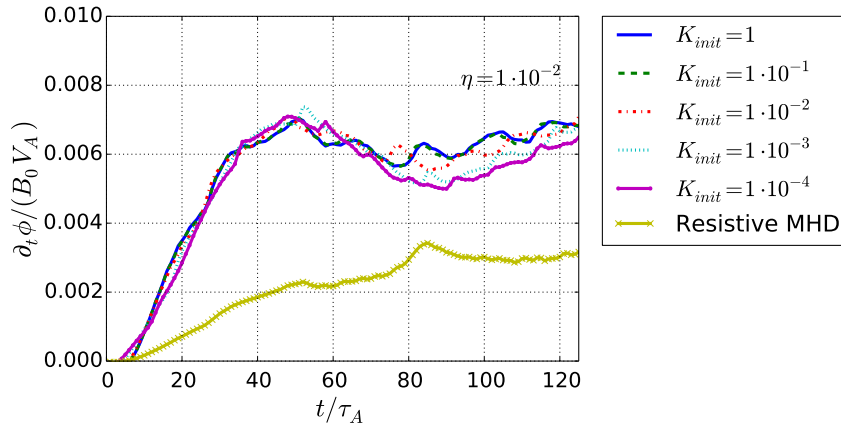


Figure 9.2: Time history of the reconnection rate for different initial values of the turbulent energy K_{init} . Magnetic resistivity is $\eta = 10^{-2}$.

I. Here τ_t is normalized to the Alfvén time and τ_A is normalized to the current sheet halfwidth L_0 .

nection is always obtained. The turbulent energy K and its dissipation rate ε are of the same order and the turbulence timescale is of the order of the time needed by an Alfvén wave to cross the current sheet width. As a result, the current sheet broadens due to the thermal pressure force while the Lorentz force due to the incoming magnetic flux is reduced. As a result, the rate of energy conversion is enhanced.

In the Kolmogorov picture of turbulence, the size of an eddy is proportional to the turbulence timescale τ_t [equation (6.10)]. In section (8.1.2), it was found that $\tau_t \approx 2.3\tau_A$ for which the associated eddy size is a bit larger than the current sheet width L_{CS} . Since, as it is shown in this section, only $\tau_t \approx 2\tau_A$ is reached, the turbulent eddy size is just a bit larger than the current sheet width which corresponds to fast reconnection.

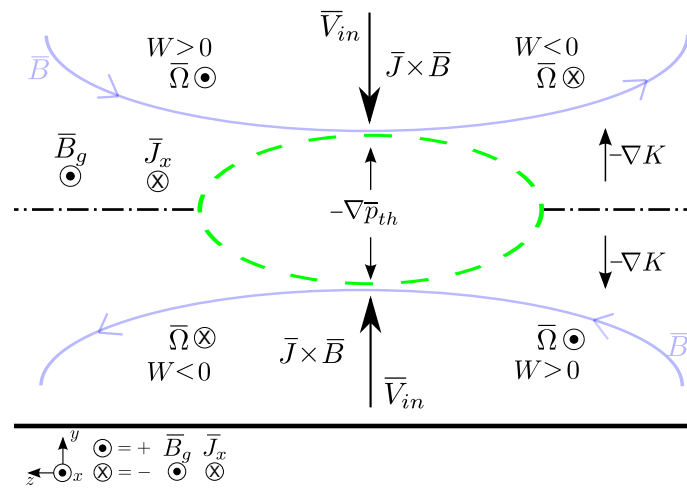


Figure 9.3: Schematics of the mean forces balance for a current sheet equilibrium. The symbol $\nabla \bar{p}_{th}$ denotes the mean thermal pressure force and $\vec{J} \times \vec{B}$ the mean Lorentz force. The negative gradient of the turbulent energy ∇K increases towards the inflow regions. A large turbulent energy gradient enhances the mean thermal pressure while a large K reduces the mean Lorentz force. The current sheet width is then enlarged by turbulence until reconnection becomes fast. The dashed-dotted line represents the symmetry line across the ‘X’-point along the current sheet and the dashed ellipse symbolizes the diffusion region.

10 Influence of Turbulence on the Plasmoid Instability

It doesn't matter how beautiful your theory is, it doesn't matter how smart you are. If it doesn't agree with experiment, it's wrong.

Richard Feynman

10.1 Introduction

A possible almost ideal MHD mechanism to reach fast reconnection is the plasmoid instability of current sheet for large-Lundquist-number-plasmas. The Lundquist number $S = LV_A/\eta$ (magnetic-Reynolds-number for $V = V_A$) provides an approximated threshold $S_{crit} \sim 10^4$ above which a Harris-type current sheet becomes unstable (section (7.5.2)).⁹⁵ Resistive MHD simulations of high-Lundquist -number-plasmas current sheets revealed the unstable growth of small magnetic islands due to reconnection of thin current sheets.^{50,52,102} While the linear growth phase is a tearing-like instability,⁴⁸ the physical role of plasmoids during the non-linear phase of reconnection is not well understood. Daughton *et al.*¹⁰³ proposed that the global reconnection rate is described by an ensemble of N_p small scale current sheets (or plasmoids). Each of them has a length $L_p \sim L/N_p$ and width $\delta_p \sim \delta/\sqrt{N_p}$ where L and δ are the global length and width of the macroscopic diffusion region. In such configurations, the global reconnection rate is enhanced by a factor $\sqrt{N_p}$ above the Sweet-Parker rate. In the following section, the non-linear phase of plasmoid reconnection is investigated by means of turbulence models.

The plasmoid instability repeatedly brakes a long current sheet into smaller ones, creating magnetic island-like structures at small scales. At each small-scale reconnection site, a large angle of reconnection between the incoming and reconnecting magnetic field is created (see [equation (7.9)]). The current density and the vorticity are enhanced near the small scales diffusion regions. As described previously (chapter (8)), increased velocities and magnetic field gradients can enhance the reconnection rate through turbulence [equation (8.44)]. The turbulent energy (K) produced at and around the diffusion region has similar properties to an anomalous resistivity (section (7.3.2)). Its strength is maximum at the center of the diffusion region and diminishes away from it. The energy of the turbulence decreases faster across the current sheet layer than along it. This is a consequence of the quadrupolar turbulent cross-helicity about the sides of the current sheet

diffusion region (section (4.3.1)). The inhomogeneous distribution of the turbulent energy produces, therefore, an ‘X’-point reconnection region. The latter has been shown to enhance the reconnection rate above a Sweet-Parker to a Petschek rate.⁴¹ The difference between Sweet-Parker- and Petschek-like reconnection rate is due to the localisation of the anomalous resistivity.²¹

At large-Lundquist-numbers, the plasmoid-unstable current sheet reconnection rate is independent on the resistivity.^{52,104} At the same time, high-Lundquist-number-plasmas are prone to turbulence.^{56,58} Turbulence might, therefore, play a key role in enhancing reconnection in the course of the non-linear evolution of the plasmoid instability, while the saturation of the instability at large-Lundquist-numbers can be due to the saturation of the turbulent energy at the ‘X’-points. In fact, as shown in section (9.1), turbulence can enlarge the diffusion region width by increasing the thermal pressure inside the current sheet. As a result, the rate of energy conversion can be enhanced.¹

The plasmoid instability is independent on the presence of a finite guide magnetic field parallel to the mean current flow. In this chapter, the plasmoid instability is used to investigate the influence of turbulence on reconnection. In particular, the physics of plasmoid reconnection is tested through the extension of the Reynolds-averaged turbulence model (section (4.2.1)) to a subgrid-scale (SGS) model of turbulence. The question of the applicability of the non-linear SGS model (section (5.2)) to the reconnection process is also addressed in the following.

Part of the results of this chapter are taken from a work submitted for publication in *Physics of Plasmas*: "Turbulent Plasmoid Reconnection". The submitted version is available on the *arXiv*.⁷¹ This concerns section (10.2), section (10.4.2) and section (10.5). The text is different but certain figures are the same. When it is the case, the citation related to the submitted version of the paper which is available on the *arXiv* is given. The discussion about the turbulent stress-tensor in section (10.4.2) is not at all considered in the submitted paper.

10.2 High Resolution Simulations of Plasmoid-Unstable Current Sheets

High resolution direct numerical resistive MHD simulations (DNS) are performed in 2.5 dimensions to investigate the influence of turbulence on plasmoid-unstable current sheets. The DNSs are carried out for both Harris-type and force-free current sheets equilibria. The former is simulated with or without a constant guide magnetic field parallel to the current flow [equation (10.6)] while the latter has a non-constant guide magnetic field with an additional constant magnetic field [equation (10.8)]. The equations solved by the

I. See the discussion about the mean-field force balance in a current sheet given at the end of section (9.1).

DNSs are

$$\frac{\partial \rho}{\partial t} = -\nabla \cdot (\rho \mathbf{V}), \quad (10.1)$$

$$\frac{\partial \rho \mathbf{V}}{\partial t} = -\nabla \cdot \left[\rho \mathbf{V} \otimes \mathbf{V} + \frac{1}{2} (p + B^2) \mathbf{I} - \mathbf{B} \otimes \mathbf{B} \right] + \chi \nabla^2 (\rho \mathbf{V}), \quad (10.2)$$

$$\frac{\partial \mathbf{B}}{\partial t} = \nabla \times (\mathbf{V} \times \mathbf{B}) + \eta \nabla^2 \mathbf{B}, \quad (10.3)$$

$$\frac{\partial h}{\partial t} = -\nabla \cdot (h \mathbf{V}) + \frac{\gamma_0 - 1}{\gamma_0 h^{\gamma_0 - 1}} (\eta \mathbf{J}^2) + \chi \nabla^2 h, \quad (10.4)$$

where the χ parameter determines the amplitude of the local smoothing sometimes locally applied for numerical stability without increasing the grid resolution (see appendix (A.2)). The mass density, the velocity and magnetic field are denoted by ρ , \mathbf{V} and \mathbf{B} . The symbol h represents the internal energy related to the thermal pressure by the equation of state $p_{th} = 2h^{\gamma_0}$ [equations (3.9)-(3.10)]. Since adiabatic conditions are assumed, the ratio of specific heat gives $\gamma_0 = C_v/C_p = 5/3$. The current density is obtained by the Ampère's law $\mathbf{J} = \nabla \times \mathbf{B}$. Equations (10.1)-(10.4) are written in normalised units (see appendix (A.1)). A pair of current sheets is initialised in order to use periodic boundary conditions. The current sheets are lying in the $y \times z$ plane, the direction across the current sheet is given by the unity vector \mathbf{e}_y while \mathbf{e}_z is directed along it. The direction \mathbf{e}_x is perpendicular to the plane of reconnection, i.e., parallel to the mean initial current flow. The mean electric field is given by the Ohm's law of resistive MHD:

$$\mathbf{E} = -\mathbf{V} \times \mathbf{B} + \eta \mathbf{J}. \quad (10.5)$$

The initial conditions for the Harris-type current sheets are

$$\mathbf{B} = B_g \mathbf{e}_x + B_0 (\tanh(y+d) - \tanh(y-d) - 1) \mathbf{e}_z, \quad (10.6)$$

$$h = \frac{1}{2} (1 + \beta_p - B^2 \mathbf{e}_z)^{1/\gamma_0}, \quad (10.7)$$

while they are given for the force-free current sheet as

$$\mathbf{B} = B_0 \sqrt{B_g^2 + \cosh^2(y+d) + \cosh^2(y-d)} \mathbf{e}_x + B_0 (\tanh(y+d) - \tanh(y-d) - 1) \mathbf{e}_z, \quad (10.8)$$

$$h = \frac{1}{2} (\beta_p)^{1/\gamma_0}, \quad (10.9)$$

where $B_g = |\mathbf{B}_g|/|\mathbf{B}_0|$ is the constant guide magnetic field normalised to the initial amplitude of the reconnecting magnetic field. The initial amplitude of the mass density, the velocity flow and the magnetic field are $\rho_0 = 1$, $\mathbf{V}_0 = 0$ and $B_0 = 1$. In order to let the instability to develop within short time, the plasmoids are triggered in a broad range of spatial frequencies as

$$\mathbf{B}_p = B_{0,p} \sum_{k=1}^{128} \xi_1 \sin \left(2\pi k \left(\frac{z}{L_z} + \xi_2 \right) \right) \mathbf{e}_y, \quad (10.10)$$

where L_z is a normalizing length scale in the e_z direction and $B_{0,p}$ is the initial perturbation amplitude set to 0.01. The parameters $\xi_{1,2}$ are random numbers in the range $[0,1]$. The box size is $L_x \times L_y \times L_z = 0.4 \times 80 \times 320 L_0^3$ for a resolution of $4 \times 3200 \times 12800$ grid points.

A finite grid resolution does not allow to follow the evolution of plasmoids over all scales down to a scale limited by the chosen resistivity η . Turbulence is then split off the mean variables by means of a Gaussian filter.^{24,26} Two turbulence models are compared concerning their information about the fluctuation amplitude during the non-linear phase of the plasmoid reconnection: i) the mean-field averaged turbulence model described in section (4.2.1) and ii) the non-linear SGS model presented in chapter (5). Since a Gaussian filter does not strictly fulfill the Reynolds rules [equations (4.4)-(4.6)], the mean-field model is extended to a SGS turbulence model. Such an extended mean-field turbulence model is valid if

$$\overline{\mathbf{f}^F} - \overline{\mathbf{f}}^F \approx 0, \quad (10.11)$$

where \mathbf{f} is any MHD field resolved by the DNS and $\overline{\mathbf{f}}^F$ is its filtered counterpart. The filter width is chosen such that equation (10.11) is almost satisfied (see appendix (D)).

10.2.1 Plasmoid Instability Reconnection Rate

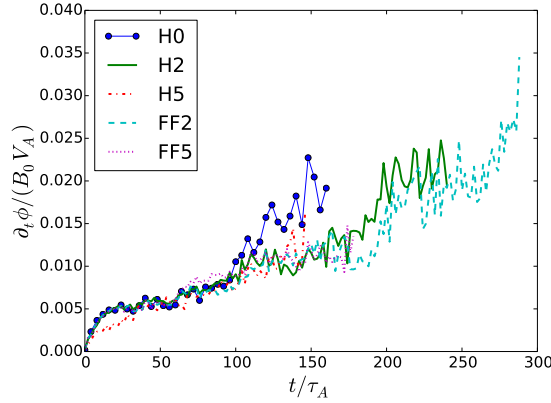


Figure 10.1: Time history of the plasmoid instability reconnection rate for: Harris-type CS $b_g = 0$ (H0), Harris-type CS $b_g = 2$ (H2), Harris-type CS $b_g = 5$ (H5), force-free CS $b_g = 2$ (FF2) and force-free CS $b_g = 5$ (FF5). Taken from Widmer *et al.*⁷¹

The dynamical evolution of the current sheet instability as well as the appearance of many reconnection sites render difficult the computation of the reconnection rate in terms of the integrated magnetic flux [equation (8.30)]. The reconnection rate is, therefore, quantified by means of the vector potential \mathbf{A} as $\mathbf{B} = \nabla \times \mathbf{A}$. For the present 2.5D geometry, e_x is the ignorable dimension in terms of vanishing spatial derivatives. In terms of the vector potential \mathbf{A} , the amount of reconnected flux $\phi(t)$ is

$$\phi(t) = \int_{z_o}^{z_x} B(x, t) e_y dz = [A(x = z_x, t) - A(x = z_o, t)] e_x, \quad (10.12)$$

where z_x is the center of a reconnection region ('X'-point) and z_o the center of a magnetic island. The reconnection rate is given by the time derivative of equation (10.12) as

$$\partial_t \phi(t) = - \int_{z_o}^{z_x} \partial_z [E(\mathbf{x}, t) \mathbf{e}_x] dz = \partial_t [A(\mathbf{x} = z_x, t) - A(\mathbf{x} = z_o, t)] \mathbf{e}_x, \quad (10.13)$$

where $E\mathbf{e}_x$ is the electric field perpendicular to the reconnection plane as obtained using equation (3.2). A local maximum of $A\mathbf{e}_x$ is, therefore, the location a magnetic island center ('O'-point) while a local minimum corresponds to an 'X'-point. By means of the vector potential A , the position of an 'X'-point can be determined and the reconnection rate is computed by equation (10.13) solved for all reconnection sites. Figure 10.1 presents the time history of the reconnection rate for various equilibria. The reconnection rate is the same for all equilibria during the first $t = 100\tau_A$. A larger reconnection rate is reached by the Harris-type current sheet equilibrium without constant guide magnetic field compared with finite guide magnetic field equilibria. It takes approximately $t = 100\tau_A$ for the reconnection rate in presence of a guide magnetic field to reach a value comparable with the Harris-type current sheet case.

Figure 10.2 depicts the spatial distribution of the magnetic field and the velocity flow for the Harris-type current sheet without constant guide magnetic field as well as for the force-free current sheet with a constant guide magnetic field strength $B_g = 2$ at $t = 100\tau_A$. The outflow velocity $V\mathbf{e}_z$ reaches a value near the Alfvén speed V_A for the Harris-type current sheet while it attains only eighty percent of it for the force-free current sheet.^{II} The largest outflow velocities are found to be located near the smallest magnetic islands. Note that the force-free current sheet holds less small magnetic islands than the non-guide field Harris-type current sheet. The finite non-zero magnetic field amplitude $|\mathbf{B}|$ is due to the out-of-plane finite guide magnetic field.

As presented in section (7.4), the reconnection rate estimated using the Lorentz force as a proxy is reduced by a guide magnetic field parallel to the current flow as

$$M_{A,B_g} = M_A \frac{B_z^2}{B_x^2 + B_z^2}, \quad (10.14)$$

where $B_x = B\mathbf{e}_x$ is the magnetic field component perpendicular to the reconnection plane and $B_z = B\mathbf{e}_z$ the reconnecting magnetic field. M_A is the reconnection rate in the absence of a magnetic field component parallel to the current flow direction. A guide magnetic field larger than the reconnecting magnetic field decreases the reconnection rate. The smaller reconnection angle in the case of guide field reconnection reduces the current density and vorticity around the 'X'-points of reconnection. Figure 10.3 depicts the spatial distribution of the current density \mathbf{J} and the vorticity $\mathbf{\Omega}$ for the Harris-type and force-free current sheet models. The amplitude of \mathbf{J} and $\mathbf{\Omega}$ are larger for the Harris-type ($B_g = 0$) current sheet without a constant guide magnetic field than the force-free ($B_g = 2$) current sheet. It is in the vicinity of the smallest magnetic structures that the amplitude of \mathbf{J} and $\mathbf{\Omega}$ are the strongest. The smaller reconnection rates can be due to: i) large magnetic structures that appear to be favored over the small ones, and ii) the formation of less plasmoids. The reconnection rate would be reduced in case i) because the angle of

II. The velocity is normalised to the Alfvén speed

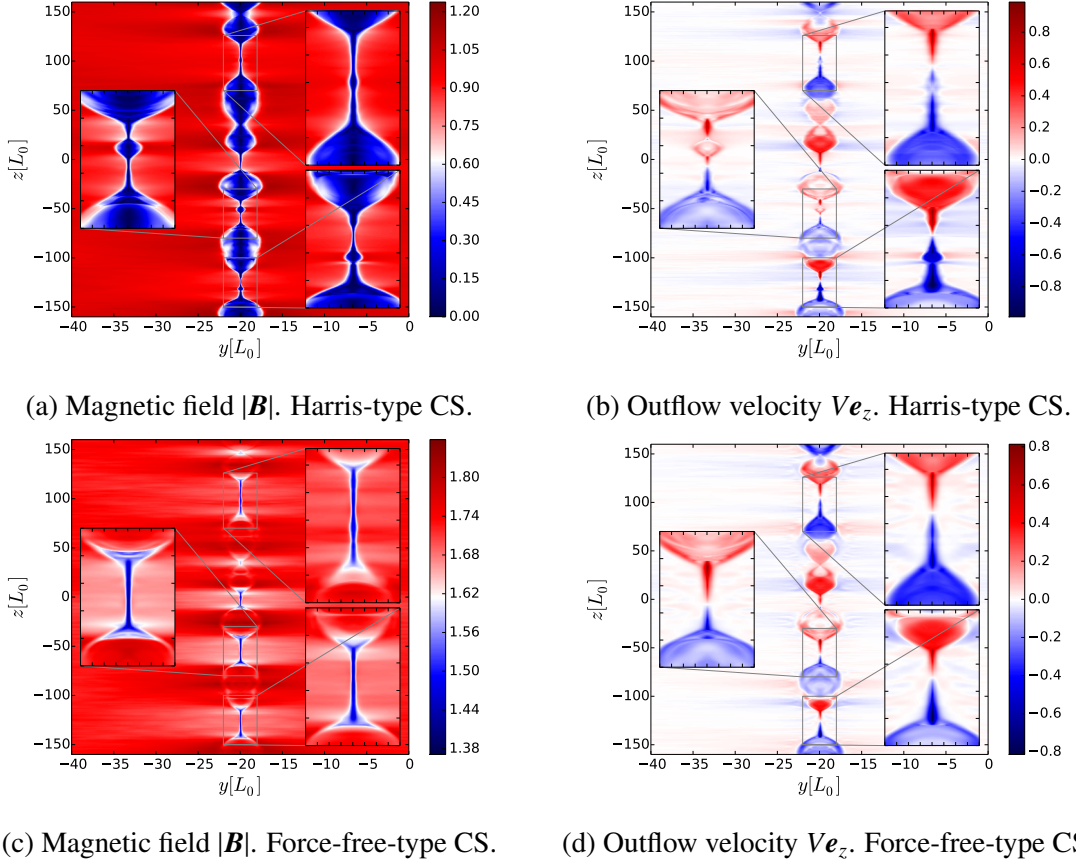


Figure 10.2: Spatial distribution of the magnetic field and velocity flow at $t = 100t\tau_A$ for: (a) - (b) Harris-type current sheet without guide magnetic field and (c) - (d) force-free current sheet with a constant guide magnetic field $B_g = 2$.

reconnection is smaller for large magnetic structures while in case ii) the small number of plasmoids N_p reduces the enhancement of a Sweet-Parker reconnection rate reconnection by a factor $\sqrt{N_p}$. Cases i) and ii) are direct consequences of the guide magnetic field directed perpendicular to the reconnection plane. Even though the observed reduction of the reconnection rate is related to the guide field strength [equation (10.14)], the reasons for this dependence has still to be find out. A turbulence viewpoint is considered to investigate the slow down of the reconnection rate in presence of finite guide field.

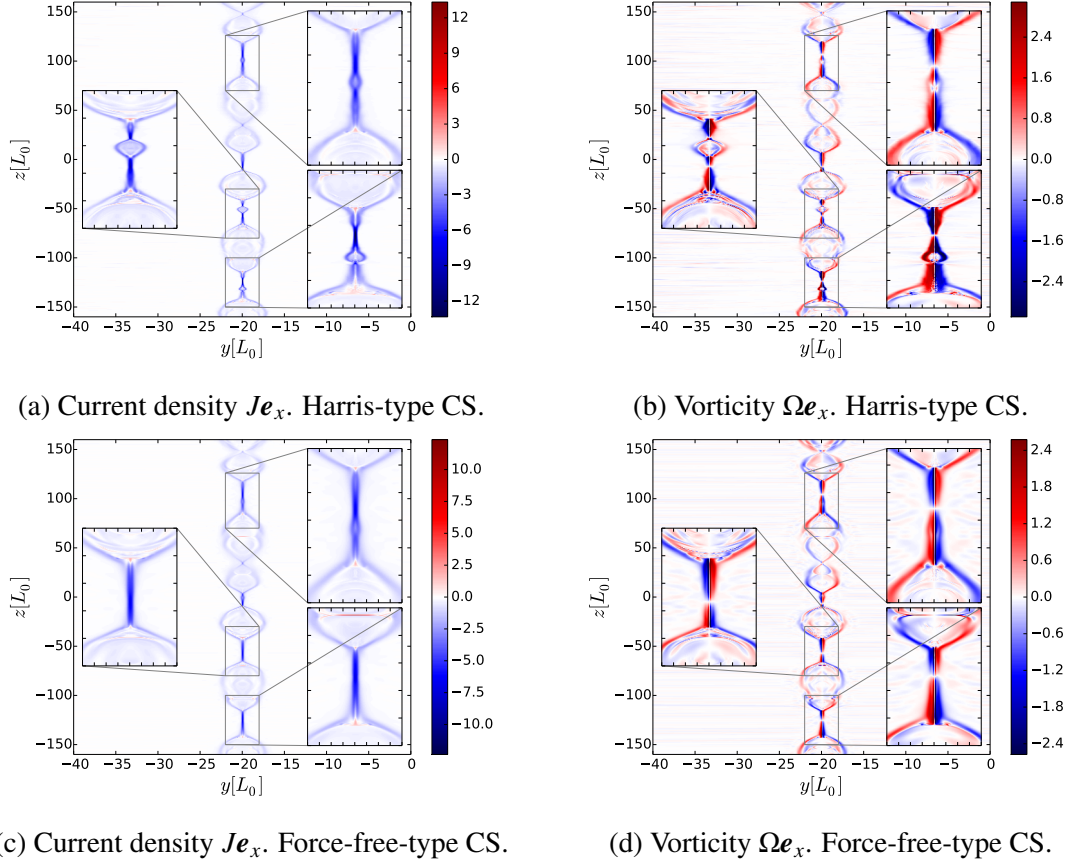


Figure 10.3: Spatial distribution of the current density and vorticity at $t = 100\tau_A$ for: (a) - (b) Harris-type current sheet without guide magnetic field and (c) - (d) force-free current sheet.

10.3 Turbulent Electromotive Force and Stress-Tensor in the Reconnection Regimes

Whether turbulence is considered using a Reynolds-averaged or an SGS model of turbulence, the consequences of turbulence is discussed in terms of a turbulence-induced electromotive force \mathcal{E} and stress-tensor R_{ij} . Both are given in the SGS approach as

$$\mathcal{E}_i = \epsilon_{ijk} \left(\overline{V_j B_k}^F - \overline{V_j}^F \overline{B_k}^F \right), \quad (10.15)$$

$$R_{ij} = \overline{\rho}^F \left(\overline{V_i V_j}^F - \overline{V_i}^F \overline{V_j}^F \right) - \left(\overline{B_i B_j}^F - \overline{B_i}^F \overline{B_j}^F \right) + \left(\overline{B_i B_i}^F - \overline{B_i}^F \overline{B_i}^F \right) \frac{\delta_{ij}}{2}. \quad (10.16)$$

They are determined by a Gaussian filtering of the data obtained by the high-resolution DNS. Figure 10.4 presents the spatial distribution of the turbulent stress-tensor R_{ij} for the Harris-type current sheet. The components R_{kk} of the Reynolds stress-tensor are of the order $\mathcal{O}(10^{-1}) - (10^{-2})$ while the other components are negligibly small compared to

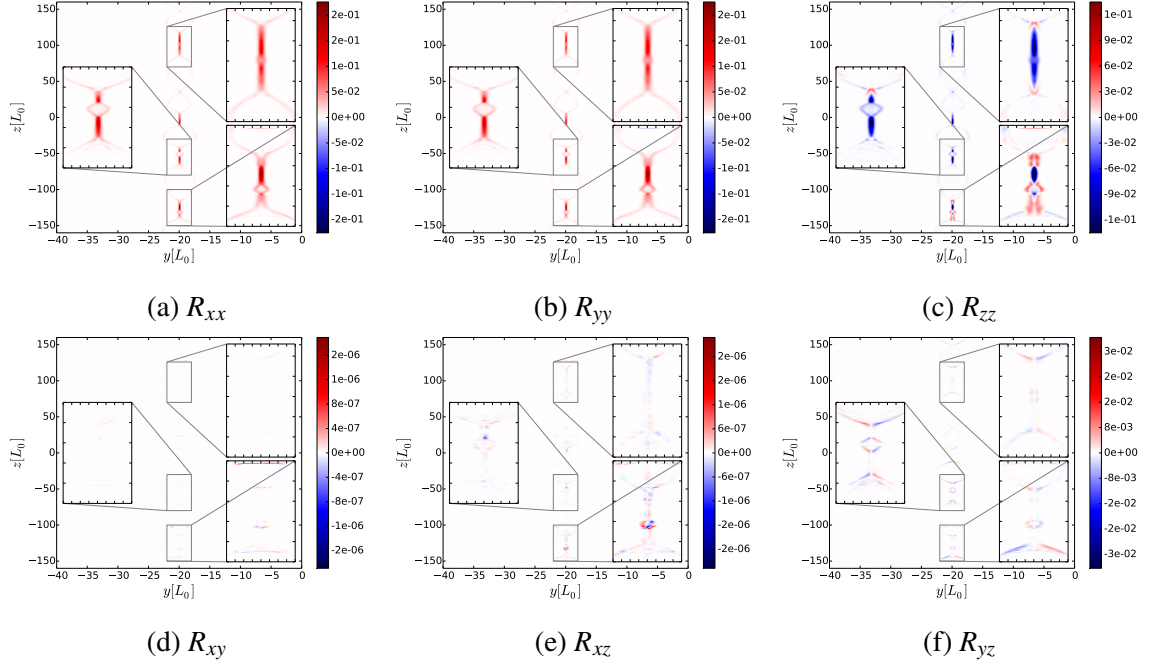


Figure 10.4: Spatial distribution of the turbulent stress-tensor components at $t = 100\tau_A$. Case of a Harris-type current sheet without guide magnetic field.

R_{kk} . In presence of a finite guide magnetic field $B_g \mathbf{e}_x$, the non-diagonal components of R_{ij} obtain, however, a non-negligible finite value as shown in figure 10.5.

Figure 10.6 depicts the turbulent electromotive force components of a Harris-type ($B_g = 0$) and a force-free ($B_g = 2$) current sheet. As obtained for the turbulent stress-tensor, the guide magnetic field causes additional components of the electromotive force. They are found to be within the reconnection plane, i.e., along \mathbf{e}_y and \mathbf{e}_z .

After applying a Gaussian filter,^{III} the momentum and induction equations become

$$\partial_t \bar{\mathbf{V}}^F = -\nabla \cdot \left(\bar{\mathbf{V}}^F \otimes \bar{\mathbf{V}}^F - \bar{\mathbf{B}}^F \otimes \bar{\mathbf{B}}^F \right) - \nabla \bar{P}_M^F + \nabla \cdot \mathbf{R} + \nu \nabla^2 \bar{\mathbf{V}}^F, \quad (10.17)$$

$$\partial_t \bar{\mathbf{B}}^F = \nabla \times \left(\bar{\mathbf{V}}^F \times \bar{\mathbf{B}}^F + \mathcal{E} - \eta \bar{\mathbf{J}}^F \right), \quad (10.18)$$

where \otimes denotes the tensorial product, \bar{P}_M^F is the mean MHD pressure [equation (4.21)] given in terms of the Gaussian filter and \mathbf{R} is the turbulent stress-tensor. The contributions of the $\nabla \cdot \mathbf{R}$ components to the filtered velocity $\bar{\mathbf{V}}^F$ are

$$(\nabla \cdot \mathbf{R}) \mathbf{e}_x \equiv \partial_i R_{ix} = \partial_y R_{yx} + \partial_z R_{zx}, \quad (10.19)$$

$$(\nabla \cdot \mathbf{R}) \mathbf{e}_y \equiv \partial_i R_{iy} = \partial_y R_{yy} + \partial_z R_{zy}, \quad (10.20)$$

$$(\nabla \cdot \mathbf{R}) \mathbf{e}_z \equiv \partial_i R_{iz} = \partial_y R_{yz} + \partial_z R_{zz}. \quad (10.21)$$

In two-dimensional situations, the components R_{zx} and R_{yx} contribute to the filtered velocity field $\bar{\mathbf{V}}^F$ in the \mathbf{e}_x direction (figure 10.4d). In two-dimensional magnetic reconnection,

III. For a mass-weighted filter formalism.

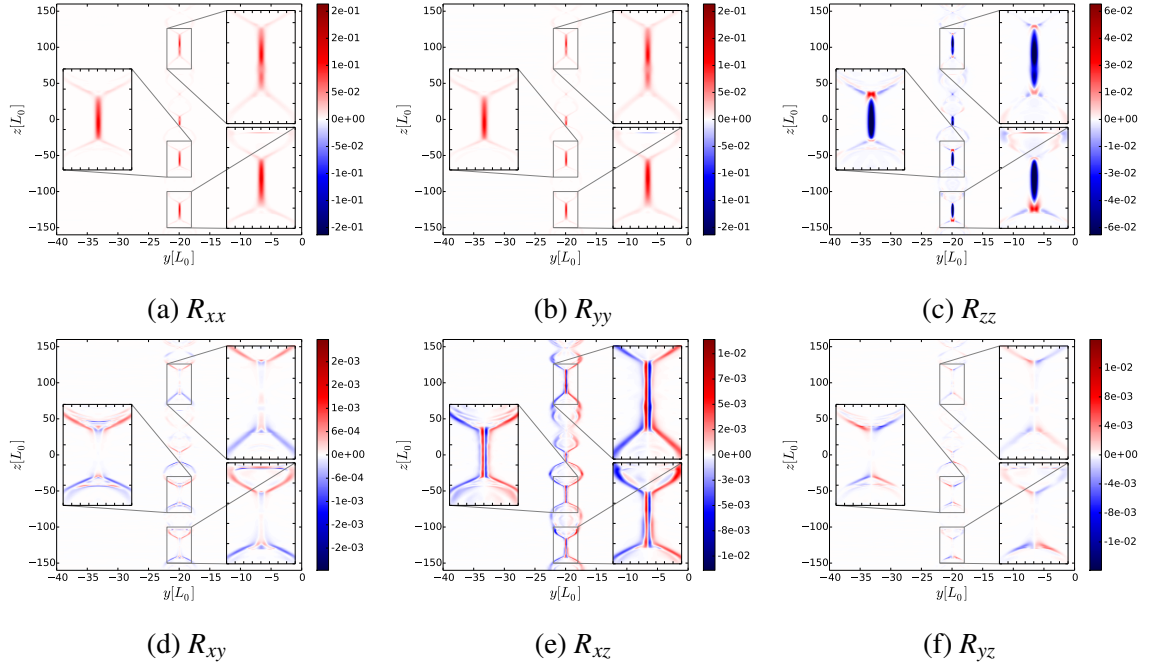


Figure 10.5: Spatial distribution of the turbulent stress-tensor components taken at $t = 100\tau_A$. Case of a force-free current sheet with constant guide magnetic field strength $B_g = 2$.

it is the ratio of the in- ($\bar{\mathbf{V}}_i^F$) and out-flow ($\bar{\mathbf{V}}_o^F$) velocities which provides a proxy for the reconnection rate. In the present geometry, they are $\bar{\mathbf{V}}^F \mathbf{e}_y$ and $\bar{\mathbf{V}}^F \mathbf{e}_z$. It is, therefore, the components R_{yy} , R_{yz} ($= R_{zy}$) and R_{zz} that can influence the reconnection rate.

The components of the curl of the turbulent electromotive force which enter the evolution equation of the mean magnetic field are

$$\partial_t \bar{\mathbf{B}}_x^F : \partial_y \mathcal{E}_z - \partial_z \mathcal{E}_y, \quad (10.22)$$

$$\partial_t \bar{\mathbf{B}}_y^F : -\partial_z \mathcal{E}_x, \quad (10.23)$$

$$\partial_t \bar{\mathbf{B}}_z^F : -\partial_y \mathcal{E}_x. \quad (10.24)$$

For a finite guide magnetic field equilibrium, \mathcal{E}_y and \mathcal{E}_z are finite. They are acting in the direction perpendicular to the reconnection plane, i.e., parallel to the guide magnetic field $\bar{\mathbf{B}}_g^F$. There is no direct influence of the in-plane components of \mathcal{E} on the reconnecting magnetic field.

Important consequences of a finite guide magnetic field are that: i) the amount of fluctuations is reduced, and ii) the components of the turbulent electromotive force and stress-tensor due to the guide magnetic field do not contribute to the mean velocity and magnetic field components lying in the reconnection plane.

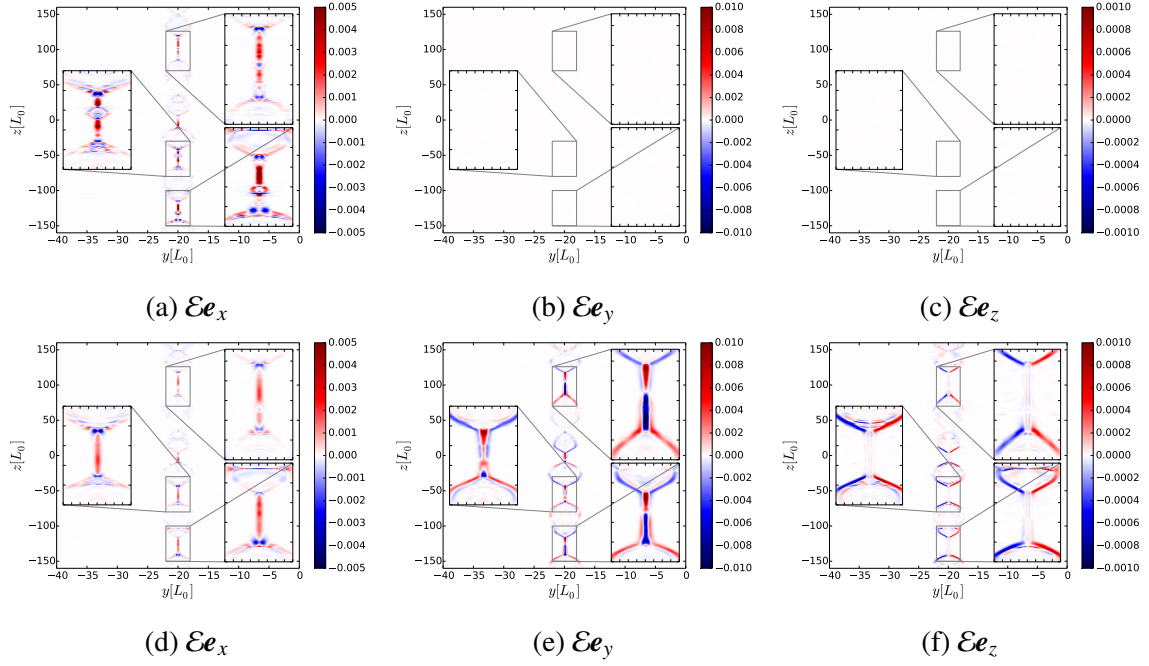


Figure 10.6: Spatial distribution of the turbulent electromotive force components at $t = 100\tau_A$ for: (a) - (c) the Harris-type current sheet ($B_g = 0$) and (d) - (f) force-free current sheet ($B_g = 2$).

10.4 Applicability of Turbulence Models to Magnetic Reconnection

The applicability of the turbulence models presented in sections (4.2.1) and (5.2) is tested by means of the data obtained from the DNSs of plasmoid-unstable current sheets. In each case, the turbulent electromotive forces and stress-tensors models are compared with their SGS counterparts [equations (10.15)-(10.16)]. In order to validate the expressions, the Pearson correlations are calculated along the center of the current sheet.

10.4.1 Applicability of the Non-linear SGS Model

For the non-linear SGS model, the turbulent electromotive force \mathcal{E}_{nl} and stress-tensor R_{ij}^{nl} are given following equations (5.22)-(5.25)

$$(\mathcal{E}_{nl})_i = \epsilon_{ijk} \Delta^2 C_{nl}^{\mathcal{E}} \partial_n \tilde{V}_j^F \partial_n \bar{B}_k^F, \quad (10.25)$$

$$R_{ij}^{nl} = R_{ij}^{nl,V} - R_{ij}^{nl,B} + \frac{2}{3} (E_{SGS}^V - E_{SGS}^B) \delta_{ij}. \quad (10.26)$$

where $R_{ij}^{nl,V}$ and $R_{ij}^{nl,B}$ are the kinetic and magnetic non-linear SGS stress-tensors [equations (5.23)-(5.24)]. The symbol Δ is a characteristic length scale related to the filter width and $C_{nl}^{\mathcal{E}}$ a model constant of order $\mathcal{O}(10^{-1})$.⁷³ Since only the e_y and e_z components of the velocity are important for the two-dimensional reconnection rate [equations (10.20)-(10.21)], only the components R_{yy}^{nl} , R_{yz}^{nl} and R_{zz}^{nl} of the non-linear SGS turbulent stress-tensor are presented. The stress-tensor depends on two model constants C_{nl}^V and C_{nl}^B

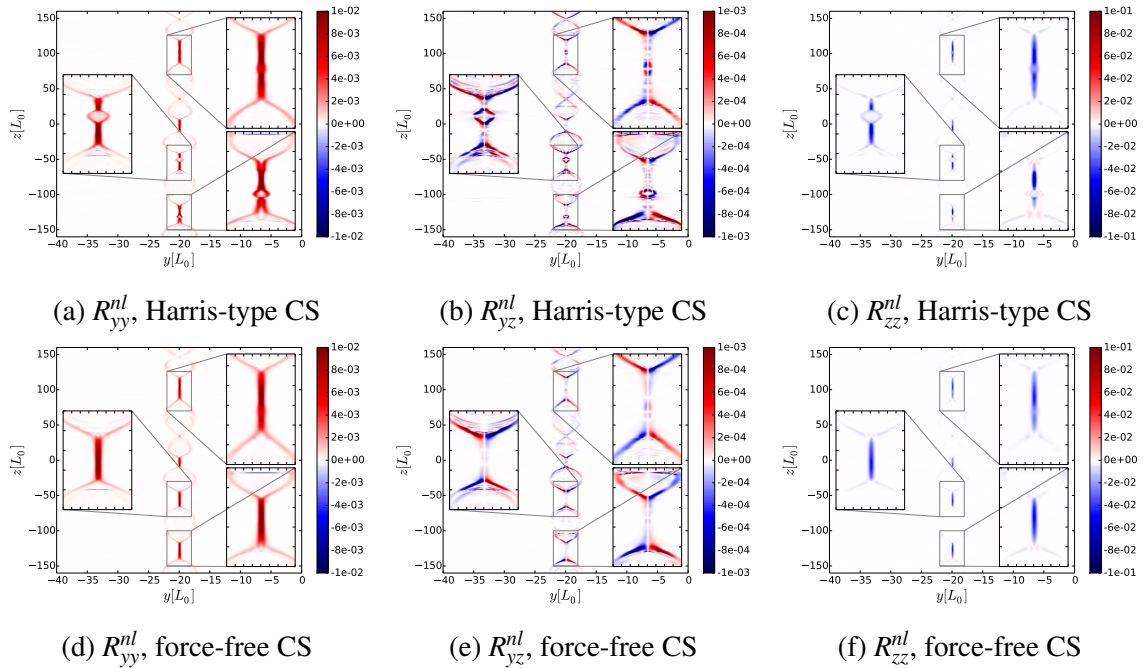


Figure 10.7: Spatial distribution of the non-linear SGS stress-tensor model components at $t = 100\tau_A$. Case of a Harris-type ($B_g = 0$) and a force-free current sheet ($B_g = 2$).

[equations (5.23)-(5.24)]. The values of the model constants are chosen as $C_{nl}^{\mathcal{E}} = 0.12$, $C_{nl}^V = 0.68$ and $C_{nl}^B = 0.77$. Figure 10.7 presents the non-linear turbulent stress-tensor components for the Harris- ($B_g = 0$) and force-free ($B_g = 2$) current sheets. The non-linear SGS model matches almost perfectly the SGS turbulent stress-tensor determined statistically. Figure 10.8 shows that the correlations of the turbulent stress-tensor component is close to 100% for all components of the non-linear SGS stress-tensor.

Figure 10.9 presents the comparison of the non-linear SGS electromotive force model \mathcal{E}_{nl} and its SGS expression \mathcal{E} [equation (5.15)] for the Harris- ($B_g = 0$) and force-free ($B_g = 2$) current sheets. The similarity between the electromotive forces are striking. The structures near and inside the magnetic islands are well resolved by \mathcal{E}_{nl} . The non-linear model is also able to capture the changing polarities of the SGS expression such that \mathcal{E}_{nl} is positive at the ‘X’-points vicinity and negative near the origins of the ‘O’-points. The \mathcal{E}_{nl} is further found to have a smaller amplitude than that of \mathcal{E} . This problem can be solved by adjusting the constant $C_{nl}^{\mathcal{E}}$ by an appropriate factor.

Finally, the correlations of the non-linear SGS electromotive force with its SGS counterparts are presented in figure 10.10. The correlation is above 90% in each equilibrium. The non-linear SGS electromotive force \mathcal{E}_{nl} and SGS stress-tensor R_{ij}^{nl} model are, therefore, applicable to the magnetic reconnection problem.

10.4.2 Applicability of the Mean-Field Turbulence Model

The mean-field turbulence model described in section (4.2.1) and used in chapters (8)-(9) is now considered after applying a Gaussian filter on the DNSs data. The model is built on statistical quantities representing turbulence: the turbulent energy K , the turbulent

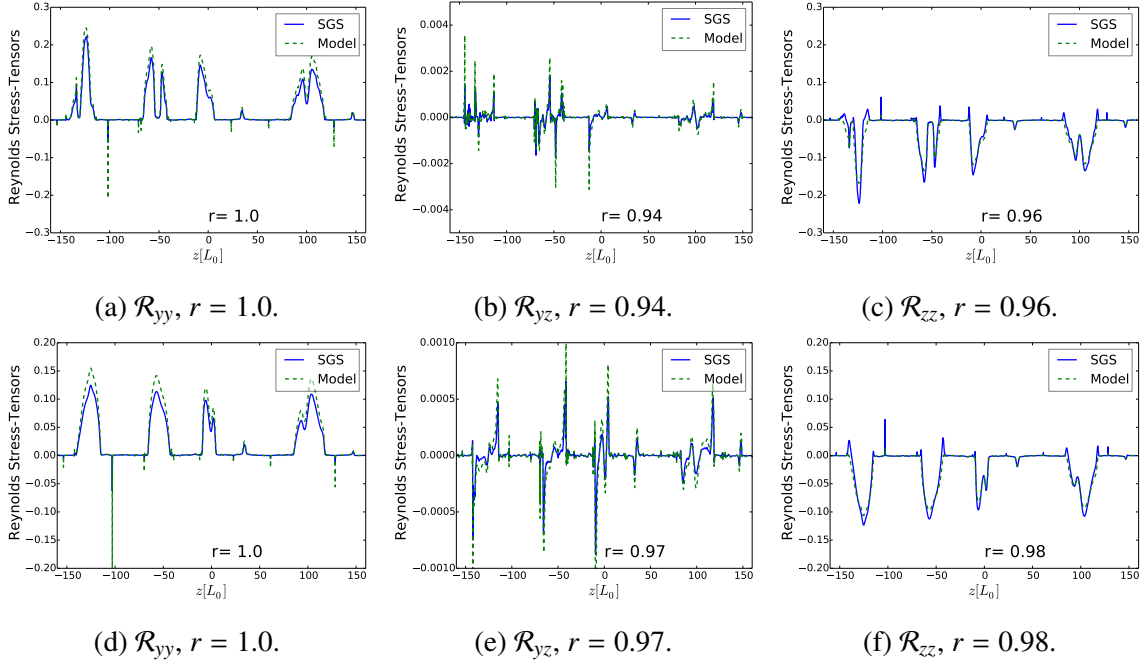


Figure 10.8: Line plots of the turbulent stress-tensors along the current sheet center at $t = 100\tau_A$ with correlation coefficient r for: (a) - (b) Harris-type current sheet without guide magnetic field and (c) - (d) force-free current sheet $B_g = 2$. The solid line represents the SGS expression R_{ij} and the dashed line is for the non-linear model R_{ij}^n . \mathcal{R}_{ij} stands for the turbulent stress-tensor model or SGS expression.

cross-helicity W and the residual helicity H . They are expressed in the SGS formulation by equations (5.16)-(5.17). The SGS expression of the turbulent stress-tensor reads

$$R_{ij}^{SGS} = \frac{7}{5}C_\beta\tau \left[K_{SGS} \left(\partial_i \bar{V}_j^F + \partial_j \bar{V}_i^F \right) - W_{SGS} \left(\partial_i \bar{B}_j^F + \partial_j \bar{B}_i^F \right) \right], \quad (10.27)$$

where $\tau = K_{SGS}/\varepsilon$ is the timescale of turbulence and C_β a model constant. Figure 10.11 depicts the SGS stress-tensor components in the reconnection plane. It has to be noted that the model is unable to reproduce the component R_{xx} . In the 2.5D geometry, any derivative with respect to e_x vanishes and so $R_{xx}^{SGS} \equiv 0$. The issue can be solved if equation (4.23e) is modeled through a statistical approach such as TSDIA. Figure 10.12 presents the correlation of the turbulent stress-tensors along the current sheet for both the Harris- ($B_g = 0$) and the force-free ($B_g = 2$) equilibria. The correlation for the R_{yy} and R_{zz} components are nearly of 90% while the negligible component R_{yz} has a correlation of only 22%. The SGS turbulence model does not capture the behavior of the R_{yz} component of its SGS counterparts expression. This component is, however, negligible in front of R_{yy} and R_{zz} .

In terms of the SGS energy K_{SGS} , cross-helicity W_{SGS} and residual helicity H_{SGS} , the SGS electromotive force model \mathcal{E}_{SGS} is given by

$$\mathcal{E}_{SGS} = \alpha \bar{\mathbf{B}}^F + \gamma \bar{\boldsymbol{\Omega}}^F - \beta \bar{\mathbf{J}}^F, \quad (10.28)$$

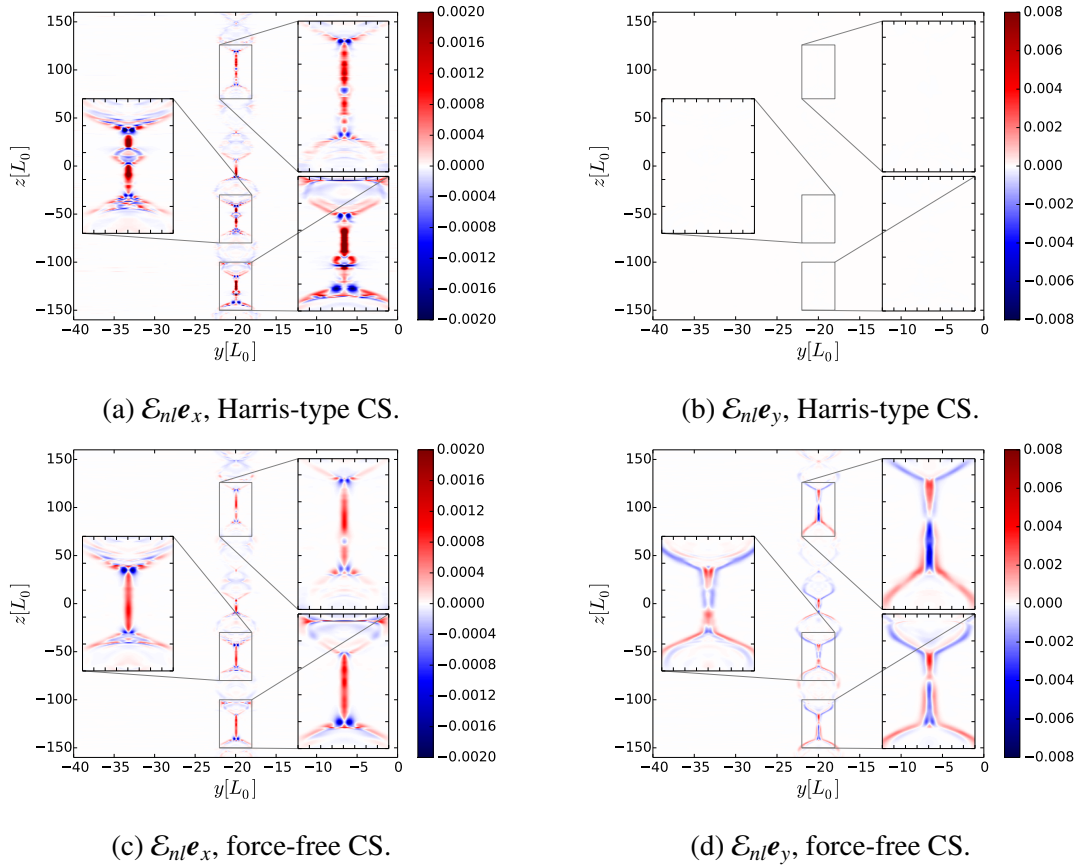


Figure 10.9: Spatial distribution of the non-linear SGS electromotive force model $\mathcal{E}_{nl}e_x$ and e_z at $t = 100\tau_A$ for: for: (a) - (b) Harris-type current sheet without guide magnetic field and (c) - (d) force-free current sheet $B_g = 2$.

where α , β and γ are modeled as

$$\alpha = \tau C_\alpha H_{SGS}, \quad (10.29)$$

$$\beta = \tau C_\beta K_{SGS}, \quad (10.30)$$

$$\gamma = \tau C_\gamma W_{SGS}. \quad (10.31)$$

The constants C_* are of the order $O(10^{-2})$ and τ a turbulence timescale. Since turbulence is fully developed during the non-linear phase of the plasmoid instability, τ is chosen to be of the order of the Alfvén transit time, i.e., $\tau = \tau_A$ in the present normalisation. This choice results from the investigation of turbulent reconnection in section (9.1). Based on Yokoi *et al.*⁷⁰, the remaining constants are chosen as $C_\alpha = 0.02$, $C_\beta = 0.05$ and $C_\gamma = 0.04$.

The spatial distribution of the SGS energy K_{SGS} and cross-helicity W_{SGS} is shown in figure 10.13. The SGS energy is found to be located mainly in places where the current density accumulates. It has an inhomogeneous structure whose maximum is decreasing away from ‘X’-point. The turbulence-related resistivity β [equation (10.30)] becomes then comparable to a localized resistivity. As the simulations confirmed, the SGS cross-helicity is spatially distributed around the maximum turbulent energy. The SGS cross-helicity has a quadrupolar shape whose polarity is that of the vorticity. The theoretical prediction

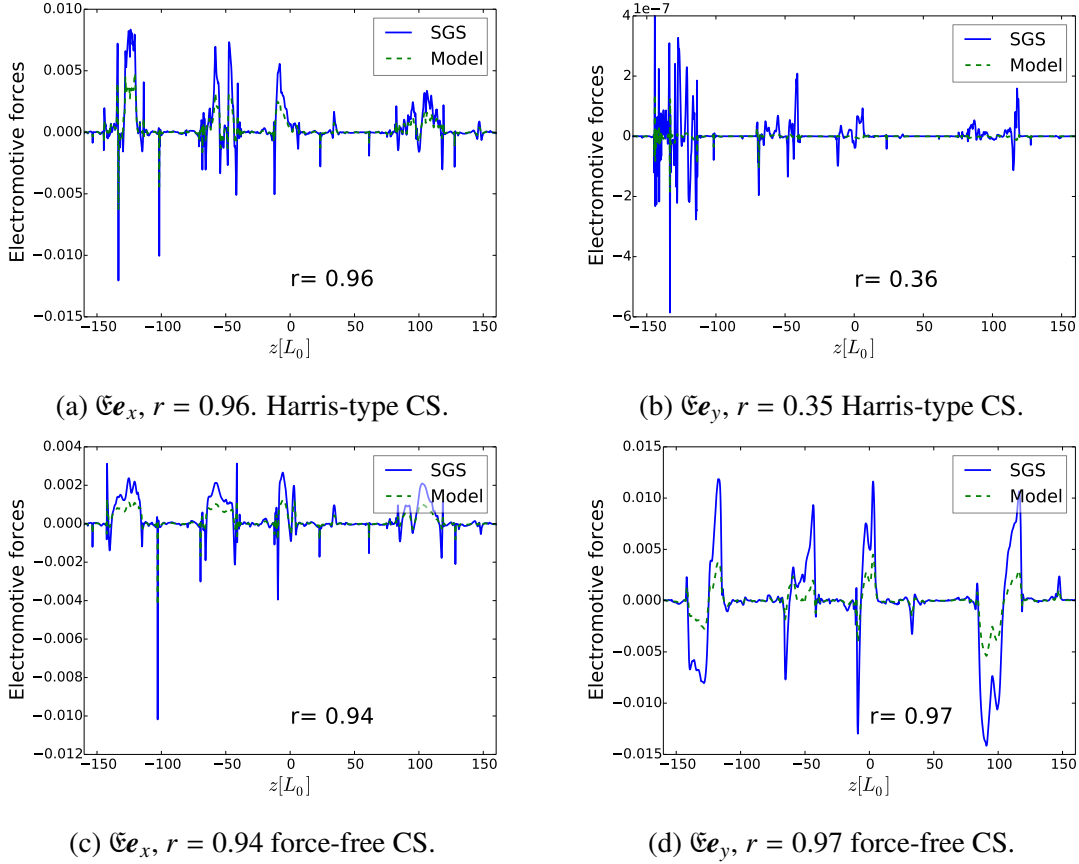


Figure 10.10: Line plots of the turbulent electromotive forces along the current sheet center at $t = 100\tau_A$ with correlation coefficient r for: (a) - (b) Harris-type current sheet without guide magnetic field and (c) - (d) force-free current sheet $B_g = 2$. The solid line represents \mathcal{E} and the dashed line is for \mathcal{E}_{nl} . \mathfrak{E} stands for \mathcal{E} or \mathcal{E}_{nl} .

of a localisation of the turbulent energy and cross-helicity during reconnection are both confirmed. The numerical solution of the transport equations for the turbulence (chapters (8)-(9)) is further validated. The assumption that turbulence dynamics is responsible for the rapid conversion of stored magnetic energy into plasma kinetic energy and heat is, therefore, confirmed.

It has been argued in section (8.1.5) that the SGS residual helicity H_{SGS} is important for the turbulence dynamics in two-dimensional numerical simulations with an guide magnetic field parallel to the current density. The reduction of the reconnection rate observed in guide field reconnection was related to H_{SGS} . The role of the residual helicity can be investigated by splitting H_{SGS} into its kinetic and magnetic part as

$$H_{SGS} = -H_{kin} + H_{mag} \quad (10.32)$$

$$= -\left(\overline{\mathbf{V} \cdot \boldsymbol{\Omega}^F} - \overline{\mathbf{V}^F \cdot \boldsymbol{\Omega}^F}\right) + \left(\frac{\overline{\mathbf{B} \cdot \mathbf{J}^F} - \overline{\mathbf{B}^F \cdot \mathbf{J}^F}}{\overline{\rho}^F}\right). \quad (10.33)$$

The spatial distribution of the two residual helicities are depicted in figure 10.14. They both vanish in the case of a Harris-type current sheet without guide magnetic field. The

10.4 Applicability of Turbulence Models to Magnetic Reconnection

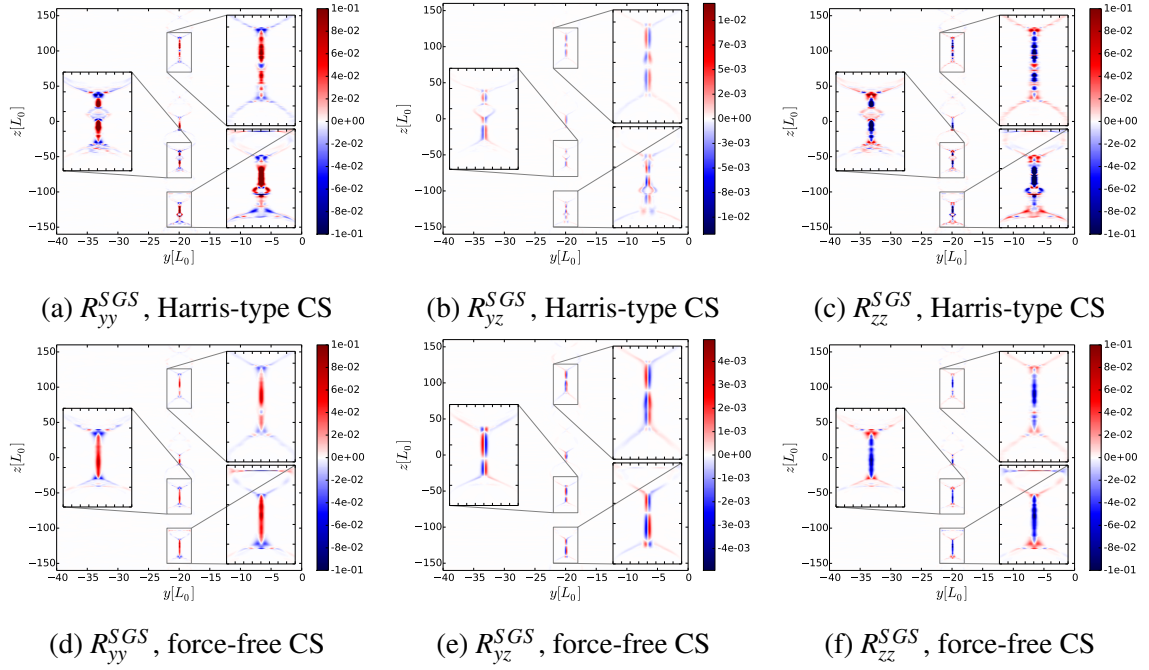


Figure 10.11: Spatial distribution of the SGS stress-tensor model components at $t = 100\tau_A$. Case a Harris-type ($B_g = 0$) and a force-free current sheet ($B_g = 2$).

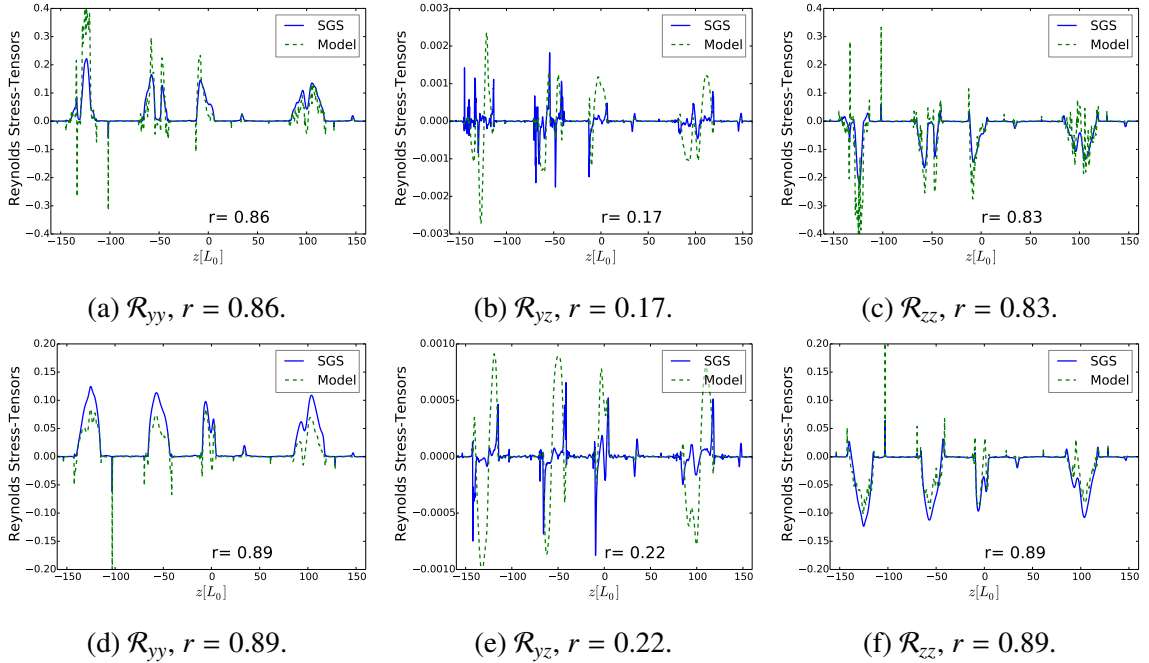


Figure 10.12: Line plots of the turbulent stress-tensors along the current sheet center at $t = 100\tau_A$ for: (a) - (b) Harris-type current sheet without guide magnetic field and (c) - (d) force-free current sheet $B_g = 2$. The solid line represents the SGS expression R_{ij} and the dashed line is for the SGS model R_{ij}^{SGS} . \mathcal{R}_{ij} stands for R_{ij} or R_{ij}^{SGS} . The correlation coefficient is r .

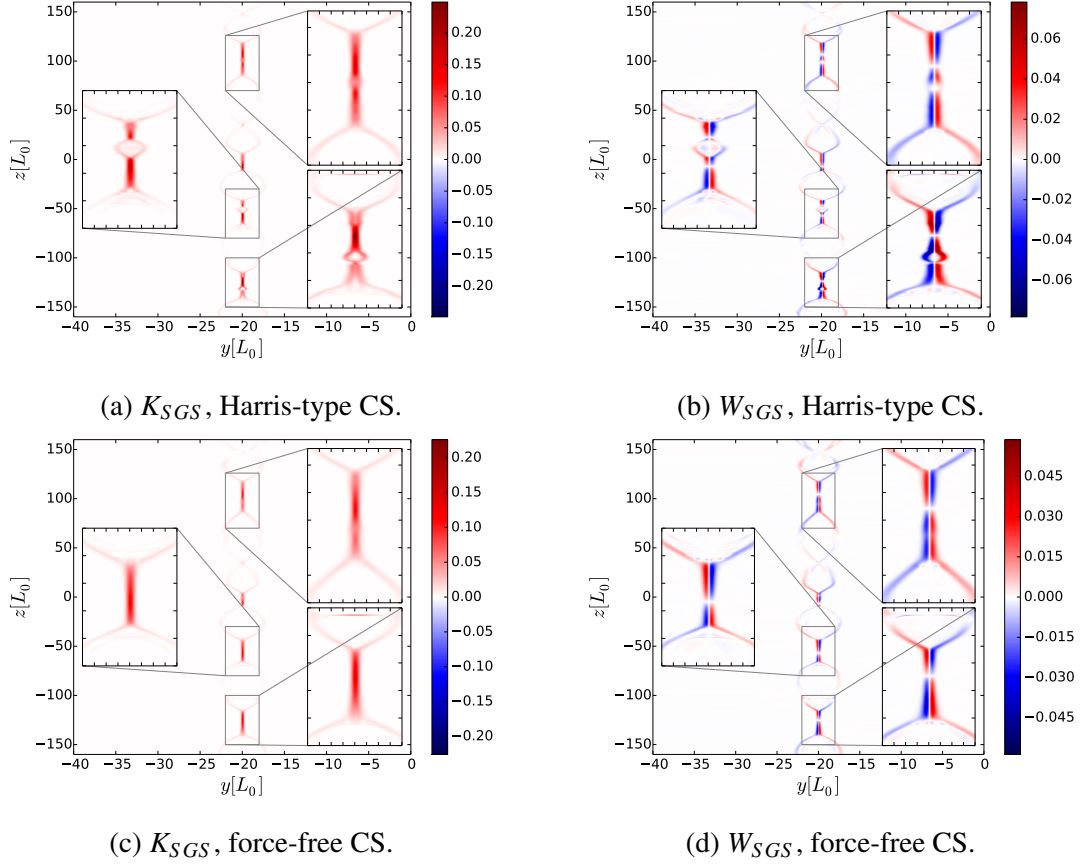


Figure 10.13: Spatial distribution of the SGS energy K_{SGS} and cross-helicity W_{SGS} for: (a) - (b) Harris-type current sheet without guide magnetic field and (c) - (d) force-free current sheet $B_g = 2$. The snapshot is taken at $t = 100\tau_A$.

additional guide magnetic field in the direction parallel to the current flow breaks the mirror-symmetry being then responsible for a finite SGS residual helicity H_{SGS} . It is found in two locations: i) near ‘X’-points and ii) close to ‘O’-points of reconnection. At the ‘X’-point, H_{SGS} is positive due to the residual magnetic helicity H_{mag} while it is found to be negative at ‘O’-points because of a finite residual kinetic helicity H_{kin} . From the initial finite guide magnetic field, a residual magnetic helicity H_{mag} is produced due to the alignment of the guide magnetic field and the mean current density. In the force-free case, a residual kinetic helicity is also produced initially due to the y -component of the current density. Together with the reconnecting mean magnetic field component \bar{B}_z , the in-plane mean current density \bar{J}_y generates a mean Lorentz force in the direction perpendicular to the reconnection plane. This force accelerates the plasma in the direction perpendicular to the reconnection plane. This resulting mean velocity \bar{V}_x parallel to the mean vorticity $\bar{\Omega}$ causes a finite H_{kin} .

The SGS electromotive force model \mathcal{E}_{SGS} [equation (10.28)] is presented in figure 10.15. It is found to be located along the current sheet in both Harris- ($B_g = 0$) and force-free ($B_g = 2$) equilibrium. The SGS electromotive force model does not reproduce the negative values observed by the statistically determined SGS electromotive force \mathcal{E} for a Harris-type equilibrium (figure 10.6a). In the force-free case, \mathcal{E}_{SGS} reproduces the pos-

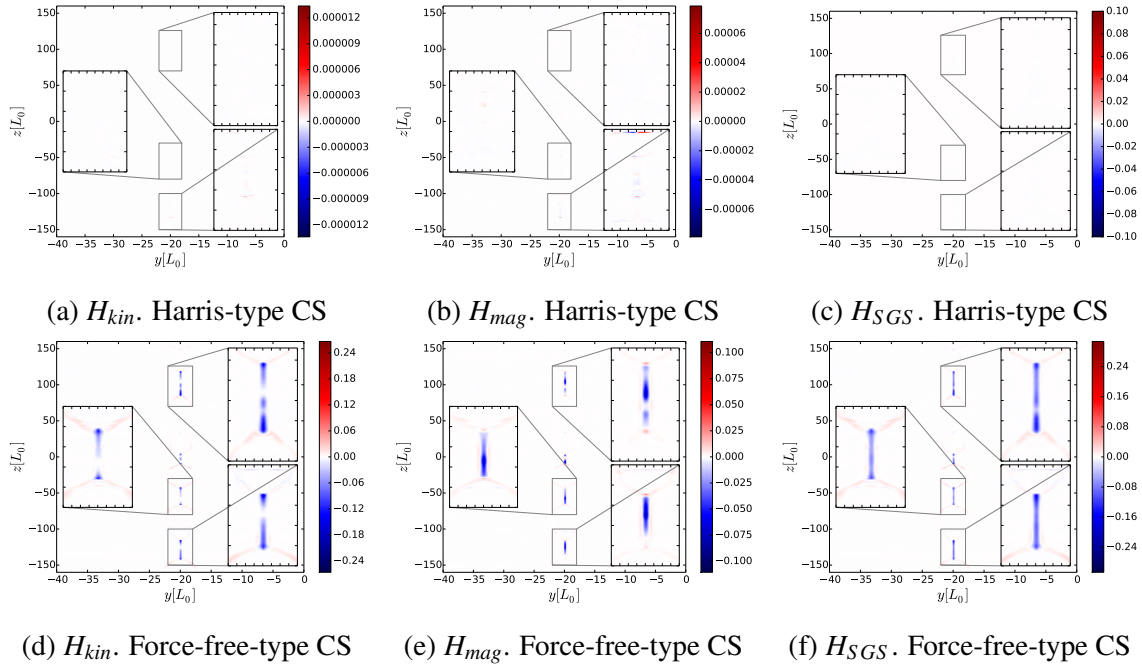


Figure 10.14: Spatial distribution of the residual helicities at $t = 100\tau_A$. Case of: (a) - (c) a Harris-type current sheet ($B_g = 0$) and (d) - (f) a force-free current sheet ($B_g = 2$).

itive and negative amplitude of \mathcal{E} properly. The negative values of \mathcal{E}_{SGS} near the location of the ‘O’-points are due to the residual helicity H_{SGS} . The component \mathcal{E}_y is, however, not present since neither the mean current density $\overline{\mathbf{J}}$, the mean magnetic field $\overline{\mathbf{B}}$ nor the mean vorticity $\overline{\boldsymbol{\Omega}}$ have a finite and non-negligible amplitude in that direction. Only the electromotive force component in the direction perpendicular to the reconnection plane (\mathbf{e}_x) contributes to the reconnection rate. The fact that the SGS model does not reproduce the y-component of \mathcal{E} is not important for the investigation of the influence of turbulence on the reconnection rate.

Figure 10.16 presents the correlation of the electromotive forces in the SGS model for Harris-type ($B_g = 0$) and force-free ($B_g = 2$) current sheets. The correlation for the x-components is above 80% which confirms the applicability of the SGS model to the magnetic reconnection problem. Even though the SGS electromotive force \mathcal{E}_{SGS} does not describe \mathcal{E} as well as the non-linear model \mathcal{E}_{nl} , the form of \mathcal{E}_{SGS} [equation (10.28)] might prove itself more useful than \mathcal{E}_{nl} for the comprehension of guide field effects on the reconnection rate.

10.5 Influence of Turbulence on the Plasmoid Instability

As shown in figure 10.1, the reconnection rate needs more time to reach saturation when a guide field is considered. A smaller reconnection rate implies slower conversion of magnetic energy into other forms. The mean magnetic energy density is then investigated in the SGS formulation. The filtered, or grid-scale (GS), magnetic field energy reads

$$\overline{\mathbf{B}^2}^F = \left(\overline{\mathbf{B}}^F\right)^2 + 2\overline{\mathbf{B}}^F \mathbf{B}' + \overline{\mathbf{B}'^2}^F. \quad (10.34)$$

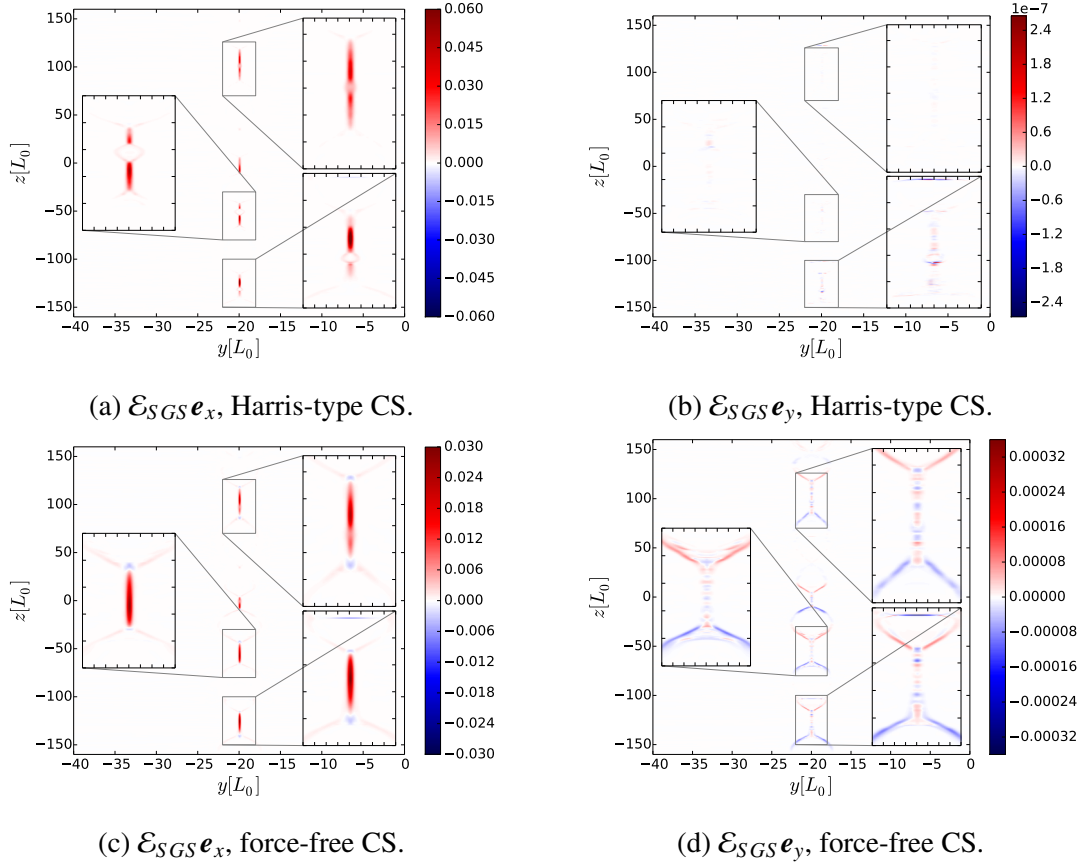


Figure 10.15: Spatial distribution of the SGS electromotive force model $\mathcal{E}_{SGS} \mathbf{e}_x$ and \mathbf{e}_z at $t = 100\tau_A$ for: for: (a) - (b) Harris-type current sheet without guide magnetic field and (c) - (d) force-free current sheet $B_g = 2$.

Since the filter width is chosen in a way that the cross terms are negligible, the second term on the right hand side of equation (10.34) can be neglected. In the SGS formulation, the evolution equation for the first term on the right hand side of equation (10.34) is

$$\frac{d}{dt} \int_V \frac{(\overline{\mathbf{B}}^F)^2}{2\mu_0} dx = \int_V \left[-\eta (\overline{\mathbf{J}}^F)^2 - \overline{\mathbf{V}}^F \cdot (\overline{\mathbf{J}}^F \times \overline{\mathbf{B}}^F) + \mathcal{E} \cdot \overline{\mathbf{J}}^F \right] dx. \quad (10.35)$$

The first term on the right hand side is the Joule heating and last term is the contribution of turbulence to the GS magnetic energy. The GS magnetic and kinetic energy are depicted in figure 10.17 for a Harris-type ($B_g = 0$) and force-free ($B_g = 2$ and 5) current sheets. The GS magnetic energy is rapidly decreasing in Harris-type current sheet without guide magnetic field while it remains at a high level in the force-free equilibrium current sheet. The GS magnetic energy increases with time in force-free current sheets. On the other hand, the GS plasma kinetic energy is rapidly increasing in Harris-type ($B_g = 0$) current sheets while a finite guide magnetic field in force-free current sheets slows down the evolution of the kinetic energy. This investigation shows that a guide magnetic field slows down the conversion of the magnetic energy. It has to be noted that the increase of the kinetic energy is similar in both equilibria during the first $t = 80\tau_A$. The differences in the

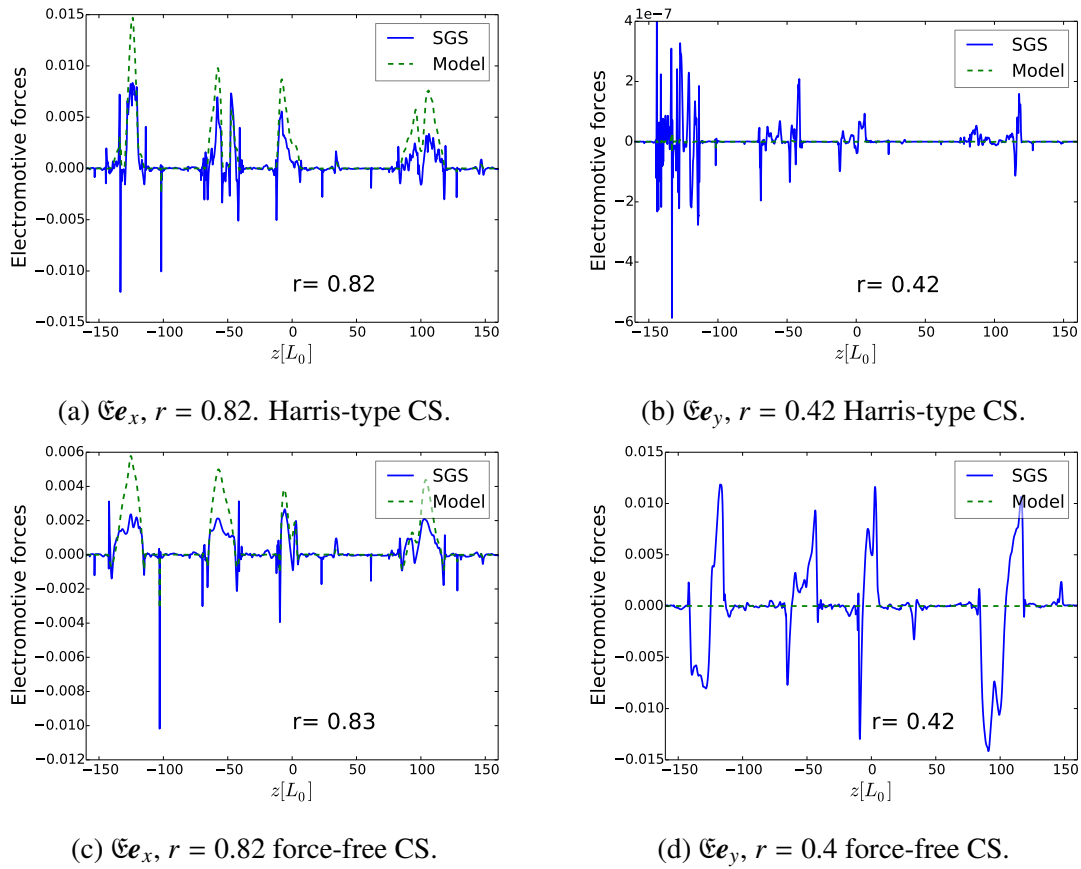


Figure 10.16: Line plots of the turbulent electromotive forces along the current sheet center with correlation coefficient r for the SGS model at $t = 100\tau_A$. Figures (a) - (b): Harris-type current sheet without guide magnetic field. Figures (c) - (d): force-free current sheet $B_g = 2$. The solid line represents \mathcal{E} and the dashed line is for \mathcal{E}_{SGS} . \mathcal{E} stands for \mathcal{E} or \mathcal{E}_{SGS} .

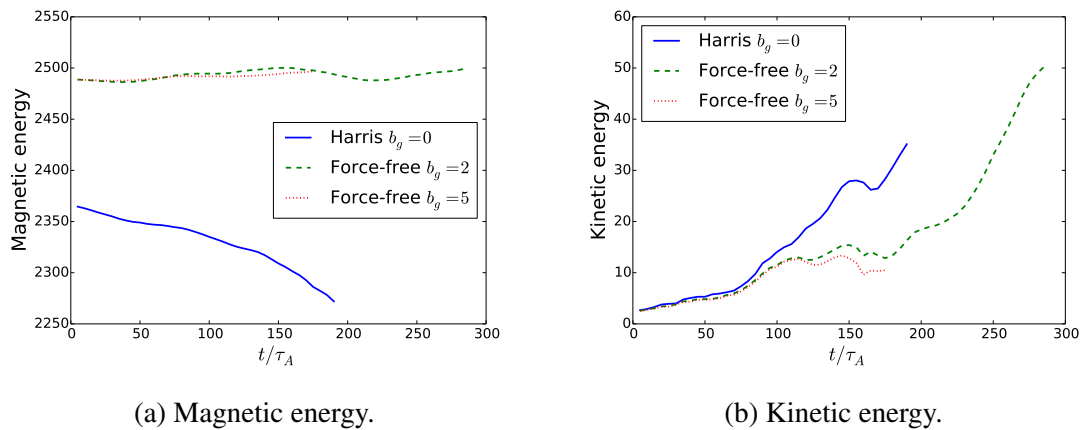


Figure 10.17: Time history of the evolution of the total magnetic and kinetic energy. The energies are computed for a Harris-type current sheet without guide field and a force-free current sheet with guide magnetic field $b_g = 2$ and 5. Taken from Widmer *et al.*⁷¹

energies between a guide and a non-guide magnetic field equilibrium can be considered through the effect of turbulence. As discussed in section (4.3), there is a balance of the turbulence induced terms around the reconnection regions. Turbulence is thought to be responsible for the reduction of the reconnection rate in presence of a finite guide field during the non-linear phase.

10.5.1 Turbulent Energy Transfer

Investigating the energy budget during the reconnection process is important. In the SGS approach, the contribution of the SGS turbulence to the GS magnetic energy density is provided by the term $\mathcal{E} \cdot \bar{\mathbf{J}}^F$. The term $\mathcal{E} \cdot \bar{\mathbf{J}}^F$ is positive at the location where the turbulent electromotive force is co-parallel with the current and negative if they are anti-parallel. As shown in sections (7.5.1) and (7.5.2), the electromotive force is anti-parallel to the current when magnetic reconnection takes place, the product $\mathcal{E} \cdot \bar{\mathbf{J}}^F$ is then negative and contributes to the reduction of magnetic energy. As depicted in figure 10.6, the electromotive force has a positive amplitude in the vicinity of ‘X’-points while its amplitude is negative close to ‘O’-points. Since the current flows in the negative x -direction (figure 10.3), the product $\mathcal{E} \cdot \bar{\mathbf{J}}^F$ is negative at and around ‘X’-points and positive near ‘O’-points. Turbulence is, therefore, enhancing the annihilation of the magnetic field at the ‘X’-points while it favors the creation of magnetic field at the origins of magnetic islands. The SGS electromotive force model is composed of three terms:

$$\text{I) Resistive-like term: } \beta \bar{\mathbf{J}}^F, \quad (10.36)$$

$$\text{II) Dynamo-like term: } \alpha \bar{\mathbf{B}}^F, \quad (10.37)$$

$$\text{III) Dynamo-like term: } \gamma \bar{\boldsymbol{\Omega}}^F, \quad (10.38)$$

where the term I) enhances the magnetic annihilation above the molecular resistive term $\eta \bar{\mathbf{J}}^F$ while the two other terms contribute to the sustainment of the magnetic field (dynamo-effect). In presence of a finite guide magnetic field, the product $\mathcal{E}_{SGS} \cdot \bar{\mathbf{J}}^F$ reads

$$\mathcal{E}_{SGS} \cdot \bar{\mathbf{J}}^F = -\beta \left(\bar{\mathbf{J}}^F \right)^2 + \gamma \bar{\boldsymbol{\Omega}}^F \cdot \bar{\mathbf{J}}^F + \alpha \bar{\mathbf{B}}^F \cdot \bar{\mathbf{J}}^F. \quad (10.39)$$

The form of equation (10.39) shows that the increased annihilation of magnetic flux at the ‘X’-points is a result of the turbulence-related resistivity β since it is positive definite and is localised where the current density accumulates (figure 10.13). The last two terms of the right hand side of equation (10.39) always create magnetic field since $\text{sign}(\gamma) = \text{sign}(\boldsymbol{\Omega})$ and $\text{sign}(\alpha) = \text{sign}(\mathbf{B}_g \cdot \bar{\mathbf{J}}^F)$ (section (4.3.1)). Since the rate of energy conversion is smaller in the presence of a finite guide field, the contribution of the SGS residual helicity in equation (10.39) to the GS magnetic field energy is now considered. The SGS residual helicity H_{SGS} is found to be negative along the current sheets, i.e., from one ‘O’-point to the other. In the vicinity of the ‘X’-points, its magnetic component H_{mag} is important while its kinetic component H_{kin} matters near the ‘O’-points (figure 10.14). The SGS energy K_{SGS} strength is reduced at the reconnection sites by H_{mag} because its production

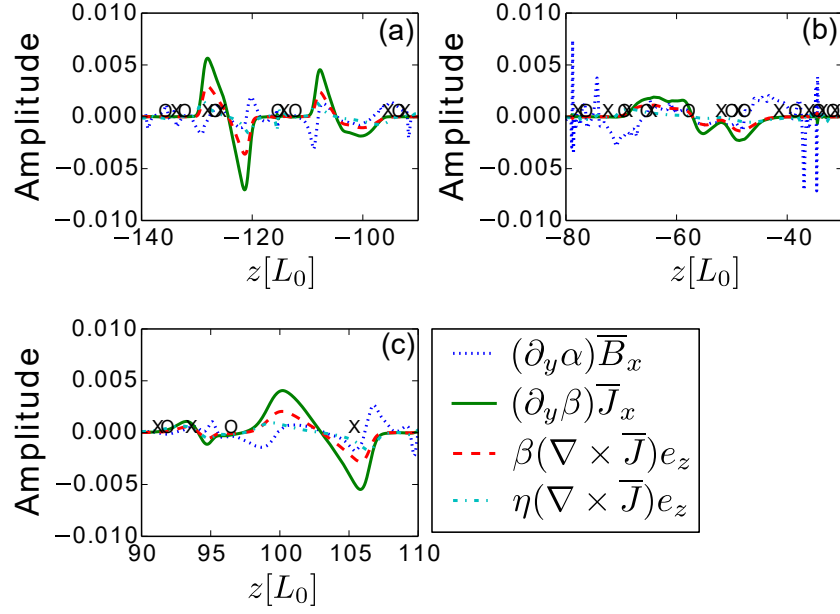


Figure 10.18: Components of $(\nabla \times \mathcal{E})_{SGS}$ along the center of the current sheet. They correspond to the zoomed regions of reconnection in figure 10.15: (a) the lower right zoom, (b) the middle left zoom and (c) the upper right zoom. The ‘X’- and ‘O’-points are denoted by **X** and **O**. The amplitude is multiplied by 100.0 for visualisation purposes. Taken from Widmer *et al.*⁷¹

P_K is given as

$$P_K = \tau \left(\beta \bar{\mathbf{J}}^F{}^2 - \alpha \bar{\mathbf{J}}^F \cdot \bar{\mathbf{B}}^F - \gamma \bar{\boldsymbol{\Omega}}^F \cdot \bar{\mathbf{J}}^F \right). \quad (10.40)$$

As a result, the efficiency of the turbulence-related resistivity β ($\propto K$) is diminished and the annihilation of magnetic field is reduced. At the origins of ‘O’-points, the conversion of the kinetic energy into magnetic energy is favored by turbulence because H_{kin} is larger than the SGS energy K_{SGS} and the SGS electromotive force becomes positive. The formation of large magnetic structures are then favored. This is not the in non-guide magnetic field reconnection because of the absence of residual helicity.

Turbulence contributes to the evolution of the GS magnetic field through the curl of the SGS electromotive force [equation (10.18)]. Since the reconnecting magnetic field is in the z -direction, the balance of turbulence terms is investigated for $\partial_z \mathcal{E}$. Figure 10.18 depicts the contribution of $(\nabla \times \mathcal{E}_{SGS})e_z$ along the current sheet center. The SGS cross-helicity does not appear since it vanishes identically at the symmetry line due to its pseudo-scalar nature. The gradients of the turbulence-related resistivity β and residual helicity related α -term have important impacts. While the terms related to β are enhancing the resistive diffusive term $\eta \nabla \times \bar{\mathbf{J}}^F$, the gradient of α are diminishing them. At some locations, the residual helicity suppresses the turbulence-related resistivity effects letting only the resistive dissipation to convert magnetic energy into plasma kinetic energy and heat. The enhancement of the reconnection rate by turbulence is suppressed. This does not happen in non-guide field reconnection since there is no asymmetry in the direction perpendicular to the reconnection plane. The reduction of the reconnection rate in guide magnetic field

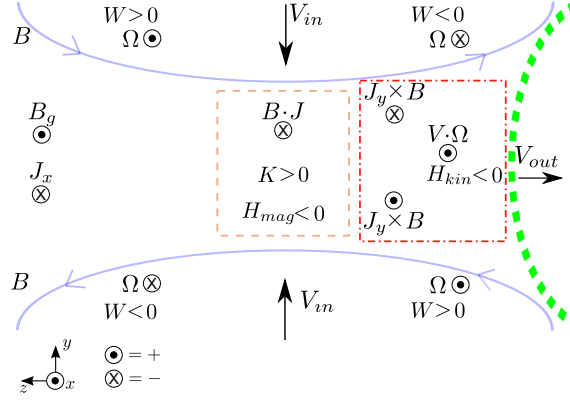


Figure 10.19: Schematic of the turbulence dynamics in the vicinity of an ‘X’-point. The dashed box represents the region where reconnection takes place. There, $K > 0$ and $H_{mag} \approx \overline{\mathbf{B}}^F \cdot \overline{\mathbf{J}}^F < 0$. The region near an ‘O’-point (curved dashed line) is depicted by the line dashed box. There, the in-plane current $\overline{\mathbf{J}}_y^F$ produces a force $\overline{\mathbf{J}}_y^F \times \overline{\mathbf{B}}^F$ which generates a velocity perpendicular to the reconnection plane (\mathbf{e}_x direction). In that region, a negative turbulent kinetic helicity is formed because $-\overline{\mathbf{V}}^F \cdot \overline{\boldsymbol{\Omega}}^F < 0$. It has to be noted that the cross-helicity W and the vorticity $\overline{\boldsymbol{\Omega}}^F$ have similar polarities. Taken from Widmer *et al.*⁷¹

reconnection current sheets can, therefore, be understood through the turbulence dynamics.

10.5.2 Reconnection Rate in Presence of Turbulence

The inhomogeneities of the GS magnetic field and velocity distribution can be related to the reconnection rate considering turbulence [equation (8.44)]. The relation is written for the SGS formulation as

$$M_A = \frac{|\overline{\boldsymbol{\Omega}}^F|}{|\overline{\mathbf{J}}_\star^F|} \left(\frac{|\gamma|}{\eta_T} \right). \quad (10.41)$$

where $\overline{\mathbf{J}}_\star^F = (\overline{\mathbf{J}}^F \sqrt{\mu_0}) / \sqrt{\rho}$, $\eta_T = \eta + \beta$. M_A is an estimation of the reconnection rate according to equation (10.41).⁹⁴ In the limit $\beta \gg \eta$, the turbulent diffusivity β determines the denominator and the conversion of magnetic into other forms of energy. In such situations, the reconnection rate is enhanced by turbulence and it becomes independent of the resistivity η (section (7.3.1) and chapter (8)). Figure 10.20 shows the reconnection rate as it is computed directly from the reconnection electric field \mathbf{E}_x and estimated by M_A according to equation (10.41). The estimated reconnection rate M_A [equation (10.41)] matches better the evolution of the reconnection rate obtained from \mathbf{E}_x for a force-free current sheet than for an Harris-type current sheet. It has to be noted that M_A underestimates \mathbf{E}_x in the first $t = 60\tau_A$ for the Harris case and during the $t = 100\tau_A$ for the force-free case.

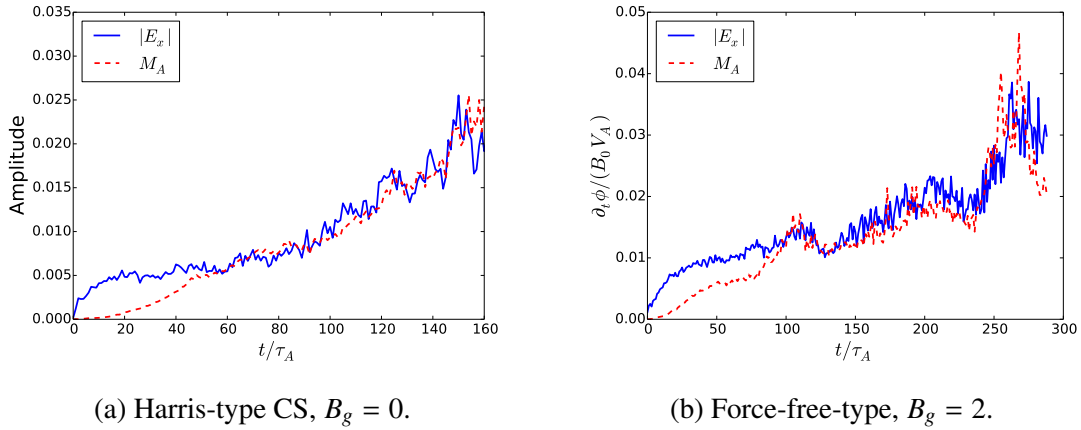


Figure 10.20: Time evolution of the reconnection rate obtained as the out-of plane electric field \mathbf{E}_x and estimated by M_A [equation (10.41)] for a Harris-type ($B_g = 0$) and a force-free ($B_g = 2$) current sheet (CS). Taken from Widmer *et al.*⁷¹

Equation (10.41) is used to determined the amount of turbulence in the system as

$$\frac{|\gamma|}{\eta_T} \cong M_A \frac{|\overline{\mathbf{J}}_\star^F|}{|\overline{\mathbf{\Omega}}^F|}. \quad (10.42)$$

Figure 10.21 presents the ratio $|\gamma|/\eta_T$ as it is estimated using expression (10.42) and calculated directly from the SGS energy K_{SGS} , the resistivity η and the SGS cross-helicity W_{SGS} as

$$\frac{|\gamma|}{\eta_T} = \frac{\tau C_\gamma |W_{SGS}|}{\eta + \tau C_\beta K_{SGS}}, \quad (10.43)$$

with $\tau = 1$, $C_\beta = 0.05$, $C_\gamma = 0.04$ and $C_\alpha = 0.02$. Expression equation (10.42) overestimates the turbulence ratio given by expression (10.43). Figure 10.21 shows that turbulence starts to be effective around $t = 60\tau_A$ for the Harris-type current sheet. This is the time at which the kinetic energy rapidly grows, faster than through a force-free current sheet (figure 10.17). The turbulence is not efficiently enhancing reconnection during the first $t = 60 - 100\tau_A$. This is the reason why M_A underestimates the reconnection rate. This also corresponds to the similar reconnection rates of finite guide and zero-guide field current sheet equilibrium during the first $t = 60 - 100\tau_A$ (figure 10.1).

Finally, turbulence can explain the deviation of the reconnection rate from the Sweet-Parker scaling $M_A \propto S^{-1/2} \sim \eta^{1/2}$.^{52,104} This deviation can be attributed to turbulence because of its ubiquitousness in large-Lundquist-number plasmas. Figure 10.22 depicts the averaged value of the reconnection rate over time as the resistivity decreases. The amount of turbulence computed from equation (10.43) is also shown. As turbulence saturates with ongoing reconnection, the deviation of the reconnection rate from the Sweet-Parker scaling is a consequence of the saturation of the turbulence. Even though a smaller resistivity η can enhance the effect of the turbulent resistivity β , the reconnection rate saturates.

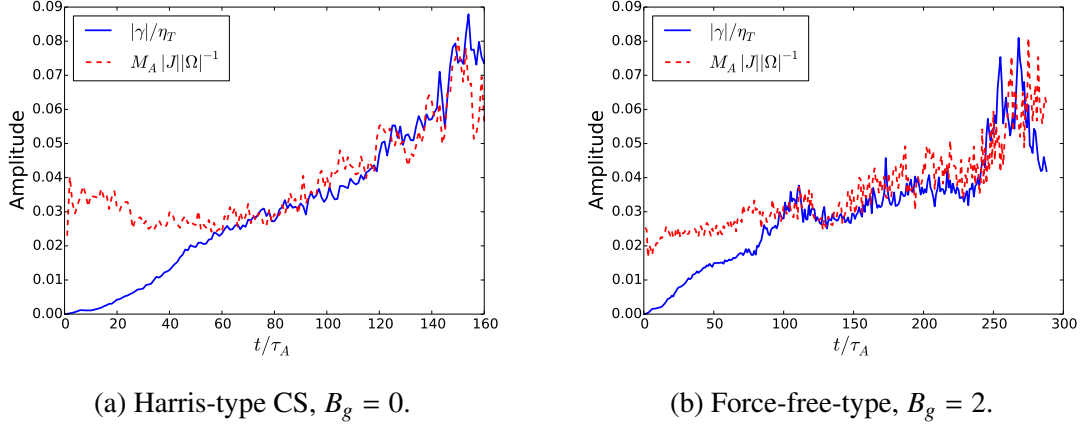


Figure 10.21: Time evolution of the amount of turbulence as it is computed from the turbulent ratio [equation (10.43)] and estimated by equation (10.42) for a Harris- ($B_g = 0$) and a force-free ($B_g = 2$) current sheet (CS). From Widmer *et al.*⁷¹

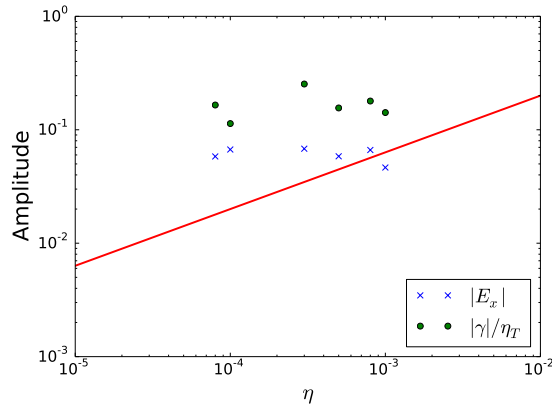


Figure 10.22: Reconnection rate $|E_x|$ and amount of turbulence $|\gamma|/\eta_T$ according to expression (10.43) averaged over time in comparison to the resistivity η . As η decreases, the reconnection rate stay constant, i.e., it deviates from the Sweet-Parker scaling (solid line). From Widmer *et al.*⁷¹

11 Conclusions

The end of a melody is not its goal:
but nonetheless, had the melody not
reached its end it would not have
reached its goal either. A parable.

Friedrich Nietzsche

A Reynolds-averaged turbulence model constructed using few parameter to describe MHD turbulence was utilized to investigate the consequences of the small scales MHD fluctuations on the rate of energy conversion by magnetic reconnection. The evolution equations for the turbulence energy and cross-helicity are numerically solved together with the MHD equations for the mean field variables. The consequences of turbulence for the reconnection rate were investigated using first a constant turbulence timescale τ . The tested cases were an Harris-type current sheet with or without a constant guide magnetic field \mathbf{B}_g perpendicular to the current flow as well as a force-free current sheet equilibrium with finite guide field.

Whether the considered equilibrium has a guide magnetic field or not, the timescale of turbulence τ controls the regimes of energy conversion. In the limit $\tau \ll \tau_A$, the rate of energy conversion is that of the resistive MHD while in the limit $\tau \gg \tau_A$ only a small amount of magnetic energy is converted into plasma kinetic energy and heat. As soon as $\tau \approx \tau_A$, the rate of energy conversion is high and fast reconnection takes place due to turbulence. Enhanced reconnection is due to the localisation of the turbulence-related resistivity at and around the diffusion region of reconnection. The production of turbulent cross-helicity around the reconnection region, with a polarity as that of the mean vorticity, enhances the turbulent energy, proportional to a turbulent resistivity, inside the reconnection layer. The gradients of the turbulent resistivity is enhanced by the turbulent cross-helicity from the center to the edges of the reconnection region resulting in a large angle of reconnection, i.e., the reconnection rate is increased. In situations of vanishing turbulent cross-helicity ($W \equiv 0$), the regimes of energy conversion are also obtained but for a smaller reconnection rate. The action of the cross-helicity is, therefore, important for the enhancement of the reconnection rate by turbulence.

It was further shown that reconnection needs time to reach its maximum if a finite guide magnetic field \mathbf{B}_g is present. The finite guide magnetic field produces an asymmetry in the direction parallel to the current flow and a finite residual helicity H is produced. The amplitude of the turbulent energy K is reduced by the residual helicity H . Because the turbulence-related resistivity enhancing the reconnection rate is proportional to the turbulent energy, the rate of energy conversion is decreased.

In fact, the regimes of energy release were obtained for a large initial amplitude of

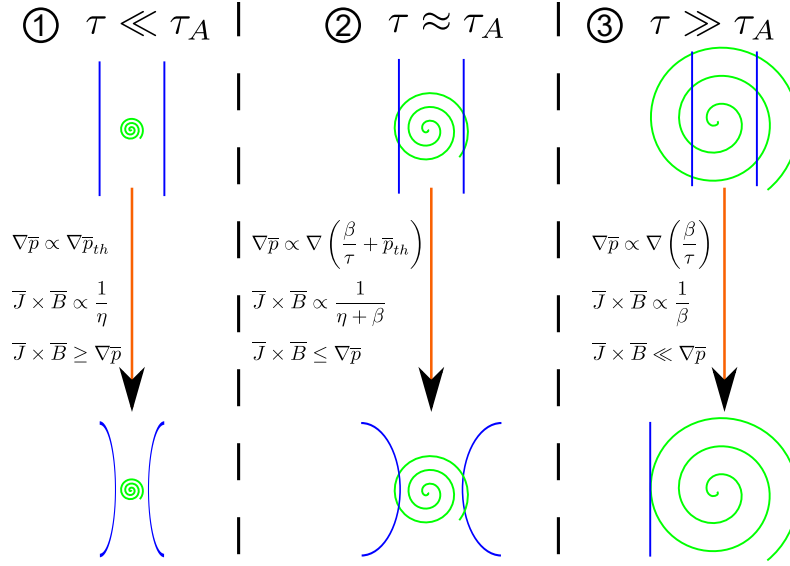


Figure 11.1: Schematics of the evolution of a current sheet depending on the turbulence timescale τ compared to the Alfvén transit time τ_A through the sheet. The blue lines depict the boundaries of the current sheet and the green spirals represent a turbulence eddy. The size of the eddy corresponds to the scale at which turbulence takes place.

turbulent resistivity $\beta_0 = \tau K_0$ compared with the molecular resistivity η . As long as an algebraic timescale is used, β_0 can be changed either by changing the initial turbulent energy K_0 or by the timescale of turbulence τ . The consequences of a variable τ and a fixed K_0 is now discussed. In the Kolmogorov self-similar transport picture, the energy is transported from the large to the dissipation scales at a rate $\varepsilon = K/\tau$. A timescale of turbulence larger than the Alfvén transit time results in a small transfer rate, only a few percent of the energy is then transferred down to small scales. On the other hand, the energy transport to small scales is enhanced by turbulence for a moderate τ . In the limit of small τ , the turbulence is almost instantaneously dissipated and cannot efficiently transport the large scales energy to the dissipation scales. The timescale of turbulence is proportional to the size of a turbulence eddy. In the limit $\tau \gg \tau_A$, the size of a turbulence eddy is much larger than the width of the current sheet. The inflow of plasma and magnetic flux does not reach the current sheet sides as they encounter turbulence before. The thermal pressure inside the current sheet widens the current sheet until it reaches the approximate size of a turbulence eddy. At that moment, a force equilibrium is reached between the Lorentz force and the thermal pressure and the process stops. Because of turbulence, the current sheet cannot thin down and magnetic reconnection is impeded. In the opposite limit $\tau \ll \tau_A$, turbulence resides at a scale much smaller than the current sheet width. It is, therefore, not contributing to the dissipation of energy and reconnection is of a Sweet-Parker rate. However, the limit $\tau \approx \tau_A$ enhances the energy dissipation; turbulence is now present at a scale close to the current sheet width. The enhancement of the thermal pressure and the reduction of the Lorentz force at the sides of the current sheet by turbulence enlarge the width of the diffusion layer and the angle of reconnection is greater. The three regimes of energy conversion described above in terms of the size of a turbulence eddy as well as the forces acting on the current sheet are depicted in figure 11.1.

The numerical experiments also showed that for a fixed τ , a strong level of turbulence (large K_0) reduces the reconnection rate. A turbulence level exceeding the magnetic field perturbation results in a suppression of the tearing instability. Furthermore, a large amplitude of turbulent energy increases the thermal pressure force above the Lorentz force. Contrary, a amplitude of the turbulent energy smaller than the magnetic field perturbation provides an instability growth rate comparable to the resistive MHD prediction. In that case, neither the thermal pressure nor the Lorentz force are enhanced by turbulence. On the other hand, a moderate turbulence amplitude boosts the instability growth rate. In this case, turbulence increases the thermal pressure force and reduces at the same time the Lorentz force, the width of the diffusion region is then enlarged.^I

In large Reynolds number plasmas, the energy dissipated by turbulence exceeds that dissipated by the molecular resistivity. As predicted by the Alfvén Mach number derived in presence of turbulence, the reconnection process is dominated by the turbulence-related resistivity β . The investigations confirmed that the rate of energy conversion is larger for a small resistivity in presence of turbulence. Such behaviour differs from the Sweet-Parker rate $M_A \propto R_M^{-1/2}$. In fact, decreasing the molecular resistivity increases the gradients of the current density and vorticity which are the source that generate turbulence. A smaller molecular resistivity implies larger gradients and therefore stronger turbulence. The relation between the current density, vorticity, turbulent energy and cross-helicity was determined and used to provide the turbulence-enhanced reconnection rate.

It was also found that the regimes of energy release obtained for a constant turbulence timescale are artefacts of the model. In fact, the turbulence timescale $\tau = K/\varepsilon$ and the initial amplitude of turbulent energy K_0 can not be chosen independently. Moreover, imposing a constant turbulence timescale is comparable as imposing turbulence externally. In order to obtain a self-consistent mean field model of turbulence, the turbulent timescale was solved from the turbulence dynamics itself. Such a turbulence timescale is obtained solving the evolution equation of the turbulent energy dissipation rate ε in addition to the governing equations for the turbulent energy K and turbulent cross-helicity W . The turbulence timescale was then consistently obtained from the evolution of K and ε . As a result, the rate of energy conversion does not depend on the initial turbulence energy strength because the turbulence energy is adjusted by its dissipation rate in a consistent manner. Taking this improvement, the reconnection rate was found to be always faster than the resistive MHD rate, i.e., solely the regime of fast turbulent reconnection is left. This means that in the limit $\tau \approx \tau_A$, fast turbulent reconnection and an eddy size of the order of the current sheet width is automatically established. Figure 11.1 resumes the different turbulent regimes: In the limit $\tau \ll \tau_A$, turbulence resides at a scale that does not affect reconnection. On the other hand, turbulence enhances reconnection when $\tau \approx \tau_A$ while it is suppressing it for $\tau \gg \tau_A$. Here τ_A is the time required by an Alfvén wave to cross the current sheet width.

Since the evolution of a current sheet model strongly depends on the turbulence model used, *a posteriori* tests of high resolution direct numerical simulations (DNS) of plasmoids-unstable current sheets (CS) were carried out. The tested equilibrium were: i) Harris-type current sheets with or without a finite constant guide magnetic field \mathbf{B}_g , and ii) force-free current sheets which always have a finite guide field \mathbf{B}_g .

I. The initial turbulent energy K_0 determines the size of a turbulence eddy.

The reconnection rates were shown to be independent of the CS model during the first 100 Alfvén time. In the presence of a guide magnetic field, more time is needed to attain the maximum reconnection rate. The guide field influence was investigated from the turbulence viewpoint. DNSs turbulence results were analysed by means of a Gaussian filter for: i) a non-linear subgrid-scale (SGS) turbulence model and ii) a Reynolds-averaged turbulence model. Since a Gaussian filter does not preserve the Reynolds rules of averaging, the Reynolds-averaged model was extended to a SGS model of turbulence. For the appropriate filter width, both models were found to be applicable to tackle the problem of turbulent magnetic reconnection. The non-linear model has correlations with the turbulent electromotive force and stress-tensor which are above 98%. The SGS extension of the mean field turbulence model revealed correlations about 85%. Even if the non-linear model is better correlated, the SGS provides answers to the implication of turbulence into reconnection. The localisation of the turbulence-related resistivity at and around the diffusion layer was confirmed to be the most important reasons for the enhancement of reconnection. Moreover, the spatial quadrupolar structure of the turbulent cross-helicity W with similar polarities as the mean field vorticity was identified as another factor. The SGS results confirmed the theoretical prediction of the turbulent energy and cross-helicity spatial distribution during reconnection. The numerical solution of the transport equations for the turbulence (chapters (8)-(9)) is further validated as well as the assumption that turbulence dynamics is responsible for the rapid conversion of stored magnetic energy into plasma kinetic energy and heat.

The SGS extension of the Reynolds-averaged turbulence model also establish that the asymmetry in the direction parallel to the current flow, caused by a guide magnetic field, generates a residual helicity H . Through its action, the turbulent energy production at the diffusion region is reduced. The slower evolution of the energy conversion in presence of a guide magnetic field is attributable to the residual helicity. The SGS extension has further shown that the reconnection rate estimated by the grid-scale (mean-) field inhomogeneities matches the reconnection electric field. Turbulence was shown to strongly influence the reconnection rate at large-Reynolds-number-plasmas. The deviation of the reconnection rate from the Sweet-Parker scaling for plasmoid unstable current sheets was found to be due to the saturation of the turbulent resistivity.

In this dissertation, it was shown that a fast reconnection rate is obtained in presence of turbulence. It was also revealed that subgrid scale models grasp the effects of small scale fluctuations without resorting to a large computational power. SGS models were shown to apply to the problem of magnetic reconnection in large Reynolds number plasmas. The turbulence evolution of the turbulent energy, turbulent cross-helicity and residual helicity revealed that fast reconnection is obtained once the turbulence is maximum. The breaking of the mirror-symmetry in the reconnection plane is represented by a growing turbulent cross-helicity. On the other hand, a finite residual-helicity expresses that the direction parallel to the current flow is asymmetric. Most astrophysical plasmas bear a guide magnetic field, in the direction perpendicular to the current flow, whose amplitude is of the order of the reconnecting magnetic field. Its influence on the energy conversion rate is then non-negligible and turbulence quantifies its impact. The Reynolds-average turbulence model was shown to produce fast reconnection allowing Petschek-like fast reconnection through the localisation of the turbulent energy in the diffusion region. Finally, the direct numerical simulations confirmed the results obtained at low resolution by the

mean-field turbulence model: turbulence produces fast reconnection at large-magnetic-Reynolds-numbers.

11.1 Outlook

The influence of the turbulent stress-tensor was neglected in this work because the reconnection rate is obtained solving the induction equation. The turbulent stress-tensor is however influencing the mean MHD momentum equation. The data of the direct numerical simulations showed that the components of the turbulent stress-tensor contributing to the velocity in- and out-flow can become finite reaching the order of the turbulence-induced electromotive force. It would therefore be interesting to consider this aspect of turbulence on magnetic reconnection.

In this work, the influence of the guide magnetic field on the magnetic reconnection process was shown to be related to the residual helicity. Numerically, solving an evolution equation for the residual helicity would be desirable to investigate more deeply the contributions to its generation. This is especially important for the three-dimensional turbulent magnetic reconnection. For instance, the dynamical balance between the turbulent energy and the residual helicity might explain the phase of inhibited magnetic reconnection before the rapid release of magnetic energy of a flare. It might also give insights to the dynamo problem.

The fluctuations of the mass density, the pressure and the heat flux are not taken into account in the present Reynolds-averaged turbulence model. The reconnection rate estimated by the Alfvén Mach number M_A of the plasma inflow showed that the pressure variations along the current sheet might be important. Also, the consequences of the mass density fluctuations might be important for compressible plasmas. Considering these fluctuations is the next important step to build a proper Reynolds-averaged turbulence model.

To investigate compressible turbulent plasmas, another point of interest is the applicability of the non-linear SGS model for the description of the consequences of turbulence for magnetic reconnection. The almost perfect correlations of the turbulent electromotive force and stress-tensor make such model extremely reliable to investigate turbulence effects on the magnetic reconnection.

Investigation of three-dimensional turbulent reconnection using an SGS or Reynolds-averaged model of turbulence is also another important point for future work. Since three-dimensional simulations resolving all scales of plasmas interactions are computationally expensive, an SGS model of turbulence provides a good alternative to grasp the physics of turbulence for three-dimensional dynamos and magnetic reconnection. The form of the Reynolds-averaged turbulence model turbulent electromotive force and stress-tensor might provide important insights in the global comprehension of three-dimensional reconnection.

The implications of the residual helicity for the reconnection rate are also an interesting point to be investigated in the framework of fusion plasmas such as Tokamak or Stellarator experiments. These experiments try to avoid magnetic reconnection in order to sustain nuclear reactions in a time sufficient to extract energy. According to the turbulence dynamics, imposing a finite guide magnetic field parallel to the current flow at the reconnection sites slows down the reconnection rate of magnetic energy conversion. For a sufficiently large guide magnetic field, the time of plasma confinement might suffice to retrieve the energy from the nuclear reactions for industrial use.

Appendices

A Normalisation and Numerical Scheme

A.1 Normalisations

The equations of magnetohydrodynamics are written in the standard units system (SI) as

$$\frac{\partial \rho}{\partial t} = -\nabla \cdot (\rho \mathbf{V}) + \chi \nabla^2 \rho \quad (\text{A.1})$$

$$\frac{\partial \rho \mathbf{V}}{\partial t} = -\nabla \cdot \left[\rho \mathbf{V} \otimes \mathbf{V} + \frac{1}{2} \left(p + \frac{B^2}{\mu_0} \right) \mathbf{I} - \frac{1}{\mu_0} \mathbf{B} \otimes \mathbf{B} \right] + \chi \nabla^2 \rho \mathbf{V} \quad (\text{A.2})$$

$$\frac{\partial \mathbf{B}}{\partial t} = \nabla \times (\mathbf{V} \times \mathbf{B}) - (\nabla \eta) \times \mathbf{J} + \frac{\eta}{\mu_0} \nabla^2 \mathbf{B} \quad (\text{A.3})$$

$$\frac{\partial h}{\partial t} = -\nabla \cdot (h \mathbf{V}) + \frac{\gamma_0 - 1}{2\gamma_0 h^{\gamma_0 - 1}} (\eta \mathbf{J}^2) + \chi \nabla^2 h \quad (\text{A.4})$$

$$\nabla \cdot \mathbf{B} = 0 \quad (\text{A.5})$$

$$\nabla \times \mathbf{B} = \mu_0 \mathbf{J} \quad (\text{A.6})$$

where η is the electric resistivity and the χ terms represent viscosity that can smooth locally steep gradients. In the energy equation (A.4), the pressure variable is replaced $p = 2h^{\gamma_0}$ where γ_0 is the specific heat ratio C_p/C_v . For the adiabatic heat exchange, the ratio takes the value $\gamma_0 = 5/3$. The symbol \mathbf{I} is the identity matrix. In order to address numerically the set of equations (A.1)-(A.4), they are normalized as

$$x \rightarrow x_0 \hat{x} \quad (\text{A.7})$$

where x is any MHD variable and \hat{x} its dimensionless counterpart. The normalisation is given in table (A.1).

Physical quantity	Units	Obtained
Magnetic field	B_0	Given
Mass density	ρ_0	Given
Length scale	L_0	Given
∇ operator	∇_0	$1/L_0$
Velocity	V_{A_0}	$B_0/\sqrt{(\mu_0\rho_0)}$
Time	t_0	L_0/V_{A_0}
Current density	J_0	$B_0/(\mu_0 L_0)$
Pressure	p_0	$B_0^2/(2\mu_0)$
Internal energy	h_0	$p_0 = 2h_0^{\gamma_0}$
Electric field	E_0	$V_{A_0} B_0$
Resistivity	η_0	$\mu_0 V_{A_0} L_0$
χ	χ_0	$(B_0 L_0)/\sqrt{(\mu_0\rho_0)}$

Table A.1: Normalisation of the MHD equations

The set of equations (A.1)-(A.4) becomes:

$$\frac{\partial \hat{\rho}}{\partial \hat{t}} = -\hat{\nabla} \cdot (\hat{\rho} \hat{\mathbf{V}}) + \hat{\chi} \hat{\nabla}^2 \hat{\rho} \quad (\text{A.8})$$

$$\frac{\partial \hat{\rho} \hat{\mathbf{V}}}{\partial \hat{t}} = -\hat{\nabla} \cdot \left[\hat{\rho} \hat{\mathbf{V}} \otimes \hat{\mathbf{V}} + \frac{1}{2} (\hat{p} + \hat{B}^2) \mathbf{I} - \hat{\mathbf{B}} \otimes \hat{\mathbf{B}} \right] + \hat{\chi} \hat{\nabla}^2 \hat{\rho} \hat{\mathbf{V}} \quad (\text{A.9})$$

$$\frac{\partial \hat{\mathbf{B}}}{\partial \hat{t}} = \hat{\nabla} \times (\hat{\mathbf{V}} \times \hat{\mathbf{B}}) - (\hat{\nabla} \hat{\eta}) \times \hat{\mathbf{J}} + \hat{\eta} \hat{\nabla}^2 \hat{\mathbf{B}} \quad (\text{A.10})$$

$$\frac{\partial \hat{h}}{\partial \hat{t}} = -\hat{\nabla} \cdot (\hat{h} \hat{\mathbf{V}}) + \frac{\gamma_0 - 1}{\gamma_0 \hat{h}^{\gamma_0 - 1}} (\hat{\eta} \hat{\mathbf{J}}^2) + \hat{\chi} \hat{\nabla}^2 \hat{h} \quad (\text{A.11})$$

where the hat quantities are dimensionless.

The turbulent electromotive force \mathcal{E}_M is written in SI units as

$$\mathcal{E}_M = -\beta \mu_0 \bar{\mathbf{J}} + \gamma \sqrt{\mu_0 \rho} \bar{\boldsymbol{\Omega}} + \alpha \bar{\mathbf{B}} \quad (\text{A.12})$$

where the mean vorticity $\bar{\boldsymbol{\Omega}} = \nabla \times \bar{\mathbf{V}}$ is the curl of the mean velocity. The units of the turbulent transport coefficients β , γ and α are given in table (A.2).

Coefficient	Units (SI)
β	$m^2 s^{-1}$
γ	$m^2 s^{-1}$
α	ms^{-1}

Table A.2: Turbulent transport coefficients SI units

The turbulent transport coefficients in equation (A.12) are related to the turbulent energy K , the turbulent cross-helicity W and the turbulent residual helicity H . They are

modeled as:

$$K = \frac{1}{2} \left\langle \mathbf{V}'^2 + \frac{\mathbf{B}'^2}{\mu_0 \bar{\rho}} \right\rangle, \quad (\text{A.13})$$

$$W = \left\langle \frac{\mathbf{V}' \cdot \mathbf{B}'}{\sqrt{\mu_0 \bar{\rho}}} \right\rangle, \quad (\text{A.14})$$

$$H = \left\langle -\mathbf{V}' \cdot \boldsymbol{\Omega}' + \frac{\mathbf{B}' \cdot \mathbf{J}'}{\bar{\rho}} \right\rangle, \quad (\text{A.15})$$

where the ' denotes the fluctuating fields. The units of the turbulent energy, cross- and residual helicity are given in table (A.3).

Quantity	Units (SI)
K	$m^2 s^{-2}$
W	$m^2 s^{-2}$
H	ms^{-2}

Table A.3: Turbulent energy, cross- and residual helicity units

The governing equations for the turbulent energy K and turbulent cross-helicity W used in SI units are

$$\begin{aligned} \frac{\partial K}{\partial t} = & -\bar{\mathbf{V}} \cdot \nabla K + C_\beta \tau K \bar{\mathbf{J}}^2 \left(\frac{\mu_0}{\rho} \right) - C_\gamma \tau W \bar{\boldsymbol{\Omega}} \cdot \bar{\mathbf{J}} \sqrt{\frac{\mu_0}{\rho}} \\ & + \frac{\bar{\mathbf{B}}}{\sqrt{\mu_0 \bar{\rho}}} \cdot \nabla W - \frac{K}{\tau}, \end{aligned} \quad (\text{A.16})$$

$$\begin{aligned} \frac{\partial W}{\partial t} = & -\bar{\mathbf{V}} \cdot \nabla W + C_\beta \tau K \bar{\boldsymbol{\Omega}} \cdot \bar{\mathbf{J}} \sqrt{\frac{\mu_0}{\rho}} - C_\gamma \tau W \bar{\boldsymbol{\Omega}}^2 \\ & + \frac{\bar{\mathbf{B}}}{\sqrt{\mu_0 \bar{\rho}}} \cdot \nabla K - C_W \frac{W}{\tau}. \end{aligned} \quad (\text{A.17})$$

where a mean variable is denoted as \bar{x} . The normalisation of the turbulent energy K , the turbulent cross-helicity W , the turbulent resistivity β and dynamo term γ are given in table (A.4). The normalisation of the dynamo coefficient α and the turbulent energy dissipation rate ε and the residual helicity H are also provided.

Turbulent timescale τ	τ_0	L_0/V_{A_0}
K	K_0	$B_0^2/(\mu_0\rho_0)$
W	W_0	$B_0^2/(\mu_0\rho_0)$
H	H_0	$V_{A_0}^2/L_0$
ε	ε_0	K_0/t_0
β_0	β_0	$V_{A_0}L_0$
γ_0	γ_0	$V_{A_0}L_0$
α_0	α_0	V_{A_0}

Table A.4: Normalisation of the turbulent quantities

The hats above the dimensionless variables are omitted throughout the monograph.

A.2 MacCormack Scheme

The governing equations for the turbulent energy [equation (8.5)], the turbulent cross-helicity [equation (8.6)] and the turbulent energy dissipation rate [equation (9.3)] are solved with a MacCormack scheme within the GOEMHD3 code.¹⁰⁰ It is a second-order spatial finite difference method and second-order in time using an explicit two-step approach which solves first a predicted value (Q_{Pr}) then a corrected one (Q_{Co}). The final value is taken as the mean between the predicted and the corrected evaluations. The scheme is written in terms of the variable Q and a flux F as

$$(Q_{Pr})_j^{n+1} = Q_j^n - \frac{\Delta t}{\Delta y} (F_{j+1}^n - F_j^n), \quad (\text{A.18})$$

$$(Q_{Co})_j^{n+1} = Q_j^n - \frac{\Delta t}{\Delta y} (F_j^n - F_{j-1}^n), \quad (\text{A.19})$$

$$Q_j^{n+1} = \frac{1}{2} \left((Q_{Pr})_j^{n+1} + (Q_{Co})_j^{n+1} \right) - \Delta t S^n, \quad (\text{A.20})$$

where the variable j runs over spatial coordinates and the components n are running over the time. The symbol S in equations (A.18)-(A.20) corresponds to the source terms $\nabla^2 \mathbf{B}$, $\eta \mathbf{J}^2$, $\rho K/\tau_i$ and the diffusive terms proportional to χ . The scheme is used to evaluate the equations (A.1)-(A.4) since they are written in conservative forms. Equations (8.5)-(8.6) are, however, not in a conservative form. To apply the MacCormack scheme, the right-hand side of equations (8.5)-(8.6) are treated as source terms without flux, i.e., the source term F in equations (A.18)-(A.20) is set to zero. Equation (A.20) is then used to compute the predicted and the corrected values (S_{Pr}^n) and (S_{Co}^n) as

$$(Q_{Pr})_i^{n+1} = Q_{i,j}^n - 2\Delta t S_{Pr}^n, \quad (\text{A.21})$$

$$(Q_{Co})_i^{n+1} = Q_{i,j}^n - 2\Delta t S_{Co}^n, \quad (\text{A.22})$$

$$Q_{i,j}^{n+1} = \frac{1}{2} \left((Q_{Pr})_{i,j}^{n+1} + (Q_{Co})_{i,j}^{n+1} \right). \quad (\text{A.23})$$

The same procedure applies to the governing equation for the turbulent energy dissipation rate ε [equation (9.3)].

Finally, the parameters χ in equations (8.1)-(8.4) are used to smooth locally large gradients. They scale the amount of smoothing at the locations where strong gradients cause numerical instability. If the derivative of an MHD variable has a minimum of maximum, the χ parameters are switched on locally. In fact, the χ parameters are written as

$$\chi = \chi_l + \chi_h, \tag{A.24}$$

where the subscript l is for 'local' and h for 'homogeneous' since χ_h is homogeneously distributed in the simulation box. The parameters are define such that $\chi_l > \chi_h$. The purpose of χ_h is to avoid the generation of non-physical oscillating waves due to a sudden localised and finite χ_l .

B Mean Mass Density Fluctuations

In section (4.1.2), the fluctuations of the mass density are neglected, i.e., $\rho' = 0$. These fluctuations are now included in the mean field equations to show their effects. The mean mass density, mean momentum and mean induction equations read

$$\partial_t \bar{\rho} + \partial_i (\bar{\rho} \bar{V}_i) = -\partial_i \langle \rho' V'_i \rangle, \quad (\text{B.1})$$

$$\begin{aligned} \partial_t (\bar{\rho} \bar{V}_i) + \partial_j (\bar{\rho} \bar{V}_j \bar{V}_i) &= -\partial_i \bar{P} + \partial_j \mu \mathcal{S}_{ij} + \epsilon_{ijk} \bar{J}_j \bar{B}_k \\ &- \partial_j \left(\bar{\rho} \langle V'_i V'_j \rangle - \frac{1}{\mu_0} \langle B'_i B'_j \rangle + \bar{V}_j \langle \rho' V'_i \rangle + \bar{V}_i \langle \rho' V'_j \rangle \right) \\ &- \partial_t \langle \rho' V'_i \rangle - \partial_j \langle \rho' V'_i V'_j \rangle - \frac{1}{2\mu_0} \partial_i \langle B'_k B'_k \rangle, \end{aligned} \quad (\text{B.2})$$

$$\text{where} \quad \mathcal{S}_{ij} = \partial_i \bar{V}_j + \partial_j \bar{V}_i - \frac{2}{3} \partial_k \bar{V}_k \delta_{ij},$$

$$\partial_t \bar{B}_i = -\epsilon_{ijk} \partial_j \bar{E}_k, \quad (\text{B.3})$$

$$\bar{E}_i = -\epsilon_{ijk} \bar{V}_j \bar{B}_k + \eta \bar{J}_i - \langle \epsilon_{ijk} V'_j B'_k \rangle. \quad (\text{B.4})$$

The symbol μ is the molecular viscosity and η is the resistivity. The mass density fluctuation directly enters the mean mass density and the mean momentum equations [equations (B.1)-(B.2)]. The governing equation for the density variance is given as

$$\frac{D}{Dt} \langle \rho'^2 \rangle = -2 \langle \rho' V'_i \rangle \partial_i \bar{\rho} - 2 \langle \rho'^2 \rangle \partial_i \bar{V}_i, \quad (\text{B.5})$$

while the governing equation for the turbulent energy [equation (4.24)] becomes

$$\frac{DK}{Dt} \equiv \frac{D}{Dt} \left\langle \frac{V'_i V'_i + B'_i B'_i}{2} \right\rangle = -R_{ik} \partial_k \bar{V}_i - \mathcal{E}_M \cdot \bar{J} \quad (\text{B.6a})$$

$$- \nu \langle \partial_k V'_i \partial_k V'_i \rangle - \eta \langle \partial_k B'_i \partial_k B'_i \rangle \quad (\text{B.6b})$$

$$\begin{aligned} &+ \partial_k \left(\langle V'_i B'_i \rangle \bar{B}_k + \left\langle - \left(\frac{V'_i V'_i + B'_i B'_i}{2} + P'_M \right) V'_k \right\rangle \right. \\ &\left. + V'_i B'_i B'_k + \nu \partial_k \left\langle \frac{V'_i V'_i}{2} \right\rangle + \eta \partial_k \left\langle \frac{B'_i B'_i}{2} \right\rangle \right), \end{aligned} \quad (\text{B.6c})$$

$$- \frac{1}{\bar{\rho}} \langle \rho' V'_k \rangle \frac{D \bar{V}'_k}{Dt}, \quad (\text{B.6d})$$

where the terms (B.6d) is the contribution of the mass density fluctuation to the turbulent energy. The governing equation of the turbulent cross-helicity [equation (4.26)] is

changed due to the mass density fluctuation as

$$\frac{DW}{Dt} \equiv \frac{D}{Dt} \langle V'_i B'_i \rangle = -R_{ik} \partial_k \bar{B}_i - \mathcal{E}_M \cdot \bar{\Omega} \quad (\text{B.7a})$$

$$- (\nu + \eta) \langle \partial_k V'_i \partial_k B'_i \rangle \quad (\text{B.7b})$$

$$+ \partial_k \left[\left\langle \frac{V'_i V'_i + B'_i B'_i}{2} \right\rangle \bar{B}_k + \left\langle \left(\frac{V'_i V'_i + B'_i B'_i}{2} - p'_M \right) B'_k \right\rangle \right. \\ \left. - V'_i B'_i V'_k + \nu \langle B'_i \partial_k V'_i \rangle + \eta \langle V'_i \partial_k B'_i \rangle \right] \quad (\text{B.7c})$$

$$- \bar{B}_j R_{ki} + \epsilon_{jnm} \bar{V}_i \mathcal{E}_n \Big], \quad (\text{B.7d})$$

$$- \frac{1}{\bar{\rho}} \langle \rho' B'_k \rangle \frac{D\bar{V}'_k}{Dt}, \quad (\text{B.7e})$$

Retaining the mass density fluctuation, the turbulent electromotive force [equation (4.37)] reads

$$(\mathcal{E}_M)_i = \alpha \delta_{ij} \bar{B}_j + \gamma \epsilon_{ijk} \partial_j \bar{V}_k + \beta \epsilon_{ijk} \partial_j \bar{B}_k - \varrho \epsilon_{ijk} \frac{D\bar{V}_j}{Dt} \bar{B}_k. \quad (\text{B.8})$$

The transport coefficients, assumed to be scalars, are given as

$$\alpha = \tau \frac{1}{3} \langle B'_j \epsilon_{jki} \partial_k B'_i - V'_j \epsilon_{jki} \partial_k V'_i \rangle, \quad (\text{B.9})$$

$$\beta = \tau \frac{1}{3} \langle V'_n V'_n + B'_n B'_n \rangle, \quad (\text{B.10})$$

$$\gamma = \tau \frac{2}{3} \langle V'_n B'_n \rangle, \quad (\text{B.11})$$

$$\varrho = \tau \frac{\langle \rho'^2 \rangle}{\bar{\rho}^2}, \quad (\text{B.12})$$

where τ is the timescale of turbulence. In addition to the α -, β - and γ -term, the ϱ -term proportional to the mean mass density fluctuation appears in the turbulent electromotive force. For simplicity, a steady state flow is considered, i.e., $D\bar{V}/Dt = (\bar{V} \cdot \nabla) \bar{V}$ and equation (B.8) becomes

$$(\mathcal{E}_M)_i = \alpha \delta_{ij} \bar{B}_j + \gamma \epsilon_{ijk} \partial_j \bar{V}_k + \beta \epsilon_{ijk} \partial_j \bar{B}_k - \varrho \epsilon_{ijk} (\bar{V}_k \partial_k \bar{V}_j) \bar{B}_k. \quad (\text{B.13})$$

The sign of the last term determines whether the mass density fluctuation contributes to the production or annihilation of the mean magnetic field. Depending on the sign of $\varrho \epsilon_{ijk} (\bar{V}_k \partial_k \bar{V}_j) \bar{B}_k$, the last term in equation (B.13) contributes to the production or annihilation of the the magnetic flux. A much complex analysis is required to properly determine the role played by the mass density fluctuation in the compressible regime of reconnection.

C Two-Scales Direct-Interaction Approximation: TSDIA

Yoshizawa (1984) related the turbulent transport coefficients by means of the two-scale direct-interaction approximation formalism (TSDIA) which steps are briefly summarized.¹

- (A) The fast variations of the fluctuating fields are distinguished from the slow variations of the mean field. A scale parameter δ is introduced to separate the space and time scales as

$$\xi(\equiv \mathbf{x}); \mathbf{X}(\equiv \delta \mathbf{x}); \tau(\equiv t); T(\equiv \delta t) \quad (\text{C.1})$$

A variable f divided into its mean \bar{f} and its fluctuation f' is written as

$$f = \bar{f}(\mathbf{X}, T) + f'(\xi, \mathbf{X}; \tau, T). \quad (\text{C.2})$$

- (B) Fourier formalism is used to express the fluctuating variables in terms of the fast space and time variations

$$f'(\xi, \mathbf{X}; \tau, T) = \int f'(\mathbf{k}, \mathbf{X}; \tau, T) \exp[-i\mathbf{k} \cdot (\mathbf{x} - \mathbf{V}t)] d\mathbf{k}, \quad (\text{C.3})$$

where $\exp(i\mathbf{k}_a \mathbf{V}_a t)$ is necessary to eliminate the convection terms $i\mathbf{k}_a \mathbf{V}_a f'_a(\mathbf{k}; t)$.

- (C) An expansion around the small parameter δ of the Fourier components is carried

$$f'(\mathbf{k}, \mathbf{X}; \tau, T) = \sum_{n=0}^{\infty} \delta^n f'_n(\mathbf{k}, \mathbf{X}; \tau, T), \quad (\text{C.4})$$

Each f'_n ($n \geq 1$) can be written in terms of the mean fields.

- (D) The approximation comes in the retained terms of the δ expansion
- (a) All terms are kept in the $O(\delta)$ solutions
 - (b) Only the velocity derivative terms are retained in the $O(\delta^2)$ solutions
 - (c) Other terms than the third-order velocity derivative terms are suppressed in the $O(\delta^3)$ solutions
- (E) The turbulent stress-tensor R_{ij} and the turbulent electromotive force \mathcal{E}_M are obtained from the solutions of f'_n .

I. A detailed description of the formalism can be found in Yoshizawa.⁶⁶

D Filtering Minimisation

The Reynolds-averaged turbulence model is extended to a subgrid-scale (SGS) turbulence model in chapter (10). In order for such extension to be valid, it is required that cross-terms such as $\langle \mathbf{V}' \times \mathbf{B} \rangle$ have a small amplitude. To avoid such issues, the mean fields are usually defined by a global average. This kind of procedure cannot be used to infer information about turbulence because the spatial variations of the mean fields reflecting the substructures of the current sheet are needed. Also, a time average cannot be utilized since the assumption that the system reaches a steady state is not valid for a plasmoid unstable current sheet. The influence of the cross-terms can be minimized by reducing the difference

$$\overline{f}^F - \overline{\overline{f}^F} = \overline{f'}^F, \quad (\text{D.1})$$

for a chosen filter width. The mean field is considered to be \overline{f}^F . To respect Reynolds rules, equation (D.1) should be as close to zero as possible and $\overline{f'}^F / \overline{\overline{f}^F}$ close to one. Figure D.1 shows that an increased filter width reduces the correspondence of the SGS to a mean-field approach. The filter width is then chosen to be equal to five in order that: i) the spatial distributions of the turbulence is sufficiently resolved to validate the model, and ii) that the Reynolds rule are almost fulfilled such that the SGS extension is valid.

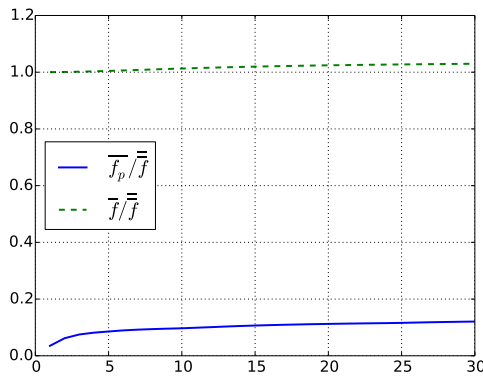


Figure D.1: Amplitude of the box average of the ratio $\overline{f'}/\overline{f}$ and $\overline{f}/\overline{f}$ with respect to the filter width. $f_p \equiv f'$. From Widmer *et al.*⁷¹

Bibliography

- [1] A. B. McDonald, M. G. Boulay, E. Bovin, M. Chen, F. A. Duncan, E. D. Earle, H. C. Evans, G. T. Ewan, R. J. Ford, A. L. Hallin, P. J. Harvey, J. D. Hepburn, C. Jillings, H. W. Lee, J. R. Leslie, H. B. Mak, A. B. McDonald, W. McLatchie, B. A. Moffat, B. C. Robertson, P. Skensved, B. Sur, I. Bleviss, F. Dalnoki-Veress, W. Davidson, J. Farine, D. R. Grant, C. K. Hargrove, I. Levine, K. McFarlane, T. Noble, V. M. Novikov, M. O'Neill, M. Shatkay, C. Shewchuk, D. Sinclair, T. Andersen, M. C. Chon, P. Jagam, J. Law, I. T. Lawson, R. W. Ollerhead, J. J. Simpson, N. Tagg, J. X. Wang, J. Bigu, J. H. M. Cowan, E. D. Hallman, R. U. Haq, J. Hewett, J. G. Hykawy, G. Jonkmans, A. Roberge, E. Saettler, M. H. Schwendener, H. Seifert, R. Tafiout, C. J. Virtue, S. Gil, J. Heise, R. Helmer, R. J. Komar, T. Kutter, C. W. Nally, H. S. Ng, R. Schubank, Y. Tserkovnyak, C. E. Waltham, E. W. Beier, D. F. Cowen, E. D. Frank, W. Frati, P. T. Keener, J. R. Klein, C. Kyba, D. S. McDonald, M. S. Neubauer, F. M. Newcomer, V. Rusu, R. Van Berg, R. G. Van de Water, P. Wittich, T. J. Bowles, S. J. Brice, M. Dragowsky, M. M. Fowler, A. Goldschmidt, A. Hamer, A. Hime, K. Kirch, J. B. Wilhelmy, J. M. Wouters, Y. D. Chan, X. Chen, M. C. P. Isaac, K. T. Lesko, A. D. Marino, E. B. Norman, C. E. Okada, A. W. P. Poon, A. R. Smith, A. Schuelke, R. G. Stokstad, Q. R. Ahmad, M. C. Browne, T. V. Bullard, P. J. Doe, C. A. Duba, S. R. Elliott, R. Fardon, J. V. Germani, A. A. Hamian, K. M. Heeger, R. M. Drees, J. Orrell, R. G. H. Robertson, K. Schaffer, M. W. E. Smith, T. D. Steiger, J. F. Wilkerson, J. C. Barton, S. Biller, R. Black, R. Boardman, M. Bowler, J. Cameron, B. Cleveland, G. Doucas, Ferraris, H. Fergami, K. Frame, H. Heron, C. Howard, N. A. Jelley, A. B. Knox, M. Lay, W. Locke, J. Lyon, N. McCaulay, S. Majerus, G. MacGregor, M. Moorhead, M. Omori, N. W. Tanner, R. Taplin, M. Thorman, P. T. Trent, D. L. Wark, N. West, J. Boger, R. L. Hahn, J. K. Rowley, M. Yeh, R. G. Allen, G. Buhler, and H. H. Chen. First Neutrino Observations from the Sudbury Neutrino Observatory. *Nuclear Physics B Proceedings Supplements*, 91:21–28, 2001. doi: 10.1016/S0920-5632(00)00918-X. 15
- [2] A. H. Gabriel. A magnetic model of the solar transition region. *Philosophical Transactions of the Royal Society of London Series A*, 281:339–352, May 1976. doi: 10.1098/rsta.1976.0031. 16
- [3] U. Narain and P. Ulmschneider. Chromospheric and coronal heating mechanisms. *Space Sci. Rev.*, 54:377–445, December 1990. doi: 10.1007/BF00177801. 16
- [4] U. Narain and P. Ulmschneider. Chromospheric and Coronal Heating Mechanisms II. *Space Sci. Rev.*, 75:453–509, February 1996. doi: 10.1007/BF00833341.

- [5] L. J. Milano, D. O. Gómez, and P. C. H. Martens. Solar Coronal Heating: AC versus DC. *ApJ*, 490:442–451, November 1997.
- [6] C. H. Mandrini, P. Démoulin, and J. A. Klimchuk. Magnetic Field and Plasma Scaling Laws: Their Implications for Coronal Heating Models. *ApJ*, 530:999–1015, February 2000. doi: 10.1086/308398. 16
- [7] M. J. Aschwanden. *Physics of the Solar Corona. An Introduction with Problems and Solutions (2nd edition)*. December 2005. 16, 17, 25
- [8] B. E. Schaefer, J. R. King, and C. P. Deliyannis. Superflares on Ordinary Solar-Type Stars. *ApJ*, 529:1026–1030, February 2000. doi: 10.1086/308325. 17
- [9] E. P. Rubenstein and B. E. Schaefer. Are Superflares on Solar Analogues Caused by Extrasolar Planets? *ApJ*, 529:1031–1033, February 2000. doi: 10.1086/308326. 17
- [10] R. G. Giovanelli. A Theory of Chromospheric Flares. *Nature*, 158:81–82, July 1946. doi: 10.1038/158081a0. 18
- [11] A. Reiners, M. Schüssler, and V. M. Passegger. Generalized Investigation of the Rotation-Activity Relation: Favoring Rotation Period instead of Rossby Number. *ApJ*, 794:144, October 2014. doi: 10.1088/0004-637X/794/2/144. 18
- [12] A. Reiners. Magnetic Fields in Low-Mass Stars: An Overview of Observational Biases. In P. Petit, M. Jardine, and H. C. Spruit, editors, *Magnetic Fields throughout Stellar Evolution*, volume 302 of *IAU Symposium*, pages 156–163, August 2014. doi: 10.1017/S1743921314001963. 18
- [13] Eric Priest and Terry Forbes. *Magnetic Reconnection*. Cambridge University Press, 2000. ISBN 9780511525087. URL <http://dx.doi.org/10.1017/CB09780511525087>. Cambridge Books Online. 18, 31, 56
- [14] S. von Goeler, W. Stodiek, and N. Sauthoff. Studies of Internal Disruptions and $m=1$ Oscillations in Tokamak Discharges with Soft-X-Ray Techniques. *Physical Review Letters*, 33:1201–1203, November 1974. doi: 10.1103/PhysRevLett.33.1201. 18
- [15] J. M. Fontenla, E. H. Avrett, and R. Loeser. Energy balance in the solar transition region. I - Hydrostatic thermal models with ambipolar diffusion. *ApJ*, 355:700–718, June 1990. doi: 10.1086/168803. 20
- [16] J. W. Dungey. Interplanetary Magnetic Field and the Auroral Zones. *Physical Review Letters*, 6:47–48, January 1961. doi: 10.1103/PhysRevLett.6.47. 20
- [17] B. C. Low and R. Wolfson. Spontaneous formation of electric current sheets and the origin of solar flares. *ApJ*, 324:574–581, January 1988. doi: 10.1086/165918. 21

- [18] E. N. Parker. Sweet's mechanism for merging magnetic fields in conducting fluids. *Journal of Geophysical Research*, 62(4):509–520, 1957. ISSN 2156-2202. doi: 10.1029/JZ062i004p00509. URL <http://dx.doi.org/10.1029/JZ062i004p00509>. 21, 23
- [19] P. A. Sweet. The Neutral Point Theory of Solar Flares. In B. Lehnert, editor, *Electromagnetic Phenomena in Cosmical Physics*, volume 6 of *IAU Symposium*, page 123, 1958. 21
- [20] H. E. Petschek. Magnetic Field Annihilation. *NASA Special Publication*, 50:425, 1964. 21, 23, 57
- [21] R. M. Kulsrud. Magnetic reconnection: Sweet-Parker versus Petschek. *Earth, Planets, and Space*, 53:417–422, June 2001. doi: 10.1186/BF03353251. 21, 57, 58, 98
- [22] D. Biskamp. *Magnetohydrodynamic Turbulence*. February 2008. 21, 30
- [23] L.D. Landau and E.M. Lifshitz. *Fluid Mechanics (Second Edition)*. Pergamon, 1987. ISBN 978-0-08-033933-7. URL <http://www.sciencedirect.com/science/article/pii/B9780080339337500118>. 21
- [24] P. Sagaut. BOOK REVIEW: Large Eddy Simulation for Incompressible Flows. An Introduction. *Measurement Science and Technology*, 12:1745–1746, October 2001. doi: 10.1088/0957-0233/12/10/707. 22, 49, 100
- [25] M. Miesch, W. Matthaeus, A. Brandenburg, A. Petrosyan, A. Pouquet, C. Cambon, F. Jenko, D. Uzdensky, J. Stone, S. Tobias, J. Toomre, and M. Velli. Large-Eddy Simulations of Magnetohydrodynamic Turbulence in Heliophysics and Astrophysics. *Space Sci. Rev.*, 194:97–137, November 2015. doi: 10.1007/s11214-015-0190-7.
- [26] W. Schmidt. Large Eddy Simulations in Astrophysics. *Living Reviews in Computational Astrophysics*, 1, October 2015. doi: 10.1007/lrca-2015-2. 22, 49, 100
- [27] P. H. Diamond, R. D. Hazeltine, Z. G. An, B. A. Carreras, and H. R. Hicks. Theory of anomalous tearing mode growth and the major tokamak disruption. *Physics of Fluids*, 27:1449–1462, June 1984. doi: 10.1063/1.864766. 22
- [28] A Lazarian and Ethan T Vishniac. Reconnection in a weakly stochastic field. *The Astrophysical Journal*, 517(2):700, 1999. 22, 23, 24
- [29] Grzegorz Kowal, A Lazarian, ET Vishniac, and K Otmianowska-Mazur. Numerical tests of fast reconnection in weakly stochastic magnetic fields. *The Astrophysical Journal*, 700(1):63, 2009. 23
- [30] N. Yokoi, K. Higashimori, and M. Hoshino. Transport enhancement and suppression in turbulent magnetic reconnection: A self-consistent turbulence model). *Physics of Plasmas*, 20(12):122310, December 2013. doi: 10.1063/1.4851976. 22, 60, 69

- [31] H. K. Moffatt. *Magnetic field generation in electrically conducting fluids*. 1978. 22
- [32] F. Krause and K.H. Rädler. *Mean-Field Magnetohydrodynamics and Dynamo Theory*. Akademie-Verlag, 1980. ISBN 9780080250410. URL <https://books.google.de/books?id=QJMJAQAATAAJ>. 22, 34, 39
- [33] E. N. Parker. Hydromagnetic Dynamo Models. *ApJ*, 122:293, September 1955. doi: 10.1086/146087. 22
- [34] A. Yoshizawa. Self-consistent turbulent dynamo modeling of reversed field pinches and planetary magnetic fields. *Physics of Fluids B*, 2:1589–1600, July 1990. doi: 10.1063/1.859484. 24, 39, 41, 42, 70, 91
- [35] J. Warnecke and A. Brandenburg. Surface appearance of dynamo-generated large-scale fields. *A&A*, 523:A19, November 2010. doi: 10.1051/0004-6361/201014287. 41
- [36] J. Warnecke, M. Rheinhardt, P. J. Käpylä, M. J. Käpylä, and A. Brandenburg. Turbulent transport coefficients in spherical wedge dynamo simulations of solar-like stars. *ArXiv e-prints*, January 2016. 22
- [37] A. Kolmogorov. The Local Structure of Turbulence in Incompressible Viscous Fluid for Very Large Reynolds' Numbers. *Akademiia Nauk SSSR Doklady*, 30: 301–305, 1941. 22, 51
- [38] O. Alexandrova, V. Carbone, P. Veltri, and L. Sorriso-Valvo. Small-Scale Energy Cascade of the Solar Wind Turbulence. *ApJ*, 674:1153-1157, February 2008. doi: 10.1086/524056. 22
- [39] O. Alexandrova, J. Saur, C. Lacombe, A. Mangeney, J. Mitchell, S. J. Schwartz, and P. Robert. Universality of Solar-Wind Turbulent Spectrum from MHD to Electron Scales. *Physical Review Letters*, 103(16):165003, October 2009. doi: 10.1103/PhysRevLett.103.165003. 22
- [40] Masaaki Yamada, Russell Kulsrud, and Hantao Ji. Magnetic reconnection. *Reviews of Modern Physics*, 82:603–664, Mar 2010. doi: 10.1103/RevModPhys.82.603. URL <http://link.aps.org/doi/10.1103/RevModPhys.82.603>. 23, 61
- [41] D. Biskamp and E. Schwarz. Localization, the clue to fast magnetic reconnection. *Physics of Plasmas*, 8:4729–4731, November 2001. doi: 10.1063/1.1412600. 23, 57, 98
- [42] Karl Schindler. *Physics of Space Plasma Activity*. Cambridge University Press, 2007. 23
- [43] J. Büchner. Astrophysical reconnection and collisionless dissipation. *Plasma Physics and Controlled Fusion*, 49:325, December 2007. doi: 10.1088/0741-3335/49/12B/S30. 23

- [44] I. Silin, J. Büchner, and A. Vaivads. Anomalous resistivity due to nonlinear lower-hybrid drift waves. *Physics of Plasmas*, 12(6):062902, June 2005. doi: 10.1063/1.1927096. 23
- [45] J. Büchner and N. Elkina. Vlasov Code Simulation of Anomalous Resistivity. *ssr*, 121:237–252, November 2005. doi: 10.1007/s11214-006-6542-6. 23
- [46] Toshio Terasawa. Hall current effect on tearing mode instability. *Geophysical research letters*, 10(6):475–478, 1983. 23
- [47] J. Birn, J. F. Drake, M. A. Shay, B. N. Rogers, R. E. Denton, M. Hesse, M. Kuznetsova, Z. W. Ma, A. Bhattacharjee, A. Otto, and P. L. Pritchett. Geospace environmental modeling (gem) magnetic reconnection challenge. *Journal of Geophysical Research: Space Physics*, 106(A3):3715–3719, 2001. ISSN 2156-2202. doi: 10.1029/1999JA900449. URL <http://dx.doi.org/10.1029/1999JA900449>. 23
- [48] N.F. Loureiro, Alexander A. Schekochihin, and Steven Charles Cowley. Instability of current sheets and formation of plasmoid chains. *Physics of Plasmas*, 14: 100703, 2007. doi: 10.1063/1.2783986. 23, 63, 67, 97
- [49] D. A. Uzdensky, N. F. Loureiro, and A. A. Schekochihin. Fast magnetic reconnection in the plasmoid-dominated regime. *Physical Review Letters*, 105:235002, Dec 2010. doi: 10.1103/PhysRevLett.105.235002. URL <http://link.aps.org/doi/10.1103/PhysRevLett.105.235002>. 23
- [50] Lei Ni, Bernhard Kliem, Jun Lin, and Ning Wu. Fast magnetic reconnection in the solar chromosphere mediated by the plasmoid instability. *The Astrophysical Journal*, 799(1):79, 2015. URL <http://stacks.iop.org/0004-637X/799/i=1/a=79>. 23, 61, 97
- [51] Y.-M. Huang and A. Bhattacharjee. Turbulent Magnetohydrodynamic Reconnection Mediated by the Plasmoid Instability. *ApJ*, 818:20, February 2016. doi: 10.3847/0004-637X/818/1/20. 23
- [52] A Bhattacharjee, Yi-Min Huang, H Yang, and B Rogers. Fast reconnection in high-lundquist-number plasmas due to the plasmoid instability. *Physics of Plasmas*, 16 (11):112102, 2009. 23, 97, 98, 119
- [53] J. W. Armstrong, B. J. Rickett, and S. R. Spangler. Electron density power spectrum in the local interstellar medium. *ApJ*, 443:209–221, April 1995. doi: 10.1086/175515. 23
- [54] R. Bruno and V. Carbone. The Solar Wind as a Turbulence Laboratory. *Living Reviews in Solar Physics*, 10:2, May 2013. doi: 10.12942/lrsp-2013-2. 23
- [55] K. T. Osman, W. H. Matthaeus, J. T. Gosling, A. Greco, S. Servidio, B. Hnat, S. C. Chapman, and T. D. Phan. Magnetic Reconnection and Intermittent Turbulence in the Solar Wind. *Physical Review Letters*, 112(21):215002, May 2014. doi: 10.1103/PhysRevLett.112.215002. 23

- [56] S. Servidio, W. H. Matthaeus, M. A. Shay, P. A. Cassak, and P. Dmitruk. Magnetic Reconnection in Two-Dimensional Magnetohydrodynamic Turbulence. *Physical Review Letters*, 102(11):115003, March 2009. doi: 10.1103/PhysRevLett.102.115003. 23, 98
- [57] S. Jabbari, A. Brandenburg, D. Mitra, N. Kleeorin, and I. Rogachevskii. Turbulent reconnection of magnetic bipoles in stratified turbulence. *ArXiv e-prints*, January 2016. 23, 24
- [58] W. H. Matthaeus and S. L. Lamkin. Rapid magnetic reconnection caused by finite amplitude fluctuations. *Physics of Fluids*, 28:303–307, January 1985. doi: 10.1063/1.865147. 23, 24, 98
- [59] A. Tsinober. *An Informal Conceptual Introduction to Turbulence*. 2009. doi: 10.1007/978-90-481-3174-7. 24
- [60] A. Yoshizawa. Turbulent Magnetohydrodynamic Dynamo: Modeling of the Turbulent Residual-Helicity Equation. *Journal of the Physical Society of Japan*, 65:124, January 1996. doi: 10.1143/JPSJ.65.124. 24, 39, 43
- [61] Eric R. Priest. *Solar Magnetohydrodynamics*. Kluwer Academic Publishers Group, 1982. 26
- [62] L. Spitzer. *Physics of Fully Ionized Gases*. 1962. 31
- [63] N. Yokoi. Cross helicity and related dynamo. *Geophysical and Astrophysical Fluid Dynamics*, 107:114–184, February 2013. doi: 10.1080/03091929.2012.754022. 39
- [64] H. Yoshimura. A model of the solar cycle driven by the dynamo action of the global convection in the solar convection zone. *apjs*, 29:467–494, December 1975. doi: 10.1086/190355. 41
- [65] A. Pouquet, U. Frisch, and J. Leorat. Strong MHD helical turbulence and the nonlinear dynamo effect. *Journal of Fluid Mechanics*, 77:321–354, September 1976. doi: 10.1017/S0022112076002140. 41
- [66] A. Yoshizawa. Statistical analysis of the deviation of the Reynolds stress from its eddy-viscosity representation. *Physics of Fluids*, 27:1377–1387, June 1984. doi: 10.1063/1.864780. 41, 42, 137
- [67] N. Yokoi. Cross helicity and related dynamo. *Geophysical & Astrophysical Fluid Dynamics*, 107(1-2):114–184, 2013. doi: 10.1080/03091929.2012.754022. URL <http://dx.doi.org/10.1080/03091929.2012.754022>. 41, 70
- [68] S. Candelaresi, A. Hubbard, A. Brandenburg, and D. Mitra. Magnetic helicity transport in the advective gauge family. *Physics of Plasmas*, 18(1):012903, January 2011. doi: 10.1063/1.3533656. 42
- [69] A. Yoshizawa, S.-I. Itoh, K. Itoh, and T. Tajima. Plasma and Fluid Turbulence: Theory and Modelling. Series in Plasma Physics. *Applied Mechanics Reviews*, 57:B5, 2004. doi: 10.1115/1.1641779. 42

- [70] N. Yokoi and M. Hoshino. Flow-turbulence interaction in magnetic reconnection. *Physics of Plasmas*, 18(11):111208, November 2011. doi: 10.1063/1.3641968. 43, 45, 71, 73, 86, 109
- [71] F. Widmer, J. Büchner, and N. Yokoi. Turbulent Plasmoid Reconnection. *ArXiv e-prints*, May 2016. 49, 98, 100, 115, 117, 118, 119, 120, 139
- [72] J. Smagorinsky. General Circulation Experiments with the Primitive Equations. *Monthly Weather Review*, 91:99, 1963. doi: 10.1175/1520-0493(1963)091<0099:GCEWTP>2.3.CO;2. 49
- [73] P. Grete, D. G. Vlaykov, W. Schmidt, D. R. G. Schleicher, and C. Federrath. Nonlinear closures for scale separation in supersonic magnetohydrodynamic turbulence. *New Journal of Physics*, 17(2):023070, February 2015. doi: 10.1088/1367-2630/17/2/023070. 49, 50, 106
- [74] G. Balarac, A. G. Kosovichev, O. Brugière, A. A. Wray, and N. N. Mansour. Modeling of the subgrid-scale term of the filtered magnetic field transport equation. *ArXiv e-prints*, October 2010. 50
- [75] P. S. Iroshnikov. Turbulence of a Conducting Fluid in a Strong Magnetic Field. *AZh*, 40:742, 1963. 51
- [76] R. H. Kraichnan. Inertial-Range Spectrum of Hydromagnetic Turbulence. *Physics of Fluids*, 8:1385–1387, July 1965. doi: 10.1063/1.1761412. 51
- [77] W. H. Matthaeus and M. L. Goldstein. Measurement of the rugged invariants of magnetohydrodynamic turbulence in the solar wind. *J. Geophys. Res.*, 87:6011–6028, August 1982. doi: 10.1029/JA087iA08p06011. 51
- [78] Katepalli R. Sreenivasan. On the universality of the kolmogorov constant. *Physics of Fluids*, 7(11):2778–2784, 1995. doi: <http://dx.doi.org/10.1063/1.868656>. URL <http://scitation.aip.org/content/aip/journal/pof2/7/11/10.1063/1.868656>. 52
- [79] J. Birn, J. F. Drake, M. A. Shay, B. N. Rogers, R. E. Denton, M. Hesse, M. Kuznetsova, Z. W. Ma, A. Bhattacharjee, A. Otto, and P. L. Pritchett. Geospace Environmental Modeling (GEM) magnetic reconnection challenge. *J. Geophys. Res.*, 106:3715–3720, March 2001. doi: 10.1029/1999JA900449. 57
- [80] A. Bhattacharjee. Impulsive Magnetic Reconnection in the Earth’s Magnetotail and the Solar Corona. *ARA&A*, 42:365–384, September 2004. doi: 10.1146/annurev.astro.42.053102.134039. 57
- [81] D. Biskamp. Magnetic reconnection via current sheets. *Physics of Fluids*, 29: 1520–1531, May 1986. doi: 10.1063/1.865670. 58
- [82] N. F. Loureiro, S. C. Cowley, W. D. Dorland, M. G. Haines, and A. A. Schekochihin. X-Point Collapse and Saturation in the Nonlinear Tearing Mode Reconnection. *Physical Review Letters*, 95(23):235003, December 2005. doi: 10.1103/PhysRevLett.95.235003. 58

- [83] B. Kliem, M. Karlický, and A. O. Benz. Solar flare radio pulsations as a signature of dynamic magnetic reconnection. *aap*, 360:715–728, August 2000. 61
- [84] P. A. Muñoz, D. Told, P. Kilian, J. Büchner, and F. Jenko. Gyrokinetic and kinetic particle-in-cell simulations of guide-field reconnection. Part I: macroscopic effects of the electron flows. *ArXiv e-prints*, April 2015. 61, 72
- [85] J. M. TenBarge, W. Daughton, H. Karimabadi, G. G. Howes, and W. Dorland. Collisionless reconnection in the large guide field regime: Gyrokinetic versus particle-in-cell simulations. *Physics of Plasmas (1994-present)*, 21(2):020708, 2014. doi: <http://dx.doi.org/10.1063/1.4867068>. URL <http://scitation.aip.org/content/aip/journal/pop/21/2/10.1063/1.4867068>. 61
- [86] R. Horiuchi and T. Sato. Particle simulation study of collisionless driven reconnection in a sheared magnetic field. *Physics of Plasmas*, 4:277–289, February 1997. doi: 10.1063/1.872088. 61
- [87] Paolo Ricci, Giovanni Lapenta, and J.U. Brackbill. Kinetic simulations of collisionless magnetic reconnection in presence of a guide field. *Physics of Plasmas*, 11:4102–4114, 2004. doi: 10.1063/1.1768552.
- [88] P. L. Pritchett and F. V. Coroniti. Three-dimensional collisionless magnetic reconnection in the presence of a guide field. *Journal of Geophysical Research (Space Physics)*, 109:A01220, January 2004. doi: 10.1029/2003JA009999. 61
- [89] B. Kliem and J. Schumacher. Dynamic three-dimensional spontaneous reconnection in a sheared current sheet. In J. Büchner, C. T. Dum, and M. Scholer, editors, *Space Plasma Simulation*, page 264, 2001. 61
- [90] M. Ugai. Three-dimensional evolution of the fast reconnection mechanism in a sheared current sheet. *Physics of Plasmas*, 17(3):032313, March 2010. doi: 10.1063/1.3369886.
- [91] M. Ugai. Three-dimensional evolution of the fast reconnection mechanism in a force-free current sheet. *Physics of Plasmas*, 17(6):062901, June 2010. doi: 10.1063/1.3431097. 61
- [92] H. P. Furth, J. Killeen, and M. N. Rosenbluth. Finite-Resistivity Instabilities of a Sheet Pinch. *Physics of Fluids*, 6:459–484, April 1963. doi: 10.1063/1.1706761. 63
- [93] R.A. Treumann and W. Baumjohann. *Advanced Space Plasma Physics*. Imperial College Press, 1997. ISBN 9781860940262. URL <https://books.google.de/books?id=8wB-QgAACAAJ>. 64, 65
- [94] F. Widmer, J. Büchner, and N. Yokoi. Sub-grid-scale description of turbulent magnetic reconnection in magnetohydrodynamics. *Physics of Plasmas*, 23(4):042311, April 2016. doi: 10.1063/1.4947211. 66, 69, 73, 74, 75, 76, 77, 78, 79, 80, 81, 82, 83, 85, 87, 92, 118

-
- [95] N. F. Loureiro, A. A. Schekochihin, and D. A. Uzdensky. Plasmoid and Kelvin-Helmholtz instabilities in Sweet-Parker current sheets. *Phys. Rev. E*, 87(1):013102, January 2013. doi: 10.1103/PhysRevE.87.013102. 67, 97
- [96] N. Yokoi and F. Hamba. An application of the turbulent magnetohydrodynamic residual-energy equation model to the solar wind. *Physics of Plasmas*, 14(11):112904, November 2007. doi: 10.1063/1.2792337. 69
- [97] N. Yokoi and G. Balarac. Cross-helicity effects and turbulent transport in magnetohydrodynamic flow. *Journal of Physics Conference Series*, 318(7):072039, December 2011. doi: 10.1088/1742-6596/318/7/072039. 69
- [98] K. Higashimori, N. Yokoi, and M. Hoshino. Explosive turbulent magnetic reconnection. *Physical Review Letters*, 110:255001, Jun 2013. doi: 10.1103/PhysRevLett.110.255001. URL <http://link.aps.org/doi/10.1103/PhysRevLett.110.255001>. 69, 71, 74, 92
- [99] F. Hamba. Turbulent dynamo effect and cross helicity in magnetohydrodynamic flows. *Physics of Fluids*, 4:441–450, February 1992. doi: 10.1063/1.858314. 71
- [100] J. Skála, F. Baruffa, J. Büchner, and M. Rampp. The 3D MHD code GOEMHD3 for astrophysical plasmas with large Reynolds numbers. Code description, verification, and computational performance. *A&A*, 580:A48, August 2015. doi: 10.1051/0004-6361/201425274. 71, 132
- [101] M. J. Nemati, Z. X. Wang, L. Wei, and B. I. Selim. Plasmoid instability in double current sheets. *Physics of Plasmas*, 22(1):012106, January 2015. doi: 10.1063/1.4906052. 72
- [102] R. Samtaney, N. F. Loureiro, D. A. Uzdensky, A. A. Schekochihin, and S. C. Cowley. Formation of Plasmoid Chains in Magnetic Reconnection. *Physical Review Letters*, 103(10):105004, September 2009. doi: 10.1103/PhysRevLett.103.105004. 97
- [103] W. Daughton, V. Roytershteyn, B. J. Albright, H. Karimabadi, L. Yin, and K. J. Bowers. Transition from collisional to kinetic regimes in large-scale reconnection layers. *Physical Review Letters*, 103(6):065004, August 2009. doi: 10.1103/PhysRevLett.103.065004. 97
- [104] N. A. Murphy, A. K. Young, C. Shen, J. Lin, and L. Ni. The plasmoid instability during asymmetric inflow magnetic reconnection. *Physics of Plasmas*, 20(6):061211, June 2013. doi: 10.1063/1.4811470. 98, 119

Scientific Contributions

Refereed publication

1. F. Widmer, J. Büchner and N. Yokoi "*Sub-Grid-Scale Description of Turbulent Magnetic Reconnection in Magnetohydrodynamics*", *Physics of Plasmas* **23**, 042311, 2016.

Submitted publication

1. F. Widmer, J. Büchner and N. Yokoi "*Characterizing Plasmoid Reconnection by Turbulence Dynamics*", *Physics of Plasmas*.

Acknowledgments

I acknowledge the SFB Project A15 of the CRC 963 as well as the International Max Planck Research School (IMPRS) for Solar System Science at the University of Göttingen (Germany) for the financial support during the PhD. I also thanks the IMPRS coordinator Dr. Sonja Schuh for her help regarding the regulations of the University of Göttingen and the Max Planck Institute for Solar System Research.

I also thanks the members of my thesis advisors committee: Prof. Dr. Laurent Gizon, Prof. Dr. Jörg Büchner and Dr. Wolfram Schmidt as well as the additional member of the thesis committee: Prof. Dr. Stefan Dreizler, Prof. Dr. Hardi Peter and Prof. Dr. Andreas Tilgner.

I wish to first thanks my supervisor Professor Doctor Jörg Büchner from the Max Planck Institute for Solar System Research in Göttingen. He gave me the opportunity to start a PhD in plasma physics (MHD) even if my knowledge about the subject was minimal. Prof. Dr. Büchner also took a lot of his time in the supervision of the papers representing my work as well as for the thesis. Finally, he acquainted me to several important persons regarding my work.

I also want to thanks the colleagues from of the theory and simulations of solar system plasma (TSSSP) group of Prof. Dr. Büchner: Dr. Patrick Kilian, Dr. Neeraj Jain, Dr. Skåla Jan and Dr. Muñoz Sepúlveda Patricio A. In particular, I thanks Jan Skåla for its patience in teaching me how to use the GOEMHD3 code but also for his friendship. My deepest thanks go to Patricio Muñoz for all the help he might have provided with respect to any subjects. Its kindness and advises were of great help. Without Jan Skåla and Patricio Muñoz, my time within the TSSSP group would not have been such an enjoyable time. I also thanks all the IMPRS and non-IMPRS students with whom I shared the office. A particular thanks to Dr. Yadav Rakesh who convinced me to use Python instead of idl to analyse my data. Additionally, I thanks Dr. Yu Sijie for its friendship and great welcoming in Beijing. Naturally I thanks all other members of my office for the great time we had together. Finally, I thanks Dr. Warnecke Jörn for the discussions about mean-field theory and advises he gave me.

I also wish to thanks the colleagues from the University of Göttingen for the valuable discussions about turbulence and subgrid-scale modelling. In particular, Dr. Wolfram Schmidt, Dr. Vlaykov Dimitar and Philipp Grete.

The last person I would like to profoundly thank is Professor Doctor Nobumitsu Yokoi from the University of Tokyo. He taught me a lot about the physics of mean field turbulence during the various time I had the chance to work with him. In particular during my extended stay for the magnetic reconnection workshop at the Nordic Institute for Theoretical Physics (NORDITA). I also want to thank Prof. Yokoi for his kindness. Especially, for his warm welcoming at the University of Tokyo. Finally, I profoundly thank him for

his kind and cheering words which were of great help during some of the difficult periods I faced during my PhD. A great thanks to all the persons I may have forgotten to acknowledge.

Les prochains remerciements sont adressés à ma femme Marie Widmer qui a toujours été présente durant ma thèse. Sa gentillesse, son amour et ses encouragements m'ont permis de finir ma thèse dans le temps imparti. Sans sa présence à mes côtés, les difficultés liées à ma vie de doctorant auraient été plus difficile à surmonter.

Pour finir je tiens à remercier ma mère Valérie Widmer. Sa confiance inconditionnelle en mes capacités à achever des études de physique a été d'un grand soutien. Sans ma mère je n'aurais probablement jamais été aussi loin dans la vie. Merci maman!

Curriculum Vitae

- ◇ Last and first name: Widmer, Fabien
- ◇ Date of birth: 12.07.1983
- ◇ Place of birth: Geneva, Switzerland
- ◇ Nationality: Swiss

-
- ‡ August 2013 - August 2016: PhD candidate at the Max Planck Institute for Solar System Research, Göttingen, Germany. Title of the thesis: "*Magnetohydrodynamic Simulation of Reconnection in Turbulent Astrophysical Plasmas*".
 - ‡ 2010 - 2012 Master of Science in Physics, University of Geneva, Switzerland. Theoretical direction. Master thesis title: "*Master Thesis in String Theory: Type IIA Massive Supergravity in Ten Dimensions*".
 - ‡ 2007 - 2010 Bachelor of Science in Physics, University of Geneva, Switzerland.
 - ‡ 2005 - 2007 Bachelor of Science in Physics, École Polytechnique Fédérale de Lausanne EPFL, Lausanne, Switzerland.
 - ‡ 2002 - 2005 High School, Maturité cantonale, Gymnase de Nyon, Nyon, Switzerland.